Western Australia School of Mines

Department of Exploration Geophysics

Seismic monitoring of carbonate reservoirs using stochastic time-lapse inversion

Mateus Góes Castro Meira

This thesis is presented for the Degree of

Doctor of Philosophy

of

Curtin University

December 2016

To my family and friends.

Declaration

"To the best of my knowledge and belief this thesis contains no material previously published by any other person except where due acknowledgement has been made. This thesis contains no material which has been accepted for the award of any other degree or diploma in any university."

Signature: 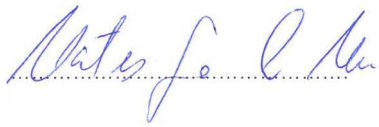

Date: 28/11/2016

Abstract

Time-lapse seismic monitoring of fluids inside reservoirs has become an established technology in the oil and gas industry and CO_2 sequestration projects. The idea of time-lapse seismic technology is to repeat seismic acquisition over a reservoir under production and compare the subsequent seismic datasets. Variations in dynamic properties, such as oil saturation or pressure, in the area between or away from the wells can then be determined. Despite success in seismic reservoir monitoring, quantitative estimation of the variations in rock and fluid properties is still challenging. One of the ways to overcome this challenge is to employ time-lapse inversion algorithms.

Carbonate reservoirs contain a significant portion of the world's oil and gas reserves but present low recovery factors motivate the development of new approaches to reservoir management. In this context, time-lapse inversion has the potential to provide valuable data on spatio-temporal distribution of dynamic reservoir properties for improved reservoir management. Ultimately, the application of this method can increase the recoverable volume of hydrocarbons.

The aim of this research is to assess the applicability of stochastic time-lapse inversion, such as the Bayesian time-lapse inversion algorithm Delivery4D, to carbonate reservoirs. To achieve this, the following objectives are proposed:

-Estimate dynamic properties in a carbonate reservoir using time-lapse stochastic inversion;

-Evaluate the uncertainty in the reservoir dynamic properties using time-lapse stochastic inversion.

To accomplish these tasks I developed a multidisciplinary workflow integrating geological, petrophysical, geophysical and reservoir engineering datasets to perform a Bayesian stochastic time-lapse seismic inversion on two datasets. The first one comprises a synthetic time-lapse seismic dataset used in a feasibility study for a CO2 injection into a saline formation. Since I had access to the flow simulation model used to generate the synthetic seismic data, I could assess the performance of the time-lapse stochastic inversion methodology in a controlled environment and compare the results to the 'ground truth'. The effects of noise and parameterization issues were addressed to evaluate the robustness of the inversion methodology. Equipped with the knowledge about the limits of the method, gathered during the synthetic data inversion, I went on to perform a

stochastic time-lapse seismic inversion on a second dataset, an Albian carbonate oilfield located in the Campos Basin, offshore Brazil.

The carbonate reservoir inversion result consists of a posterior distribution of model's parameters which had its maximum singled out and was also sampled to provide a statistical description of each parameter. Although the inversion algorithm allows for many types of outputs, I focused my analysis on dynamic properties (fluid saturation and pressure) and porosity. When compared with the flow simulation model I found that the oil saturation maximum *a posteriori* (MAP) model presents areas with different levels of quantitative and qualitative agreement. The results indicate compartmentalization in the field that was not incorporated into the flow simulation model. Additionally, when comparing the oil saturation standard deviation before and after the inversion, the decrease is up to 20% in areas presenting relatively high porosity (larger than 20%). I associate this result with a higher detectability of the time-lapse signal.

In conclusion, I have found that the stochastic time-lapse inversion methodology, in its current design, helps to understand the movement of fluid inside a carbonate. I have also concluded that the results are more reliable when the porosity is relatively high. In that case, the uncertainty regarding the fluid saturation is diminished by the introduction of the seismic information. In the present case, the porosity cut-off was 20%.

Acknowledgments

Firstly, I would like to thank my supervisor Professor Boris Gurevich for his guidance and inspiring ideas. I would also like to thanks Dr. James Gunning for all the assistance and guidance in the understanding of the code and for supply figures for this thesis.

I am also grateful for the interesting technical discussions with Dr. Stephanie Vialle and collaboration with Dr. Stanislav Glubokovskikh.

I would like to thank all the staff members of the Department of Exploration Geophysics, who have assisted me in the course of my research with special thanks to Ms. Deirdre Hollingsworth for her administrative help and Mr. Robert Verstandig for his technical help.

I would also like to thank my colleagues at the Department of Exploration Geophysics for the useful discussions and friendship throughout my PhD project, specially Dr. Qiamu Qi and Dr. Eva Caspari

I am also grateful to the financial assistance of Petrobras, the state-owned Brazilian oil company through the commitment of the following E&Pmanagers who endorsed this project: Solange da Silva Guedes, Carlos Eugênio da Conceição, Paulo Johann and Carlos Pedroso. Their encouragement and support during all stages of this journey were extremely important and very much appreciated.

Thanks are due to the extremely helpful Juarez E. R. da Silva for all his hard work and guidance regarding the arrangements associated with my PhD in Australia.

I am also grateful to all the Petrobras team who helped me with my PhD, specially, Marcos Grochau, Marimônica Roberta Jaeger de Carvalho, Marcos Sebastião, Elizabeth Kautscher De Barros, Leonardo Alvim, Álvaro Favinha and Biazid Halabi Filho.

I would also like to express thanks to ANP, the Brazilian national petroleum agency, for the authorization to utilize the data presented in this work.

The Otway Stage 2C Project received CO2CRC funding through its industry

members and research partners, the Australian Government under the CCS Flagships Programme, the Victorian State Government, and the Global CCS Institute. The authors wish to acknowledge financial assistance provided through Australian National Low Emissions Coal Research and Development (ANLEC R&D) supported by the Australian Coal Association Low Emissions Technology Limited and the Australian Government through the Clean Energy Initiative.

I would like to acknowledge Schlumberger for kindly providing the Petrel exploration and production software platform for this study.

Finally, I would like to thank my wife Milena and my sons, João Paulo and Antônio for their support and patience.

List of publications

Extended abstracts

Meira, M. G. C., Gurevich, B., Gunning, J., and Pevzner, R. (2015). Stochastic Time-lapse Inversion of a CO2 Sequestration Synthetic Seismic Data.ASEG Extended Abstracts, 2015(1), 1-4.

Meira, M., Gunning, J., Gurevich, B., and Pevzner, R. (2015, December). Implications of Noise Contamination in Stochastic Time Lapse Inversion. In2015 SEG Annual Meeting. Society of Exploration Geophysicists.

Meira, M. Pevzner, R. Caspari, E. and Gurevich, B. (2014). Stochastic Time-lapse Inversion of a CO2 Sequestration Synthetic Seismic Data, in 76th EAGE Conference & Exhibition, 16-19 June 2014. Amsterdam, Netherlands: European Association of Geoscientists and Engineers.

Contents

Nomenclature

Glossary of abbreviations

MAP Maximum *a posteriori*

RMS Root mean square

VSP Vertical seismic profiling

NG Net-to-gross

Symbols

μ shear modulus

AI Acoustic impedance

K bulk modulus

V_P compressional wave velocity

V_S shear wave velocity

σ_n “noise rms”

ρ density

CHAPTER 1. INTRODUCTION

1.1 TIME-LAPSE SEISMIC MONITORING

Time-lapse seismic monitoring of fluids inside reservoirs has become an established technology in the oil and gas industry and CO_2 sequestration projects. Many successful applications of time-lapse seismic data for reservoir monitoring are presented in the literature (Calvert, 2005). According to Johnston (2013), the addition of value to the field is the fundamental factor to the success of a time-lapse seismic monitoring project. Amundsen and Landrø (2007) highlight that, on average, the application of time-lapse seismic technology to a project will represent an estimated 6% reduction in drilling costs and 5% addition of reserves per field. The economic impact represented by these numbers in many cases can justify the investment in seismic acquisition for reservoir monitoring. Johnston (2013) also points out that geological, geomechanical and fluid simulation models are more predictive if constrained by time-lapse seismic data.

Deepwater fields such as the ones located in Brazil, West Africa and the Gulf of Mexico are among the cases where time-lapse seismic data has had the biggest economic impact (Johnston, 2013). The reasons for this are the very high drilling and intervention costs when compared with seismic acquisition costs and uncertainties associated with sweep efficiency like compartmentalization and baffling. These problems can be minimized by the application of time-lapse seismic technology.

The promise of time-lapse seismic technology is that by repeating seismic acquisition over a reservoir under production and comparing the differences between the subsequent seismic datasets (vintages), it would be possible to determine the variation in dynamic properties (Calvert,2005). The differences between seismic acquisition vintages can be expressed as amplitude differences created by changes in the layer's impedance contrast or time-shifts created by variations in the layer's velocities and/or thicknesses.

Reservoir monitoring using time-lapse seismic technology is a multidisciplinary effort involving geophysics, geology, reservoir engineering, rock physics and

petrophysics. It relies on iterations on a cycle (Figure 1) that starts with 1) a previous reservoir model followed by 2) the planning, acquisition and processing of time-lapse seismic data, 3) interpretation of time-lapse seismic data by a multidisciplinary team of geoscientists and finishes with 4) an updated model that can explain the differences between seismic vintages based on variations in dynamic properties of the reservoir.

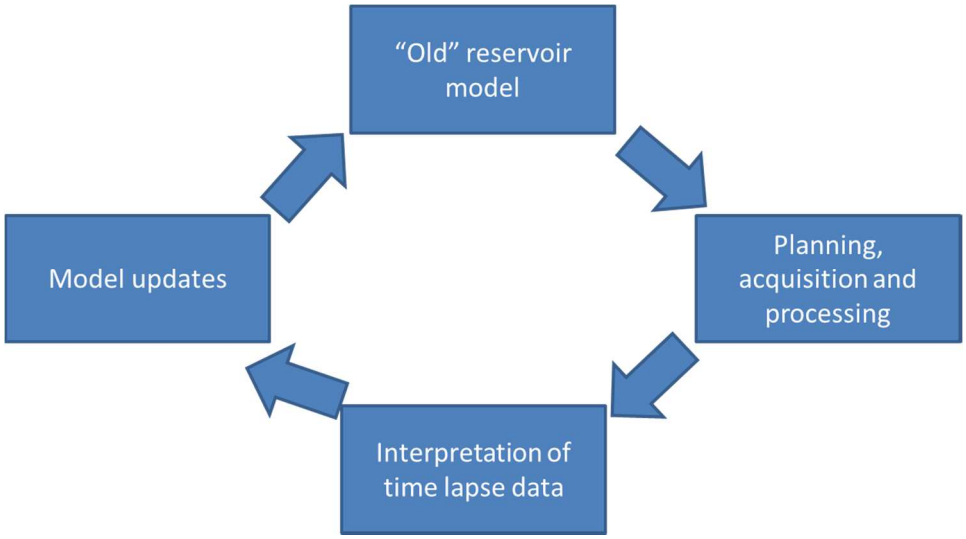

Figure 1 *Reservoir monitoring cycle with time-lapse data.*

Ideally, a static model comprising the porosity and permeability fields would be completely defined before the time-lapse data acquisition and all the changes found in the time-lapse seismic data would be explained by the changes in dynamic variables. In reality, many unexpected effects revealed by the time-lapse seismic data are associated with unknowns in the static model and updates in the static model are required. This work focuses on the third step of the reservoir monitoring cycle: the interpretation of time-lapse data.

1.2 INTERPRETATION OF TIME-LAPSE SEISMIC DATA

The interpretation of time-lapse seismic data can be qualitative or quantitative. The choice of interpretation strategy depends on the quality of the data and the objectives of the geoscientist. If the quality of data ranges from poor to good quality and the geoscientist wants to identify bypassed oil, baffles, flood fronts and contact movements, qualitative interpretation of saturation changes in terms of sweep is applicable. If the same data quality requirements hold and the geoscientists are interested in inferring connectivity, fault seal and compartmentalization, qualitative

interpretation of pressure changes should be used. When the seismic data quality is of relatively higher quality and processed with amplitude preservation, it can be inverted into saturation and pressure changes to be compared directly with reservoir-simulation predictions. Quantitative interpretation of time-lapse seismic data is an active research area and can be used to solve ambiguities regarding pressure and saturation responses, estimate uncertainty and provide numerical data for history-match algorithm (MacBeth, Floricich and Soldo, 2006). An example of quantitative interpretation can be found in the work of Chadwick et al. (2010). In this work, the authors used model-based inversion of time-lapse data and other ancillary quantitative methods, such as frequency decomposition, to monitor a CO_2 storage operation on the Sleipner field, North Sea.

In comparison to qualitative interpretation, the presence of non-repeatable noise may represent a bigger challenge to time-lapse quantitative interpretation because, in many situations, it cannot be discriminated from the time-lapse signal. This is especially harmful to reservoirs consisting of highly stiff rocks since the amplitude of its time-lapse signal is inherently low and may become undetectable if surpassed by the non-repeatable noise amplitude. Quantitative interpretation is also critically dependent on the rock physics model, also known as the petroelastic model, utilized to map the changes in the reservoir´s dynamic properties (fluid saturation, pressure and temperature) into elastic properties (Vp, Vs and ρ) (Qi, Müller and Gurevich, 2016).

The determination of the correct rock physics model is a key step in the time-lapse interpretation workflow and is initiated by the analysis of the reservoir's geological history to determine the geological processes the reservoir has gone through. This step is followed by a petrographic thin-section examination of the reservoir's rock samples. The thin-section examination aims to visually or automatically determine the petrophysical elements of the rocks, such as the types of pores and the types of cements. These elements can determine the choice of petroelastic model used in the time-lapse interpretation. After that, well logs and core analysis data are crossplotted using appropriate templates in order to identify the petroelastic models that better describe the reservoir rocks. Finally, synthetic seismic data can be generated using different petroelastic models and compared with real data to determine which model should be employed in the interpretation. Petroelastic models are also used in qualitative interpretation, modelling and feasibility studies.

The determination of a model can be a challenging exercise due to the number of parameters employed in the models, the heterogeneity of the reservoir, the different spatial and temporal scales of data acquisition, uncertainty in the data values and overlapping of model predictions. The most popular petroelastic model is given by Gassmann (1951). His model is commonly applied to predict velocity variations derived from different pore fluid saturation and predominates in the analysis of time-lapse reservoir monitoring (Han and Batzle, 2004). As mentioned previously, the seismic response of reservoirs is determined by the elastic properties (Vp, Vs and ρ). However, neither Vp nor Vs is a good indicator of fluid saturations because of the coupling between Vp and Vs through the shear modulus and the bulk density. In contrast bulk modulus and shear modulus behave independently to the change in fluid saturation (Han and Batzle, 2004). This happens because "*The bulk-volume deformation produced by a passing seismic wave results in a pore-volume change and causes a pressure increase in pore fluid. This pressure increase stiffens the rock frame and causes an increase in bulk modulus. Shear deformation, however, does not produce a pore-volume change, and consequently, different fluids do not affect shear modulus. Therefore, any fluid-saturation effect should correlate mainly to a change in bulk modulus*" (Han and Batzle, 2004). The model assumes that the porous material is isotropic, elastic, monomineralic and homogenous, the pore space is well connected and in pressure equilibrium, the medium is a closed system with no pore fluid movement across boundaries and there is no chemical interaction between fluids and rock frame. If these conditions are satisfied, at seismic frequency range, Gassmann's equation gives a constant shear modulus, and provide a simple way to calculate the bulk modulus of a saturated rock. If the assumptions and frequency range involved in the measurement of the rock's elastic properties do not satisfy Gassmann's assumptions, other models can be selected from the literature. Mavko, Mukerji and Dvorkin (2009) compile a number of rock physics models that can be used for different experimental conditions. On the other hand, one of the advantages in performing time-lapse quantitative interpretation over qualitative interpretation is uncertainty quantification.

In his book, Johnston (2013) mentions three key technical issues in time-lapse technology: seismic repeatability, seismic detectability and seismic interpretability. The first one is the capacity to highlight only the signal that was affected by production

in the reservoir. Non-repeatable noise and the result of random noise subtraction are effects that cannot be destroyed by time-lapse processing and, when possible, are modelled out. The repetition of seismic acquisition parameters and parallel processing of vintages are measures taken to increase the seismic repeatability. The second issue, seismic detectability, can be described as the capacity distinguish the amplitude changes generated by alterations in the elastic properties from the background noise. Finally, seismic interpretability is the capability to integrate information from additional sources, such as flow simulations, to explain the causes of these anomalies.

A fourth key issue to be considered would be the uncertainty quantification. According to Tarantola (1987), *"All physical measurements are subjected to uncertainties. Therefore, the result of a measurement act is not simply an 'observed value' (or a set of 'observed values') but a 'state of information' acquired on some observable parameter. If* $d = (d^1, d^2,...,d^n)$ *represents the set of observable parameters, the result of the measurement act can be represented by a probability density* $\rho_D(d)$ *defined over the data space D"*. In reflection seismic applications, since the sources and receivers are on the surface and the target reservoir kilometres deep in the subsurface, the interpreter relies on indirect measurements to infer the rock's properties. To create a rock properties model from seismic data, the geoscientist will need to perform a seismic inversion. Due to seismic resolution and noise issues (Buland and El Ouair, 2006) the seismic inversion outputs are inherently non-unique. Therefore, the measurement of the uncertainty in the rock properties derived from seismic data is a necessary step in the interpretation of such data (Grana, 2013). During time-lapse interpretation, the measurement of rock and fluid properties uncertainty is even more important than in 3D seismic interpretation. This is due to the fact that multiple seismic vintages are involved, and the signal often has high frequency and low amplitude characteristics. In this context, a machine-intensive technique, such as stochastic petrophysical time-lapse seismic inversion, emerges as an appealing tool for quantitative interpretation. This technique can quickly model and compare a large number of possible scenarios that fit the data and select the most plausible ones. The uncertainty characterization derived from the application of such a technique can create a business impact when applied to the risk analysis in the decision-making process.

1.3 SEISMIC MONITORING ON CARBONATE RESERVOIRS

Carbonates are defined by Palaz and Marfurt (1997) as "*calcareous sediments composed of shredded and reworked remains of shelly invertebrate animals and calcareous algae, microscopic lime-secreting organisms and coated faecal pellets mixed with lime mud matrix*". In addition to these shallow-water carbonates, in deep water, lime organism debris is found. According to Misaghi et al. (2010), in comparison with other rocks, carbonates show less mineralogical variability and are composed mainly of calcite, dolomite and aragonite.

The importance of carbonate reservoir studies rests on the fact that these reservoirs stores 60% of global oil reserves and 40% of the world's gas reserves (Burchette, 2012) but, in general, have recovery factors lower than 35% on average (Montaron, 2008). Time-lapse seismic data can be a valuable tool for increasing the recovery factors of carbonate reservoirs by improving well location, identifying bypassed oil, investigating reservoir compartmentalization and locating fracture corridors. However, the interpretation of time-lapse signals in carbonate reservoirs is a complex exercise. Lucia (2007) argues that time-lapse interpretation in carbonate reservoirs is more complex than in its sandstone counterparts. The reasons for this are:

- Carbonates rocks present higher incompressibility modulus, making the rock's seismic signal less sensitive to fluid content. Therefore, the time-lapse signals in carbonates are weak.
- Carbonate rocks are more likely to undergo diagenetic processes. Diagenesis refers to changes taking place in sediments after deposition (Berner, 1980). Diagenesis generally diminishes porosity, rearranges the pore space and modifies permeability and capillary properties (Lucia, 2007). Hence, the interpreter should expect larger variability in rock textures and pore types and need more complex reservoir models since reservoir properties (porosity, velocities, and permeability) vary within smaller volumes of the reservoir. Lateral facies changes are also expected and sometimes difficult to detect with seismic data. The most common diagenetic processes in carbonate reservoirs are calcite carbonate cementation, mechanical and chemical compaction, selective dissolution,

dolomitization, evaporite mineralization, massive dissolution, cavern collapse and fracturing (Lucia, 2007).

- Carbonate reservoirs are often permeated by fractures corridors. These corridors can range from tens to hundreds of meters in width and height and may extend for kilometres. The presence of fracture corridors in carbonate reservoir creates extremely anisotropic permeability fields with permeability inside the corridors being thousands of times higher than in their surroundings. The fractures may improve the permeability, as well as facilitate certain types of diagenesis (for example, dolomitization), in regions of the reservoir that originally do not have these characteristics. Therefore, the identification of regions with high fracture density is an important additional step for the characterization of carbonate reservoirs.
- Pore space of carbonates is often very complex, containing voids of diverse shapes, often with very small pore throats or even completely isolated voids. These features often mean that fluid pressure cannot be equilibrated within one period of the wave. Therefore, the presence of isolated pores will violate Gassmann's assumption that pressure must be equilibrated throughout the volume of rock undergoing seismic velocities measurements. In terms of time-lapse seismic data, this will restrict the reservoirs that can be analysed using a standard Gassmann-based forward modelling algorithm.

  In a comparative study, Misaghi et al. (2010) conclude that Gassmann's model gives a good estimation in carbonate rocks with connected pores at low frequency. For rocks containing a mix of connected and isolated or quasi-isolated pores measured using ultrasonic frequencies, other models like Xu and Payne (2009) and the modified differential effective model (Mukerji et al. 1995) are options to be considered.

  Moreover, since the presence of pore types are affected by diagenesis (Lucia, 2007) and, as shown before, carbonate reservoirs are prone to diagenesis, velocities are expected to vary sharply throughout the reservoir due to pore type variability.
- Carbonate rocks may experience rock-fluid interactions. An ongoing research topic is the study of rock-fluid chemical interactions in carbonates. These interactions can be divided into categories defined by how long it

takes for the interaction to occur.

- Long-term interactions take place during the migration of fluids into the reservoir and are associated with diagenetic processes inside it. From the time-lapse user's point of view, the long-term interactions do not affect the signal because they do not happen during the interval between the seismic acquisitions. Short-/medium-term interactions occur during the interval between vintage acquisitions. It takes place after the beginning of the production, mainly guided by the injection of fluids into the reservoir, and can affect the time-lapse signal.
- Many works investigate the short-/medium-term rock-fluid interactions. An example of a case history regarding short-term rock-fluid interaction can be found in the work of Houston et al. (2007). In this work, the authors demonstrate that substantial mineral-fluid interactions happen in the reservoir on a time scale of months in a North Sea oilfield due to changes in the mineralogy of the injected water.
- Although oil, gas and other fluids are also injected into the reservoir, water and CO_2 are the most likely to react with the carbonate rock. Water is injected in the oilfields by injector wells to displace the oil while maintaining the pressure of the reservoir. The water injected in oilfields can be harvested from various sources. While offshore, seawater and reinjected formation water - mainly used for environmental reasons - are sources of typically injected water. While onshore, water from another formation and reinjected formation water are options that can be utilized as sources of injected water. The chemical characteristics of the injected water (mineral components, pH and saturation) must be assessed and modified if necessary to avoid interactions with the reservoir rock that may affect production. Obstruction of pores and clogging of wells derived from the generation of crystals inside the borehole are examples of problems that originate from poor water management.

  CO_2 is injected into a formation for two main reasons: enhanced oil recovery and sequestration. In an enhanced oil recovery (EOR) project, CO_2 is injected into an already developed field to mix with

the oil from the formation. It makes the mixed solution less dense than the original oil, detaches it from the pore walls and causes the oil to flow to the producing well (Melzer, 2012). CO_2 sequestration projects aim to capture a volume of gas from anthropogenic or natural sources that would eventually be released into the atmosphere and inject it into a geological formation. Carbonate minerals are extremely reactive towards CO_2.

Studies (Adam, Batzle and Brevik, 2005; Adam, Batzle, and Brevik 2006; De Lucia et al., 2012; Vanorio et al., 2008 and Lucia, 2007) show that both water and CO_2 are capable of interacting with carbonate reservoir rocks. This interaction modifies the rock framework, changing the value of the elastic moduli, porosity and permeability. An important outcome of this interaction is the variation of shear moduli during fluid substitution. During fluid substitution, Adam, Batzle and Brevik (2006) and other authors have detected increase, as well as decrease, of shear moduli in different samples. This phenomenon has substantial implications in the use of Gassmann's equation for fluid substitution (Gassmann, 1951) because one of the premises of his theory is the constancy of shear modulus during fluid replacement. Modern reservoir management practices are focused on control and frequent monitoring of fluid-rock interaction effects in production. For most reservoirs, these effects are relatively weak at seismic frequency range and the Gassmann's prediction holds.

Although all these challenges seem to complicate the application of a time-lapse inversion methodology based on Gassmann's theory, they do not apply to every carbonate reservoir. Adam et al. (2006) state that "*For our carbonate set at high differential pressures and seismic frequencies, the bulk modulus of rocks with high-aspect-ratio pores and dolomite mineralogy is predicted by Gassmann's relation*". This is indicative that, under certain conditions (high differential pressures, seismic frequencies, high aspect ratio pores and dolomite mineralogy), Gassmann's relation can be applied to carbonate reservoirs. Moreover, Misaghi et al. (2010) conclude that Gassmann's model gives good estimation in rocks with connected pores at low-frequency measurements.

In this work, I inverted a time-lapse dataset of an Albian carbonate field located offshore Brazil in the Campos basin. This is a very depleted field (high differential pressure), examined using frequencies in the seismic range and whose best reservoir facies, described as porous grainstone (oncolites), presents high aspect-ratio pores as will be demonstrated in Chapter 5. The only difference between the field presented in this work and the one described by Adam et al. (2006) is that it is primarely limestone since it did not undergo dolomitization. On the other hand, if I follow the criterion presented in the work of Misaghi et al. (2010), the reservoir presented here could be modelled using Gassmann. This prompted me to implement the time-lapse inversion methodology in the field knowing that some restrictions regarding the results would apply. To improve my results I applied a methodology that employs a Bayesian formulation. The Bayesian formulation is applied to many geophysics problems, and one of its main advantages is the possibility of using prior information and the uncertainty associated with its properties to reduce the non-uniqueness of the ill-posed inverse problem (Asnaashari et al., 2015).

Prior information can be defined as all information obtained independently of the measurements (Tarantola, 1987). In the present case, it would be all information obtained independently of the time-lapse seismic data. In other words, for this case, prior information was everything the geoscientists knew about the data without making a time-lapse seismic measurement. Core measurements, production history and pressure measures can be enlisted as sources of prior information. Prior information is used to regularize the inversion procedure in many ways. It can favour smoother results, "anchor" the inversion operator to search around an *a priori* model or limit the model space to be searched for solutions. In summary, the use of prior information limits the possible scenarios. The quantity of independent data has a direct impact on the reduction of scenarios. Fortunately, the dataset used in this work is very thorough, comprising cores, flow simulation models, seismic horizons, well logs and capillary curves. This combination of circumstances and the modelling studies carried out during the data analysis and quality control phase, as seen in chapter 5, encouraged me to perform the inversion even in the presence of the challenges expressed above.

1.4 OBJECTIVES

The aim of this research is to assess the applicability of Stochastic time-lapse

inversion to carbonate reservoirs. To achieve this, the following objectives are proposed:

-Estimate dynamic properties in a carbonate reservoir using time-lapse stochastic inversion;

-Evaluate the uncertainty in the reservoir dynamic properties using time-lapse stochastic inversion;

To accomplish these tasks I inverted two reservoir datasets, a synthetic dataset derived from a feasibility study CO_2 sequestration project, and a carbonate reservoir dataset from an Albian field located at the Campos Basin, offshore Brazil.

1.5 APPROACH

The stochastic time-lapse inversion methodology used in this work inverts for layer's rock properties, meaning it is a layer-based petroelastic inversion. It uses standard forward modelling in both elastic inversion, when amplitude versus offset (AVO) analysis and the convolutional method are applied to invert for elastic properties, and petroelastic inversion, when Gassmann's theory is employed to perform fluid substitutions. To calculate the inversion results, Bayesian formalism is utilized. This generates a posterior probability density function (PDF) of models that can be either searched for a maximum *a posteriori* (MAP), a model with the highest probability or sampled using the Markov chain Monte Carlo (MCMC) algorithm. The maximization process generates a result similar to those found in standard inversion algorithm implementations that can be used for interpretation and quality control purposes. On the other hand, the posterior PDF's sampling process can be used to supply the uncertainties associated with elastic as well as petrophysical properties from time-lapse seismic data (Gunning, 2013).

The methodology employed in this work is presented in Figure 2, and comprises 4 steps: data analysis and quality control, construction of the prior model, inversion and result analysis. In the first step, an exploratory data analysis is carried out, and quality control metrics and cut-offs are defined in order to determine the type of inversion that will be conducted while dismissing unreliable data. In the second step, the data that qualified to be used in the inversion is translated into inversion parameters used to create an initial model. Velocity-depth trends and distribution of net-to-gross

(NG) within a layer are examples of model parameters defined in this phase. In the third step, the Bayesian time-lapse stochastic inversion described above is carried out. During inversion, the interpreter has to deal with technical issues such as parallel processing and data storage. Finally, the results are analysed in the light of flow simulation results: to validate my results, I compare them with flow simulator models for dynamic properties.

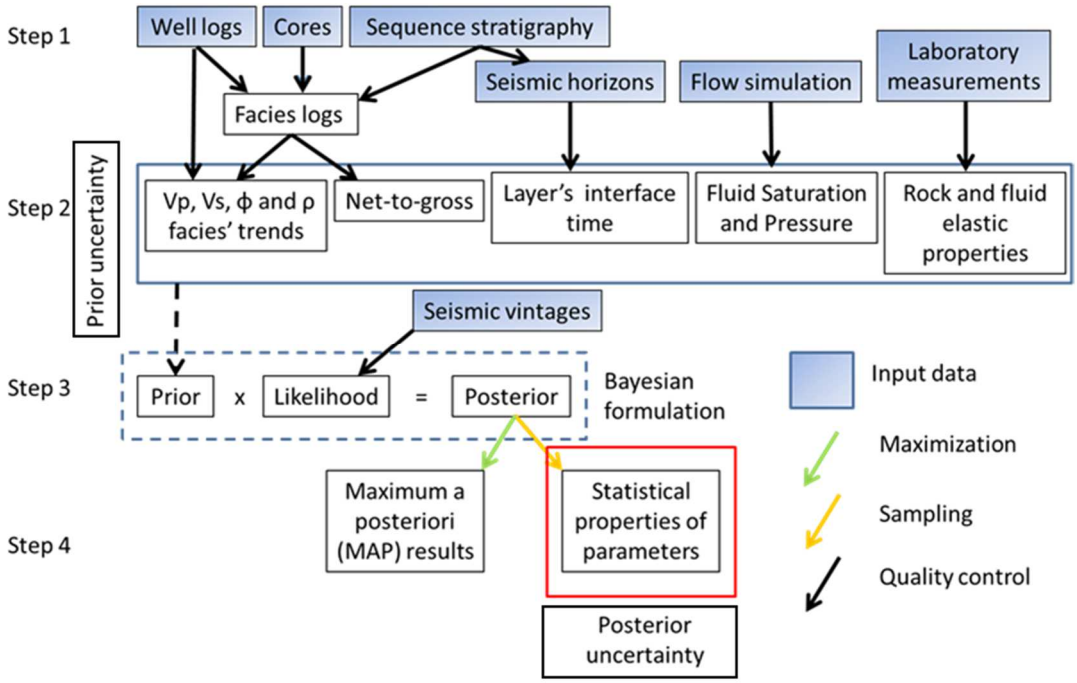

Figure 2 *Bayesian stochastic time-lapse inversion workflow.*

This workflow was applied to two datasets. The first one comprises a synthetic time-lapse seismic dataset used in a feasibility study for a CO_2 sequestration project into a saline formation. Since I had access to the flow simulation model used to generate the synthetic seismic data, I could assess the performance of the time-lapse stochastic inversion methodology, independently and in a controlled environment, before applying it to a real dataset. Noise and parameterization issues were addressed to evaluate the inversion methodology robustness while facing these factors. The second dataset is from an Albian carbonate oilfield located at the Campos Basin, offshore Brazil. Although the production in this reservoir started in the late seventies, a water injection campaign only took place in the early 2000s, resulting in a substantial decrease of pore pressure and release of gas out of solution. These factors create a complex scenario for the application of a time-lapse inversion methodology.

1.6 THESIS CONFIGURATION

This thesis is composed of six chapters. After this introductory chapter, in chapter 2 I will describe the theoretical background used in this research. In chapter 3, I will explain the stochastic time-lapse inversion methodology and the limitations of the technique. In chapter 4, I will present the application of the method to a synthetic dataset to test its validity and limitations by comparing the inversion outputs with the known models used in the generation of the synthetic dataset. Different scenarios with coherent and random noise as well non-optimized initial parameterizations are tested to evaluate the sensitivity of the method to these factors. In Chapter 5, I will present a case study in which the methodology was applied to a real dataset from a carbonate field located offshore Brazil. In chapter 6, conclusions are drawn.

CHAPTER 2. THEORETICAL BACKGROUND

In this chapter, I will present a brief description of the theoretical concepts used in this work. The first topic describes the time-lapse seismic monitoring method. Additionally, the rock physics models used to explain how the time-lapse signals are generated from changes on the rock properties are presented, as well as their limitations. Once the time-lapse signal causes are understood, the likelihood to detect these signals on real data is examined. The detection of the time-lapse signal is highly dependable on the repeatability of the time-lapse data. The evaluation of the time-lapse repeatability is explained through the definition of the repeatability metrics in the second topic. Flow simulation and seismic inversion can produce the same attributes as an output. Therefore, a critical step in validating the inversion results is comparison with the flow simulation outputs. In this work, I focused on the analysis of the fluid saturation attribute. Fluid saturations are limited by the capillary forces acting inside the rock pores. To have a more realistic scenario of fluid saturation, the application of these limits to the seismic inversion result is a necessity. The third topic, therefore, describes a reservoir simulator, its uses and the data employed to create a reservoir simulation model. Finally, the fourth topic briefly explains the capillary pressure measurement process, as well as the relationship between capillary pressure, saturation and relative permeability and the information that can be derived from it.

2.1 TIME-LAPSE SEISMIC MONITORING

Time-lapse seismic technology is a natural extension of the seismic method and can be defined as the repetition of seismic data acquisition over reservoirs undergoing production and/or injection to quantify the change in the seismic response after human interference (Corzo, MacBeth and Barkved, 2013). According to Barkved (2012), when hydrocarbon reservoirs are concerned "*time-lapse seismic surveys or 4D seismic surveys offer snapshots of a producing hydrocarbon reservoir and its surroundings and are the most common seismic surveillance technique in the oil and gas industry*". As stated by Labat et al. (2012), variations in fluid saturation, pore pressure and

temperature due to production, as well as reservoir compaction, alter the elastic properties of the reservoir: acoustic impedance (the product of a rock's acoustic velocity, V_p, and density, ρ), shear impedance (the product of a rock's shear velocity, V_s, and density, ρ), and the rock's density. These variations, in turn, change the amplitudes and traveltimes of seismic signals recorded during successive seismic surveys over a reservoir under production. To completely understand the above statement, definitions of fluid saturation and pore pressure are necessary. However, before defining fluid saturation, it is important to outline the meaning of porosity. Porosity is the fraction of rock volume V that is not occupied by solid matter. Hence, if the volume occupied by solid matter is V_{sm}, porosity (Φ) is defined as $\Phi = (V-V_{sm})/V$. In turn, fluid saturation is the ratio of the fluid volume to the pore volume of the rock; therefore, if the volume occupied by a fluid is V_f, fluid saturation (S_f) can be written as $S_f = V_f/(V- V_{sm})$. Under normal conditions, the sum of the saturation of all fluids present in a rock is 1. Finally, pore pressure (P_p) is the pressure of the fluid inside the pores of the reservoir rock.

The key objective of a time-lapse seismic project is to analyse the changes between successive seismic vintages in terms of fluid saturation, pore pressure and temperature to discover bypassed oil, improve well location and identify baffles. Ultimately, the time-lapse analysis aims to enlarge the recovery factor of the reservoir (Calvert, 2005). In order to do so, rock physics models linking elastic and rock properties are needed.

2.1.1 Rock physics models

In general, rock physics models consider the rock as a combination of two elements: a mineral frame and the pore fluid (Dvorkin, Gutierrez, and Grana, 2014). Figure 3 shows a thin section of a carbonate reservoir rock. In this picture, the mineral frame is mainly composed of calcite. The pores are depicted in blue. Different pore fluids (water, oil or gas) can be stored in the pore space. Because rocks are typically composed of more than one mineral and can be saturated with more than one fluid, it is important to understand the underlying relations that govern mineral mixing and fluid mixing before scrutinzing how the rock's elastic properties are affected by the variation of fluid saturation, pressure and temperature.

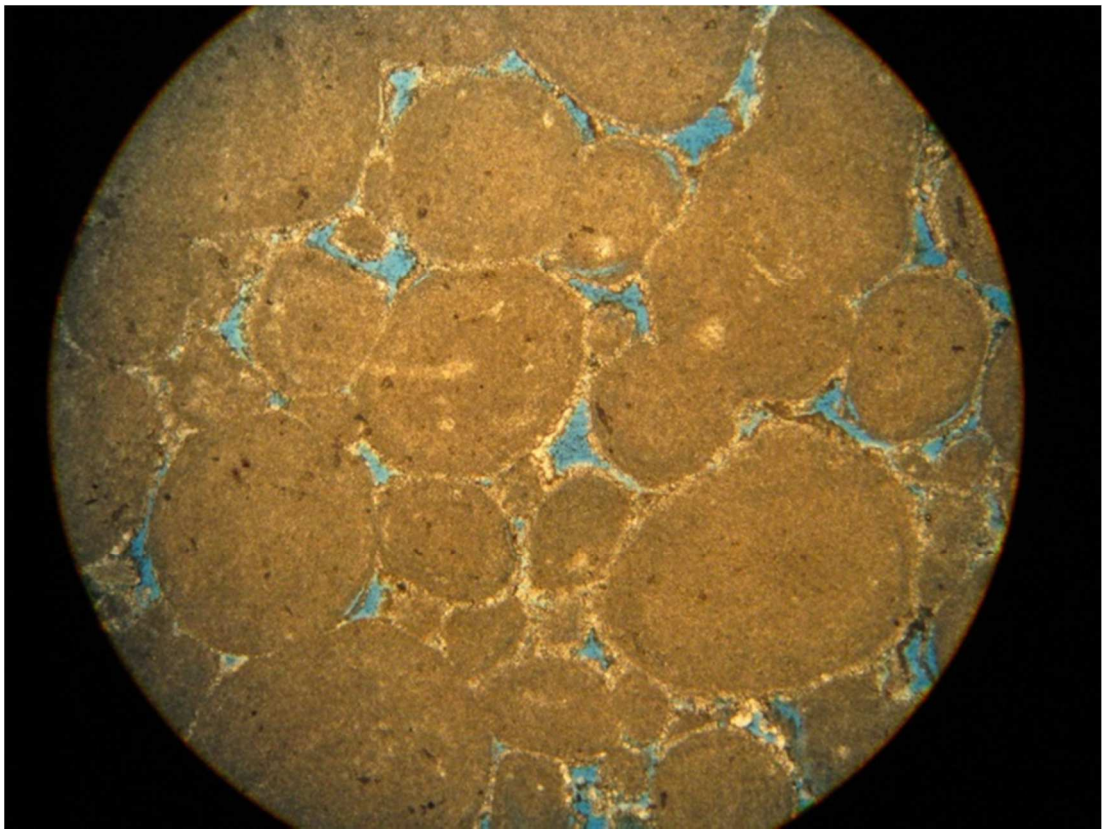

Figure 3 *Thin section of grainstone carbonate rock. The mineral frame is mainly composed of calcite, with micritic cement. The pores are depicted in blue. Scale was not provided in the dataset.*

2.1.1.1 Mineral mixing

The mineral frame is usually a combination of different minerals - a dry porous polymineralic entity. To deal with this dry porous polymineralic entity, the concept of an effective medium is often applied. The effective medium is a hypothetical medium composed of one constituent whose elastic properties are calculated using the elastic properties of all constituents found in the original rock. To evaluate the effective medium properties I specify the proportion of the constituents within the rock, the elastic properties of each constituent and the geometric arrangements of the constituents in relation to each other. To illustrate this point Figure 4 shows an example of a thin section of a carbonate reservoir rock. Although both Figure 3 and Figure 4 depict rocks composed almost entirely of calcite minerals with approximately the same proportion of constituents and elastic properties of each constituent, the geometrical arrangements are different, leading to different elastic behaviours.

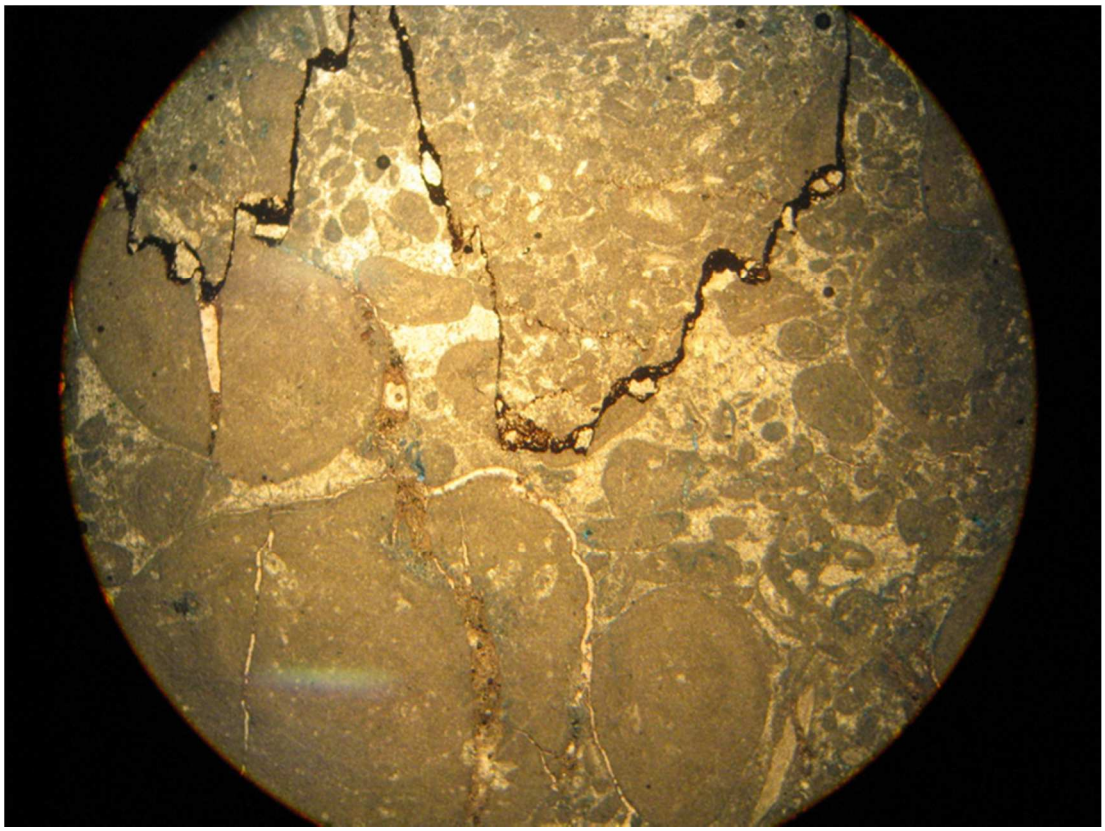

Figure 4 *Another example of a thin section. Again, the mineral frame is mainly composed of calcite. Scale was not provided in the dataset.*

In most cases, however, the definition of the geometrical arrangement is quite uncertain. Due to this limitation, one solution is the estimation of lower and upper bounds using a proportion of the elastic properties of the rock constituents. In this approach, the rock's elastic properties will fall between the bounds, but the exact value will depend on the geometric details of the constituents arrangement (Mavko, Mukerji and Dvorkin 2009). The narrowest possible bounds for an isotropic mixture of isotropic constituents without specification of the geometrical state of the rock's constituents is provided by the work of Hashin and Shtrikman (1963),

$$K^{HS\pm} = K_1 + \frac{f_2}{(K_2 - K_1)^{-1} + f_1\left(K_1 + \frac{4}{3}\mu_1\right)^{-1}} \tag{2.1}$$

and

$$\mu^{HS\pm} = \mu_1 + \frac{f_2}{(\mu_2 - \mu_1)^{-1} + 2f_1(K_1 + 2\mu_1)/\left[5\mu_1\left(K_1 + \frac{4}{3}\mu_1\right)\right]}, \tag{2.2}$$

where K_1 and K_2 are the bulk moduli of individual constituents, μ_1 and μ_2 are the shear moduli of individual constituents and f_1 and f_2 are the volume fractions of the

individual constituents. The equations give the upper bound if the stiffer material is termed 1 and give the lower bounds if the stiffer material is termed 2. This method assumes that the constituent with the higher bulk modulus has the higher shear modulus and, therefore, the constituent with the lower bulk modulus has the lower shear modulus. However, it is not always true. Rocks might contain mineral constituents whose bulk modulus is higher than that of the other constituent but the shear modulus is lower than the corresponding property in the other constituent. For this reason, an improvement in the Hashin-Shtrikman was developed in the form of the Hashin-Shtrikman-Walpole bounds, developed by Walpole (1966),

$$K^{HS\pm} = K_1 + \frac{f_2}{(K_2 - K_1)^{-1} + f_1\left(K_1 + \frac{4}{3}\mu_m\right)^{-1}} \tag{2.3}$$

and

$$\mu^{HS\pm} = \mu_1 + \frac{f_2}{(\mu_2 - \mu_1)^{-1} + f_1\left[\mu_1 + \frac{\mu_m}{6}\left(\frac{9K_m + 8\mu_m}{K_m + 2\mu_m}\right)\right]^{-1}}, \tag{2.4}$$

where K_1, K_2, μ_1 and μ_2 are the bulk and shear moduli of components 1 and 2 and K_m and μ_m are the extreme values of bulk and shear moduli.

In these equations the upper bounds, K^{HS+} and μ^{HS+}, will be calculated when K_m and μ_m are respectively the maximum bulk modulus and shear modulus and the lower bounds, K^{HS-} and μ^{HS-}, will be calculated when K_m and μ_m are respectively the minimum bulk modulus and shear modulus. In that case, if the same constituent has the maximum bulk and shear moduli while the other have the minimum bulk and shear moduli, the equations will reduce to the Hashin-Shtrikman bounds. If the shear moduli are the same, the upper and shear bounds of both bulk and shear moduli will be same. Finally, if the shear moduli of the constituents are the same, the bounds will be the same (Mavko, Mukerji and Dvorkin, 2009). An average curve (Figure 5) can be estimated by calculating the mean between the bounds,

$$K^{HS} = \frac{K^{HS+} + K^{HS-}}{2} \tag{2.5}$$

and

$$\mu^{HS} = \frac{\mu^{HS+} + \mu^{HS-}}{2}, \tag{2.6}$$

where K^{HS} represents the bulk modulus average values and μ^{HS} represents the shear modulus average values.

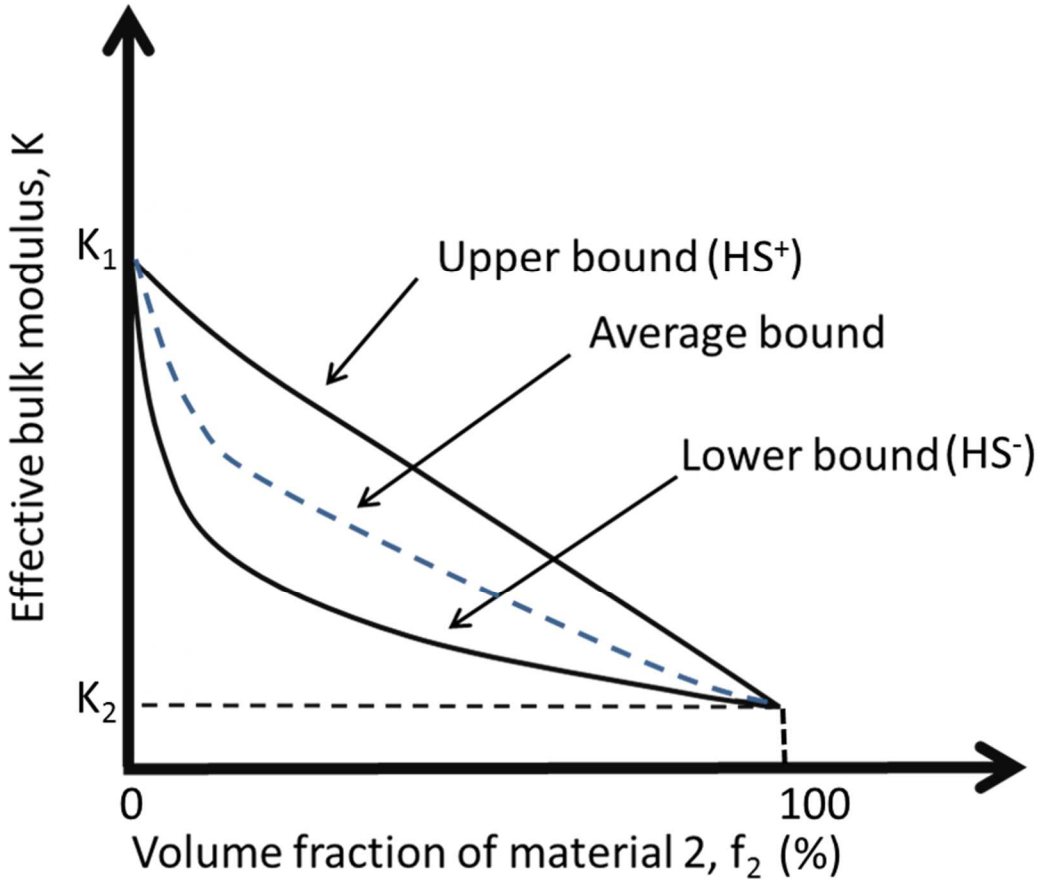

Figure 5 *Representation of lower and upper bounds and the average of effective bulk modulus calculated using Hashing-Shtrikman. K1 and K2 represent the bulk modulus of the constituents.*

It is important to note that an exact analytical solution is known only for some very simple distributions (such as finely layered media, or a medium with a dilute concentration of ellipsoids). On the other hand, for any given geometry it is possible to compute effective properties numerically. However, this is impractical, as the exact geometry is never known. Specifically, in the case of finely layered media, Backus (1962) showed that, in the long wavelength limit, a stratified medium composed of isotropic layers is transversely isotropic and can have its plane wave modulus, $M = K + \frac{4}{3}\mu$, calculated using a running harmonic average window. In that case,

$$\langle M \rangle = \left(\frac{1}{n}\sum_{i=1}^{n}\frac{1}{M_i}\right)^{-1}, \tag{2.7}$$

where M_i are the individual consecutive plane wave modulus measurements and $\langle M \rangle$ is the upscaled plane wave modulus derived from the upscaled stiffness tensor comprising 5 elastic moduli that characterize the transversely isotropic effective medium after the application of Backus average. To successfully perform Backus average, the window length should be comparable to the seismic wavelength (Dvorkin, Gutierrez, and Grana, 2014). Since we are averaging only in the z direction, the application of the previous equation is sufficient to our model: nevertheless, it ignores the effects of the elastic moduli acting parallel to the bedding plane.

2.1.1.2 Pore fluids mixing

When pore fluids are concerned, a similar strategy can be employed to calculate the bulk modulus of the mixture of fluid inside the pores of a rock: an effective fluid can be designed to substitute for the fluid mixture. Moreover, for fluids the effective modulus does not depend on geometry and only depends on the volume fractions of the constituents. Assuming that all the fluid phases remain in hydraulic communication and that the fluids are immiscible but mixed at the finest scale, the effective fluid bulk modulus, K_f, can be calculated using a geometric averaging, the Reuss average (Mavko, Mukerji and Dvorkin, 2009),

$$\frac{1}{K_f} = \frac{f_w}{K_w} + \frac{f_o}{K_o} + \frac{f_g}{K_g}, \tag{2.8}$$

where f_w, f_o and f_g are, respectively, the volume fractions of water, oil and gas and K_w, K_o and K_g are, respectively, the bulk modulus of water, oil and gas. Most fluids do not resist shear deformation; therefore, their shear moduli are zero (Dvorkin, Gutierrez, and Grana, 2014).

The effective fluid bulk modulus can be used to calculate the effective fluid velocity, also known as Wood's velocity (Wood, 1955).

$$V = \sqrt{\frac{K_f}{\rho_f}}. \tag{2.9}$$

In this equation, the fluid density, ρ_f, is given by

$$\rho_f = f_w\rho_w + f_o\rho_o + f_g\rho_g, \tag{2.10}$$

where ρ_w, ρ_o and ρ_g are the densities of water, oil and gas respectively. The properties of pore fluids strongly depend on water salinity, oil gravity, gas gravity, gas-oil-ratio (GOR), pressure and temperature (Dvorkin, Gutierrez, and Grana, 2014). These properties can be calculated from the empirical relations described in the work of Batzle and Wang (1992).

2.1.2 Effects of fluid substitution

Once the effective medium properties for the mineral frame and the pore fluid have been defined, I need to combine them into a saturated rock. Gassmann (1951) expressed the bulk modulus (K) and the shear modulus (μ) of a saturated rock as

$$K_s = K_d + \frac{K_0\left(1-\frac{K_d}{K_0}\right)^2}{1-\Phi-\frac{K_d}{K_0}+\Phi\frac{K_0}{K_f}} \tag{2.11}$$

and

$$\mu_s = \mu_d, \tag{2.12}$$

where K_s is the saturated bulk modulus, K_d is the dry bulk modulus, K_0 is the mineral bulk modulus, Φ is the porosity, K_f is the fluid bulk modulus, μ_s is the saturated shear modulus and μ_d is the dry shear modulus. The dry moduli corresponds to moduli measured "*in a drained experiment in which pore fluids can flow freely in or out of the sample to ensure constant pore pressure*" (Mavko, Mukerji and Dvorkin, 2009).

Equations 2.11 and 2.12 show that the bulk modulus is affected by the presence of fluids in the pore space, while the shear modulus is not affected by it. This is a result of the fact that fluids do not support shear stress. The assumptions behind Gassmann's equations are:

- The rock is isotropic;
- The rock is monomineralic and homogeneous;
- The rock behaviour is elastic;
- The rock's pore space is connected and in pressure equilibrium;
- There are no rock-fluid chemical interactions.

These assumptions are seldom if ever valid for real rocks. Hence, in order to apply Gassmann's equations to real reservoirs, some of these assumptions need to be relaxed.

The rock is isotropic:

All minerals and rocks are anisotropic to some degree. Therefore, the assumption that the rock is isotropic is always violated. Indeed, if the rock is composed of preferentially oriented anisotropic minerals this assumption is violated, and the application of Gassmann's equation is invalid. However, if the rock matrix consists of anisotropic mineral grains with random (isotropic) orientation mixed in a fine scale, this rock can be considered as nearly isotropic, and therefore Gassmann's equation can be used (Brown and Korringa, 1975).

The rock is monomineralic and homogeneous:

Most reservoirs are polymineralic and, as explained above, an average of mineral bulk modulus weighted by the abundance of each constituent is used to calculate an effective mineral bulk modulus homogeneously distributed around the pores. Brown and Korringa (1975) state that "*A constituent with a markedly different-from-average compressibility is not in positions in the clastic framework where this constituent would be subjected to more or less stress than it would in the average positions in the elastic framework*". In that case, the difference between their theory, in which geometrical as well elastic parameters of all rock constituents are necessary (e.g. a micro-heterogeneous rock model), and Gassmann's would be negligible. These results, although commonly used, are contradicted by the work of Glubokovskikh and Gurevich (2015) who calculated an analytical solution for an idealized double shell model that departs from Brown and Korringa's estimates and can be described as "*the upper bound of the effect of micro-heterogeneity on the effective stress coefficients and undrained bulk modulus*". Smith, Sondergeld and Rai (2003) also argue that if the rock frame comprises minerals with a significant contrast in elastic properties, this assumption is violated. To avoid these extreme cases, in this work I assume small contrasts between constituents elastic properties and use Brown and Korringa´s (1975) arguments to justify the use of Gassmann's equation.

The rock behaviour is elastic:

At a low frequency limit and far from the source location, the rock can be considered approximately elastic. This is due to the fact that the effects of attenuation due to friction and squirt flow can be ignored in a first approximation for most clastic reservoirs at the seismic frequency range (2 to 80 Hz) and the rock will go back to its initial geometry after the passage of the wave.

The rock's pore space is connected and in pressure equilibrium:

For most sandstone reservoirs, the pore space is considered connected and in pressure equilibrium at seismic frequency range *"such that pore pressures are equalized over a length much greater than a pore dimension and much less than the wavelength of the passing wave"* (Smith et al. 2003). The same, generally, cannot be said about the carbonates reservoirs, which are prone to isolate pores due to diagenetic processes and will need a different approach based on effective medium theory such as Xu and Payne (2009) and the modified differential effective model (Mukerji et al. 1995). Nevertheless, if the carbonate reservoir is formed by grain-supported rocks (e.g. porous grainstones) with connected pores, these requirements of Gassmann's equation can also be fulfilled at seismic frequencies. In the data set presented in this work, the rock is a porous grainstone and the inversion methodology based on Gassmann's theory can be applied.

There are no rock-fluid chemical interactions:

Analyzing Gassmann's equations one can note that dry elastic moduli should be constant during fluid substitution. Changes in the dry elastic moduli can be generated, among other causes (e.g. pressure, as shown below), by fluid-rock interactions. One of the effects of the dry elastic moduli variation is the change of shear moduli with fluid saturation, leading to variation of P- and S-wave velocities. Recent experimental studies have shown that weakening and strengthening in shear modulus can be attributed to fluid-rock chemical interaction. Although the effects of the fluid-rock chemical interaction are clearer in carbonate rocks injected with reactive fluids such as CO_2 (Adam, Batzle and Brevik, 2006; Vanorio, Scotellaro and Mavko, 2008), sandstones with carbonate cement present similar effects when injected with reactive fluids (Joy, Vanorio, and Sen, 2011). As explained before, the causes and frequency of these variations during production are still ongoing research topics (Vanorio et al., 2008).

As shown above, for fluid mixtures, the fluid elastic properties (K_f and ρ_f) are a function of the volumetric fraction and bulk modulus of each constituent. Hence, production of hydrocarbon or injection of water or CO_2 will affect the bulk modulus and density of the saturated rocks because they change the volumetric fraction (fluid saturation) of an existing fluid in a mixture (during production) or add a new fluid to the mixture (during injection). Gassmann's fluid substitution methodology is a way to update the value of the bulk and shear modulus of a saturated rock when the pore fluid elastic properties vary.

2.1.3 Effects of temperature variation

Likewise, variations in temperature affect the rock compressional velocity because it changes the velocities of the fluids present in the reservoir. The increase in temperature generally makes the fluid bulk modulus and viscosity decrease, which reduces the compressional velocity of the rock. The temperature effect is particularly relevant for heavy oil reservoirs (Zhang and Larson, 2016). Based on a USGS definition: "*heavy oil is an asphaltic, dense and viscous oil that is chemically characterized by its content of asphaltenes with API gravity from 22^o to less than 10^o (ultra-heavy oil or bitumen)*" (Han, Liu, and Batzle, 2006). Viscosity, in turn, is the measure of a fluid's resistance to gradual deformation by shear stress or tensile stress and is normally given in centipoises.

2.1.4 Effects of pressure variation

Biot and Willis (1957) demonstrated that, for consolidated rocks, variations in effective pressure affect the rock's bulk and the shear moduli. Effective pressure is given by

$$P_{effective} = P_{confining} - \eta P_{fluid}, \tag{2.13}$$

where $P_{effective}$ is the effective pressure, $P_{confining}$ is the confining pressure and P_{fluid} is the fluid pressure. The factor η differs for each rock property that is dependent on $P_{effective}$ (Hofmann et al. 2005). A list of η for a range of rock properties is given by Berryman (1993). In most reservoirs, $P_{confining}$ is approximately constant; therefore, changes in $P_{effective}$ are mostly caused by changes in P_{fluid}. P_{fluid} decreases with fluid production, since a volume of fluid is being removed from the

reservoir, and increases with fluid injection. The effect of production and injection in $P_{effective}$ is opposed to the effect in P_{fluid}: $P_{effective}$ will increase with production and will decrease with injection. The dependence of saturated rock's shear and bulk modulus with pressure is controlled by porosity, dry bulk modulus, dry shear modulus, fluid modulus and fluid density.

Porosity

Because the fluid inside the compliant pores push the pore walls apart, changes in pressure can change the volume of the pores. Conversely, by decreasing pore pressure, crack-like pore walls get closer. These conditions will cause porosity to vary with pressure.

Dry bulk modulus and dry shear modulus

A higher $P_{effective}$ will result in a closing of cracks and a larger grain contact area will stiffen the rock framework. As a result, K_d and μ_d will increase. The opposite will occur for a drop in $P_{effective}$. Figure 6 shows that until all the cracks and compliant grain contacts are closed, K_d and μ_d will increase with $P_{effective}$. After that, the velocities versus $P_{effective}$ curve will flatten and very little variation will happen until the rock starts to fail.

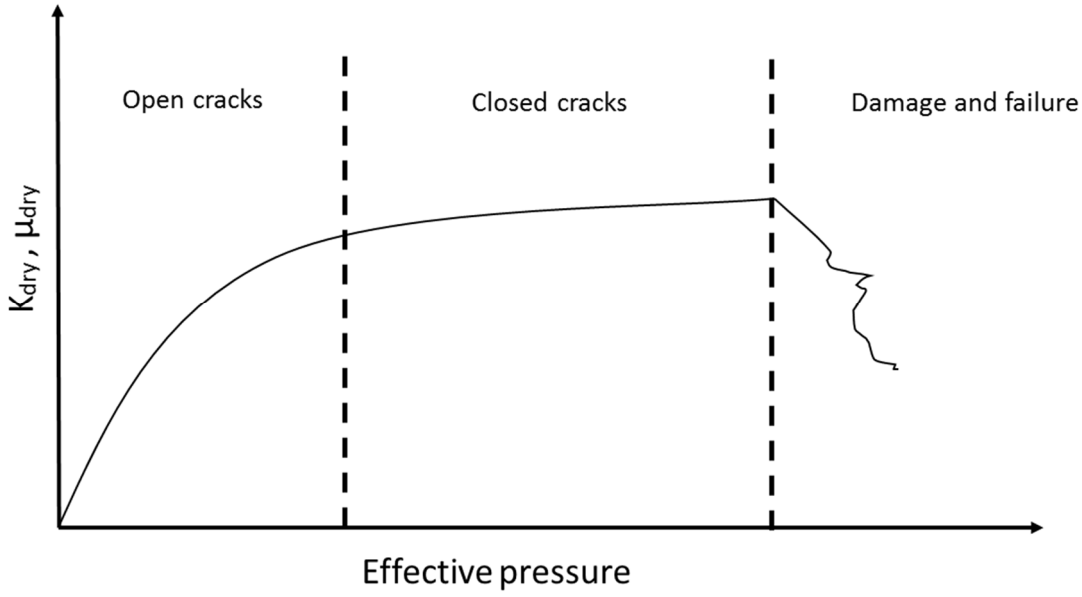

Figure 6 *Schematic representation of the variation of K_{dry} or μ_{dry} with effective pressure.*

Fluid bulk modulus and fluid density

Fluid density and bulk modulus will increase with increasing fluid pressure. If the pressure decreases below the bubble point, gas will be liberated from solution. This gas may create a secondary gas cap in the reservoir (Calvert,2005). Physics-based models such as the one published by Kuster and Toksöz (1974) and the empirical models such as the presented in Avseth, Flesche and Van Wijngaarden (2003) are currently used to predict the eventual velocities variation with pressure in advance of a time-lapse seismic acquisition. Although the technology has progressed a lot in recent years, with advances in low-frequency measurements of rock samples under stress (Mikhaltsevitch, Lebedev and Gurevich, 2011; Spencer, 1981; Paffenholz and Burkhardt, 1989), a great deal of uncertainty is still found in these evaluations and more studies are required.

2.1.5 Compaction effects

In the event of the drilling of a well, the reservoir releases fluids through a pressure gradient either naturally created (primary drive mechanisms) or man-made (secondary drive mechanisms). Following the decrease in pore pressure, compaction of the reservoir may occur. The compaction of the reservoir can be a major depletion mechanism, especially in an unconsolidated clastic reservoir and in chalks, and can lead to surface subsidence and changes in the stress field around the reservoir. Regarding time-lapse effects, compaction can cause changes in the thickness and porosity of the reservoir. Reservoir compaction may lead to an increase in velocity in the reservoir and the sideburden (the flanks of the reservoir) and a decrease in velocity in the overburden and underburden. These alterations create time shifts that have to be taken into account in the time-lapse interpretation in order to isolate the fluid saturation and pressure variation effects from compaction effects (Barkved, 2012). Finally, the simultaneous effects of the factors mentioned above can interact constructively or destructively, and modelling of scenarios is needed in order to establish the causes of variation in elastic parameters.

2.1.6 Other rock physics relations

Most of the seismic modelling schemes presented above depend on the knowledge of acoustic velocity, V_p, shear velocity, V_s, and the bulk density, ρ_b, but sometimes only V_p is available, making necessary the establishment of relations

between V_p and ρ_b, and V_p and V_s. In such cases, an the empirical acoustic velocity - bulk density relation described in Gardner, Gardner and Gregory (1974) is often used

$$\rho_b = dV_p^f, \tag{2.14}$$

where d is a multiplication factor and f is the exponent factor. When averaged over many types of rock, the values of these parameters are found to be d=1.741 and f=0.25 for velocities given in km/s and density in g/cm^3. Castagna and Backus (1993) later refined the parameters values for specific lithologies, improving the resultant correlation with the measurements. Among the numerous V_p-V_s relationships found in the literature, the V_p-V_s relationship employed in this work is a linear empirical one,

$$V_s = a + bV_p, \tag{2.15}$$

where a and b are dependent on the lithology of the rock. These types of relationships can be found in the works of Castagna and Backus (1993), Greenberg and Castagna (1992) and (Han, Nur and Morgan, 1986).

2.2 METRICS OF REPEATABILITY

Once the time-lapse signal causes are understood, the likelihood of detecting these signals on real data must be examined. The detection of the time-lapse signal is highly dependent on the repeatability of the time-lapse data. The subtraction of the base vintage from the monitor vintage results in a difference volume. Ideally, if no human intervention had taken place in the earth volume where data was acquired, there would be no amplitude in the difference volume. On the other hand, if human intervention generated changes in the elastic properties of the reservoir, all the amplitudes present in the resultant difference volume should, ideally, be traceable back to variations in the reservoir dynamic properties. In this case, as explained above, all the amplitudes would be located around (or below) the reservoir. However, the difference volume actually presents seismic amplitudes caused by factors other than the human interference in the reservoir, located not only around the reservoir area but also away from it. The sources of this time-lapse noise may be differences in acquisition, such as differences in the positions of the receivers, source or receiver coupling, environmental factors (such as seawater velocity), or ambient noise from natural or man-made factors.

In the ideal scenario, one would have access to a perfectly repeatable time-lapse seismic dataset, however, in reality, most seismic data contain non-repeatable time-lapse signals to some extent. The degree to which the data is non-repeatable can make the interpretation of the difference volume extremely difficult. However, in many cases useful interpretation is still possible even if the data is not perfectly repeatable. For this reason, after time-lapse processing, the time-lapse seismic volumes pass through a repeatability evaluation before interpretation. This phase is critical to ensure that the seismic anomalies encountered in the difference volumes are not due to noise but to changes in the reservoir elastic properties. Many operators exist to calculate repeatability and this evaluation typically takes place in a window located above the reservoir to avoid time-shift effects. An exception is the case of compaction, where the window has to be moved above and away from the reservoir.

The normalized root-mean-square difference (NRMS) is the standard reference for seismic repeatability (Barkved, 2012) and is defined by

$$NMRS = 2 * \frac{RMS(A-B)}{RMS(A)+RMS(B)}, \tag{2.16}$$

where A and B represent the base and monitor vintages' amplitudes respectively and RMS denotes the root-mean-square operator inside a time window. From the analysis of Equation 2.14, one can realize that the lower the number, the better the repeatability. If NRMS=0 the data is completely repeatable, if the traces are anticorrelated NRMS=2 and if the traces are just random noise the value is NRMS= $\sqrt{2} \approx 1.41$. The NRMS is sensitive to noise, amplitude differences, phase differences and time-shifts. Another important metric of repeatability is the predictability. According to Kragh and Christie (2002), predictability is given by

$$PRED = \frac{\sum Xcorr^2(A,B)}{\sum Acorr(A) \times Acorr(B)}, \tag{2.17}$$

where Xcorr is the cross-correlation between base and monitor and Acorr is the auto correlation. If PRED=1 the traces are completely correlated. If PRED=0 the base and monitor vintages are uncorrelated. However, if the volumes are anti-correlated, PRED is also equal 1, creating the need for further examination of the data. The values of PRED are not very sensitive to time-shifts but extremely responsive to noise. Predictability and NRMS can be used together to plan the interventions in the processing necessary to improve the repeatability of the vintages.

2.3 RESERVOIR SIMULATION

Reservoir simulation models are developed by petroleum engineers to estimate the distribution of fluids and pressure inside a reservoir through time. The flow simulator normally applies finite difference or finite element algorithms on a three-dimensional grid to estimate the movement of fluids and other properties, such as pressure, throughout the reservoir and is usually constructed in the depth domain. According to Fanchi (2005), the main reasons to implement a reservoir simulation are the development of an optimal production strategy (well placement and reservoir management) to maximize recovery, coordination of reservoir management activities, evaluation of project performance (to understand reservoir behaviour), estimation of project life, prediction of recovery versus time, and selection and optimization of reservoir design. The preparation of the input data set of a flow simulation model is a multidisciplinary effort (Fanchi, 2005). For example, the porosity and permeability information are upscaled from a geologic model, a much finer grid built by the interpolation of well logs guided by seismic horizons, while saturation estimates usually come from petrophysical studies.

The flow simulations provide not only an estimation of the spatial distribution of fluids and pressures but also generate estimates of production curves in every well, which can be later compared with the actual well production curves to validate the reservoir model in an exercise called the history match. Additionally, flow simulation predictions can be transformed into seismic volumes, using a forward-modelling technique known as a petroelastic modelling, and compared with the actual seismic vintages to aid the interpretation of the time-lapse seismic data. Therefore, in this work, in order to validate my results (time-lapse inversion results included), I compared them with the dynamic properties from the reservoir simulator models.

2.4 CAPILLARY PRESSURE AND RELATIVE PERMEABILITY

One of the possible outputs of seismic inversion is fluid saturation. Fluid saturations are limited by the capillary forces acting inside the pores of a rock. In order to have more realistic scenarios of fluid saturation, the inversion needs to be

constrained by the factors caused by capillary pressure. Additionally, capillary pressure studies aid the characterization of the pore space in terms of pore throat size and wettability. In this section, I will examine the effects of capillary pressure on pore fluid behaviour, as it is a critical parameter in the characterization of reservoirs containing two or more immiscible fluids.

Capillary pressure is derived from the interfacial tension between the fluid phases and, in conjunction with gravitational and viscous forces, dictates the flow and spatial distribution of the fluid phases (Bognø, 2008). It is used to determine pore size, fluid distribution and irreducible saturation. The two most common methods used to quantify capillary properties are the injection of mercury into a sample containing air under pressure and the displacement of water by oil in a centrifuge (Lucia, 2007). The volume of non-wetting fluid at increasing pressure is quantified as saturation, and a plot of pressure versus saturation is made. This plot is named the drainage curve. When the wetting phase is injected and gradually displaces the non-wetting phase it yields an imbibition curve. According to Anderson (1986), wettability is the "*tendency of one fluid to spread on or adhere to a solid surface in the presence of other immiscible fluids*". In the capillary pressure versus saturation crossplot, a vertical asymptote (where capillary pressure tends to infinity) indicates the irreducible wetting phase saturation (Skjaeveland et al. 1998). In Figure 7, I show two asymptotes for a water-wet reservoir rock. The water saturation marked by the asymptote closer to the y-axis corresponds to the irreducible water saturation (S_{wi}). It can be interpreted as the boundary where the capillary pressure goes to infinity and is incapable of displacing the irreducible water from the pores. The second asymptote is the analogous situation but for the non-wetting fluid: in this case, oil. It marks the maximum water saturation possible, or, for an oil reservoir, the irreducible oil saturation (S_{oi}).

Absolute permeability is the permeability of a rock that is completely saturated with a single fluid. Relative permeability is the permeability measured at a specific fluid saturation and expressed as a fraction of the total or absolute permeability. Graphs of relative permeability versus saturation can be used to predict changes in production rates with changes in water saturation and to identify the irreducible water saturation (S_{wi}), the point where the water relative permeability curve goes to zero. By inspection of Figure 7, one can see that capillary pressure, relative permeability and saturation are related and can be used to determine fluid contacts. In an oil reservoir, oil becomes

mobile only after reaching the saturation defined by the non-zero value in the relative permeability curve. Since the values of the relative permeability curve are linked to the capillary pressure curve by saturation values and the capillary pressure is distributed in the reservoir according to the pore throat sizes and height of oil column in the reservoir, this saturation value represents a level that defines the field oil-water contact. Oil and water are produced above this reservoir height until the water relative permeability is zero and only oil flows. While the capillary pressure is positive, it is called the spontaneous imbibition or drainage, and the rock is saturated with fluid without the application of additional pressure. The negative capillary pressure is named "forced" imbibition or drainage and represents the situation where additional pressure is applied to the fluid in order to saturate the rock. In the next chapter I will examine how to translate the information gathered by the methods presented here into the formalism used to create an initial model for a stochastic time-lapse seismic inversion.

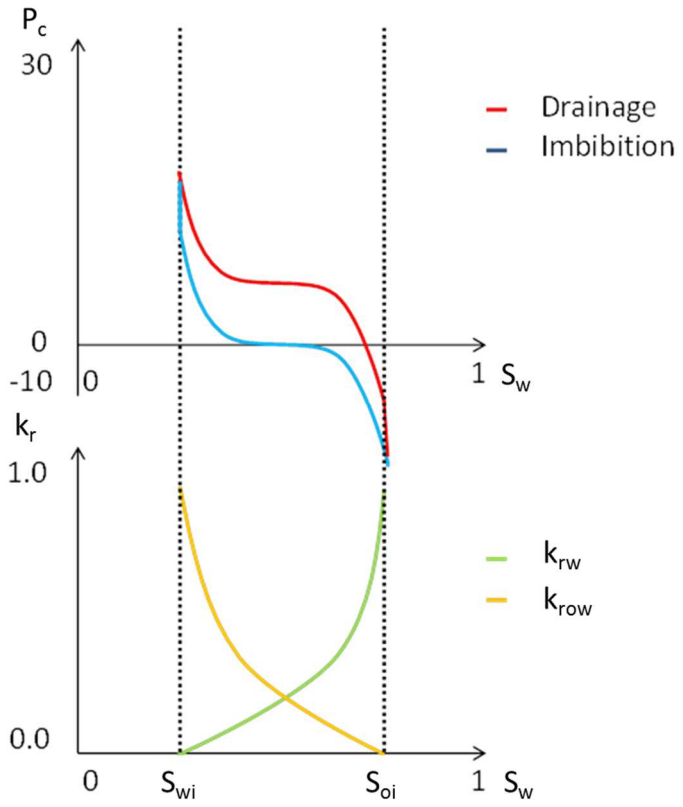

Figure 7 *Schematic plots of capillary pressure (P_c) and relative permeability (k_r) against water saturation for a water-wet reservoir.*

CHAPTER 3. METHODOLOGY

In this work, I employed the stochastic time-lapse inversion algorithm, Delivery4D (Gunning, 2013), which estimates the most probable time-lapse changes in the reservoir and calculates the uncertainty of these estimates. In this chapter, I will present the computational methodology and will help the reader to understand the assumptions and limitations of the method. After that, I will discuss the Bayesian formulation on which the algorithm is based. Following this, I will detail the parameterization of the model used in the inversion. In the fourth section, I will describe the strategy employed to model the pore pressure variation. Next, I will explain the scheme utilized to model the fluid saturation variation. Finally, I will describe and give examples of the methodology outputs. If the reader requires more information about technical implementation details, I suggest the original paper by Gunning (2013).

3.1 TIME-LAPSE INVERSION

A group of methods designed to separate the time-lapse signal from the noise is time-lapse inversion. During the interpretation phase, time-lapse inversion will separate time-lapse signal from noise through an iterative workflow comprising three phases: (1) the generation of a model parameterized by elastic or rock properties, (2) the forward modelling of this model into seismic data and (3) the comparison of this synthetic seismic data with the acquired time-lapse data. If successful, the methodology will be able to point out the changes in properties that lead to the generation of time-lapse signals in the seismic data while disregarding the rest of the seismic record as noise. Since the time-lapse inversion solutions are quantitative, the use of time-lapse inversion makes it possible to perform quantitative interpretation.

During the early attempts to invert time-lapse data, vintages were inverted individually and then their impedance volumes were subtracted. The resultant volumes revealed areas with positive changes in impedance (indicating a hardening of the rock), negative changes in impedance (indicating softening) and regions with no changes in impedance. As one can recall from previous sections, hardening could be an indication

of higher bulk modulus fluid displacing a lower bulk modulus fluid, an increase in the effective pressure or, in compacting reservoirs, the decrease of porosity. Softening could be an indication of gas getting out of solution and displacing oil or pressure rising, especially close to injectors. Finally, no impedance change could be a signal of no change in the dynamic properties, the destructive interaction between diverging effects or absence of reservoir.

Subsequent studies (Asnaashari et al., 2015; Sarkar, Gouveia and Johnston, 2003) showed that some coupling between the vintages could bring improvements to the inversion results by reducing the probability of having artefacts that could lead to erroneous interpretations. The attempts to create algorithms that linked the vintages can be divided into three approaches: 1) inversions schemes that invert directly for the difference between the vintages; 2) inversion schemes that use the base vintage result as a prior model for the inversion of the monitor vintage; and 3) joint inversions, where base and monitor vintages are incorporated in the same objective function. In an example of approach 1, a Bayesian time-lapse inversion was performed directly on the seismic difference volume (Buland and El Ouair, 2006). In this work, the authors present and test an inversion algorithm on the difference of full stack datasets of the Norne field, Norway. This field was subject to injection and production data and the results indicate that the pressure variation effect was negligible. The method was successful in calculating the water saturation variation's mean and standard deviation using Monte Carlo simulation realizations. In a comparative study, Routh et al. (2012) tested approach 2 (coupling the vintages and utilizing the base full waveform inversion (FWI) model as the prior model for the monitor FWI) against approach 1 (inverting the difference volume). The analysis of the results showed that the approach 2 improves the signal-to-noise ratio while eliminating artefacts from the final model. This result is in agreement with Sarkar et al. (2003). In that paper, the authors review the current techniques and also suggest that some coupling is necessary between the inversions of time-lapse vintages.

In an example of joint inversion, approach 3, a three-stage inversion, was carried out by Labat et al. (2012). In the first step, each seismic dataset (base and monitor for PP and PS data) was inverted separately. After that, a time-shift correction was calculated using the P-impedances volumes obtained from the previous step and constraining the time-shifts with the P-wave velocities variation while assuming that

density changes are negligible. Lastly, the impedance and density models were optimized with the evaluated time-shifts while employing the same constraints to invert all the seismic cubes simultaneously. The methodology was applied to the CO_2 Storage reservoir at the Sleipner field in the North Sea with better results when compared with independent inversions. The main advantage of this method is the integration of the time-shift correction in the workflow while most methodologies require the pre-alignment of the vintages. This guarantees that all the vintages are in the same traveltime basis allowing the interpreter to obtain a quantitative estimation of impedance variations.

Finally, Asnaashari et al. (2015), by inverting a Marmousi model (Bourgeois et al. 1991) using three different time-lapse FWI strategies, show that if the noise level is low the inversion of the difference, approach (1), is a robust process and can be used instead of the coupling strategy approach (2). On the other hand, if the noise level is high, the subtraction of vintages will lead to an increase in the noise standard deviation and the amplitude of noise will overwhelm the signal, making the inversion of the difference driven by the noise. In that case, the coupling method, called by them the sequential method, will lead to better results, especially if prior information is used to focus the inversion algorithm on the time-lapse variation areas.

One important area of research on time-lapse inversion is the distinction between pressure and saturation variation effects. Due to constructive and destructive interaction, few works in the literature try to separate the elastic effects coming from fluid saturation variation from those derived from pressure variation, if both variations took place in the same location during production (Landrø, 2001). This topic is the subject of ongoing research. In his book, Johnston (2013) gives examples of works that try to isolate the pressure effect from saturation effects using the fact that S-impedance is only affected by pressure, while P-impedance is affected by both effects. He warns, however, that all these approaches are applied on a case-by-case basis and highly dependent on the choice of rock physics model. He also points out that most of the works dealing with this problem in literature aim at clastic reservoirs and apply map-based techniques. Another aspect that plays an essential role in the study of time-lapse inversion procedures is the integration of data from other disciplines, such as petroleum engineering and geology. Since multidisciplinary studies are inherent in any project involving time-lapse seismic data, this sort of work is always relevant. In an

example of such multidisciplinary examination, a time-lapse pre-stack elastic inversion was constrained by the use of rock physics and reservoir engineering information used to create the prior model (Blanchard and Thore, 2013). In this work, the authors conclude that data integration enhances the quality of the final model.

The approach used in the present work is a Bayesian methodology; therefore, it utilizes the interpreter's prior knowledge of the field. It applies facies trends to describe the properties of the lithologies within layers, making it possible to invert for facies. This approach also utilizes forward modelling based on well-known rock physics models (Gassmann equations for fluid substitution, Backus averaging for calculus of effective properties in laminated medium, Gardner equation for density calculation from velocity) to calculate a large number of realizations from which statistical analysis can be carried out. This last property makes it possible to evaluate the uncertainty associated with each parameter of the model. Another advantage of this methodology is that it is open-source, permitting the user to grasp a deeper understanding of the method. Such a method has applications in problems where geomechnical, flow simulation and structural geology effects do not need to be described in a three-dimensional model and are relatively weak. In that case, the method is capable of bringing useful information to the user.

3.2 CLASSIFICATION OF INVERSION METHODOLOGY

Delivery4D is a stochastic inversion method, so instead of giving only the best estimate of model parameters it will sample from a statistical probability distribution of models (Buland and Omre, 2003). This statistical distribution of models can go through a maximization process and return the most probable model or through a sampling process for the purposes of computing sampling statistics. The method used in this work is a simultaneous petrophysical inversion, which implies that relations between the elastic and rock properties are used in the prior distribution of models during the inversion process. Following Grana (2013), this approach improves the consistency between the information provided by elastic properties P-impedance, S-impedance and density outputs but also associated rock properties including porosity, net-to-gross (NG) and fluid saturation.

The present method is a time-lapse inversion and has the capability to use multiple vintages or difference volumes as inputs. It returns elastic and rock properties outputs for each vintage, as well as outputs regarding time-lapse calculation as a variation of pressure and fluid saturations for every vintage. The model construction is layer-based and works in a trace-by-trace fashion, meaning that the properties are considered constant inside the layer for each trace. It is possible to make properties vary in space by specifying different priors to different locations inside a layer, but no inter-trace coupling has been modelled, meaning that the results for each trace remain independent of the neighbouring traces. The user has to specify facies and define loading trends for the facies properties. The facies are end-member lithology (e.g. 100% sand) and fluid substituted for a reference fluid saturation state (e.g. 100% brine). An initial estimate of the fraction of each facies is also required, in the form of NG, the fraction of the porous facies in the layer. The volume mixing of facies fractions is assumed to occur in a finely laminated sense. Effective media models using the fraction of each facies are used to calculate the layers' effective properties. After inversion, an updated distribution of facies is provided via a posterior marginal distribution of Net-to-Gross. In the next sections, I will provide more information about this methodology and its Bayesian foundations.

3.3 BAYESIAN INVERSION

The Bayesian stochastic framework is widely used in geophysical inverse problems due to its capacity to integrate prior information and, in doing so, restrict the model space (Tarantola, 1987). In Gunning (2013) a Bayesian time-lapse inversion methodology is presented for multivintage migrated seismic data. Bayes' theorem is usually expressed as

$$P(m|S) = \frac{P(S|m)P(m)}{P(S)}, \tag{3.1}$$

where S is a vector of data, m is a vector of model parameters, $P(m|S)$ is the posterior distribution, $P(S|m)$ the likelihood, $P(m)$ the prior distribution, and P(S) the probability of the data. The theorem states that one can update the prior distribution through the integration of new data via the likelihood term (Tarantola, 1987). Each term in this equation requires an explanation and a contextualization in terms of

Bayesian time-lapse seismic inversion. The denominator P(S) is constant for the purposes of this inversion; its presence is dropped, henceforth. In the Bayesian time-lapse inversion, base and monitor vintages of true amplitude imaged seimic reflectivity are the main inputs. They are represented in Equation 3.1 by the vector S. The model is based on a layer parameterization and the model parameters are presumed constant throughout a layer. In this sense, the model parameters vector, **m**, is a vector of layer parameters. The prior distributions of elastic and petrophysical parameters, encompassed in $P(m)$, are obtained from wells, cores and plugs, and represent all the information gathered by the interpreter before all the data in vector S was acquired.

The likelihood $P(S|m)$ is the probability of the data given the model. In the present approach, it is the product of two terms. The first term is associated with the mismatch between the input seismic data and the synthetic data created by convolution of the reflectivity series R and the chosen wavelet w. This is the "seismic" likelihood, and can be written as

$$L(S|m) = \exp(-f_{error} * \frac{\sum_{error-sampling\ points} ||S_i - w*R(m)||^2}{2\sigma_s^2}), \tag{3.2}$$

where f_{error} is a correction factor for the error sampling procedure as presented in Gunning and Glinsky (2004). The correction factor discounts any effects of oversampling so that the statistical power in the mismatch is not overstated. The signal-to-noise ratio (S/N) is implied by the noise level σ_s supplied by the user. The forward-modelling approach used to generate the synthetic data employs a one-dimensional (1D) convolutional modelling operator. It treats layers as isotropic homogeneous entities. In the permeable layers, the effective elastic properties are computed from the successive application of Gassmann's fluid substitution (Equation 2.20) assuming constant saturation of an effective fluid with properties described by Equation 2.17 and Equation 2.19 throughout the layer. In the case of the impermeable layers, the effective elastic properties are computed through the application of Backus averages (Equation 2.16). The other term that composes the likelihood is the "isopach" likelihood term. It constrains certain layers to have a known thickness ΔZ_j within an error $\sigma_{\Delta Z_j}$, and can be modelled as

$$L_{iso} = \exp(-\sum_j \frac{\left(v_{j,p,eff}(t_j - t_{j-1}) - \Delta Z_j\right)^2}{2\sigma^2_{\Delta Z_j}}) \,, \tag{3.3}$$

where $v_{j,p,eff}$ is the effective acoustic velocity of layer j and t_j is the time of layer j top. The likelihood achieves its maximum value at the "maximum likelihood" model, with the model that best fits the data.

The Posterior distribution $P(m|S)$ is the probability of a certain model given the data. It represents the updated distribution that integrates the prior beliefs of the interpreter with the new data. It is important to highlight that if the prior distribution is too broad, indicating a complete ignorance of model parameters, the posterior distribution will be dominated by the likelihood. Alternatively, if the prior is too narrow, models that lie far away from the prior mean will be disproportionally penalized (Gunning and Glinsky, 2004).

3.4 MODEL PARAMETERS

The layers in the model are defined by the top horizon time, the discrete variable fluid (brine, oil, condensed gas or gas), fluid saturation for each vintage, pressure, and NG (Figure 8). Additionally, an estimation of the fluid probability must be informed in order to model the time-lapse behaviour of the reservoir based on the initial model. The parameters of the layers can be categorized as global (the same for all layers: e.g. acoustic velocity for the reservoir end member's matrix), local (different for each layer: e.g. layer's top time) or vintage dependent (different for each vintage: e.g. gas saturation). The NG is defined as the fraction of permeable end-member in the layer. Optionally, a second kind of NG, net-to-gross-hard (NG-hard), is defined as the fraction of one impermeable end-member in the impermeable fraction of the layer (1-NG). This happens to accommodate a second impermeable end-member in the model. The end-members are combined in the layer via Backus average procedure.

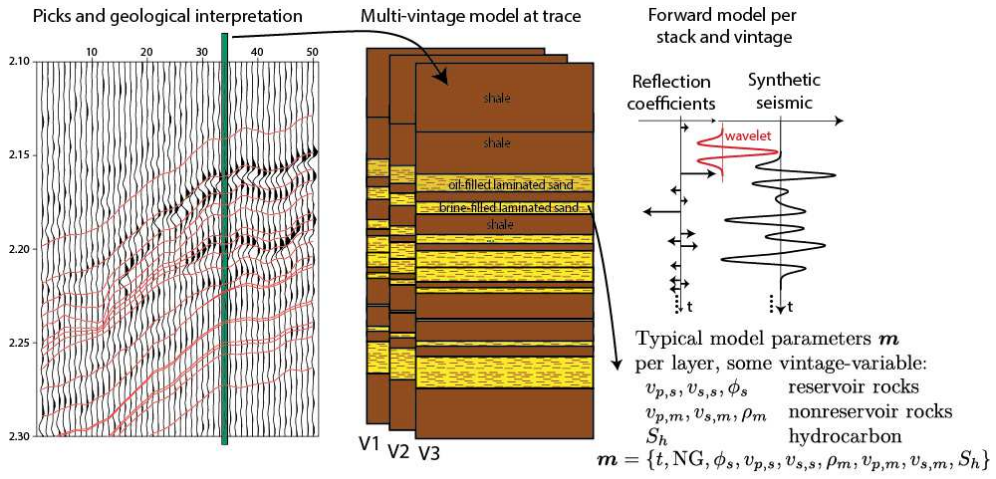

Figure 8 *Schematic of model parameterization and forward modelling (Courtesy of James Gunning).*

For the simplest kind of model without a second kind of impermeable rock ("hard"), there are two kinds of end-members: permeable and impermeable. The permeable rock is defined by linear regressions of Vp with depth, Vs with Vp and porosity (∅) with Vp, respectively given by

$$V_{pb} = \left(A_{vp} + B_{vp}d + C_{vp}LFVI\right) \pm \sigma_{pb}, \tag{3.4}$$

$$V_{sb} = \left(A_{vs} + B_{vs}V_{pb}\right) \pm \sigma_{sb}, \tag{3.5}$$

and

$$\emptyset_b = \left(A_{\emptyset} + B_{\emptyset}V_{pb}\right) \pm \sigma_{\emptyset b}\ , \tag{3.6}$$

where d represents the depth. The subscription b is utilized to indicate the use of brine as a reference fluid, which completely saturates the samples via fluid substitution. LFIV is the low-frequency interval velocity, a local mean vertical P-wave velocity obtained from pure seismic data such as VSP, moveout or stacking considerations. This variable helps adapt the regression for most stratigraphic, compaction and overpressure effects. The As, Bs and Cs are the regression coefficients and the σ's represent the standard deviation from each regression curve.

The impermeable end-members are defined by linear regressions of Vp with depth, Vs with Vp and a power law regression of density (ρ) with Vp, respectively given by

$$V_{pb} = \left(A_{vp} + B_{vp}d + C_{vp}LFVI\right) \pm \sigma_{pb}, \tag{3.7}$$

$$V_{sb} = \left(A_{vs} + B_{vs}V_{pb}\right) \pm \sigma_{sb} \tag{3.8}$$

and

$$\log \rho_b = \left(\log A_\rho + B_\rho \log V_{pb}\right) \pm \eta_{\rho b} \text{ or } \rho_b = A_\rho V_{pb}^{B_\rho} \pm \sigma_{\rho b}, \tag{3.9}$$

where the same notation used for the permeable regression curve equations applies and the $\eta_{\rho b}$ represents the standard deviation in Equation 3.9. The regression equations are used to define a normal distribution model for the rock properties in each layer. The top-horizon time of each layer (t) and the bottom-layer base-time (t_b) must be provided by the user. The means of these times are estimated from manual or computer-assisted interpretation and the picking uncertainty is used to estimate the standard deviation of the times.

3.5 PRESSURE

Pore pressure effects on acoustic and shear velocities are modelled as

$$V_{p,F,i,T} \equiv V_{p,F,i,1} + R^{eff}_{p,F,T} U_{i,i_{reff}} \Delta p_T \tag{3.10}$$

and

$$V_{s,F,i,T} \equiv V_{s,F,i,1} + R^{eff}_{s,F,T} U_{i,i_{reff}} \Delta p_T \,, \tag{3.11}$$

where $V_{p,F,i,T}$ is the acoustic velocity for the F end-member in the *ith* layer at vintage T. $V_{p,F,i,1}$ is the acoustic velocity for the same end member and layer in the base vintage (T=1). Δp_T is the variation of pore pressure experienced by the reservoir between the acquisition of the vintages. The effective stress path coefficient $R^{eff}_{p,F,T}$ is the gradient of acoustic velocity with pore pressure for each end-member F. In the reference layer, the variation of velocities is assumed to have a linear, reversible relation to the pore pressure. The other layers' velocity-pressure relationships employ a stress correlation coefficient $U_{i,i_{reff}}$. When the stress correlation coefficient $U_{i,i_{reff}}$

is equal to 1 it means that the pressure variation in the layer is the same as in the reference layer. On the other hand, when the stress correlation coefficient $U_{i,i_{reff}}$ values are smaller than 1, it indicates that the pressure variation in that layer is smaller than the one in the reference layer. By definition, the reference layer will have $U_{i_{reff},i_{reff}} \equiv 1$. As shown before, Vs is considered linearly dependent to Vp, therefore, the effect of pressure must also be incorporated to Vs. In Equation 3.11, $V_{S,F,i,T}$ is the shear velocity for the *F* end-member in the *ith* layer at vintage *T*. In the same equation, $V_{S,F,i,1}$ is the shear velocity for the same end member and layer in the base vintage (*T*=1) while $R^{eff}_{S,F,T}$ is the effective stress path for shear velocity – the gradient of shear velocity with pore pressure for each end-member.

3.6 SATURATION

The methodology provides two ways of parameterizing the fluid state in each layer for each trace. The first one is the "enumeration mode". In this approach, fluids are chosen from a suite of fluid types: oil, gas, brine or low-saturation gas. The chosen fluids are considered to saturate the entire reservoir layer. For each vintage (base, monitor 1, monitor 2), the user assigns fluid probabilities for every fluid in the reservoir layer. The user has the option to impose fluid ordering following a density order. In that case, low-density fluids sit on top of fluids with higher density in adjacent permeable layers. For fluid variation between vintages, it is possible to constrain the later vintage saturation from the saturation found in the previous vintage. The options are to let the saturation of the late vintage be less than, equal to or greater than the saturation of the previous vintage. The constraint can also be dropped if insufficient engineering knowledge is available to justify it. The alternative method of specifying fluid variation is through fluid contacts. This approach should be applied if the fluid contact is visible in every vintage. In that case, only one sequence of fluids will be modelled, and the depth of the contact can be constrained to vary in a certain way by choosing the late vintage fluid contact depth to be less than, greater than or equal to the previous vintage fluid contact depth.

3.7 OUTPUTS

In a Bayesian inversion, the estimation of associated parameter uncertainty is an integral part of the inverter result (Buland and El Ouair, 2006). The main output of a Bayesian inversion is the posterior distribution. The posterior distribution is a multidimensional probability density function (PDF) whose dimensions are the model parameters. As with any multivariate PDF, to extract the distribution of a single model parameter − known as a marginal posterior distribution − one needs to integrate the posterior distribution over all the other parameters.

The methodology used in this work utilizes two procedures to generate useful information from the posterior. The first one is a maximization process that aims to calculate the maximum *a posteriori* (MAP) model (Figure 9), the model with the highest probability given the data. The MAP has advantages over the maximum likelihood model since it integrates prior information to the likelihood, and thus decreases the multidimensional volume of acceptable models in the model space. Additionally, in the presence of noise, the best fit between synthetic and acquired data will not guarantee the best result because noise could be mistakenly inverted as signal. The prior information helps to regularize the posterior distribution, and it makes the MAP more resilient to noise than the maximum likelihood model alone. Obviously, discretion should be exercized, because, if the prior information is unreliable, the MAP point will become biased. The second kind of statistical output is a sampling process that is explained in detail by Gunning and Glinsky (2004). The sampling algorithm uses Markov chain Monte Carlo to generate *n* samples from the posterior at each trace (Figure 10). At each layer in each trace, statistical properties such as the mean and standard deviation of model parameters can be recovered from the ensemble of *n* samples, where *n* is the number of samples determined by the user.

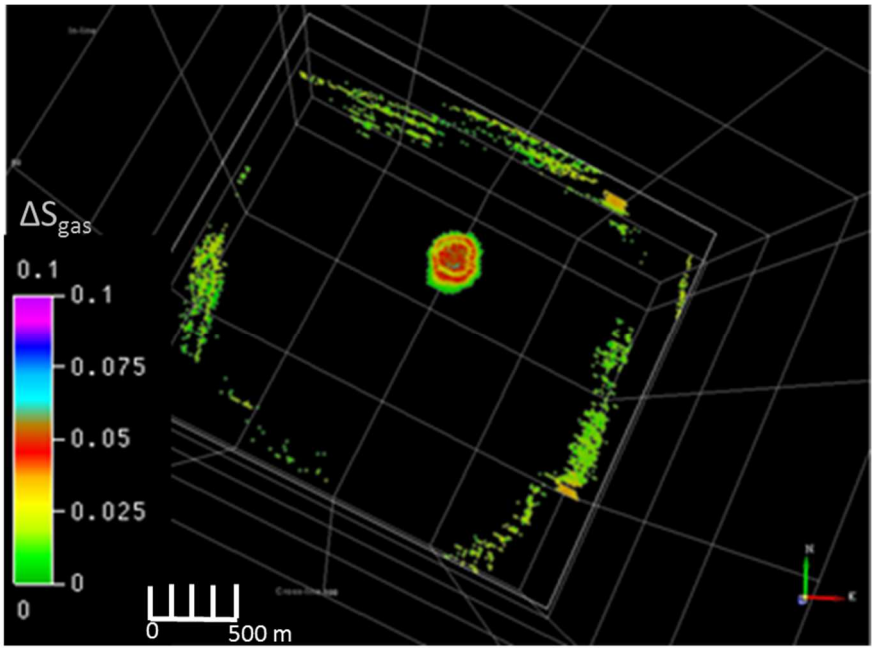

Figure 9 *Example of gas saturation MAP model. This inversion result was calculated for a synthetic monitor vintage in a CO_2 injection feasibility study presented in chapter 4.*

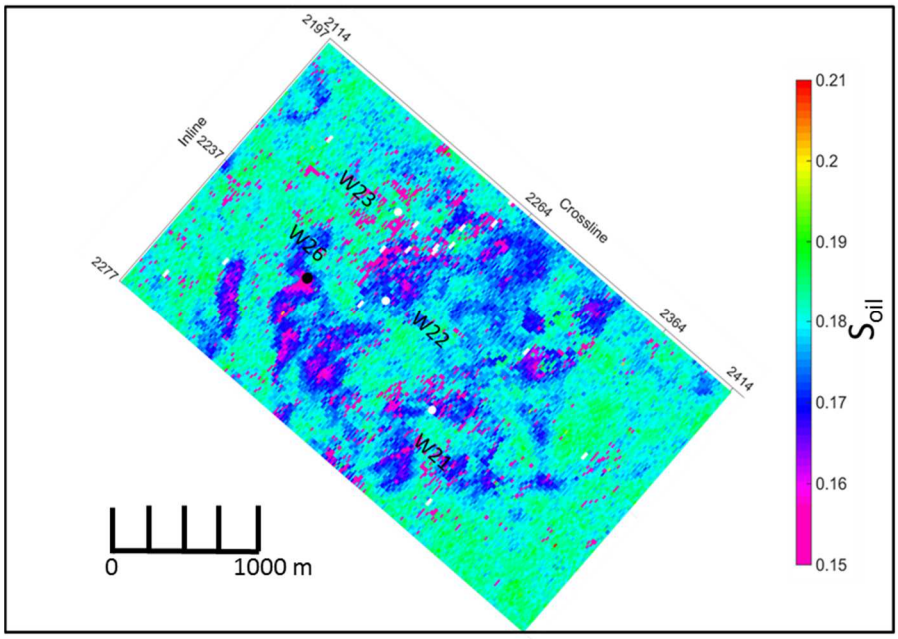

Figure 10 *Example of oil saturation standard deviation calculated from 10000 samples over the top of the reservoir studied in chapter 5.*

CHAPTER 4. STOCHASTIC TIME-LAPSE INVERSION OF A SYNTHETIC DATA SET

Here I present a practical example of the Bayesian formulation employed in the stochastic inversion used on a synthetic data set created for a feasibility study on the detection of CO_2 injected into a saline solution (CO2CRC Otway Project). The motivation behind the study of an inversion procedure used on synthetic data relies on the possibility of knowing the true model and, hence, assessing the performance of the inversion independently. The model used here is a realistic instance of a geophysical problem, as presented by Pevzner et al. (2013). Previous synthetic examples were presented by Gunning (2013).

In the following sections I will discuss the input data and describe an optimally parameterized inversion of a noise-free version of the data set, the baseline case. Subsequently, I will present the results of the inversion with alternative parameterizations for the prior model of the monitor gas (CO_2) saturation (Sg_2) mean and standard deviation. After that, I will compare these results with the baseline results to evaluate the ability of the methodology in finding the solution starting from a non-optimized initial model. This example is included to simulate the very common situation where the interpreter is not certain about the fluid saturation values present in parts of the reservoir away from the wells. Following this, I will perform the inversion with noise-contaminated input seismic data. Two types of noise (coherent and random) are used to evaluate the robustness of the methodology to noise contamination. Once more, I will compare the results with the baseline results. The comparison involves the analysis of the posterior distributions of gas saturation variation in the reservoir layer as well as its maximum *a posteriori* (MAP) model. The importance of such an evaluation resides in the fact that one's main interest while doing stochastic time-lapse inversion is in quantitatively interpreting the gas saturation anomalies found in time-lapse seismic data. Thus, the limitations of the method must be known for the sake of determining the uncertainty in the predictions for future projects using real time-lapse seismic data, as per the study presented in the subsequent chapter.

4.1 SYNTHETIC SEISMIC DATA

The dataset used in this work was originally aimed at a feasibility study for a time-lapse acquisition that took place at the Otway Basin, in the southern part of Australia, after the injection of supercritical Buttress gas (78.7% CO_2, 18.9% CH_4). A detailed description of the data set modelling is presented in Pevzner et al. (2013). The CO2CRC Otway project is the first Australian project to explore deep CO_2 storage opportunities. It comprises two phases: In stage 1, approximately 65 tonnes of CO_2 rich mix were injected in a depleted portion of Naylor field, Otway Basin, Victoria, Australia. In stage 2, the Paraate formation, a sandstone reservoir with a saline aquifer, was injected with 15000 tonnes of supercritical Buttress gas.

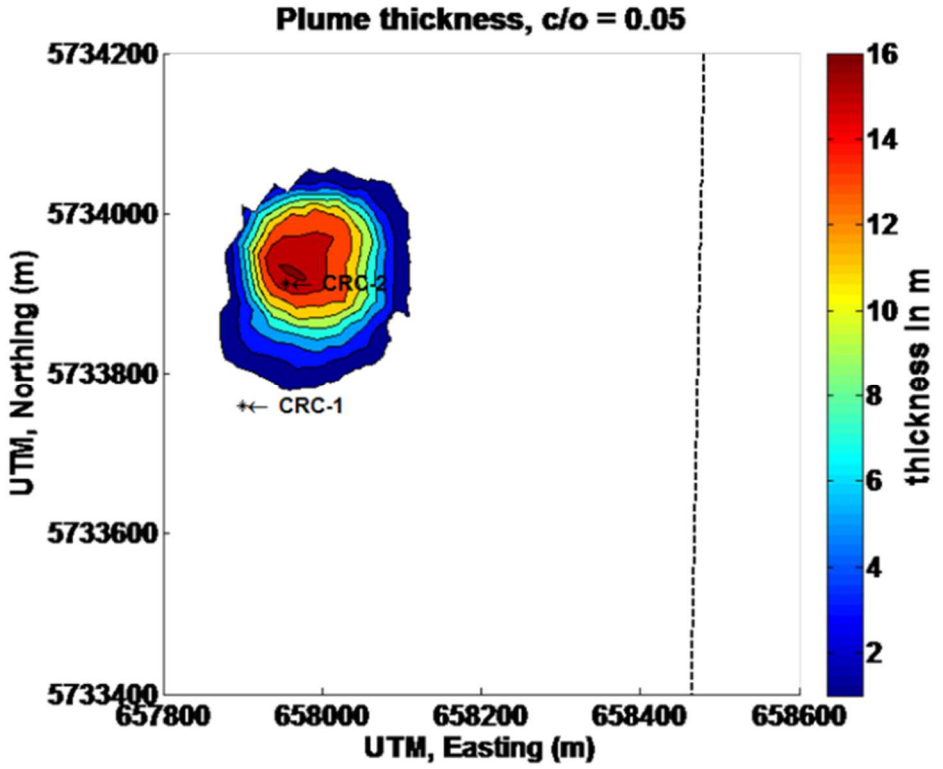

Figure 11 *Thickness of gas column model used to create the 5% anomaly in the time-lapse seismic data.*

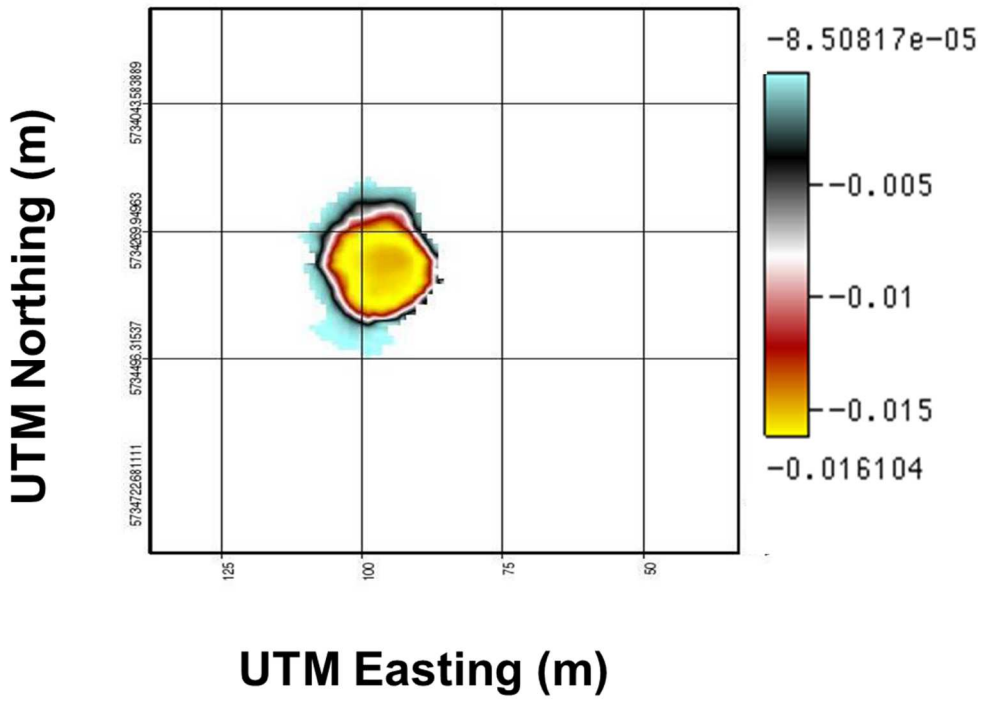

Figure 12 *Anomalies in the difference volume (monitor – base) showing the seismic effect of the injections of 10 k tonnes of Buttress gas. Source: Pevzner et al. (2013).*

Pevzner et al. (2013) modelled five scenarios of injection in the Paraate formation and used them in the feasibility study for the CO2CRC Otway project. In the first two scenarios, 10000 and 30000 tonnes of supercritical Buttress gas were injected in a depth range of 1392 − 1399 m TVDSS, a 7 m-thick clean sandstone interval. The third and fourth scenarios of injection of 10000 and 30000 tonnes of Supercritical Buttress gas took place in a deeper interval (1445 − 1465 m TVDSS), a 20 m-thick interval of shaly sandstone. The fifth scenario was used to validate the other four and is a 2D finite difference modelling along an inline direction (base and monitor vintages) using a fourth-order elastic 2D FDTD (Finite difference time domain) algorithm with a cell size of 0.5x0.5 m.

I chose to investigate the third and fourth scenarios because, unlike the first scenario that only slightly exceeded the noise level (Pevzner et al., 2013), their time-lapse response greatly exceeded the noise level of the area. This gives a greater confidence in the determination of the plume location from the seismic data. Among them, I opted to invert the 10000 tonne injection of supercritical Buttress gas (third scenario) because the actual volume of gas injected (15000 tonnes) lies in between

10000 and 30000 tonnes. If it was detectable with 10000 tonnes, I expect a larger volume to be detectable too. All scenarios went through the same workflow that encompasses reservoir modelling, rock physics, and seismic forward modelling.

The reservoir modelling comprises the generation of a static geologic model and the subsequent flow simulations. A compositional numerical reservoir simulator implemented the flow simulations with an injection rate of 111 tonnes per day. A two-phase (brine and gas) flow modeller employed relative permeability and capillary pressure functions adapted from a CO_2-brine flooding dataset calculated using cores from the Paraate formation (Krevor et al., 2012). Peng-Robinson (Peng and Robinson, 1976) equation was employed to model the phase of the CO_2−CH_4 mixture. The dissolution of CO_2 in formation water was modelled using the equations described in Chang, Coats, and Nolen (1996).

During the modelling of elastic properties, due to the small thickness of the gas plume predicted by the flow simulations (Figure 11) the authors built the model by interpolating the well logs. Initially, 1D models were created for wells CRC-1 and CRC-2 and changes in elastic properties were calculated for different plume thicknesses. The authors used these models to run full waveform forward modelling. Subsequently, the authors created a 3D model utilizing horizon-guided log extrapolation and interpolation, using the wells present in the area (CRC-1, CRC-2 and Naylor-1) to account for the shape of the plume. The estimated elastic changes away from the wells are based on the flow simulation results and the porosity from interpolated log data and the static model. Finally, the authors calibrated the seismic velocities with well CRC-2. The authors also performed fluid substitutions using Gassmann's equations (Gassmann, 1951) and applied Wood's mixing rule to calculate the fluid bulk modulus. They also utilized an average of Hashin-Shtrikman bounds to derive the effective bulk modulus for a mixing of sandstone and shale. These models were used to calculate the fifth injection scenario.

The three most important steps for the construction of the synthetic seismic data sets were: 1) Computation of synthetic seismograms for the 1D velocity models for different plume thicknesses with 5% of gas saturation. 2) Generation of 3D seismic volumes for models with gas plumes presenting infinite lateral extent and constant thickness using the same acquisition geometry, and the synthetic seismograms from

the previous step, 3) Construction of synthetic seismic volumes that represent the presence of gas plume with actual finite lateral extent and thickness predicted by the flow simulator. To perform this last step, for each trace position a plume thickness is specified, a synthetic volume generated in step 2 using a model with the specified plume thickness is selected and a trace from this volume is positioned in the trace location of the new volume. Figure 12 displays the difference volume (the subtraction of the base vintage from the monitor vintage). One significant advantage of such data is to provide a model with constant gas saturation and at the same time one that incorporates the acquisition geometry used in the real seismic data previously acquired in the area. This allows me to easily determine the quality of my results by analyzing the posterior gas saturation variation distribution.

4.2 LITHO-CLASSIFICATION

The lithoclassification was based on the neutron-density crossover and the volume of clay logs (Watson et al. 2012) combined with the formation micro image (FMI), core analysis and seismic horizons to create a facies association (Watson et al., 2012). The facies identified in wells CRC-1 and CRC-2 were: distal mouth bars (clay rich) grading to proximal mouth bars (clean sandstones) and distributary channels (sandstones and gravel) at the top. The bounding flooding surfaces for each of these are marked where there have been delta front mudstones (potential seals recognized in the cores and logs). All of this was overprinted with diagenetic carbonate cement layers which serve as seals of varying quality (Watson et al., 2012). I classified the distal mouth bar and the delta front as shaly facies, proximal mouth bar and distributary channel as reservoir facies, and diagenetic carbonate cement as cemented facies. Therefore, I constructed the model layer using two impermeable end-members (shale and cement) in addition to the reservoir end-member.

4.3 CONSTRUCTION OF THE PRIOR MODEL

The *a priori* information consists of a complete suite of logs from two wells present in the area. I employed twelve layers to model the time window of interest around the reservoir (Figure 13). These layers consist of a combination of two facies, a reservoir

and a cemented end-member or a reservoir and a shaly end-member. No layer comprised cemented and shaly end-members at the same time, due to the absence of this facies combination in the logs. In all layers, the net-to-gross value was defined as the ratio between the reservoir and the non-reservoir end-members. I constructed trend curves of velocities (Vs and Vp) and density (or porosity in the reservoir layer) for each facies with the respective uncertainties based on well log measurements. Figure 14 to Figure 22 depict the process of calculation of trend curve parameters from the well data. Because the well logs were acquired before the injection of Buttress gas, the fluid in the pores was brine. Thus, I did not need to perform fluid substitution in the calculation of the trend curves used in the inversion. Table 1 presents the elastic properties of Brine and Buttress gas. The trend curves' parameters for each end-member are summarized in Table 2.

Since only one well was available to construct the curves, the correlations were not ideal and biased by the well location, as suggested by the coefficient of determination R^2 at Table 2. Nevertheless, since this was my unique source of "hard data" in the field I decided to use it. The uncertainty generated in that step had to be taken into account during comparison of the inversion result with the true model.

Table 1 *Fluid Properties.*

Fluid	Brine	Buttress gas
Acoustic velocity	1575 m/s	286 m/s
Density	0.993 g/cm^3	0.3372 g/cm^3

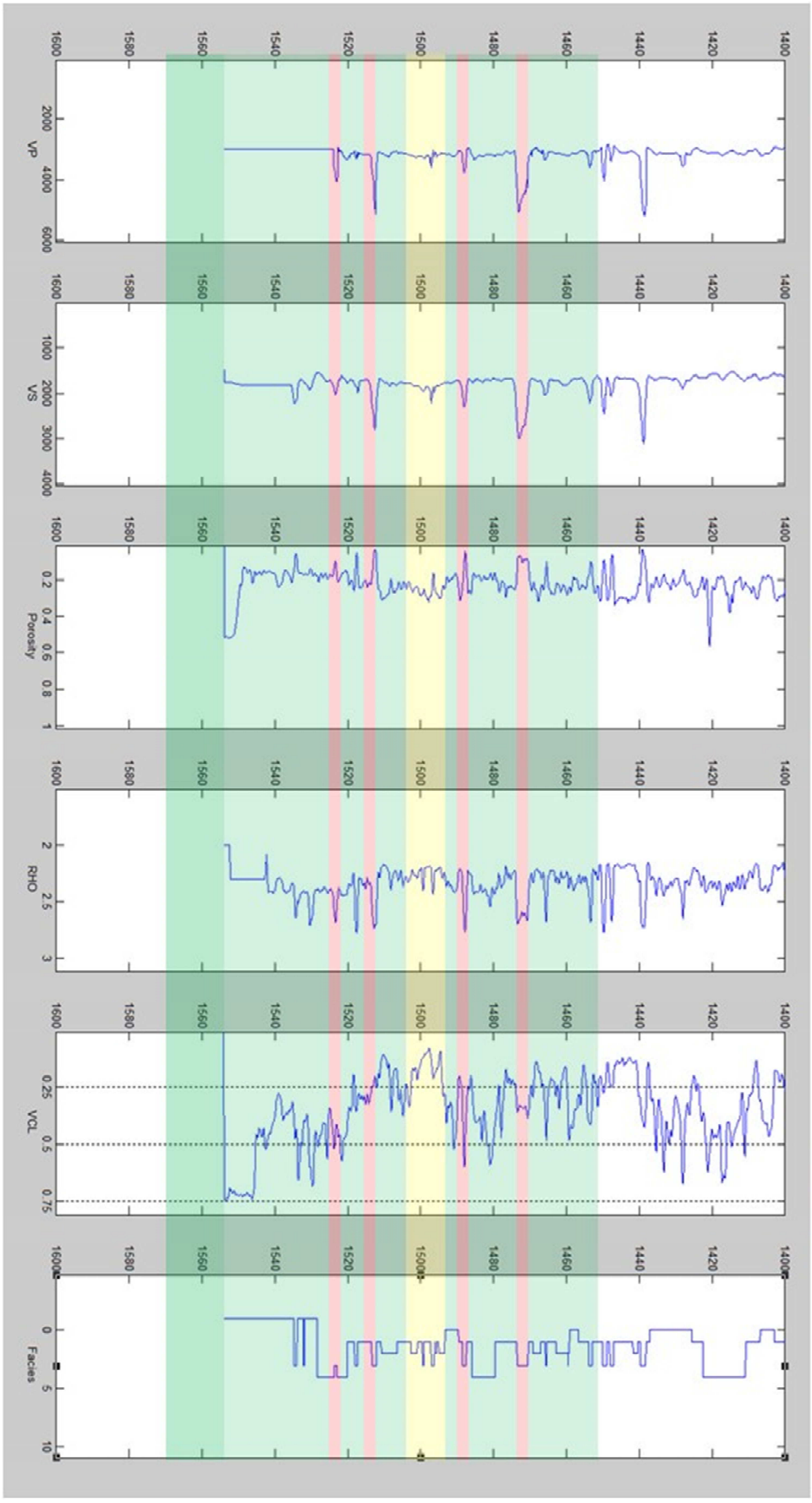

Figure 13 *Superposition of twelve layers used in the model over the logs.*

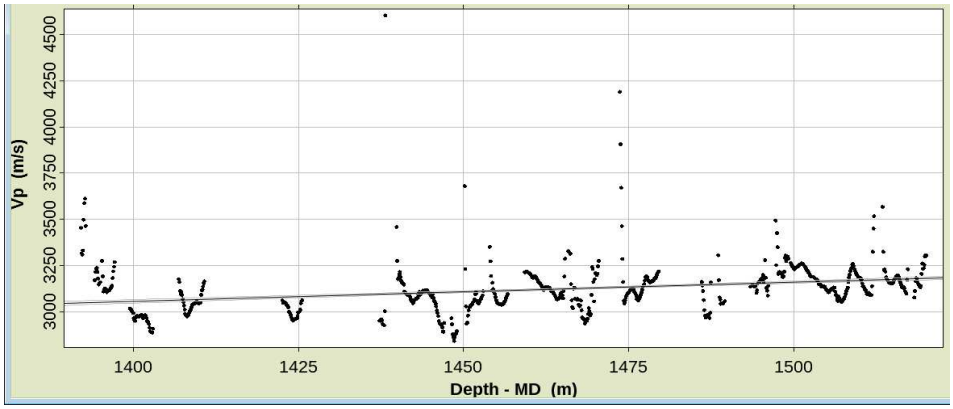

Figure 14 *Compressional velocity versus true vertical depth (TVD) relation for reservoir (sand) end-member with best-fit line.*

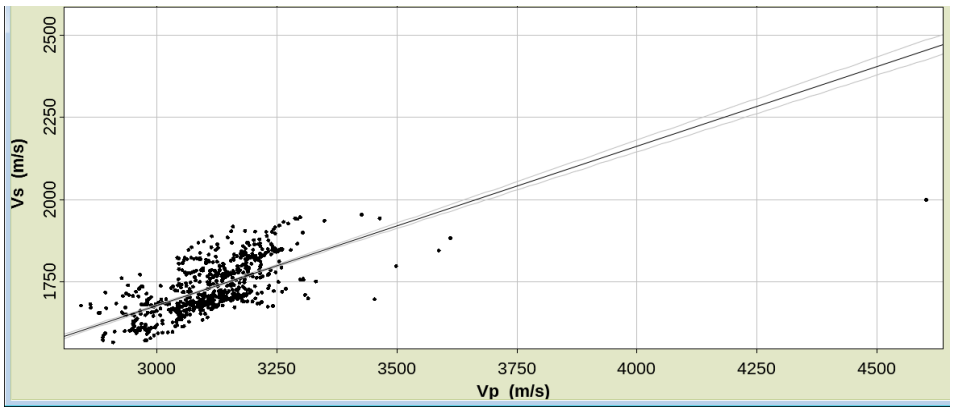

Figure 15 *Shear velocity versus compressional velocity relation for reservoir (sand) end-member with best-fit line.*

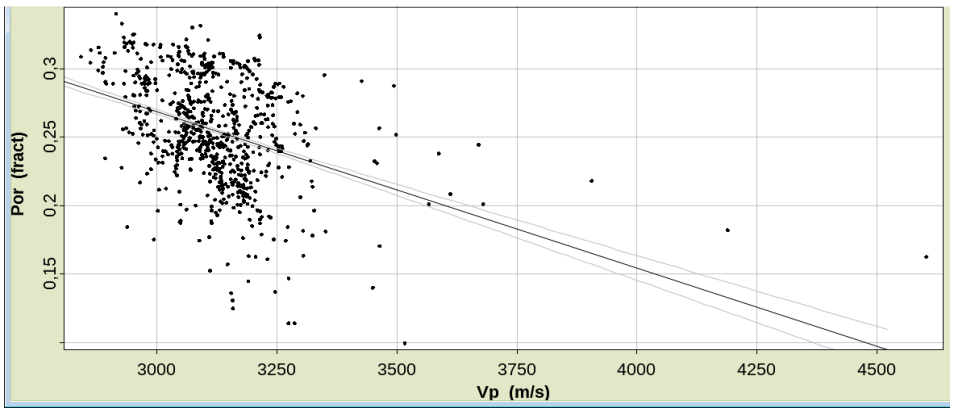

Figure 16 *Porosity versus compressional velocity relation for reservoir (sand) end-member with best-fit line.*

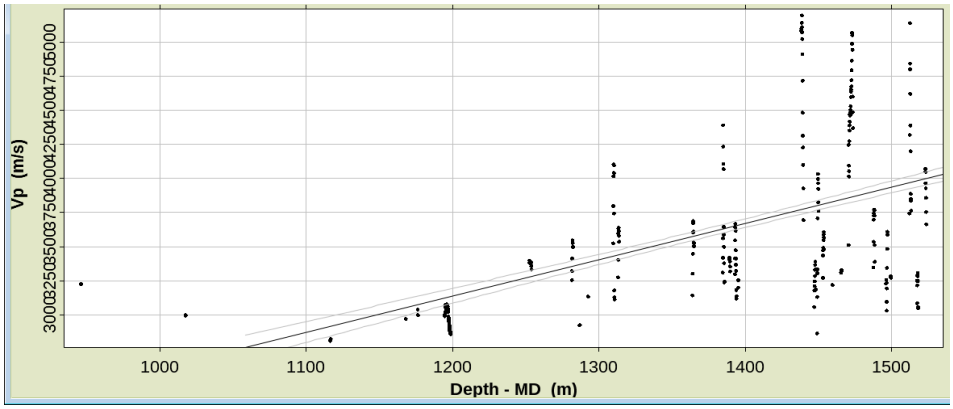

Figure 17 *Compressional velocity versus true vertical depth (TVD) relation for cemented end-member with best-fit line.*

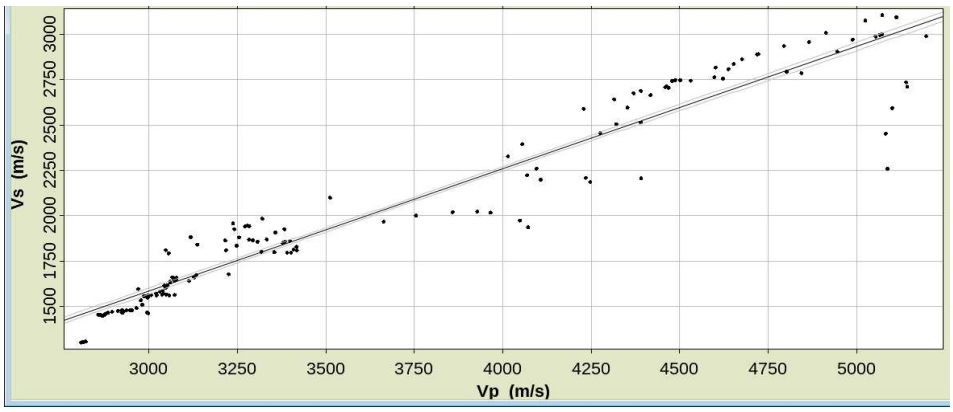

Figure 18 *Shear velocity versus compressional velocity relation for cemented end-member with best-fit line.*

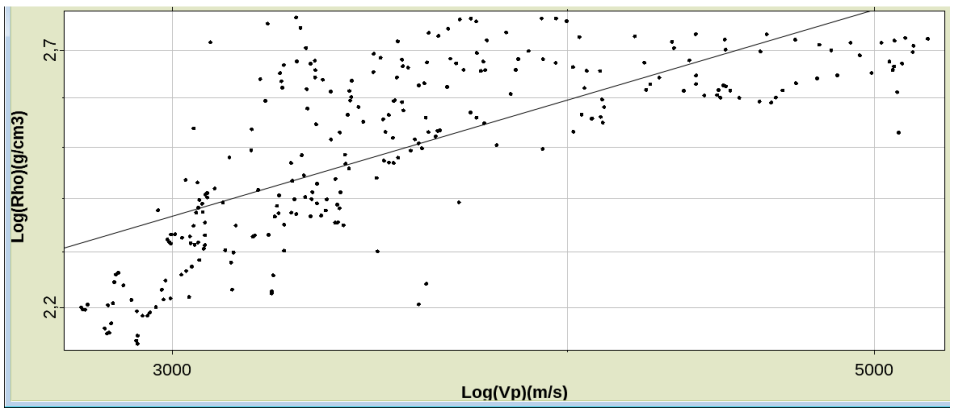

Figure 19 *Logarithm relation between density and compressional velocity for the cemented end-member with best-fit line.*

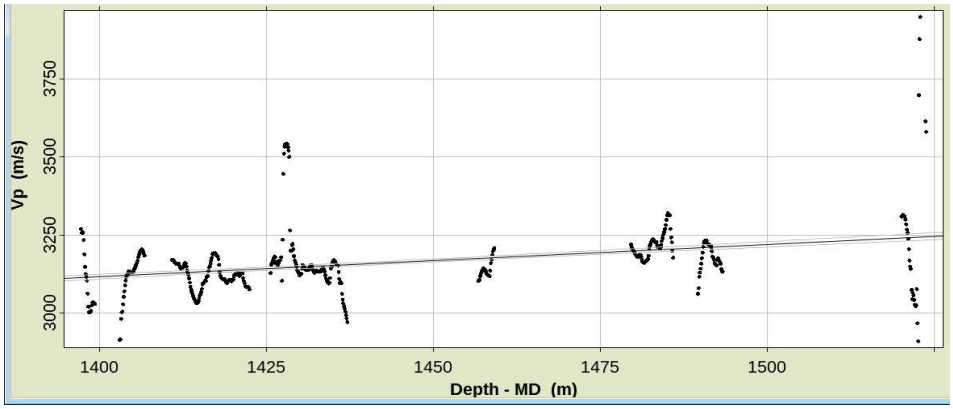

Figure 20 *Compressional velocity versus true vertical depth (TVD) relation for shaly end-member with best-fit line.*

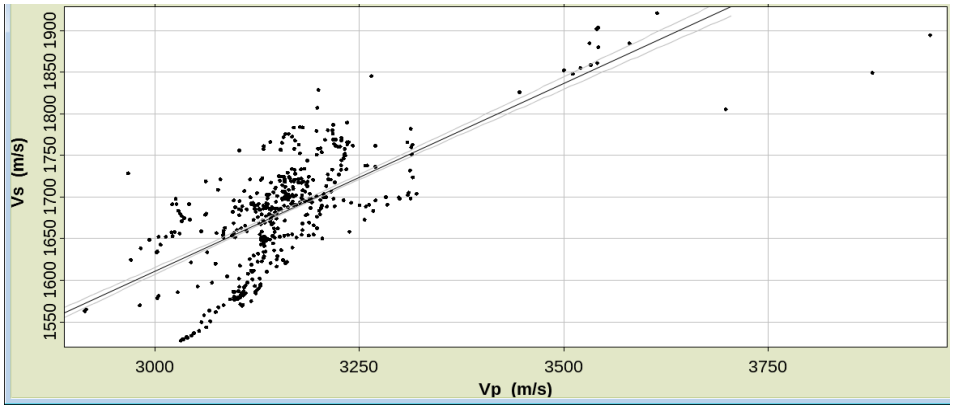

Figure 21 *Shear velocity versus compressional velocity relation for shaly end-member with best-fit line.*

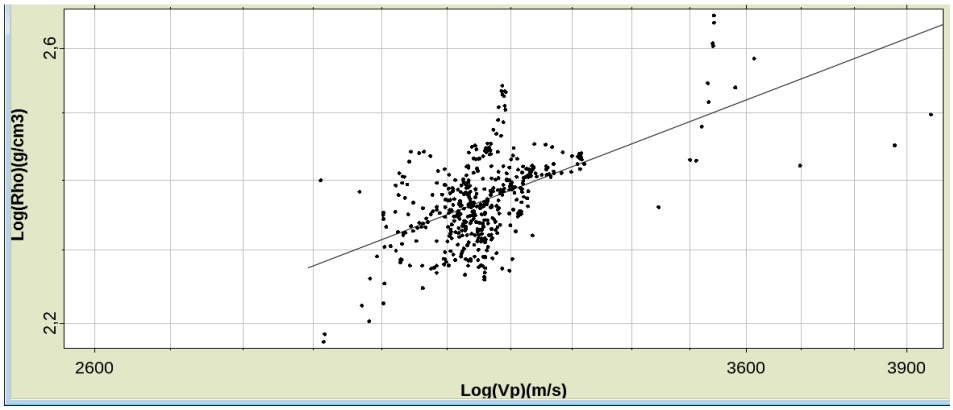

Figure 22 *Logarithm relation between density and compressional velocity for the shaly end-member with best-fit line.*

Table 2 *Trend parameters*.

Regression	Facies	Parameter A	Parameter B	R^2	Fit type
Vp x Depth	Sand	1601	1.038	0.08	Linear
Vp x Depth	Shale	1662	1.038	0.12	Linear
Vp x Depth	Cement	405.6	2.3	0.29	Linear
Vs x Vp	Sand	-107.8	0.5952	0.47	Linear
Vs x Vp	Shale	285	0.4421	0.50	Linear
Vs x Vp	Cement	-138.9	0.6217	0.92	Linear
Porosity x Vp	Sand	0.6101	-1.14×10^4	0.15	Linear
Density x Vp	Shale	0.057	0.4654	0.58	Power law
Density x Vp	Cement	0.2053	0.3058	0.19	Power law

As shown in Table 3, I set the NG mean to be 10% for the layers below and above the reservoir and 100% in the reservoir layer. I maintained the NG standard deviation at a minimum because the presence of shale and the presence of gas have similar effects in decreasing the acoustic impedance; therefore their simultaneous presence in the layer creates ambiguities and increases the uncertainty of the results. While the NG was constant before and after the injection, gas saturation changed. For all layers, I set the gas saturation mean and standard deviation before the injection to 0. After injection, the gas saturation mean and standard deviation on the layers below and above the reservoir remained 0. However, the gas saturation in the reservoir layer after injection is different from 0.

Table 3 presents the settings of the gas saturation prior. To simulate the real-life situation where the interpreter is unware of the exact location of the gas plume, I supposed that the reservoir layer was completely saturated with Buttress gas (Figure 23). The synthetic seismic data was generated with a Ricker wavelet of 45Hz peak frequency and a matching wavelet was used in the inversion. Finally, due to the small amount of pore pressure variation in the actual sequestration project (due to high permeability), I did not include any pore pressure variation in the model. Therefore, I only studied estimates of (Buttress) ΔSg with injection.

Table 3 *Properties used in the model layers.*

Layer	Net-to-gross	Gas saturation after injection	Non-reservoir facies
Top layer	0	0	Shale
Cement 1	N(10%,$(10\%)^2$)	0	Cement
Shale 1	N (10%,$(10\%)^2$)	0	Shale
Cement 2	N (10%,$(10\%)^2$)	0	Cement
Shale 2	N (10%,$(10\%)^2$)	0	Shale
Reservoir	N (100%,$(10\%)^2$)	N (3%,$(8\%)^2$)	Shale
Shale 3	N (10%,$(20\%)^2$)	0	Shale
Cement 3	N (10%,$(10\%)^2$)	0	Cement
Shale 4	N (10%,$(20\%)^2$)	0	Shale
Cement 4	N (10%,$(20\%)^2$)	0	Cement
Shale 5	N (10%,$(20\%)^2$)	0	Shale
Base layer	0	0	Shale

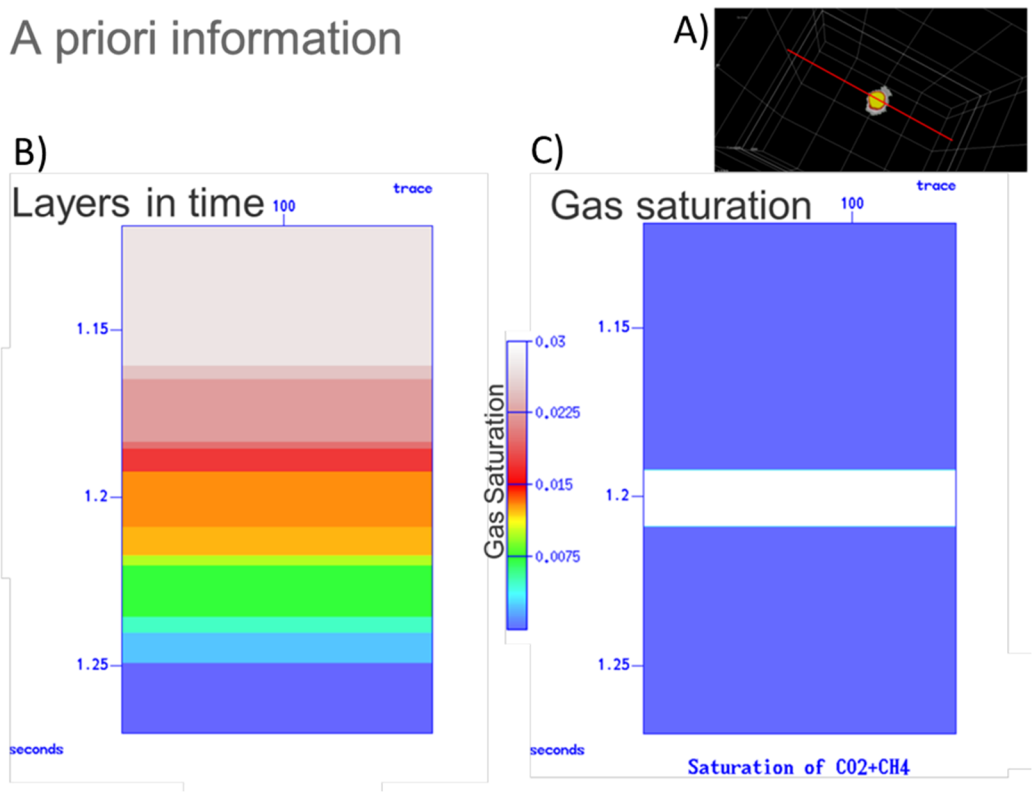

Figure 23 *A priori information used in the model showed by A) a section crossing the plume, B) the geometry of the layers utilized in the model, and C) the initial supposition about the spreading of gas throughout the entire reservoir layer.*

4.4 BASELINE CASE

To create a baseline case I used a noise-free synthetic seismic dataset and based my inversion parameters on those that were used in the construction of the model. An important exception was the selection of the prior distribution of the gas saturation present in the reservoir during the acquisition of the monitor vintage (Sg_2). In the interest of ensuring that my example resembles the real-life problem of detecting gas saturations without knowing the gas plume exact spatial distribution, I avoided the use of any spatial constraints. Specifically, I assumed that, after the injection, the gas could be present in the entire reservoir layer, in contrast with the "true" model used in the generation of the synthetic data in which the gas was concentrated in the region indicated by the flow simulator results shown in Figure 11. In doing this I avoided creating a bias towards the true model in the inversion procedure and achieved a clear evaluation of the quality of the inversion result.

In order to create a realistic model, I set the probability of gas as a constant (80%) instead of using a gas probability map from the flow simulator. I also had to establish the prior distribution of the gas saturation for the monitor vintage in the entire reservoir. To do this I had two options: 1) set the mean equal to the one utilized in the flow simulation (5%), with a considerable uncertainty to accommodate areas with and without gas (0% gas saturation). This option would have the disadvantage that half of my distribution (values above 5%) would not reflect the true disttribution because there was no point where the gas saturation's value was bigger than 5%. 2) set the mean with a value in between the gas saturations for points with gas (5%) and without gas (0%), and use a smaller uncertainty and guarantee a higher probability for both cases. In order to use a distribution that better reflects the expected gas saturation scenarios, I decided to choose the second option. I set a prior gas saturation for the monitor vintage as a normal distribution with mean 3% and standard deviation 8%, $Sg_2 \sim N(3\%,(8\%)^2)$. Before the injection took place, there was no gas in the saline aquifer at the Paraate formation, so the gas saturation distribution for the base vintage was set to N (0%, 0%). Thus, there was no reason to refer to pre-injection gas saturation, and, henceforth, I will refer to post-injection gas saturation simply as gas saturation variation (ΔSg). After the inversion, one can examine the MAP model's values and the posterior distribution for all parameters of the model. In this work, I focused my analysis on the ΔSg outputs. The MAP model's ΔSg is shown in Figure 24 and resembles the model used to generate the synthetic seismic data (Figure 11) regarding localization of the anomaly and its values apart from some peripheral noise created due to the end of the seismic data known as edge effects.

The initial mean and standard deviation gas saturation used in the base and monitor vintages was used to create the prior distribution of gas saturation in the vintages. In the context of Bayesian inversion, prior distribution assigns high probability to models that are expected considering prior knowledge, and low probability to unexpected models. If the prior distributions are in accordance with the true model, the likelihood and the prior distribution will point to the same solution: the true model. On the other hand, where the prior distribution disagrees with the true model, prior distribution and likelihood will point in different directions. In that case the term with the highest probability value will prevail Therefore, the choice of prior distribution has a large effect in the inversion result.

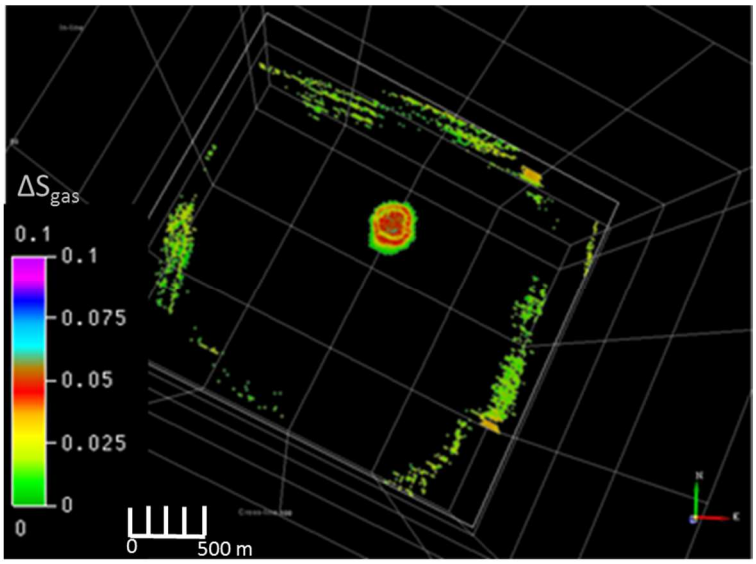

Figure 24 *MAP model's ΔSg as a result of the use of prior Sg_2 distribution set to N (3%,$(8\%)^2$) and a noise-free input seismic data.*

To facilitate ΔSg posterior distribution analysis, I designed a new indicator, the ζ indicator (Meira et al., 2015). The ζ indicator calculates the ratio of the probability that a realization has the correct value of the monitor's ΔSg (5%), within an error margin of 1% (4% to 6%, in this case), for the prior and posterior distribution. It is defined as

$$\zeta = \frac{P_{posterior}(4\%<\Delta S_g<6\%)}{P_{prior}(4\%<\Delta S_g<6\%)}. \quad (4.1)$$

The objective of this indicator is to quantify the relative propensity of the posterior monitor's ΔSg distribution in comparison to the prior's in determining the real ΔSg (5%) used in the generation of the synthetic seismic data. To calculate the ζ indicator, I selected traces in the middle of the anomaly and generated the same number (10^4) of ΔSg realizations at the reservoir layer by sampling the prior and the posterior distributions separately. After that, I counted how many ΔSg realizations lie between 4% and 6% for each distribution and finally divided the counts to find the ζ indicator. The ζ indicator takes positive values and operates in such a way that a ζ value of 1.5 indicates a 50% increase in the number of ΔSg realizations that lie between 4% and 6% for the posterior distribution when compared with the prior distribution. In the baseline case, while using only one trace's samples, the ζ value was 1.82. This value represents an improvement of 82% in the right ΔSg detectability

in the posterior distribution in comparison with the prior's detectability as can be inferred from Figure 25 and Figure 26.

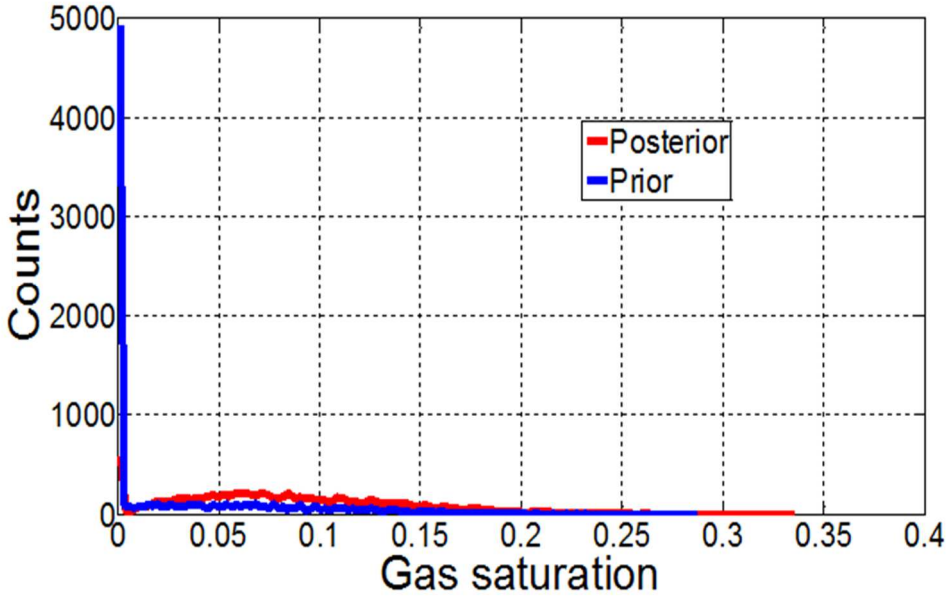

Figure 25 *Posterior and prior full distributions of ΔSg. Prior distribution is set at* $N(3\%,(8\%)^2)$.

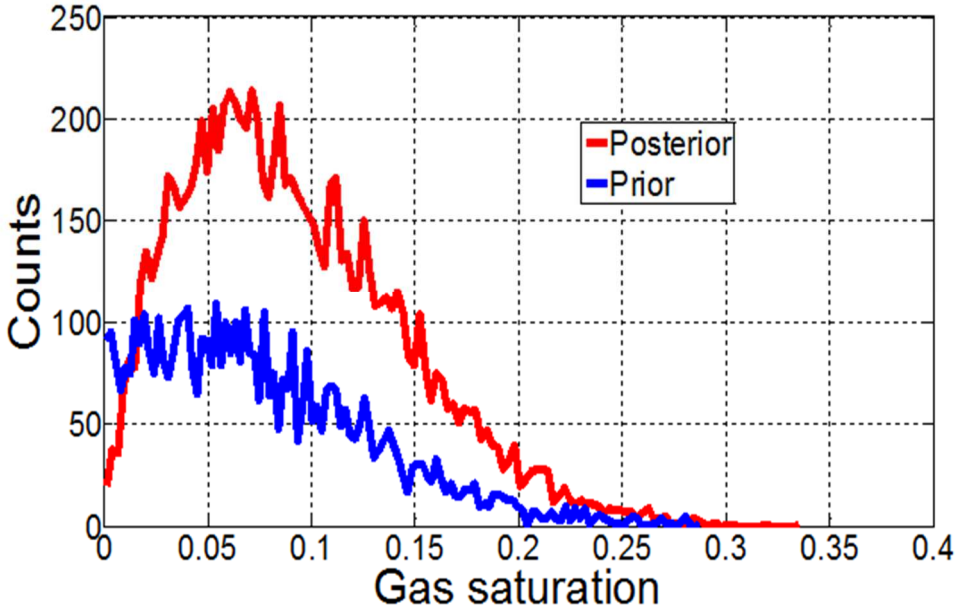

Figure 26 *Prior and posterior distributions assuming the presence of some gas* ($Sg_2 \neq 0$).

In Figure 25 and Figure 26, prior and posterior distributions of ΔSg are

presented. Figure 25 displays the distributions generated using all the samples. One can identify two peaks at zero gas saturation: a bigger one for the prior distribution and a smaller one for the posterior distribution. The existence of these peaks is explained by the fact that I chose to have a space-invariant prior distribution. In other words, I chose a prior distribution that worked well inside the anomaly plume and outside it, and allowed the existence of zero ΔSg values inside the anomaly. Since I evaluated ΔSg at reservoir level in a trace located inside the gas plume, which can be checked using the MAP model as complementary information, I could assume the presence of some gas and eliminated the peaks at zero to facilitate the analysis. This correction led to the plot in Figure 26. In this plot, it is clear that the posterior distribution is a satisfactory description of the actual model: a very narrow distribution around 5% ΔSg.

4.5 EFFECTS OF NON-OPTIMAL PARAMETERIZATIONS

Using Gassmann's fluid substitution equation, I computed a curve that quantifies the sensitivity of the reservoir rock's acoustic impedance to gas saturation (Figure 27). Analyzing the curve, one can separate two regions: a steep, more sensitive part (gas saturation less than 10%) with significant variations of acoustic impedance, and a lower slope segment (gas saturation bigger than 10%) with mild variations. In this experiment, I performed the inversion assuming the enumeration fluid mode (explained in the previous chapter), and that gas saturation is changing while all remaining parameters in the prior model remain the same between the vintages. I tested three prior distributions for Sg_2, namely: (a) $N(1\%,(17\%)^2)$;(b) $N(80\%,(17\%)^2)$; and (c) $N(80\%,(200\%)^2)$. In the steeper part of the curve, the (a) $N(1\ \%,(\ 17\%)^2)$ case's MAP model's ΔSg (Figure 28) revealed a strong resemblance to the true model. This case produced a ζ value of 1.87, which indicates an improvement in the detectability by the posterior even larger than the baseline case because, in the latter, the prior distribution peak was already close to the actual gas saturation. In the flatter portion of the curve, I tested scenarios with 80% mean for prior Sg_2 distributions using two different standard deviations: (b) 17%, representing an under-evaluated uncertainty and (c) 200%, representing a quasi-non-informative prior distribution. Figure 29 presents the MAP ΔSg model for the first case. No resemblance to the true model was

found due to the small assigned uncertainty observed in Figure 30. In this plot, neither prior nor posterior distributions were capable of generating a significant number of realizations with ΔSg between 4% and 6%.

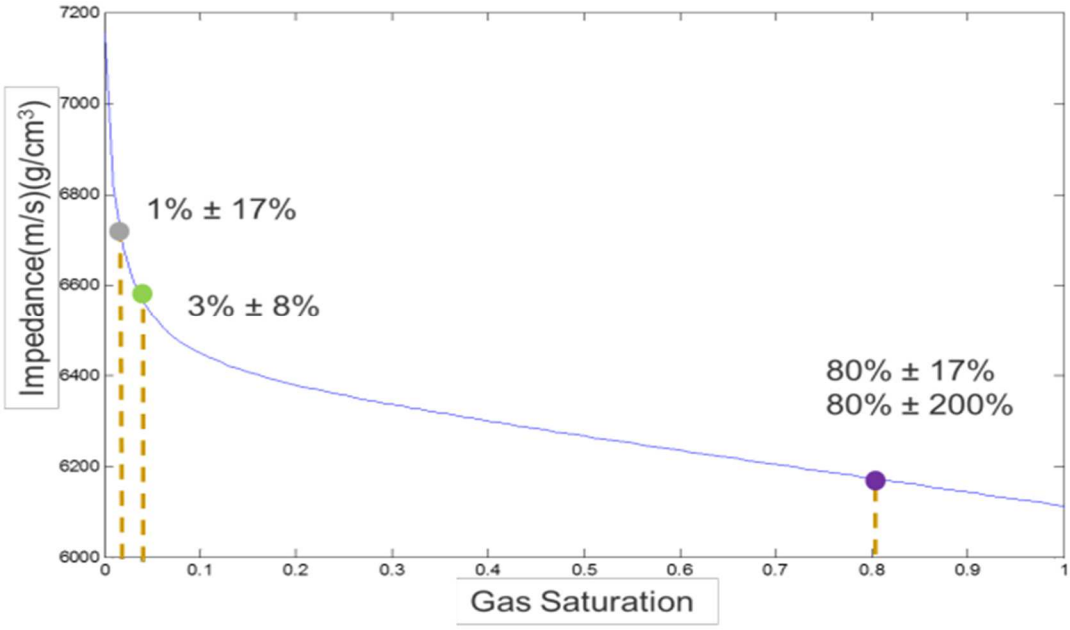

Figure 27 *Variation of acoustic impedance with gas saturation at reservoir level.*

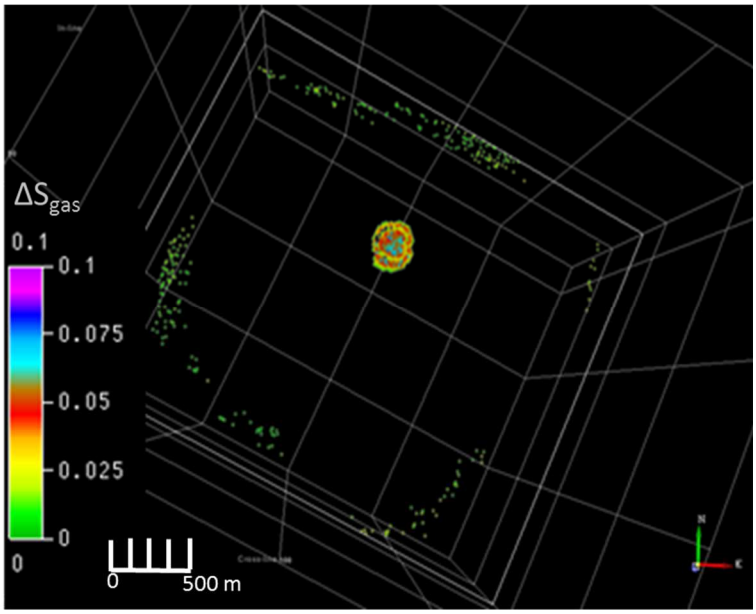

Figure 28 *MAP models ΔSg as a result of the use of prior Sg_2 distribution set to a) $N(1\%,(17\%)^2)$.*

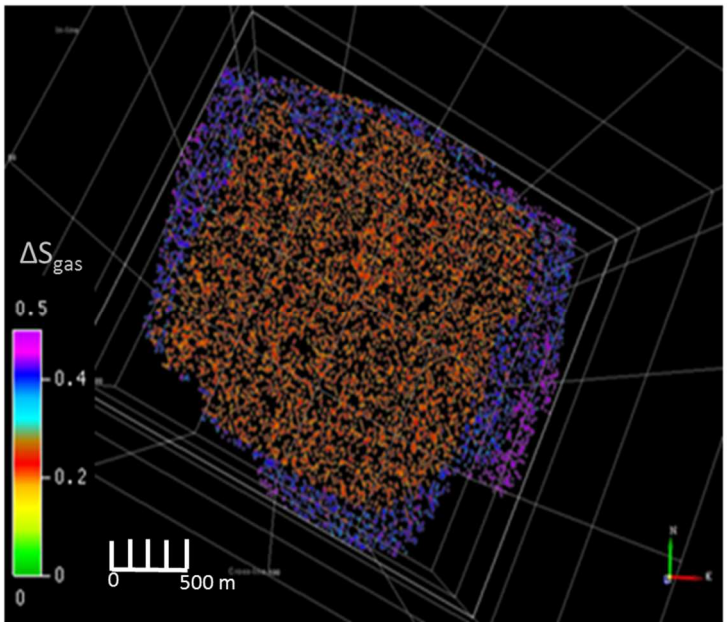

Figure 29 *MAP models of ΔSg as a result of the use of prior Sg_2 distribution equal to $N(80\%,(17\%)^2)$.*

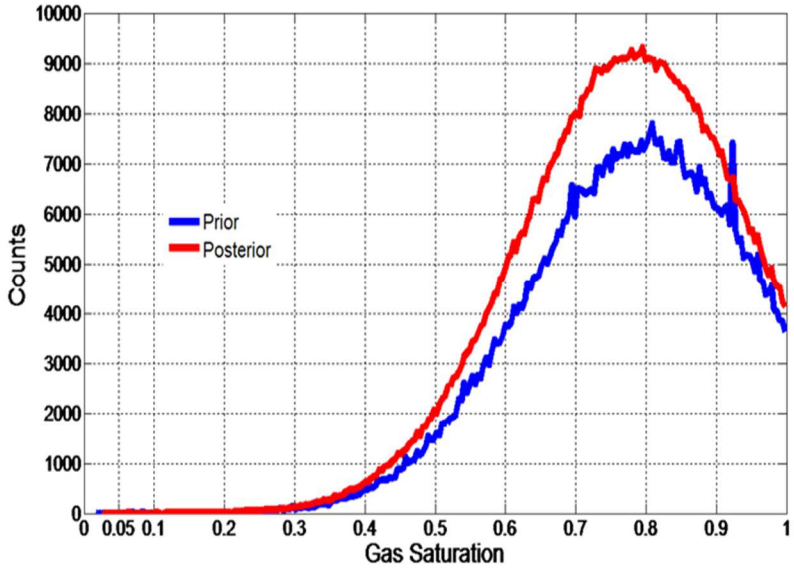

Figure 30 *Posterior and prior distributions of ΔSg. Prior distribution was set to $N(80\%,(17\%)^2)$ assuming presence of some gas ($Sg_2 \neq 0$).*

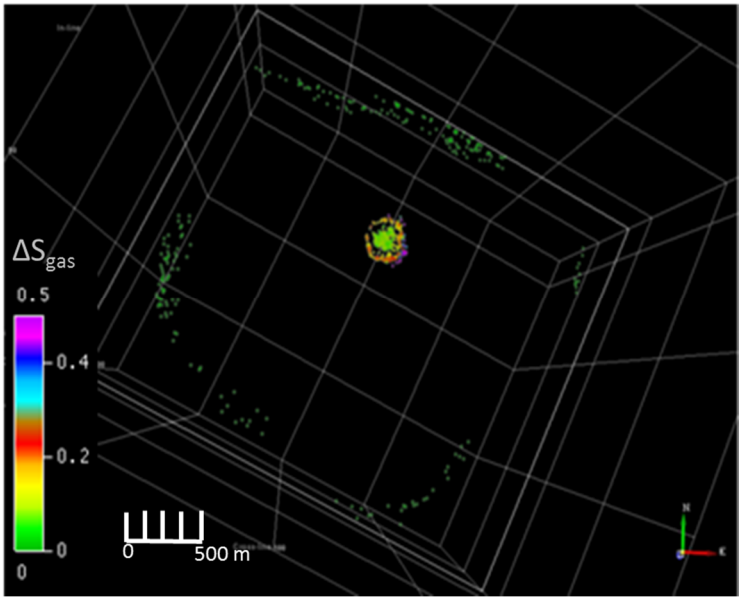

Figure 31 *MAP models ΔSg as a result of the use of prior Sg_2 distribution set to N(80%, (200%)^2).*

Figure 31 shows that a quasi-non-informative prior distribution can lead to a relatively reasonable MAP model in terms of spatial detectability as well as quantitatively (values inside anomaly are close to 5%). Nevertheless, the posterior distribution was not very successful in improving the detectability of the real model with a ζ indicator of 1.39. For a complete evaluation of the algorithm's response to Sg_2 parameterization issues, I will engage in the analysis of

Figure 32, which presents the ζ values calculated for a bigger number of combinations of Sg_2 means and standard deviations. To verify the prevalence of the same behaviour for more than one position inside the anomaly, I calculated the ζ indicator for ten traces inside the anomaly (Figure 33).

For the mean values on the steeper part of the impedance-versus-gas saturation curve (values below 10%) the improvement is larger because the rock impedance is more sensitive to pore fluid saturation. Thus, a small change in gas saturation creates a significant difference in the impedance of the reservoir layer. By means of forward modelling, this difference significantly affects the amplitude of the synthetic seismic data. The seismic misfit changes significantly from the previous step in the iteration process, making it easier for the algorithm to define the gradient of the error function. In the flat part of the curve (values greater than 10%), the further the tentative prior

Sg_2 distribution mean is from 5%, the larger the uncertainty required to achieve adequate results. In this portion of the curve, a relatively large change in gas saturation leads to a small shift in the reservoir layer impedance. The reflectivity of the reservoir layer's top interface is not considerably affected and when the synthetic traces were compared with the input data set, the error does not vary very much between two successive steps in the iteration process. Hence, it is harder for the algorithm to prefer this iteration's model compared to the previous one. For models in the low gas saturation portion of the curve and away from 5%, a bigger uncertainty in the prior model guarantees that more points in the region of the true model are supported by the prior distribution. Therefore, the basis of attraction of the MAP model optimization is wider. Since a maximum in the posterior distribution is found there and the posterior distribution is sampled more often inside maxima, a bigger uncertainty is associated with a bigger ζ value. Values of ζ can be smaller than one, meaning that the posterior distribution has a lower probability associated with the true model than the prior. This is especially true if the prior mean lies on the higher gas saturation portion of the curve (Figure 27), and its standard deviation is small. Such a choice of parameter represents a situation where the result is certain about a Sg_2 value that is actually wrong. In that case, one can say that the interpreter is precise but not accurate. In

Figure 32 one can see an example of this behaviour in the N (36%, $(30\%)^2$) case.

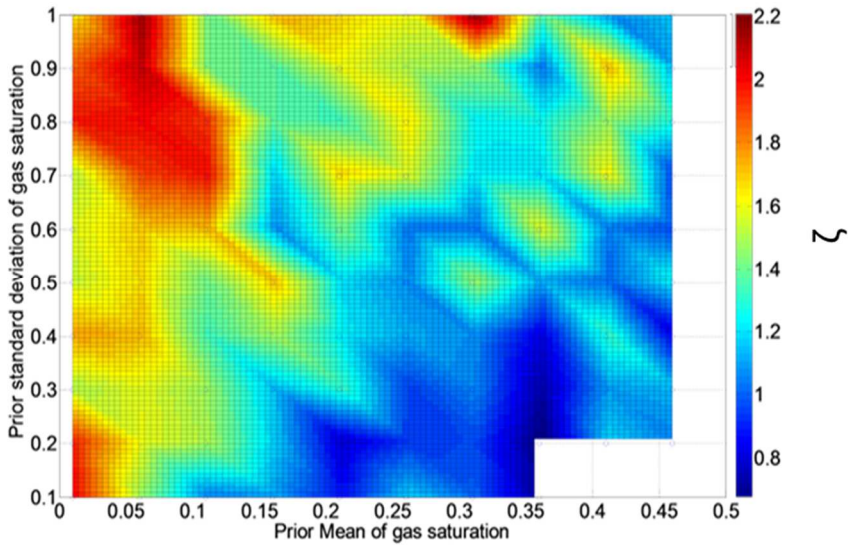

Figure 32 *Plot of ζ values for Sg_2 prior means and prior standard deviation calculated using one trace inside the anomaly.*

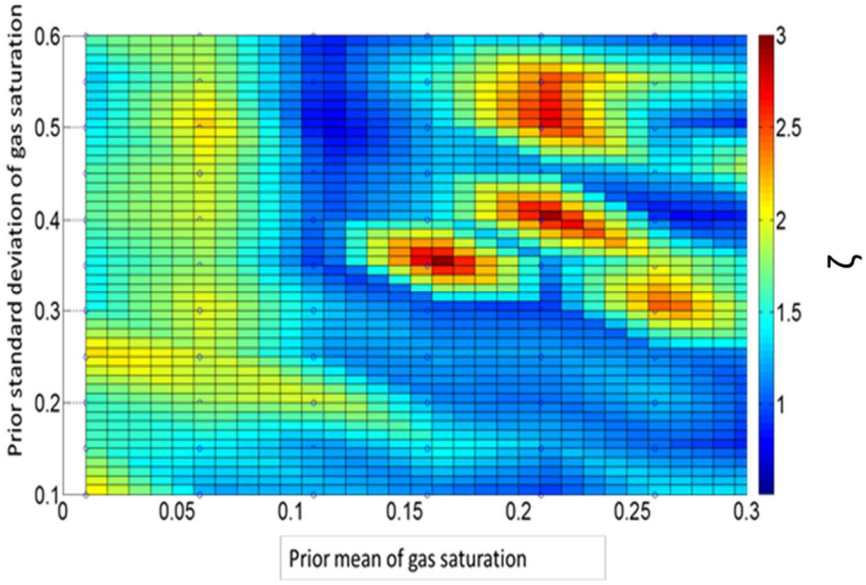

Figure 33 *Plot of ζ values for Sg_2 prior means and prior standard deviation calculated using ten traces inside the anomaly.*

4.6 EFFECTS OF NOISE CONTAMINATION

To quantify the sensitivity of the posterior distribution to noise contaminations in the input seismic stacks, I added different amounts of coherent and random noise to one vintage, and carried out the inversion (Figure 34). During the parameterization of the prior model, the user has to input the root mean square (RMS) amplitude of the noise. In the previous chapter, it was introduced as an estimate of the seismic noise power, but I prefer the "noise rms"(σ_n) denomination because it represents an RMS noise amplitude comparable to the RMS value of the signal. In this case, the typical RMS amplitude of the noise-free seismic data was 1.8×10^{-2}, while the RMS amplitude of the difference volume of the noise-free vintages was 8.4×10^{-4}. All RMS values present in this text were calculated over a window of 200 ms around the reservoir. In the first example (Figure 35), I added Gaussian random noise with various RMS amplitudes and the same frequency range as the noise-free seismic data (f1=2Hz, f2=10Hz, f3=55Hz and f4=80Hz). In this figure, the "noise RMS" σ_n was set to 0.1 and 0.01. This random noise was created with the command suaddnoise from seismic unix (SU) software (Cohen and Stockwell, 2008). The value of 0.1 was very large when compared with the real noise level of 1.8×10^{-2} but still led to good results, as shown by the MAP's model ΔSg results in the top row (Figure 35). The same cannot be said about the results achieved using 0.01, present in the bottom row. These

findings indicate that the algorithm was capable of distinguishing random noise from signal if the σ_n was bigger than the real noise level.

If one analyses a range of combinations of the real noise RMS amplitude values and the σ_n values for one position inside the gas anomaly, shown in Figure 36, it is clear that the ζ indicator presents two regions. The first region presents for σ_n smaller than 0.06, with low values of ζ, insensitive to the RMS amplitude of random noise. The second region presents σ_n higher than 0.06 with high values of ζ insensitive to the RMS amplitude of random noise. The black line indicating the same values for the real and expected noise does not correlate with any high values of ζ beyond 0.06. This suggests that, for the range of values studied, the expected level of noise in the model had a bigger effect on the detectability of the true model scenario than the RMS amplitude of the added random noise. For a higher uncertainty associated with the seismic data (high σ_n), a large range of noise level (RMS amplitude of 0.015 to 0.15) did not interfere with the detectability improvement of the true model. When the uncertainty was smaller, the level of noise affected this detectability. This also means that, due to the statistical nature of random noise, if sufficient freedom was given to the inversion operator it could separate noise from the signal. These findings were in agreement with the MAP results. Again, to verify the prevalence of the same behaviour for more than one position inside the anomaly I calculated the ζ indicator for ten traces inside the anomaly (Figure 37) and the same conclusion held.

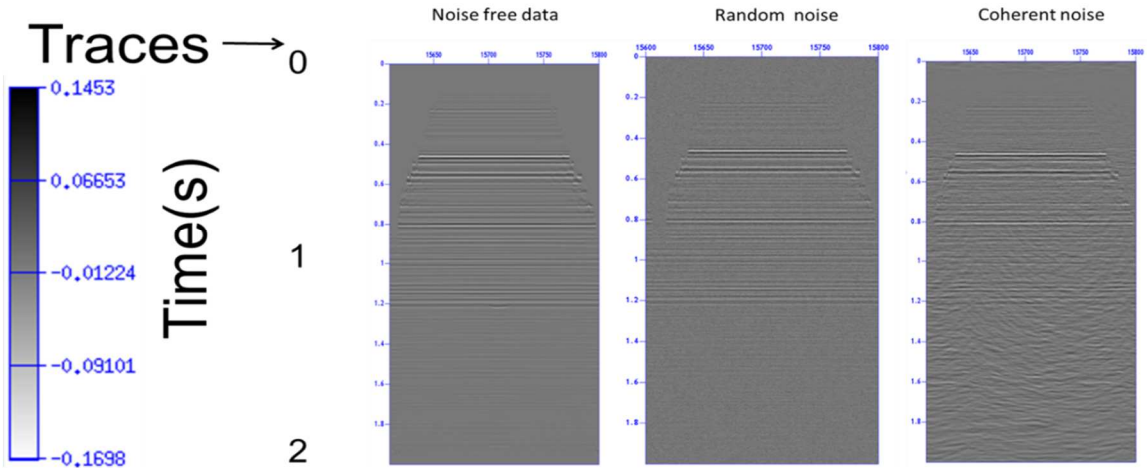

Figure 34 *Result of the addition of random and coherent noise to the synthetic data.*

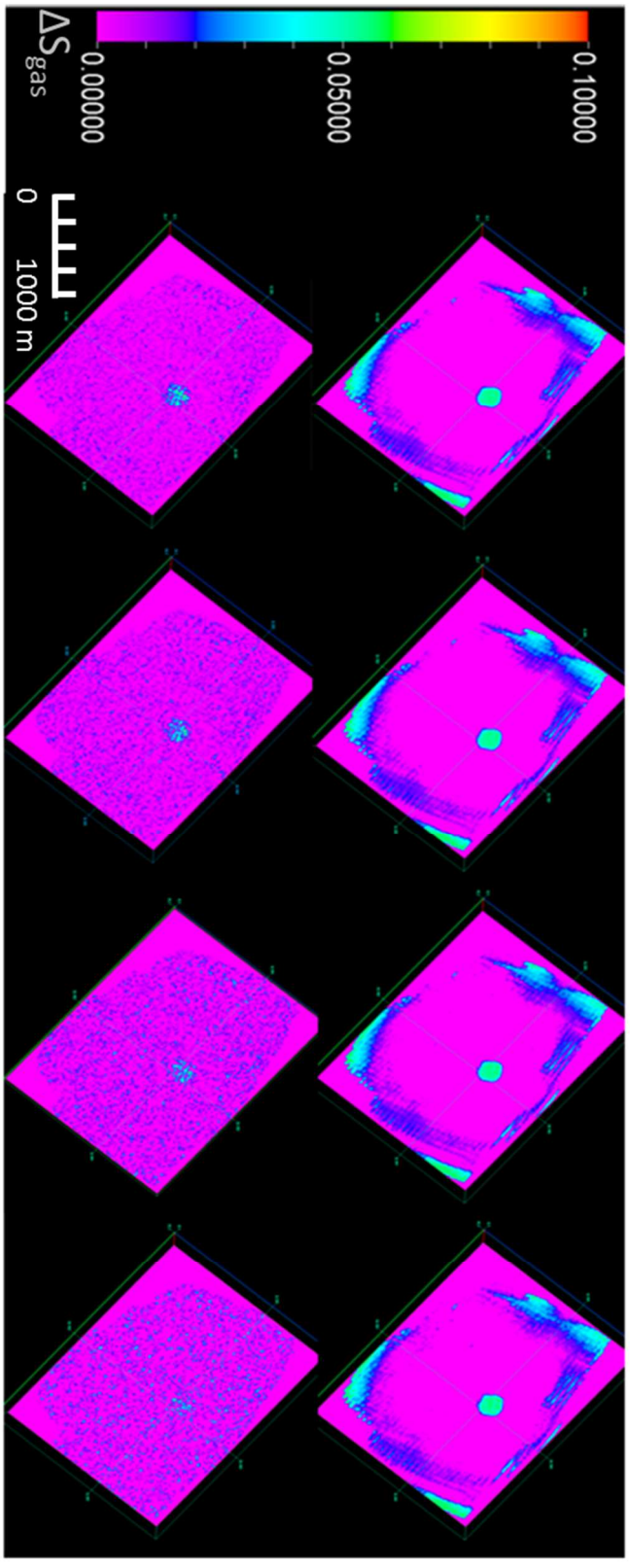
ΔSgas
0.00000
0.05000
0.10000
0
1000 m
Noise level
Seismic misfit

Figure 35 *MAP ΔSg models for input data contaminated with random noise with RMS amplitude at reservoir level of 0.0093 (signal-to-noise ratio 20), 0.0125 (signal-to-noise ratio 15), 0.0187 (signal-to-noise ratio 10), 0.0374 (signal-to-noise ratio 5). The RMS amplitude misfit was set to 0.1 and in the bottom row 0.01. The above is displayed in Schlumberger's Petrel software.*

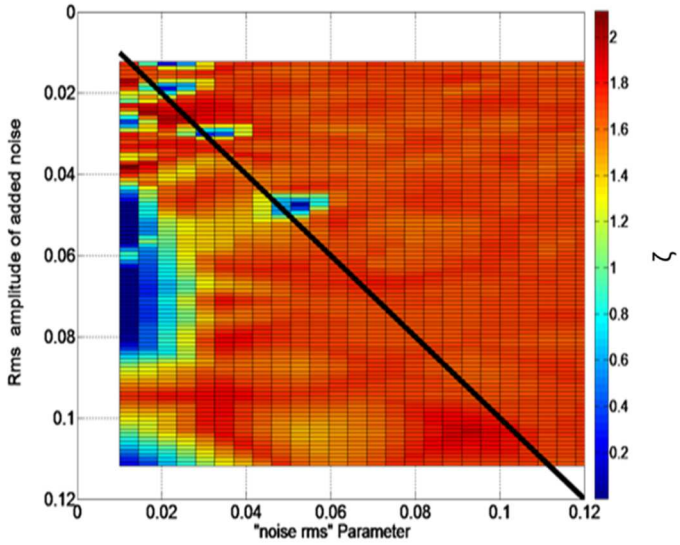

Figure 36 *View from the top of ζ values 3D plot for random noises calculated using one trace inside the anomaly. Same values for the σ_n and RMS amplitude of added random noise are indicated by a black line.*

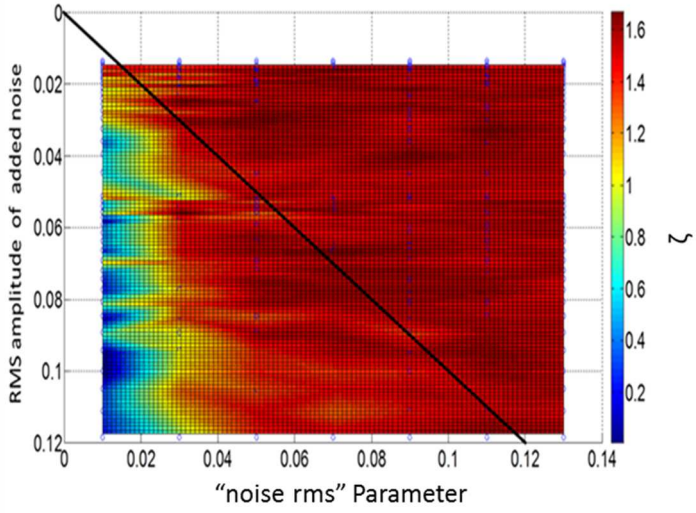

Figure 37 *View from the top of ζ values 3D plot for random noises calculated using ten traces inside the anomaly. Same values for σ_n and RMS amplitude of added random noise are indicated by a black line.*

In the second example, I added a time-lapse coherent noise realization to the noise-free seismic data. To do so, I generated coherent noise realizations based on the actual noise of time-lapse seismic data acquired in the Otway basin using the technique described in Alajmi, Bona, and Pevzner (2013). In this work, the authors construct a variety of time-lapse noise models by matching the amplitude spectra (both temporal and spatial), in a running window, to the actual time-lapse noise while using random phase spectra. The final time-lapse noise realization can be understood as a time-lapse difference between two cross-equalized migrated volumes. Figure 35 displays MAP's ΔSg models for different σ_n values and RMS amplitudes of the added coherent noise. The analysis of this figure shows that only when the σ_n was 1.0×10^{-2} (bottom row) and the RMS amplitude of noise was comparable to the RMS amplitude of the difference volume (1.8×10^{-3} and 8.4×10^{-4}, respectively), was the software able to differentiate signal from noise. Therefore, the results with these parameters (located in the first column of the bottom row) show a spatial configuration and values close to those in the actual model. Again, if one analyses Figure 39, it is clear that the values of the ζ indicator are larger than 1.6 in only two points (4 and 6) at the top right region of the graphic.

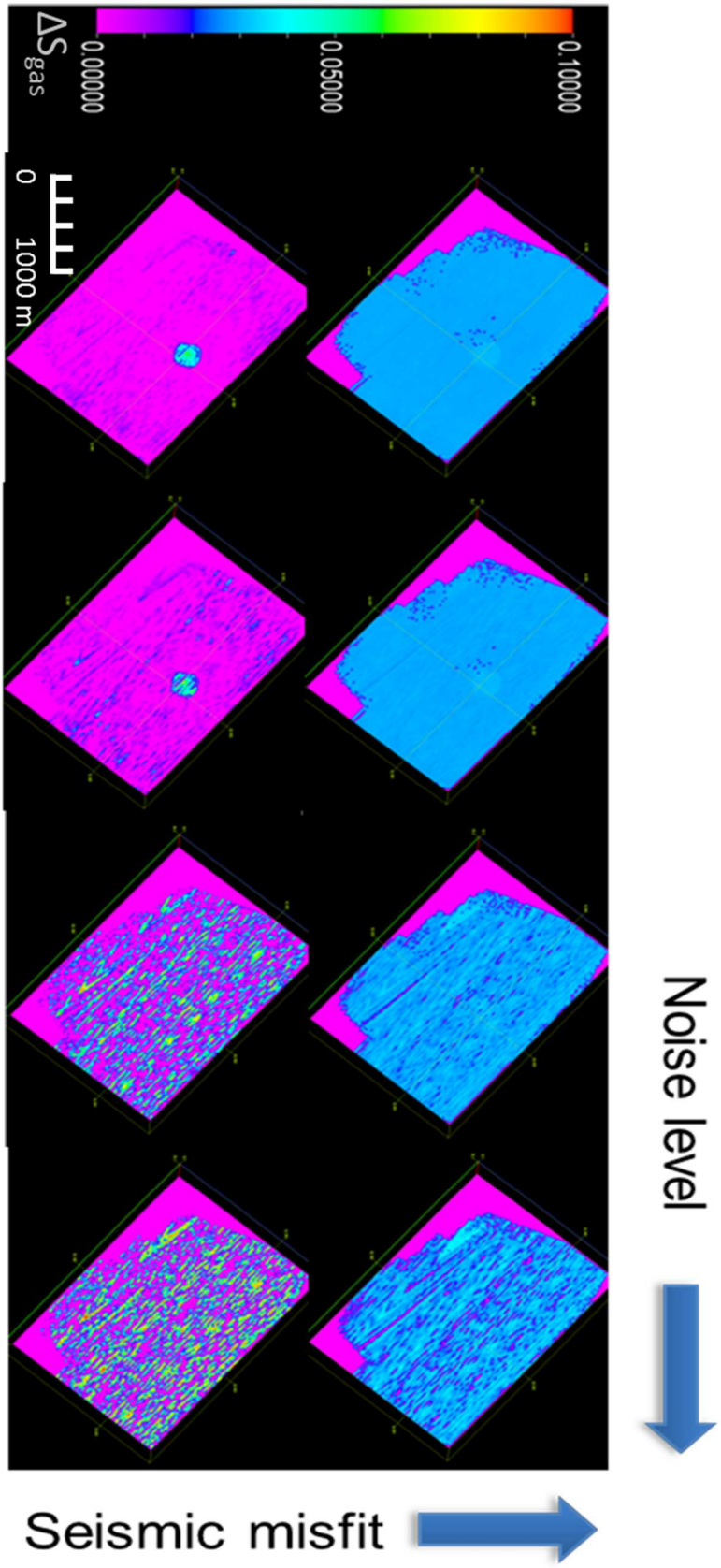

Figure 38 *MAP ΔSg models for input data contaminated with coherent noise with RMS amplitude at reservoir level of 0.0018 (signal-to-noise ratio 20), 0.0036*

(signal-to-noise ratio 15), 0.0182 (signal-to-noise ratio 10), 0.0365 (signal-to-noise ratio 5). The RMS amplitude misfit was set to 0.1 and in the bottom row 0.01. The above is displayed in Schlumberger's Petrel software.

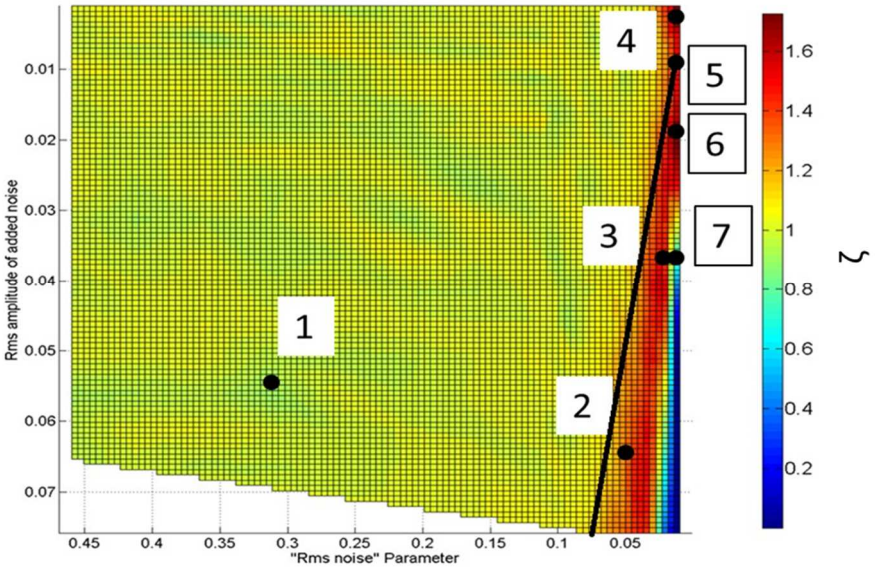

Figure 39 *Values of ζ for coherent noise overprinted with points indicating the combination of parameters and noise level analysed below. This figure was calculated using one trace inside the anomaly. Same values for σ_n and RMS amplitude of the added coherent noise are indicated by a black line.*

I also performed a detailed inspection of the different regions of Figure 39 while choosing pairs of parameters depicted here by points. Point 1 lies in a region of the plot where the values vary between 0.9 and 1.1. This range of values means that no significant improvement was detected in the posterior distribution when compared with the prior distribution. Points 2 and 3 are localized in the region with intermediate ζ values and have $\zeta \approx 1.2$ and $\zeta \approx 1.4$ respectively, which show an evolution of the detectability of the actual model when compared with point 1 ($\zeta \approx 0.9$). These values are close to the black line indicating equal values for the σ_n and RMS amplitude of added coherent noise. The low ζ values achieved by these points, and any points over and close to the mentioned line, indicate that, although the user-defined value is correct, the software could not differentiate coherent noise from signal due to the more destructive effect of coherent noise. Finally, points 4, 5, 6 and 7 in Figure 39 share the same values for the σ_n, 0.01, but represent coherent noises with different RMS

amplitudes. and Figure 41 show the results of the addition of scaled versions of coherent noise with the RMS amplitudes assigned to points 4, 5, 6 and 7 to a monitor trace and the correspondent difference trace (monitor minus base), respectively. Point 4 has an extremely low level of noise added to it as can be seen from Figure 40 and Figure 41. Obviously, point 4 ΔSg posterior distribution resembles the shape of the noise-free data one with a peak in 5% as can be seen in Figure 42

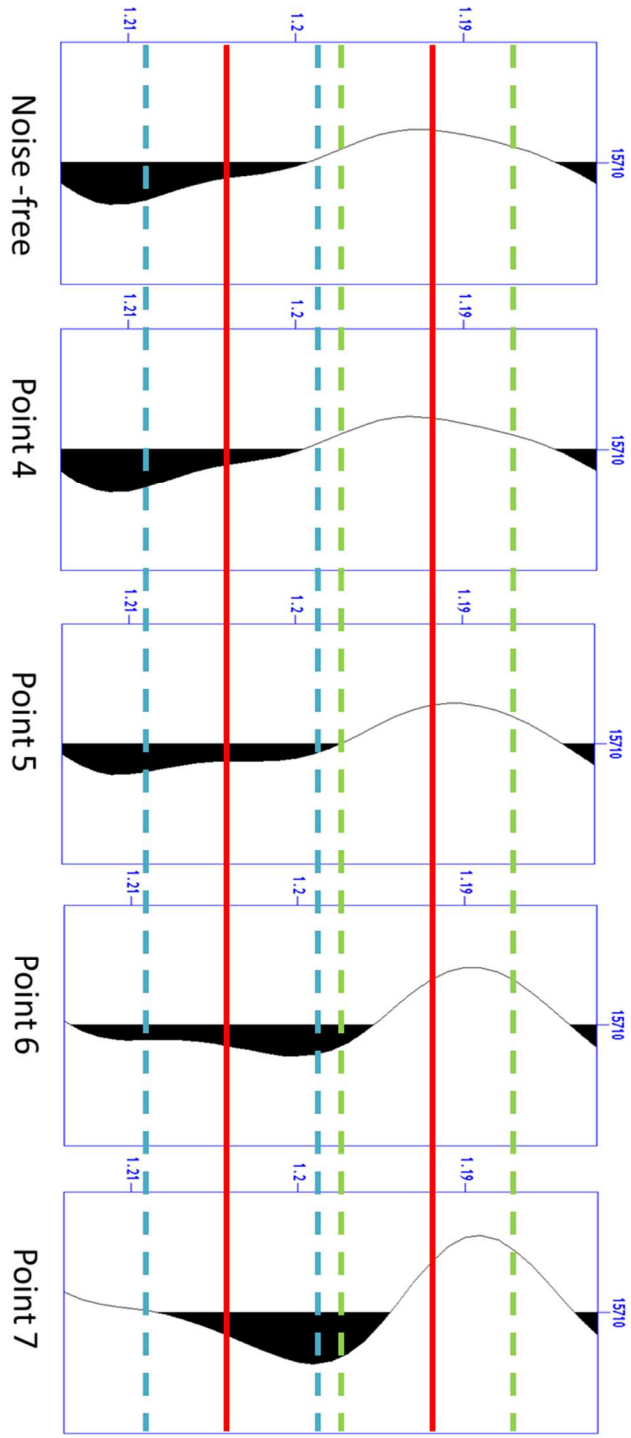

Figure 40 *Noise-free trace followed by traces contaminated with coherent noise with increasing RMS amplitude (Point 4 with 0.0001, Point 5 with 0.009, Point 6 with 0.021 and Point 7 with 0.36). Red lines represent the initial position of the reservoir in the m model. Green dashed lines represent the uncertainty in time of the top of reservoir boundary. Blue dashed lines represent the uncertainty in time of the base of reservoir boundary.*

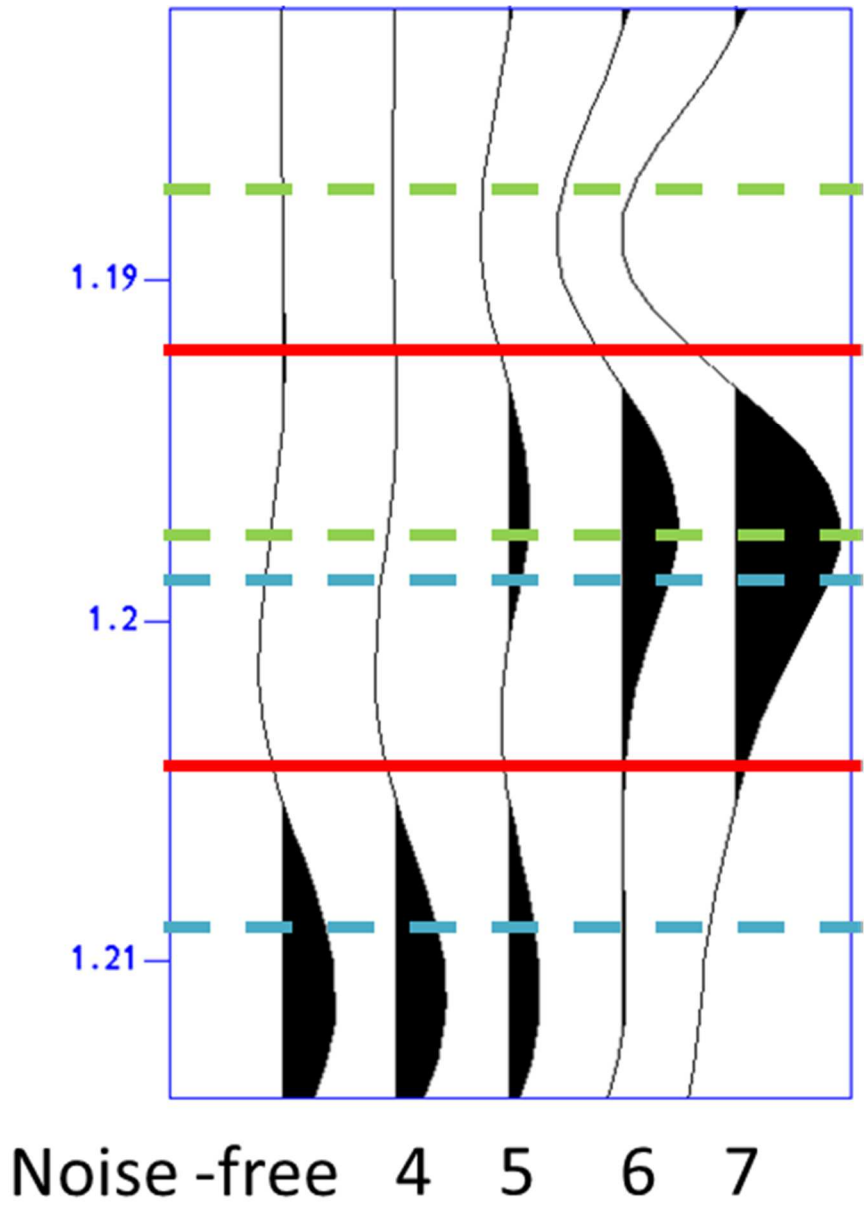

Figure 41 *Noise-free difference of base and monitor followed by differences contaminated with coherent noise with increasing RMS amplitude (Point 4 with 0.0001, Point 5 with 0.009, Point 6 with 0.021 and Point 7 with 0.36). Red lines represent the initial position of the reservoir in the model. Green dashed lines represent the uncertainty in time of the top of reservoir boundary. Blue dashed lines represent the uncertainty in time of the base of reservoir boundary.*

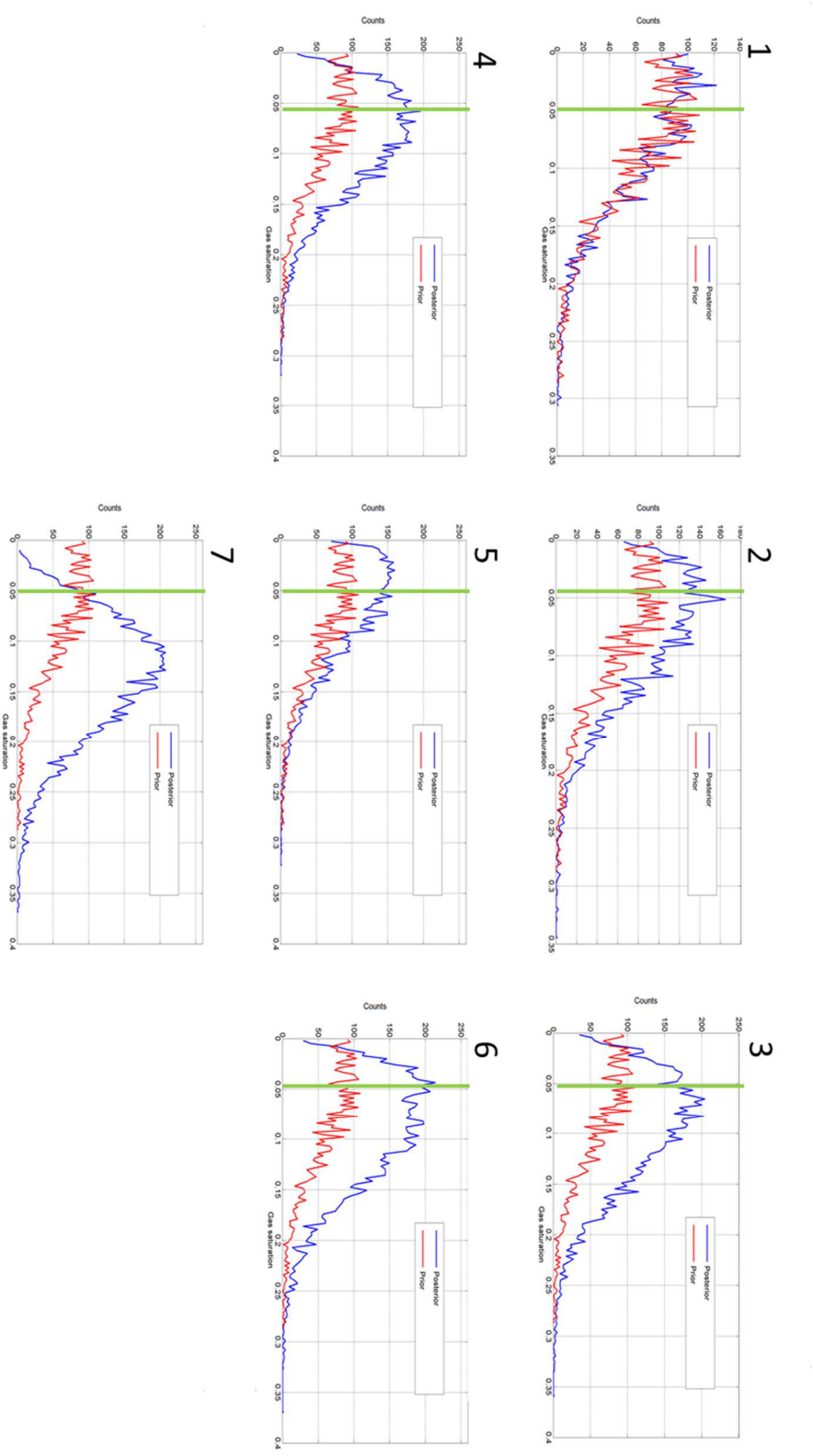

Figure 42 *Prior and posterior distributions for the points in Figure 39. The green line shows the approximate position of the true* ΔSg.

Figure 42 shows the prior and posterior distribution for Point 1, 2, 3, 4, 5, 6 and 7 in Figure 39. In this figure, the peak of the ΔSg posterior distribution is shifting as an result of the addition of coherent noise. At Point 5, the level of noise is equal to the RMS amplitude of the difference volume, 8.4×10^{-4}. In Figure 41, the result of interference between the difference trace and noise is shown as an almost constant trace. The small amplitude values in the difference trace explain the low values of ΔSg posterior distribution. This is so because, for a time-lapse experiment in which the pre-injection scenario presented no gas in the reservoir layer, no anomaly in the difference trace is an indication of no injection in the area. The peak at point 6 depends heavily on the form of the coherent noise and reflects a situation where the overall interference completely obliterates the original signal: in that case, the ζ value is similar to the noise-free case. It generates a peak at 5% but is completely uncorrelated with the trace's original shape as can be seen in Figure 40. Finally, point 7 marks the beginning of the region where the noise starts to be so large that the inversion algorithm cannot distinguish any time-lapse signal (Figure 40 and Figure 41). At this point, the software starts to invert not only the signal but also a much larger amount of noise.

Analyzing these results one can conclude that, with the addition of coherent noise, quantitative interpretation is only possible if the RMS amplitude of the noise is about the same order of the RMS amplitude of the difference volume. The interference between the signal and noise is responsible for the variation of ζ values between these points. To disperse any doubts about the independence of these results from the particular time-lapse coherent noise realization, I generated eight realizations and calculated the ζ values for ten different points inside the anomaly. This helps demonstrate the general character of the ζ values behaviour as shown in Figure 43.

In the previous chapter, it was observed that statistical methods have less difficulty separating coherent noise from signal. The results of this study are in agreement with this statement. However, it is important to note that, if the RMS amplitude of the noise is comparable to the size of the RMS amplitude of the anomaly resulting from the injection in the difference volume, it is still possible to generate quantitative results. If this is not the case, only qualitative interpretation may be attempted only.

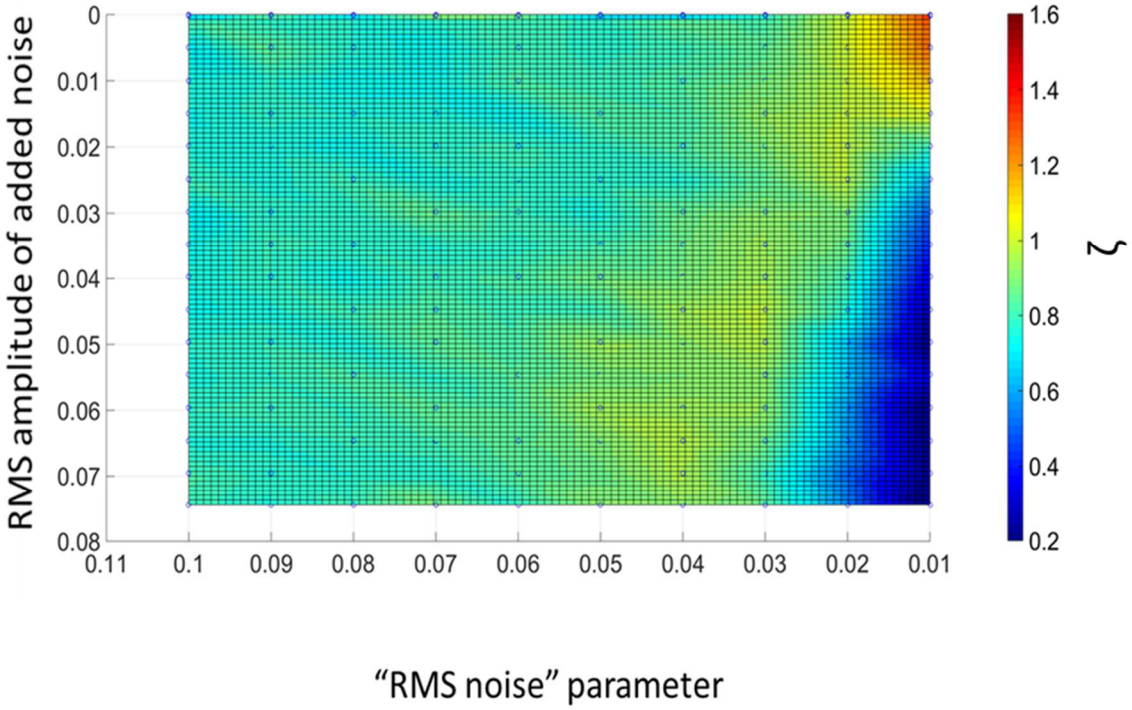

Figure 43 *Values of ζ for coherent noise calculated using ten traces inside the anomaly and eight different time lapse noise realizations.*

4.7 CONCLUSIONS

In this chapter, I demonstrated an example of the application of the stochastic inversion software Delivery4D on a dataset created for a feasibility study in a CO_2 sequestration project. The study focused on the robustness of the stochastic time-lapse inversion while facing noise and parameterization issues. In a attempt to simulate real cases where the ΔSg spatial distribution is not known, the test was carried out without any spatial constraints for the presence of gas. The findings for the effect of wrong parameterization (mis-specification in the statistical literature) were consistent with the theory. The result showed that the success of the inversion is dependent on the sensitivity of the reservoir rock's acoustic impedance to fluid saturation and the choice of the prior fluid saturation distribution parameters. The higher the sensitivity of the rock's impedance to fluid saturation, the faster the convergence to the correct value of saturation. The significant role of *a priori* uncertainty, in the form of Sg_2 standard deviation, was also highlighted. The example showed that the Sg_2 standard deviation

must form a Gaussian distribution that covers the gap between the assigned mean saturation and the actual value of saturation, with a reasonable probability at the true value. This choice of parameters improves the chance that the convergence to the latter is to be achieved. In other words, to achieve convergence, the bigger the difference between the assigned Sg_2 mean and the true value, the bigger the assigned Sg_2 standard deviation should be.

When random noise was added to the input seismic data, the approach was able to recover the true model within an acceptable margin of error. This means that the statistical nature of the methodology was adequate to separate the random noise from the signal. On the other hand, the addition of coherent noise had deleterious effects on the inversion results, and in most cases convergence to the correct model was not achieved. However, when the RMS amplitude level was comparable to the RMS amplitude level of the anomaly in the difference volume the algorithm was able to distinguish the noise from the signal. The presence of coherent noise represents a major challenge for automated time-lapse interpretation because the statistical workflow used to process it has difficulties distinguishing coherent noise from signal. One of the reasons for this is that this type of noise does not randomise over experiments (Gunning, 2013). These findings support the idea of careful seismic data collection and processing to avoid coherent noise and allow judicious interpretation when it is unavoidable. Finally, a new indicator was developed to calculate the improvement in detectability after the input of new data using the stochastic time-lapse inversion.

This exercise was fundamental in the preparation for the inversion of real seismic data to be presented in the following chapters. Firstly, it served as a test for the methodology, highlighting its strengths and limitations. Secondly, it was important to familiarize the author with the methodology, giving him experience with the sensitivity of the parameters and adjusting the expectations towards the results. Finally, as the results are in accordance with the theory, and no outcome was left unexplained, the exercise presented here was deemed as a confirmation the methodology's capability to deal with the stochastic time-lapse inversion problem in environments with moderate complexity.

CHAPTER 5. CARBONATE DATASET DESCRIPTION

In this chapter, I will present the dataset from a carbonate field located 75 km offshore of Brazil at a water depth of 125 m used as input for a stochastic time-lapse inversion. The field, henceforth named field X, presents a highly structured oil- and gas- bearing carbonate reservoir. The dataset was provided by Petrobras, the Brazilian state-owned oil company, and the Agencia Nacional do Petroleo (ANP), the Brazilian national petroleum agency. Although very comprehensive, it presents critical challenges. The large time interval between well logs and seismic acquisitions, absence of shear velocity logs and the presence of obstructions on the sea surface during acquisition are examples of such challenges. In the next sections, I will present the geology of field X, and describe the dataset, and the quality control procedures. Then, I will demonstrate a time-lapse calibration study to ensure that the seismic vintage repeatability is sufficient to perform a seismic inversion.

5.1 GEOLOGY

Field X was discovered in 1974 in the Campos Basin while testing for an oil accumulation in the Albian carbonates of the Macae group (Nascimento, 2013). The Campos basin has its origins during the breakup of the supercontinent Gondwana and the formation of the southern Atlantic Ocean. The Campos basin genesis is customarily divided into three intervals: rift, transitional and drift (Figure 45). During the rift phase, around 133 million years ago, volcanic activity took place at the limits of the South American and African plates. Between 131 and 120 million years ago, rift basins were formed (Riccomini, Sant and Tassinari, 2012). The palaeogeography consisted of a succession of higher areas where coquinas accumulated, and lower regions where lake sediments rich in organic matter were deposited (Chang et al. 2008). According to Riccomini et al. (2012), in the transitional phase, the sea periodically entered the basin from the South enabled by height variations of a palaeohigh, probably constituted from basaltic rocks, and created a gulf. The hot climate and the salinity of the water in this constrained environment created exceptional conditions for the generation of an evaporitic succession (Chang et al. 2008). In the drift phase (between 122 and 111 million years ago) the basin broadened with the creation of the southern Atlantic Ocean

and transitional and maritime sediments, as platform carbonates, microbiolites, shallow water sandstones, deepwater shales and turbidites started to deposit.

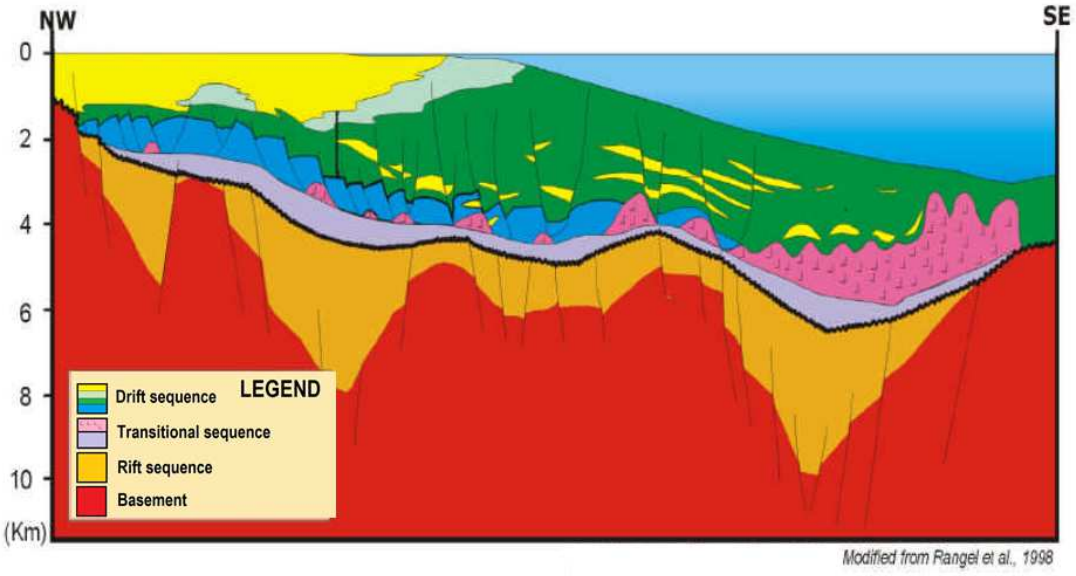

Figure 44 *Geologic section of Campos Basin.*

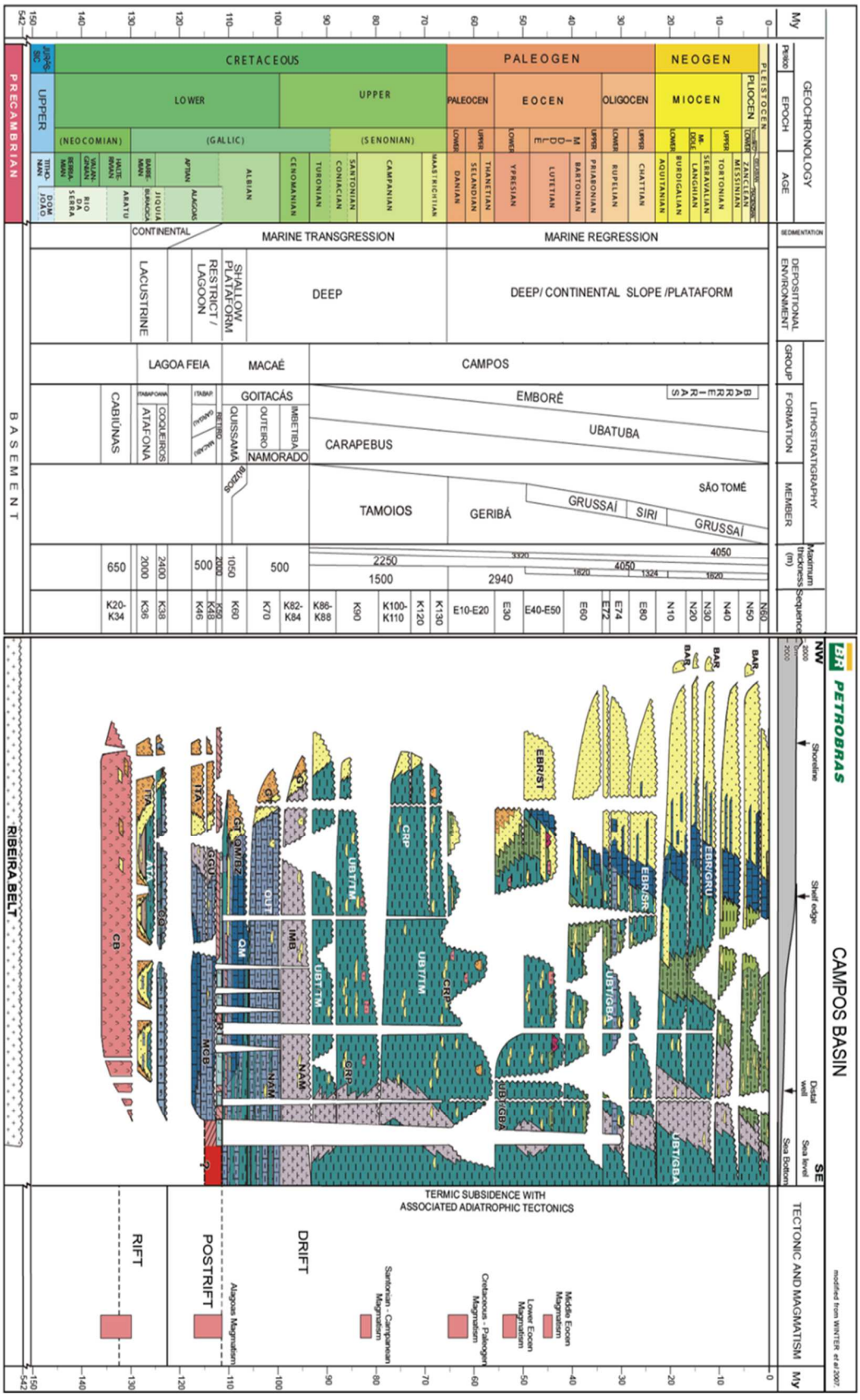

Figure 45 *Campos Basin stratigraphic chart. Modified from (Winter, Jahnert and França, 2007).*

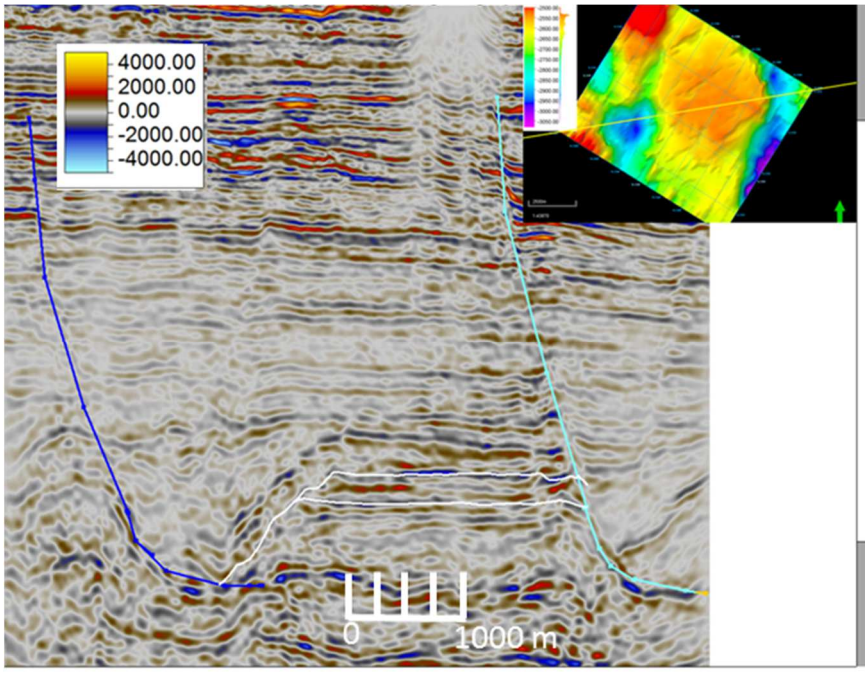

Figure 46 *Geophysical interpretation showing listric faults in the East and West of field X. The horizons in white represent the top and base of the reservoir.*

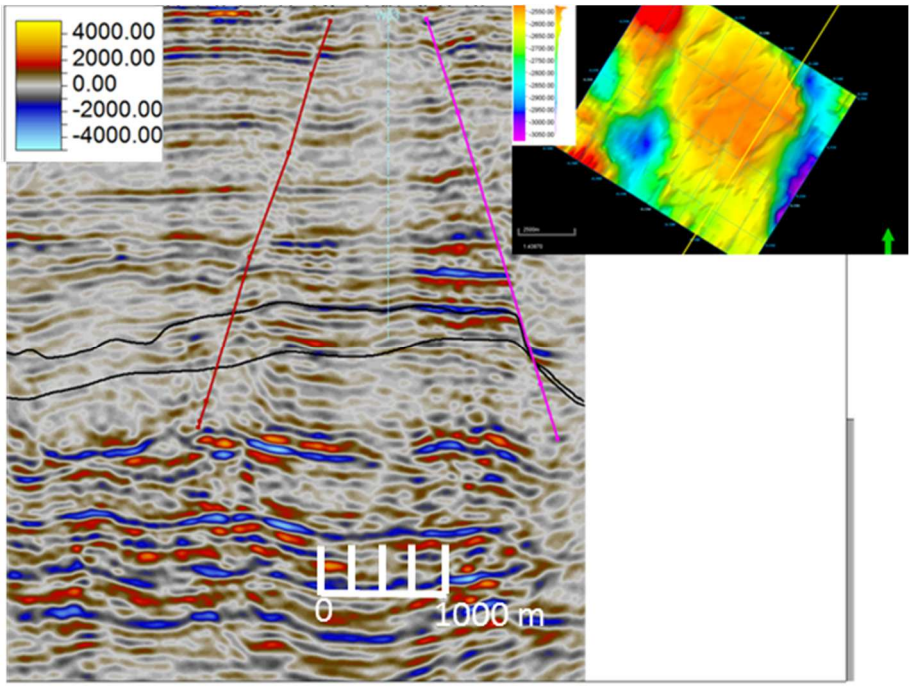

Figure 47 *Geophysical interpretation showing the horst and graben system in field X. The horizons in black represent the top and base of the reservoir.*

5.2 THE CARBONATE RESERVOIR DATASET

After presenting the geology of the area, I will introduce the dataset used to characterise the reservoir and utilised as the input for the inversion. I will also present the quality control procedures used to guarantee the reliability of the data.

5.2.1 Seismic data

The seismic dataset can be divided into a base vintage set, a monitor vintage set and a difference set. The base vintage dataset was acquired in 2002 and comprises:

- a full stack seismic dataset;
- a near angle stack with angles ranging from 0 to 10 degrees;
- a middle angle stack with angles ranging from 8 to 18 degrees;
- a far angle stack with angles ranging from 16 to 26 degrees;
- and an ultrafar angle stack with angles ranging from 24 to 34 degrees

The monitor vintage was acquired in 2011 and has seismic angle stacks analogous to those found in the base vintage dataset with the same angle ranges and a full stack dataset. The difference set gathers the difference volumes (monitor vintage minus base vintage) between the angle stacks with same angle ranges and full stacks. All the seismic volumes present in this thesis are in time domain.

5.2.1.1 Obstructions

During marine seismic acquisition, the presence of surface obstructions in the survey area, such as platforms or drilling rigs, is responsible for creating artefacts in the seismic data. Obstructions limit the possible positions assumed by the source and receivers during acquisition. Therefore, they decrease the number of recording positions associated with the angles at which a given data point in the subsurface reflects the seismic waves. An example of this is shown in Figure 50, for small angles (near angle stack). These obstructions can be man-made, as drilling rigs and production facilities or natural, such as sand banks. A number of techniques are used to avoid the impediments created by obstructions. Undershooting is the most common technique used when streamer acquisition is being shot. It is performed by two vessels, one towing the airguns and acting as the source vessel and the other towing the streamers and acting as the receiver vessel, sailing at opposite sides of the obstruction. As an example of such approach Johann et al. (2006) applied undershooting in the Marlin

field. According to the authors "*Seismic quality control was so relevant for this project that, for the first time in Brazil, we caused six different FPSOs* [Floating Production, Storage and Offloading unit] *to be rotated to align with the seismic vessel which towed 10, 6 km-long cables. This was done to reduce the holes in seismic imaging around the production platforms in view of the importance attributed to the reservoir characterization in these areas*". Usually, undershooting reduces the effects of obstructions but does not eliminate them and has better results for deeper targets and larger angles.

Another option to avoid obstructions is the use of nodes or ocean bottom cables (OBC). These devices are receivers located on the sea bottom. The seismic data is acquired using a source vessel towing only airguns. Since the dimensions of the source boats are much smaller than streamer-towing vessels, which can achieve 12 kilometres in length, their deployment closer to the restriction zones around the obstruction is enhanced. Therefore, an expanded area is surveyed when compared with traditional streamer acquisition. This approach has been optimised in the North Sea, with the permanent reservoir monitoring system using ocean bottom cables being one of the most successful examples in shallow waters (80 m) (Barkved et al., 2012). In deep waters, the Jubarte field, an ultra-deepwater field at 1300 m water depth, has successfully been equipped with a permanent reservoir monitoring system employing a fibre optic OBC. Additionally a topside installation in a platform is capable of performing both active and passive seismic acquisitions (Seth et al., 2013).

In the studied field, the presence of a platform obstructing the seismic acquisition over the reservoir area created the need to perform undershooting operations during the acquisition of both vintages. As a result, areas with reduced fold were formed in the seismic data, affecting, with dissimilar intensities and distribution, the angle stacks. To visualise the complete extension of the area affected by the obstruction, Figure 48 and Figure 49 show the effect in time slices close to the sea bottom in the base and monitor vintages respectively. To provide a qualitative assessment of the obstruction effect on the seismic data, the crossline 2169, portrayed in yellow in Figure 48 and Figure 49, is displayed for all available seismic volumes (Figure 50 to Figure 54).

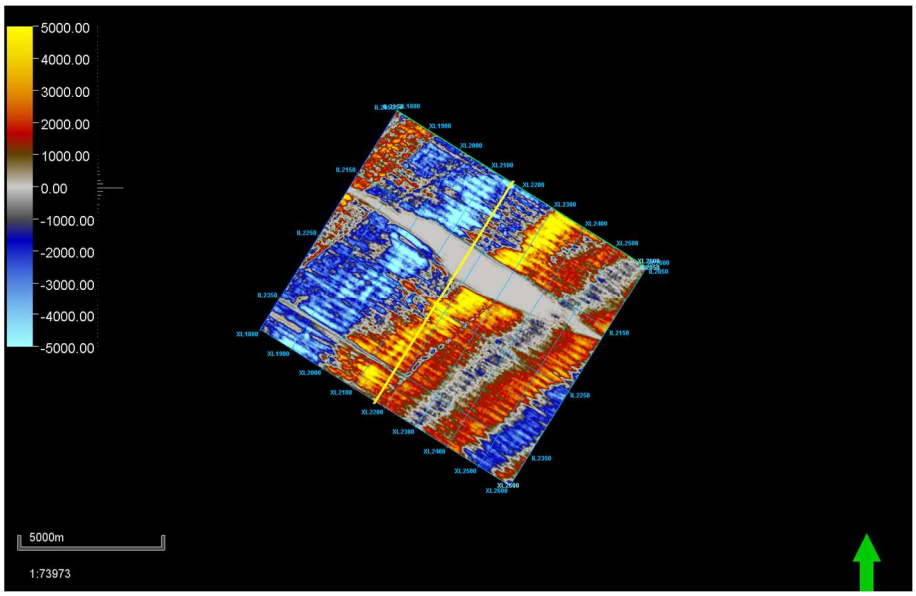

Figure 48 *Time slice of base vintage at 268 ms.*

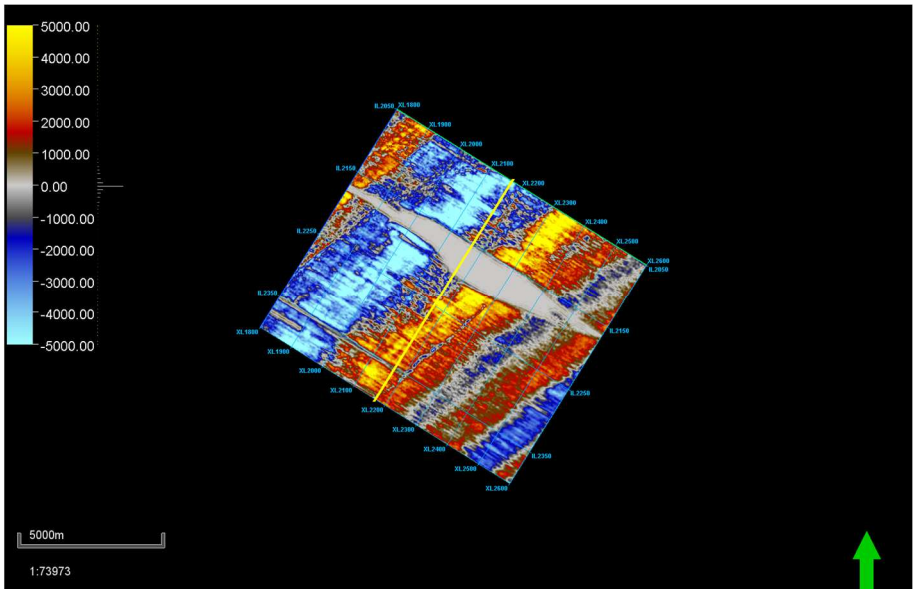

Figure 49 *Time slice of monitor vintage at 268 ms.*

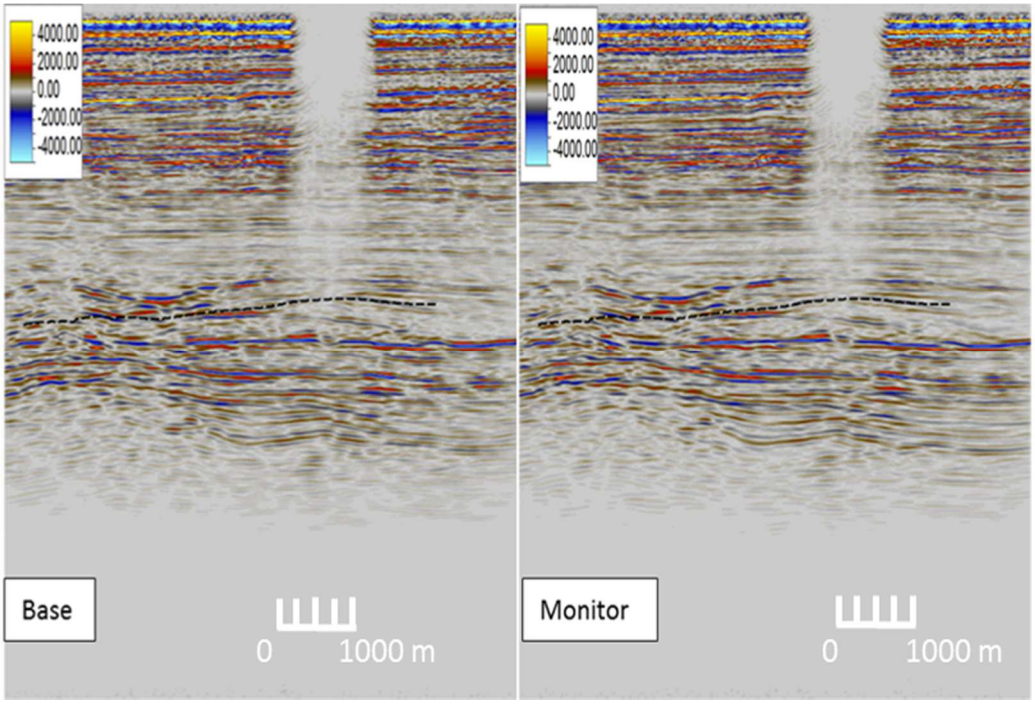

Figure 50 *Base and monitor vintage full stacks showing the gap in the seismic volume caused by platform obstruction. The dashed black horizon indicates the top of the reservoir.*

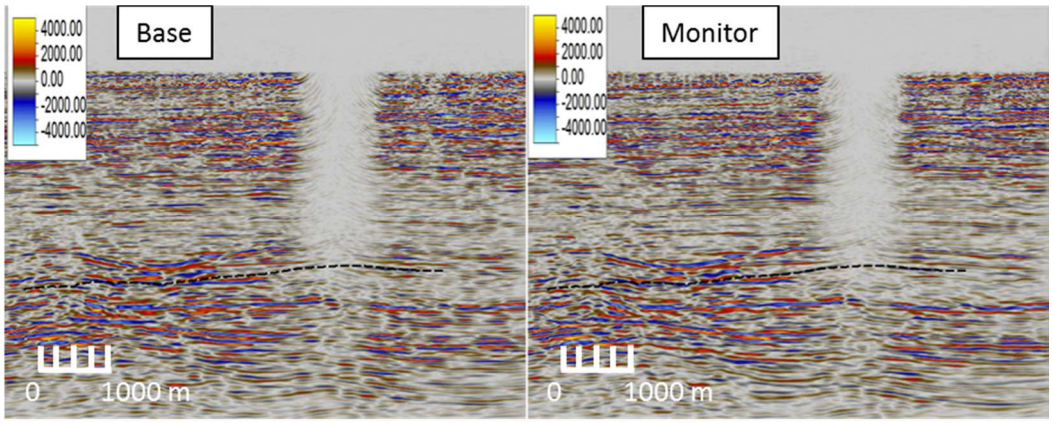

Figure 51 *Base and monitor vintage near stacks showing the gap in the seismic volume caused by platform obstruction. The dashed black horizon indicates the top of the reservoir.*

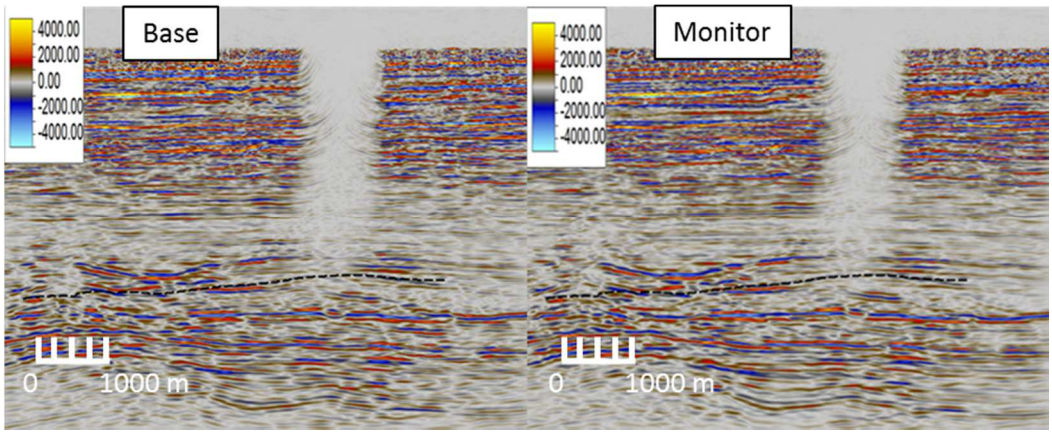

Figure 52 *Base and monitor vintage mid stacks showing the gap in the seismic volume caused by platform obstruction. The dashed black horizon indicates the top of the reservoir.*

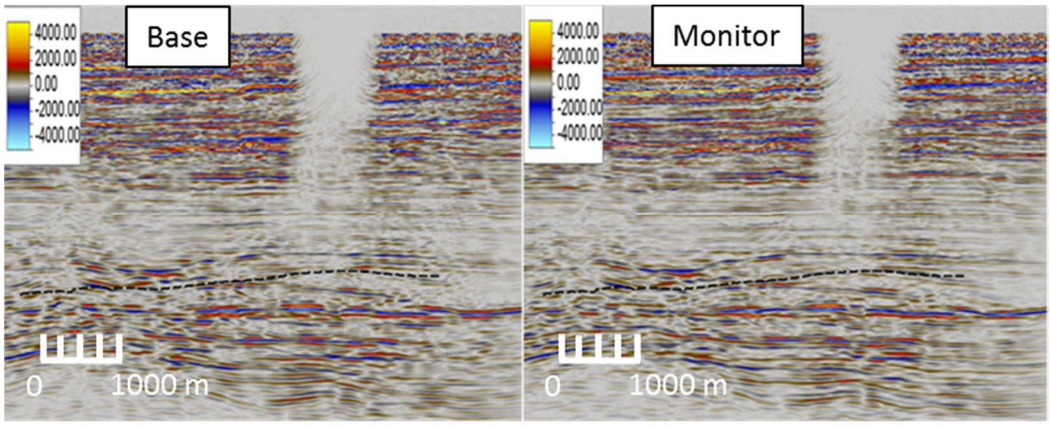

Figure 53 *Base and monitor vintage far stacks showing the gap in the seismic volume caused by platform obstruction. The dashed black horizon indicates the top of the reservoir.*

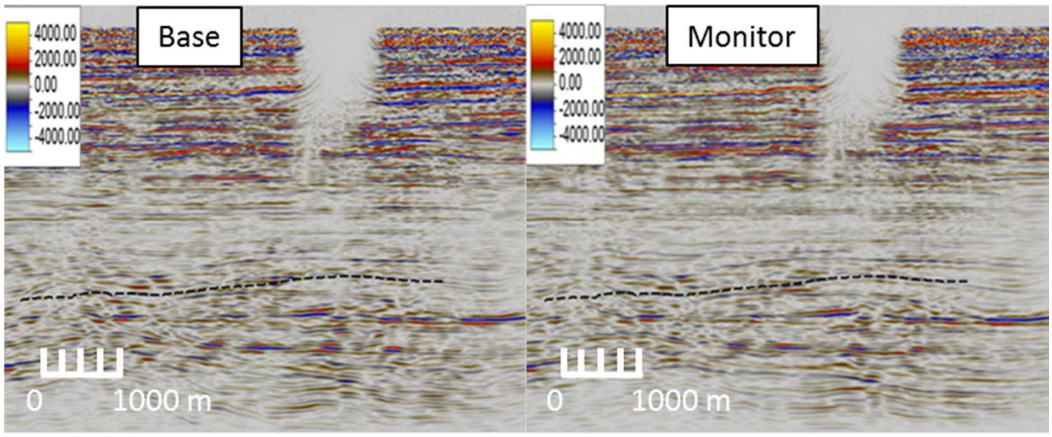

Figure 54 *Base and monitor vintage ultra-far stacks showing the gap in the seismic volume caused by platform obstruction. The dashed black horizon indicates the top of the reservoir.*

To quantitatively compare the effects of the acquisition obstruction on the seismic amplitudes, for different angle ranges, I show, in Figure 55, the average energy for the base vintage's near angle stack. Figure 56 shows the same attribute for the base vintage's ultrafar angle stack. It is clear from the maps that a bigger area is affected in the former than in the latter indicating that that the near and mid angle stacks are more affected by the obstruction than the far and ultrafar. Figure 57 displays the average energy of the base vintage's full stack calculated in a time window 10 ms below the top of reservoir horizon. This picture makes clear the effect that the hole in the acquisition has over the seismic signature on the top of the reservoir. This effect is especially significant in the red rectangle between inline 2157 and 2194 and crosslines 2500 and 1980. Figure 57 shows that many wells (W15, W17, W24, W25, W27, W28, W29, W31, W32, W33, W34, W35, W36DB and W36D) are inside the affected zone. A complex effect is expected regarding these wells' ties with seismic data.

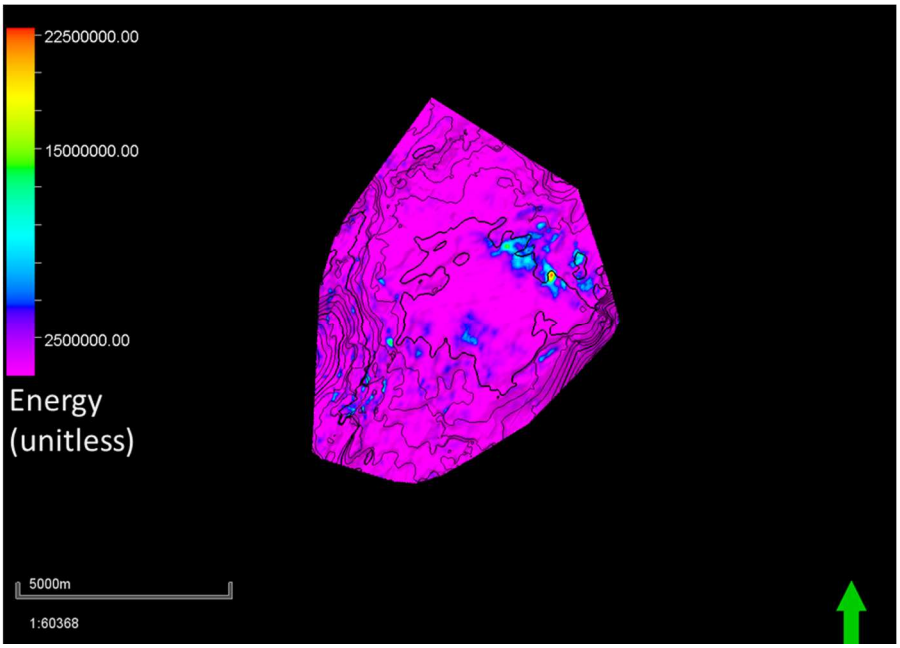

Figure 55 *Average energy calculated in a time window 10ms below the top of the reservoir horizon for the base near angle stack.*

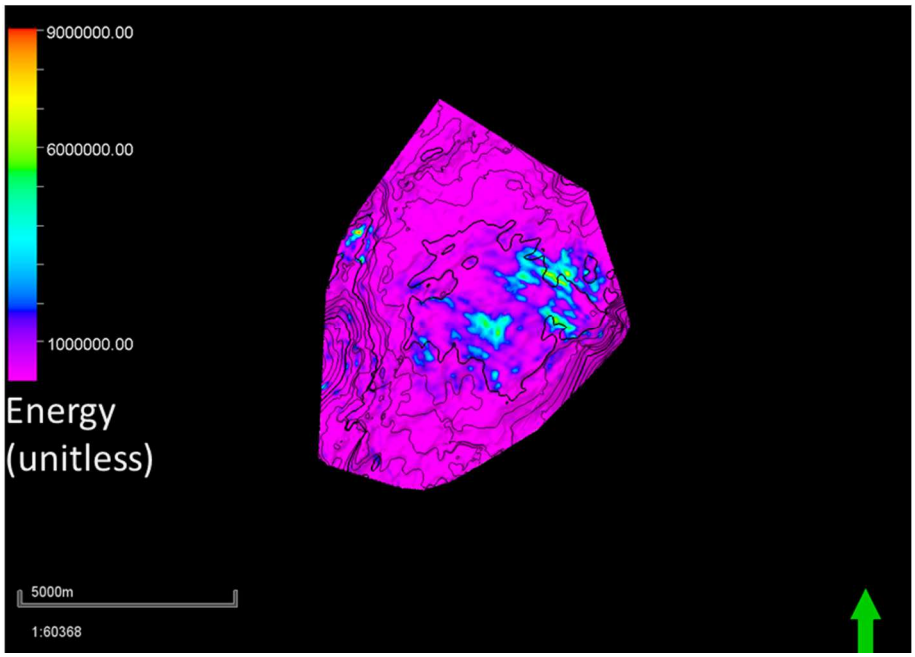

Figure 56 *Average energy calculated in a time window 10ms below the top of the reservoir horizon for the base ultrafar angle stack.*

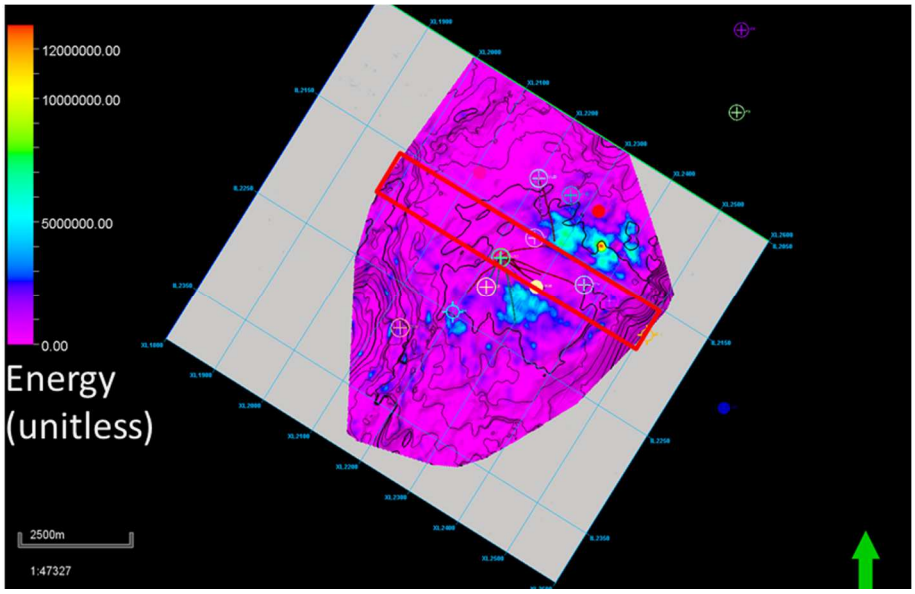

Figure 57 *Average energy of the Full stack base vintage calculated in a time window 10ms below the top of the reservoir horizon.*

5.2.2 Lithology

The facies classification was based on the description of cores extracted from wells W2, W9, W25, W33 and W34, capillary pressure and relative permeability curves and a joint analysis of gamma ray, sonic and density logs. The data provider defined 4 eletrofacies presented in Table 4 alongside their respective type of porosity. The sequence stratigraphic model adopted was the shallowing upwards model (Figure 58). According to Michael Allaby, a shallowing upwards sequence is "*a stratigraphic sequence found on platforms, shelves and some former lake beds, where carbonates have been deposited in progressively shallower water. The sequence develops where the rate of carbonate deposition exceeds the rate at which the receiving basin sinks, so the sediment surface repeatedly rises towards the water surface, while at the same time the deposit progrades*" (Allaby, 2013). Figure 58 presents the facies colour scheme.

Table 4 *Eletrofacies description and the respective type of porosity found in the reservoir.*

Eletrofacies	Type of porosity
Facies 1 – porous grainstone	Enlarged intragrain
Facies 2 – cemented grainstone	Microporosity in the grains and some intergranular
Facies 3 –packstone/wackestone	Microporosity
Facies 4 – cemented bioturbated grainstone	Microporosity

Figure 58 *Representation of shallowing upwards cycle comprising facies and colour scheme.*

In the reservoir under study, the cycle starts with low energy packstone or wackestone, called hereafter as facies 3. The porosity of this facies was classified as microporosity and a thin section of a facies 3 sample is presented in Figure 59. In Lucia's petrophysical classification it would be a class 3 mud-dominated limestone (Lucia, 2007). The low-energy facies 3 is followed by the intermediate energy cemented grainstone, facies 2 (thin section displayed in Figure 60) that was described as having microporosity in the grains and intragrain porosity. The cementation present in this facies is a diagenetic process that alters the rock fabrics. Calcium carbonate cement propagates from pore walls to pore space and reduces pore size (Lucia, 2007), porosity

and permeability of the rock. It may initiate right after deposition, with deposition of carbonate cement over the grains, and continue throughout the sedimentation process. According to Lucia (2007), after the burial, the sources of ions may be *"(1) grain dissolution associated with grain compaction, (2) dissolution of unstable minerals such as aragonite, and (3) long distance transport of ions by ground-water flow"*. On top of facies 2 in the cycle lies the high-energy porous grainstone, facies 1 (Figure 61), the more permeable and porous reservoir facies, whose type of porosity was described as intragrain. According to Lucia's classification, it would be a class 1 grainstone (Lucia, 2007). This rock is grain supported and lacks mud. These high-energy deposits are found in shelf margins, back reef sands associated with landward transportation and local middle shelf with inner-island gaps. Finally, the cycle is topped by a cemented bioturbated grainstone called here facies 4 (Figure 62) whose porosity is described as intragranular. This kind of deposit is typically found on tidal flats and caps the shallowing upwards cycle. Those facies were used to generate facies logs on the wells (Figure 63). I utilized the facies logs in the construction of the initial model of the inversion, especially in the calculation of net-to-gross.

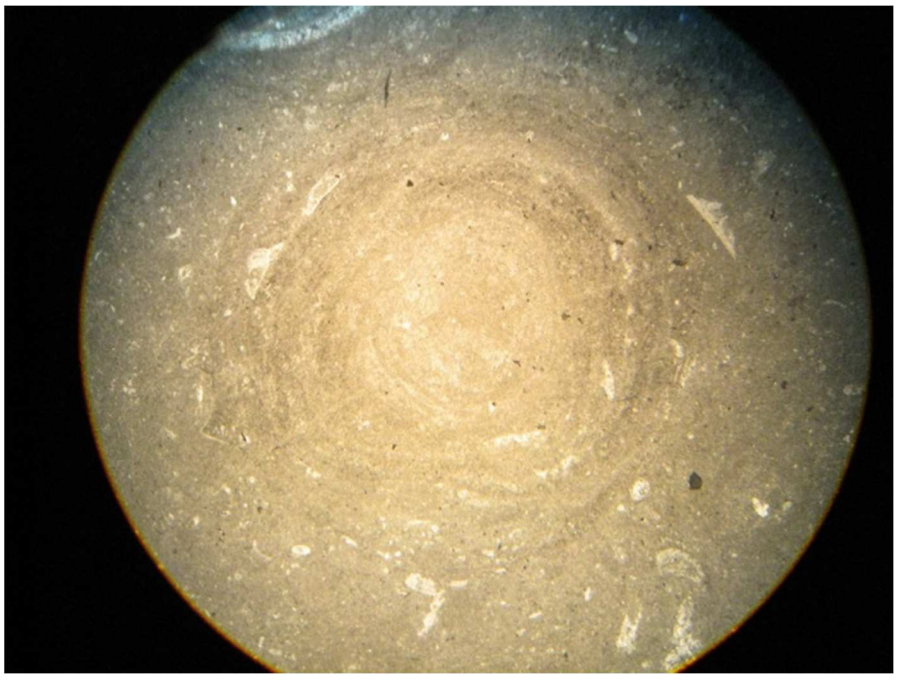

Figure 59 *Example of wackestone/packstone facies 3. Scale was not provided in the dataset.*

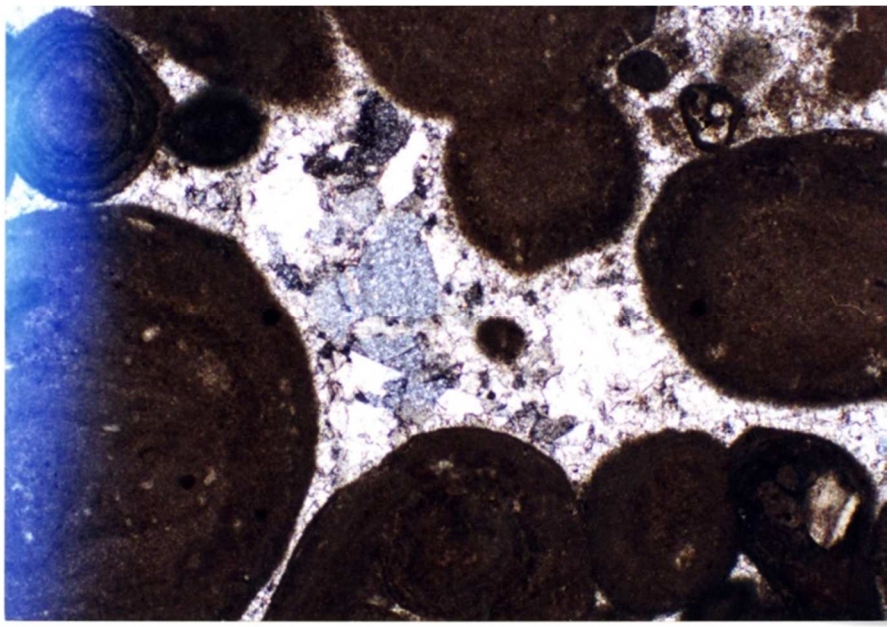

Figure 60 *Example of cemented grainstone facies 2. Scale was not provided in the dataset.*

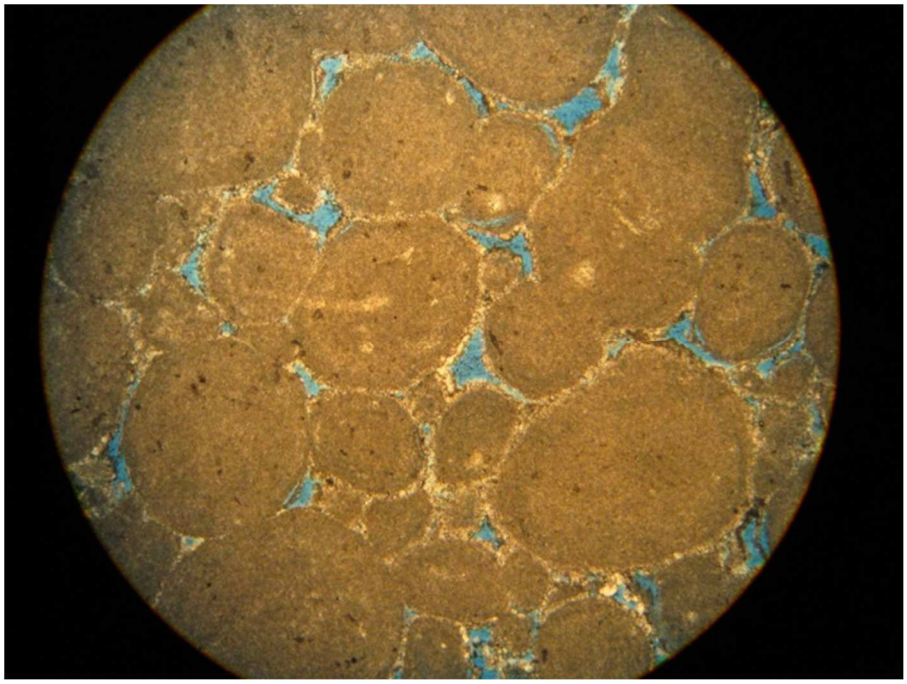

Figure 61 *Example of porous sandstone facies 1. Scale was not provided in the dataset.*

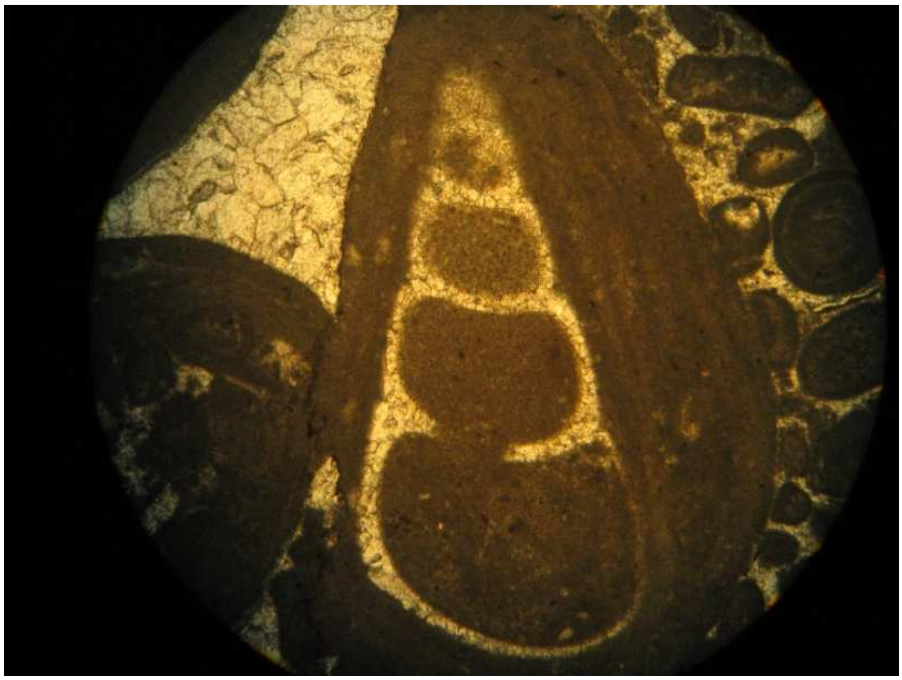

Figure 62 *Example of cemented grainstone bioturbated facies 4. Scale was not provided in the dataset.*

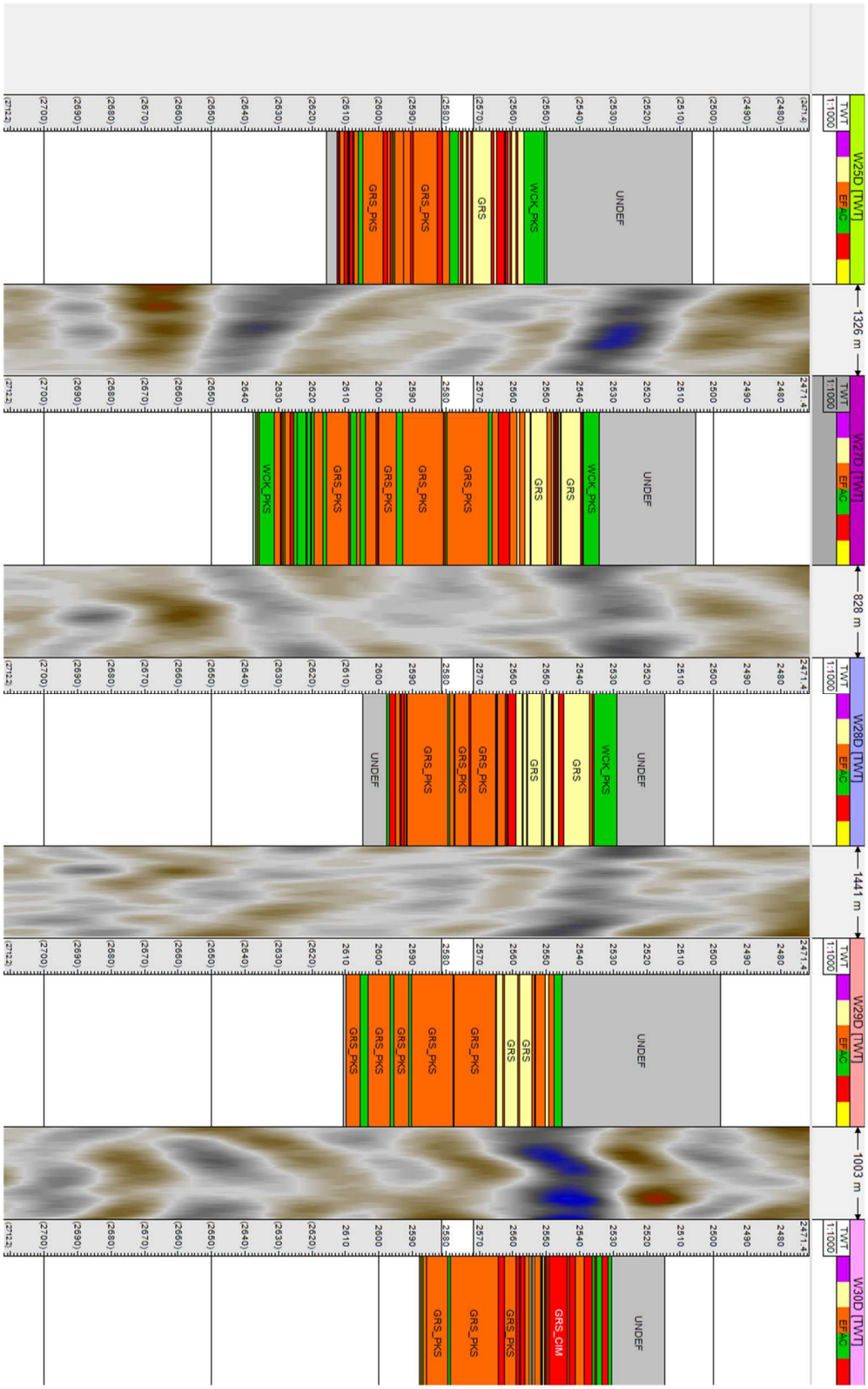

Figure 63 *Example of facies logs on production wells. The colours represents the facies according to Figure 59.*

5.2.3 Wells Logs

There were 40 wells in the dataset (Table 5). The data provider classified the wells into four categories: vertical wells, directional wells, injector wells and producer wells. The first two classes of wells (vertical and directional) provided information used to delineate the field. The injector wells injected water into the field to push the oil and gas to the producer wells, which brought the oil and gas to the surface. All the wells were drilled and logged between 1978 and 1984. Hence, information gathered from their logs cannot be representative of the elastic and petrophysical properties present during the vintage's acquisitions, which took place in 2002 and 2011. Too many years of production had altered the fluid saturations and pore pressure inside the reservoir.

Table 5 *Wells present in dataset.*

Well category	Well ID
Vertical	from W1 to W13
Directional	W14D, W15D, W15DC, W16D, W17D, W18D, W19D, W14DB, W20D, W36D, W36DB, W37D.
Injectors	W21D, W22D, W23D, W24.
Producers	W25D, W26D, W27D, W28D, W29D, W30D, W31D, W32D, W33, W34, W35D.

As discussed in Chapter 3, the inversion workflow used in this study demands that the elastic property logs used to carry out the inversion be fluid substituted to 100% brine. Therefore, based on water saturation logs provided, I conducted fluid substitutions to generate logs used in the seismic inversion. To select the wells for fluid substitution, I implemented a quality control (QC) workflow. In this workflow, I excluded the wells that were out of seismic bounds or contained no reservoir facies. I also included wells that showed water saturation logs inconsistent with resistivity logs

(indicating problems with the acquisition or processing of the resistivity logs or problems in the derivation of the saturation logs), or lacked Vp or density logs. Table 6 lists the wells that I excluded using these criteria. Finally, the remaining wells, W7, W18, W19, W21, W22, W23, W25, W26, W27, W28, W34 and W35 underwent the fluid substitution process. These wells have sonic, density, water saturation, facies and gamma ray logs. Unfortunately, because these are older wells, they do not have shear velocity logs. The absence of Vs logs and the effect of the platform obstruction on the near and mid angle stacks for both vintages makes the AVO analysis of these datasets extremely uncertain. Therefore, as a first order approximation, I implemented an acoustic version of the stochastic time-lapse inversion.

Table 6 *Wells excluded after quality control.*

Well	Reason for rejection
W1	Out of seismic bounds
W2	Out of seismic bounds
W3	Out of seismic bounds
W4	Out of seismic bounds
W5	Out of seismic bounds
W6	Only cemented facies was found
W8	Out of seismic bounds
W9	Present odd density values, probably linked to the well excavation
W10	Out of seismic bounds
W11	Out of seismic bounds
W12	Out of reservoir limits
W13	Absence of Vp log
W14	Problems in water saturation log
W15	The logs do not reach the reservoir

W16	Problems in water saturation log
W17	Absence of Vp log
W20	Problems in water saturation log
W24	Absence of Vp log
W29	Absence of Vp log
W30	Absence of Vp log in the reservoir
W31	Problems in water saturation log
W32	Has no density log
W33	Absence of Vp log

5.2.4 Horizons

Three horizons were part of the dataset: Top-of-Macae marking the top of the Macae group, Top-of-reservoir and Base-of-reservoir marking the outer geometry of the reservoir. Additionally, I interpreted 5 horizons in a five-by-five mesh, four of them inside the reservoir: Peak-1 (the first peak below Top-of-reservoir), Trough-1 (the first trough below Peak-1), Peak-2 and Peak-3 (the first and second peaks below Trough-1). Finally, the horizon below the base of the reservoir and above the top of salt, called here Lower-bound, was used as a deeper limit before the base of the inversion to avoid deleterious boundary effects during inversion. The highly structured area and the high velocities from the carbonate rocks created many challenges to the interpreter. Figure 64 displays the resulting horizons. The negative horizon located between Peak-2 and Peak-3, called Trough-2, is very restricted and was not intersected by any wells (Figure 65), which makes it impossible to be described in terms of net-to-gross (NG). Therefore, the whole interpretation in the area below this horizon was deemed as not reliable. Thus, I focused my interpretation in the layers above and beside this reference horizon.

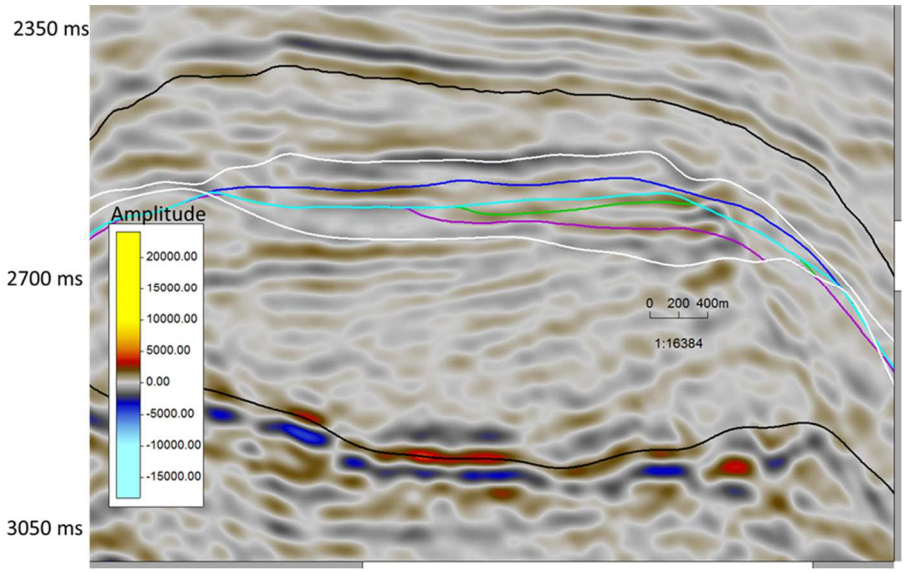

Figure 64 *Seismic section of Base vintage full stack (inline 2214) crossing the reservoir with horizons. The Black horizons represent the top (Top-of-Macae) and Base (Lower-bound) of the model. The white horizons represent top (Top-of-reservoir) and base (Base-of-reservoir) of the reservoir. The coloured horizons represent the horizons interpreted inside the reservoir Peak-1 (blue) Trough-1 (cyan), Peak-2 (green) and Peak-3 (purple).*

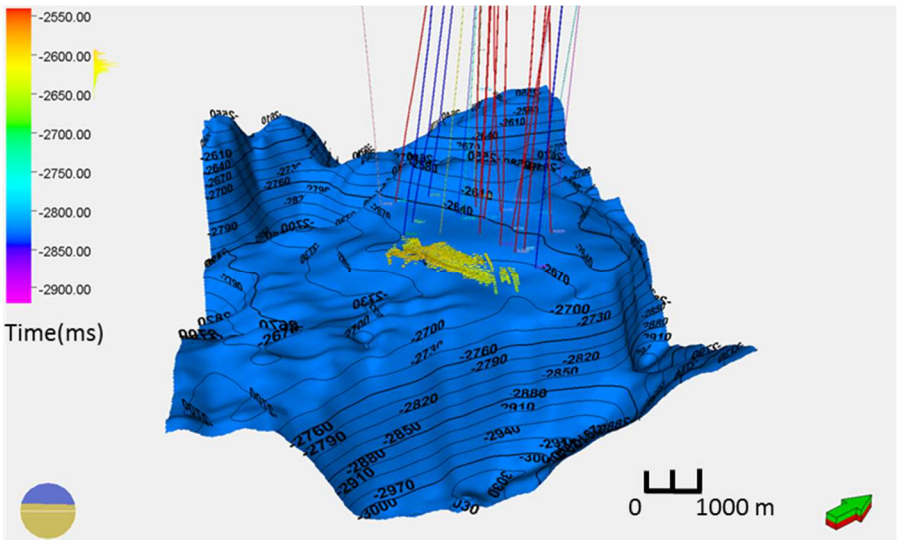

Figure 65 *Points in yellow/green colour represents interpretation of negative horizon between Peak-2 and Peak-3 over Base-of-reservoir horizon (in blue) showing that it is restricted and not crossed by wells.*

After the interpretation, I smoothed the horizons using a 5 inline by 5 crossline smooth filter and truncated them at the horizon immediately above. Additionally, I marked the time where the surface crosses the wells and created markers for the

horizons in the wells. The horizons Top-of-reservoir (Figure 66) and Base-of-reservoir (Figure 67) showed the structural high and the fault-delimited boundaries of the field. It is interesting to note that while Top-of-reservoir is relatively flat, Base-of-reservoir presents a protuberance reaching 2250 ms. To analyse the thickness in time between the layers, I calculated isochores. Isochores are the vertical difference in time between layers. The isochore calculated using Top-of-reservoir and Base-of-reservoir (Figure 68) shows a region in the west flank with small isochore values (purple colour). This indicates an area with small deposition thickness associated with the elevation present in the Base-of-reservoir horizon. In the east flank, hot colours indicate an area with a pronounced thickness of reservoir.

The isochores in time were extracted between the internal surfaces and depicted over the most inferior surface (e.g. the isochore calculated between horizons Peak-2 and Peak-3 is depicted over horizon Peak-3). The isochores are displayed from Figure 69 to Figure 72 and indicate that the three upper layers (Top-of-reservoir to Peak-1, Peak-1 to Trough-1 and Trough-1 to Peak-2) concentrate the reservoir thickness. The deepest layer in display (between Peak-2 and Peak-3) is not crossed by the well in the region indicated by the yellow circle in Figure 72, indicating that no waterflood had occurred within that layer.

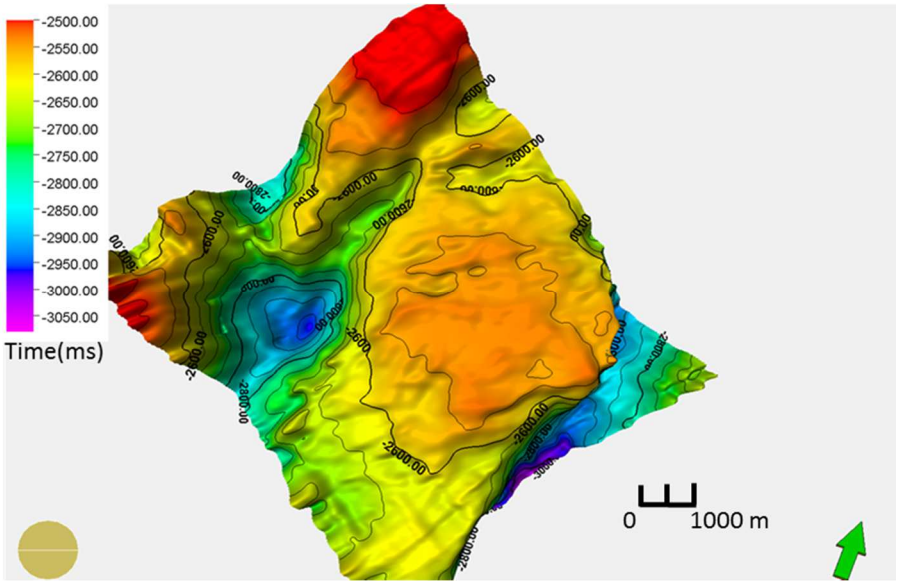

Figure 66 *Top-of-reservoir horizon.*

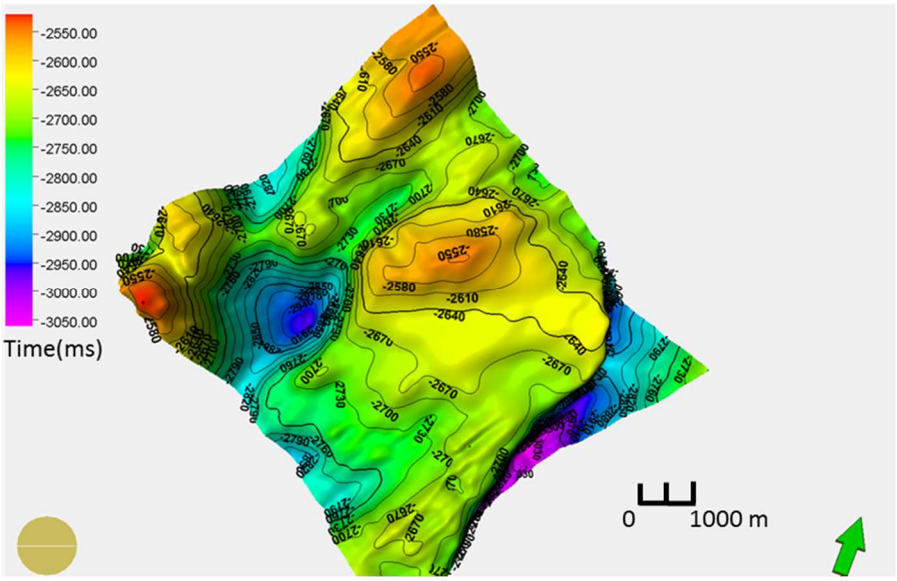

Figure 67 *Base-of-reservoir horizon.*

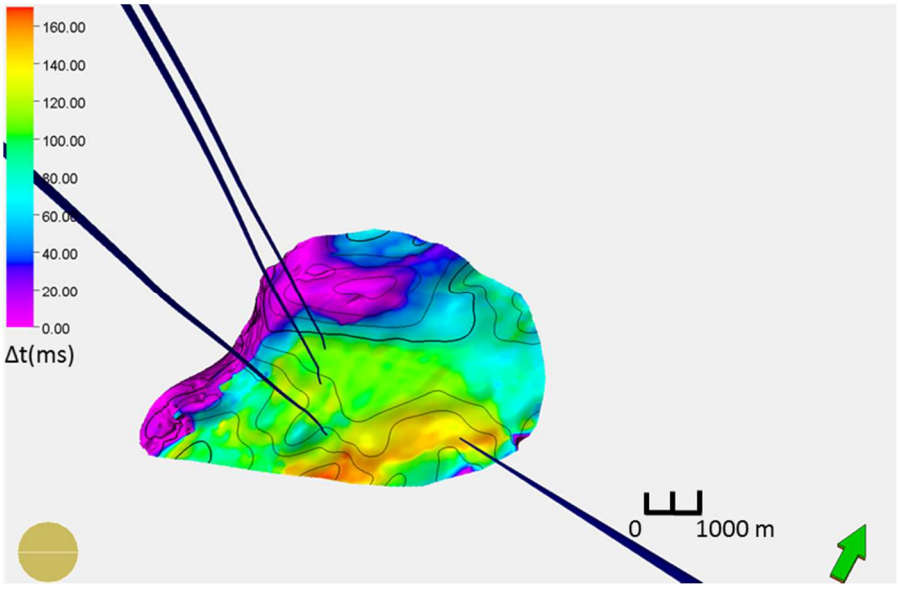

Figure 68 *Isochore map between top and base of reservoir showing a depocenter in yellow and orange and an area with almost no depositions shown in purple.*

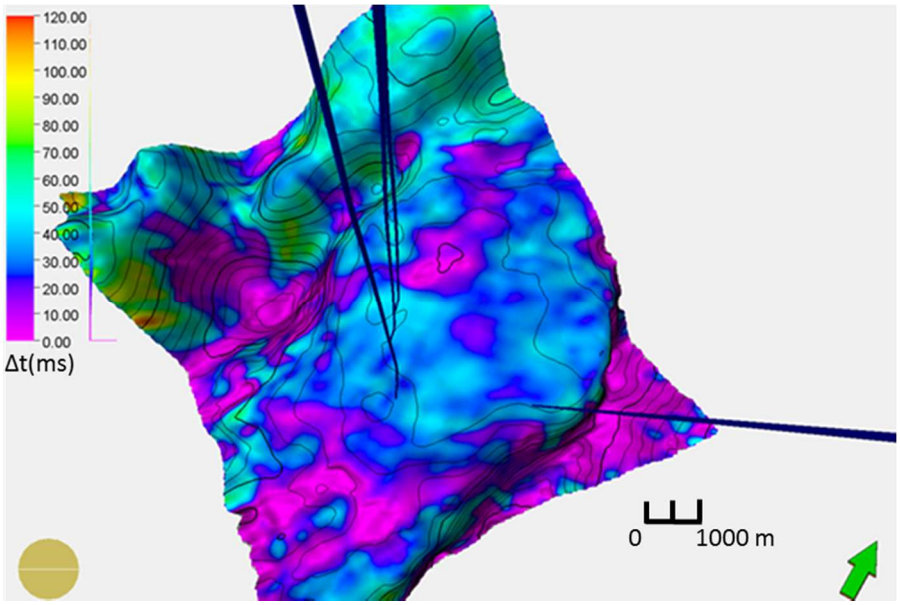

Figure 69 *Isochore between horizons Top-of-reservoir and Peak-1. The wells shown in the figure are injectors.*

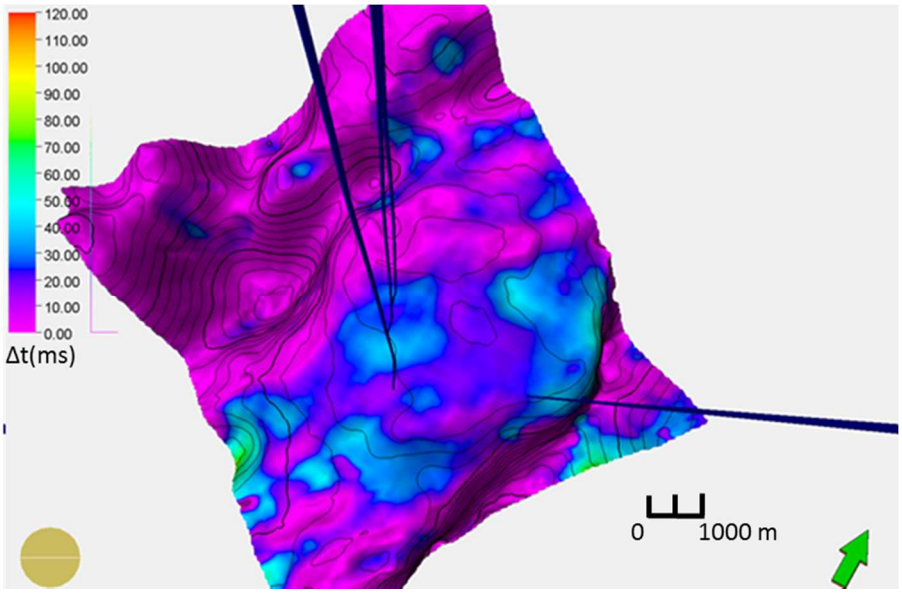

Figure 70 *Isochore between horizons Peak-1 and Trough-1. The wells shown in the figure are injectors.*

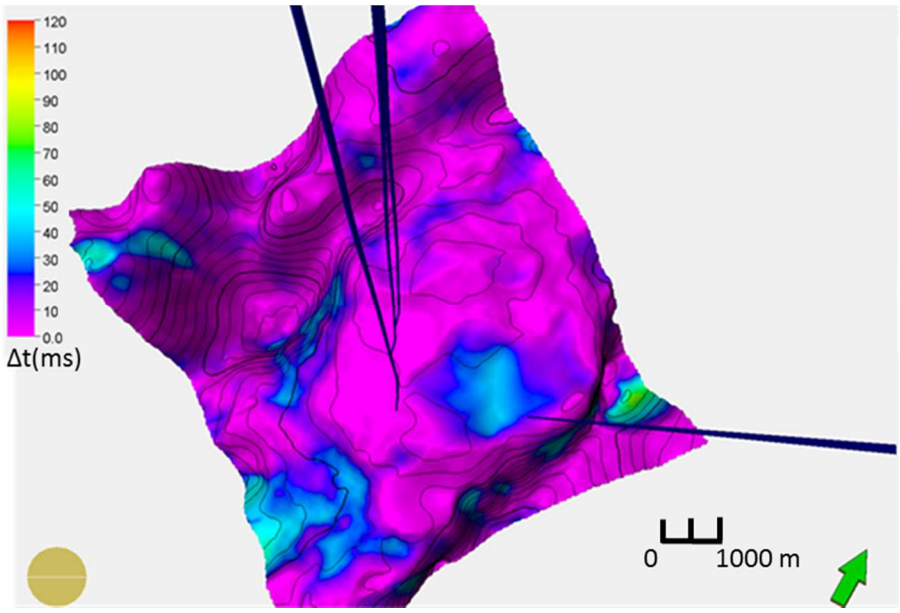

Figure 71 *Isochore between horizons Trough-1 and Peak-2 (left).*

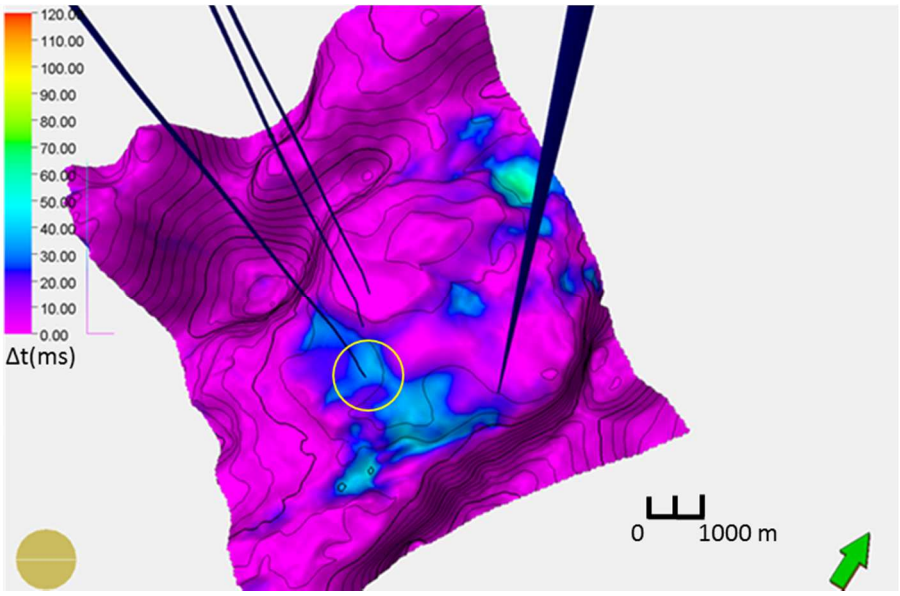

Figure 72 *Isochore between horizons Peak-2 and Peak-3 (right). Yellow indicates the position where the injection well does not cross the zone between Peak-2 and Peak-3.*

5.2.5 Flow simulation results

The reviewed dataset also includes flow simulation results from three years: 2002, 2011 and 2014. They present gas saturation, oil saturation, water saturation and pressure models for every year in the depth domain. I selected two flow simulation results for the years of 2001 and 2012, to represent a statistical realisation of the fluid state present in the reservoir during the successive seismic vintages that took place in

the years 2002 and 2011. The flow simulation models contain 346,320 cells, each one with an area of 75 m x 75 m and a height of 2 m, and were used to determine the statistical properties of fluid states utilized in the generation of the initial model. Figure 73 displays an example of a model for oil saturation in 2002. Time-lapse interpretation must be tied to dynamic reservoir information such as flow simulation. However, because the models are not unique solutions but realizations that match production history, I only used large-scale features of the model to compare with my final results. Due to uncertainties associated with time-to-depth conversion, most of the comparison was map-based.

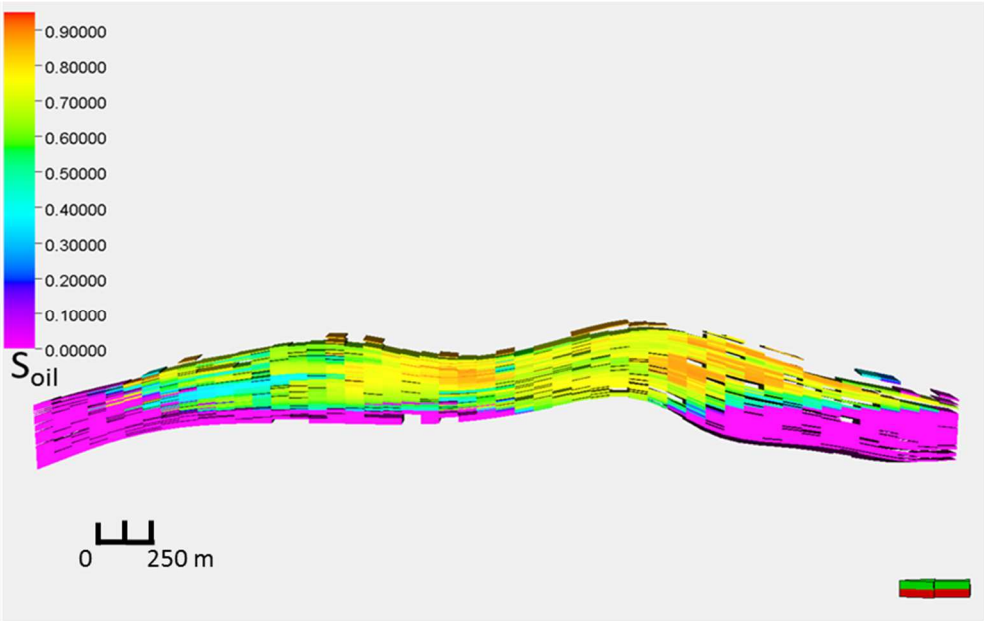

Figure 73 *Detail of oil saturation 3D grid.*

5.3 TIME-LAPSE CALIBRATION

In order to calculate the repeatability and evaluate the quality of the vintages present in the dataset, I employed a time-lapse post-stack calibration workflow (Figure 74) present in CGG's Hampsell-Russel (HR) software. In this HR workflow, the base vintage is used as a reference volume and the monitor vintage is modified. I aimed to minimize the differences between the vintages in regions not affected by production, by calibrating the monitor vintage. Therefore, I defined a time window of 200 ms above the Top-of-Macae horizon to be used in the calculation. The entire interval is located above the reservoir to avoid production effects such as time-shifts. No

compaction effects were reported in the area and the same parameters were used during the processing of both vintages (2001 and 2012). Thus, differences present in the data inside the time window must be associated with seismic acquisition (e.g. streamer feathering, source and receiver depth variation) or environmental sources (e.g. changes in the water temperature and salinity (Calvert,2005).

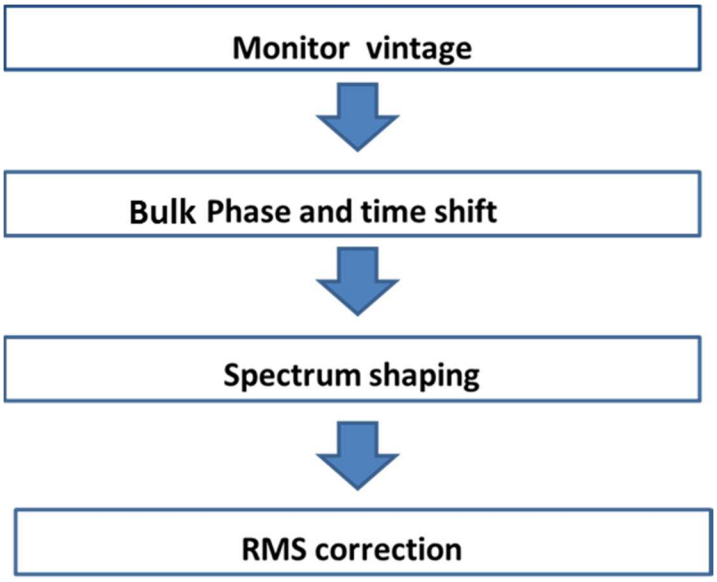

Figure 74 *Workflow for 4D calibration.*

The first steps of the workflow are the computation of cross-correlation (Figure 75) and predictability (Figure 76) attributes between base and monitor vintages. One can see in Figure 75 that the largest value of correlation was 1 and the minimum 0.76, indicating that time-lapse noise in the original data is not very high. Predictability values are close to 1, indicating an acceptable repeatability of the data. This indicator is very sensitive to the time window, where it is calculated, but not to amplitude variations. The phase shifts and time shifts between vintages were calculated and applied to the monitor vintage. Figure 77 and Figure 78 show the maps resulting from the calculation of phase and time-shifts respectively. In Figure 77, most areas present phase-shifts smaller than 10 degrees. In Figure 78, most of the map displays time-shifts smaller than 2 ms, which is less than one sample. These results indicate that the data is reasonably well aligned. I applied the time and phase-shifts calculated in the previous step to the monitor vintage. Figure 79 shows the comparison of differences before and after the application of phase and time-shift corrections. The left section shows the difference between the original monitor and base vintages and the right section shows the difference between the corrected monitor and the base vintage. The

difference is not discernible visually. I used the output of the phase and time-shift application as an input for the spectrum-shaping step. Here, the amplitude spectrum of the base vintage is used to filter the shifted monitor vintage. In Figure 80, the base vintage spectrum is compared with the filtered monitor vintage's spectrum showing good agreement between the trace spectra. In the last step, I used the amplitude root-mean-square of the base vintage as a reference to calculate the correction factor needed in the filtered monitor vintage and applied the correction. This correction aims to equalize the filtered monitor amplitudes to values close to those found in the base vintage in areas where no production took place in order to minimize the time-lapse noise. Figure 81 shows the comparison of differences before and after application of amplitude root mean square (RMS) corrections. Again, the difference is minor.

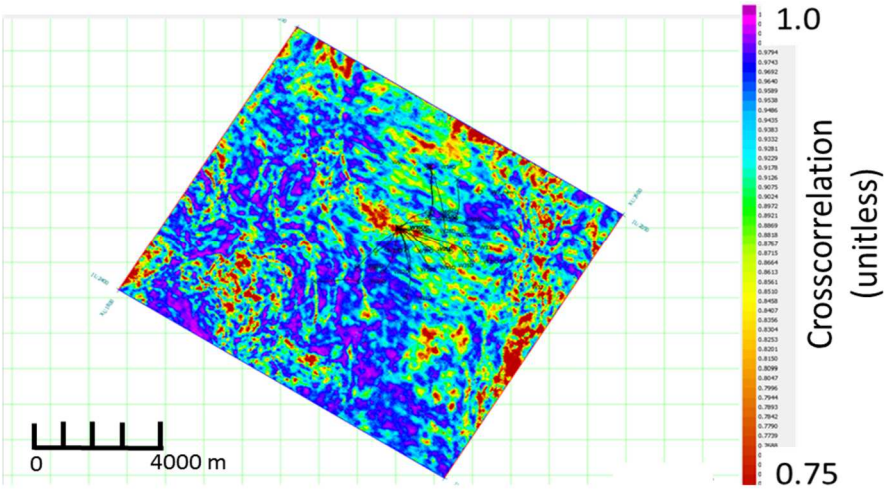

Figure 75 *Map of monitor cross-correlation in a window of 200 ms above the Top-of-Macae horizon. The larger time lag used in the calculation of the cross correlation was 25ms.*

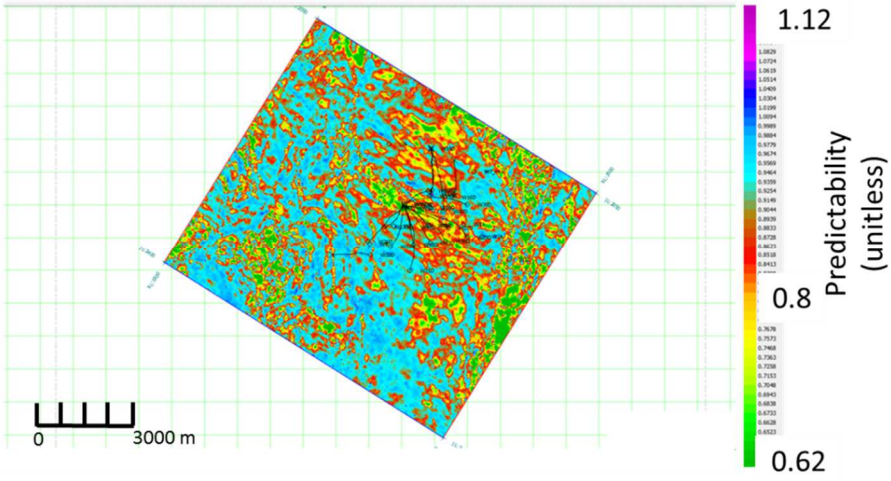

Figure 76 *Map of monitor predictability in a window of 200 ms above the Top-of-Macae horizon. The larger time lag used in the calculation of the correlation used in the predictability evaluation was 25ms.*

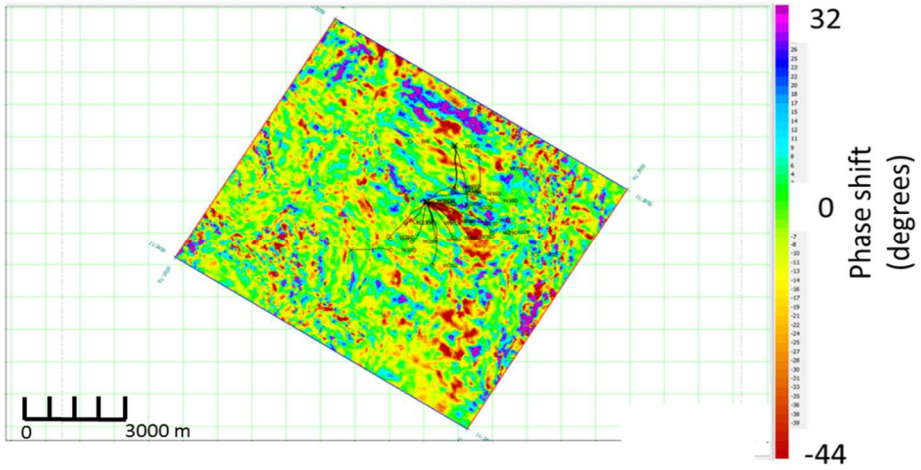

Figure 77 *Map of phase-shift in a window of 200 ms above the Top-of-Macae horizon. The larger time lag used in the calculation of the correlation used in the phase-shift evaluation was 25ms.*

.

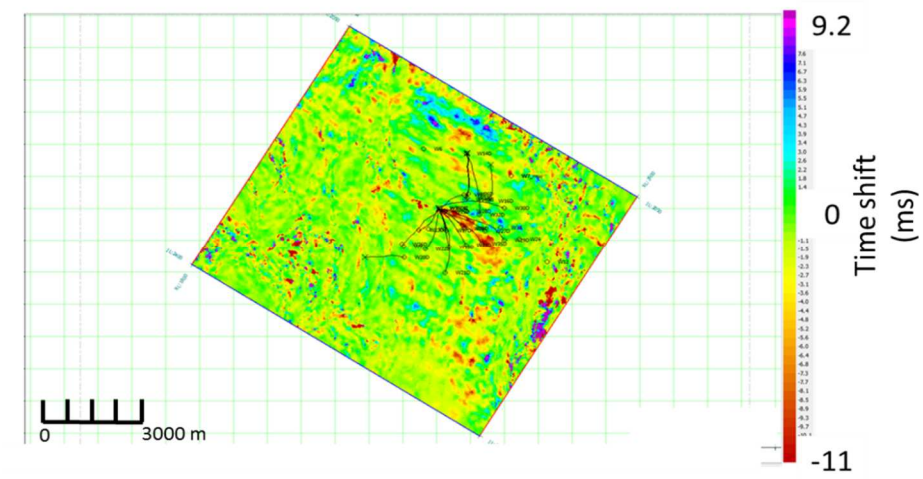

Figure 78 *Map of time-shift in a window of 200 ms above the Top-of-Macae horizon. The larger time lag used in the calculation of the correlation used in the time-shift evaluation was 25ms.*

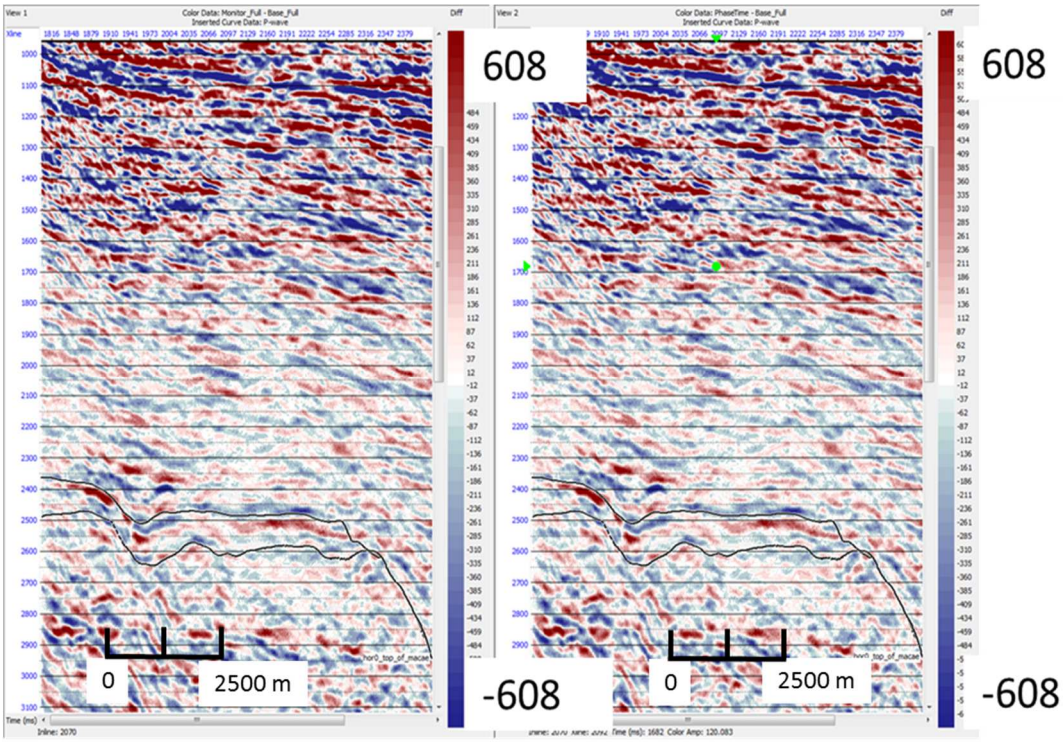

Figure 79 *Comparison of differences before and after application of phase and time-shifts corrections.*

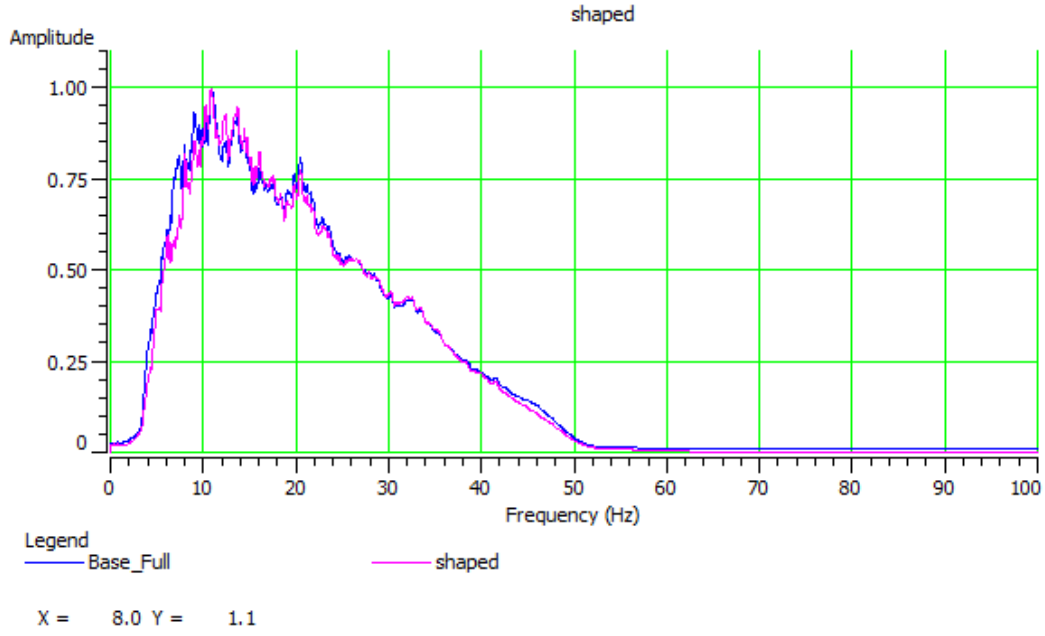

Figure 80 *Comparison between base vintage spectrum (blue) and the filtered monitor vintage spectrum (pink).*

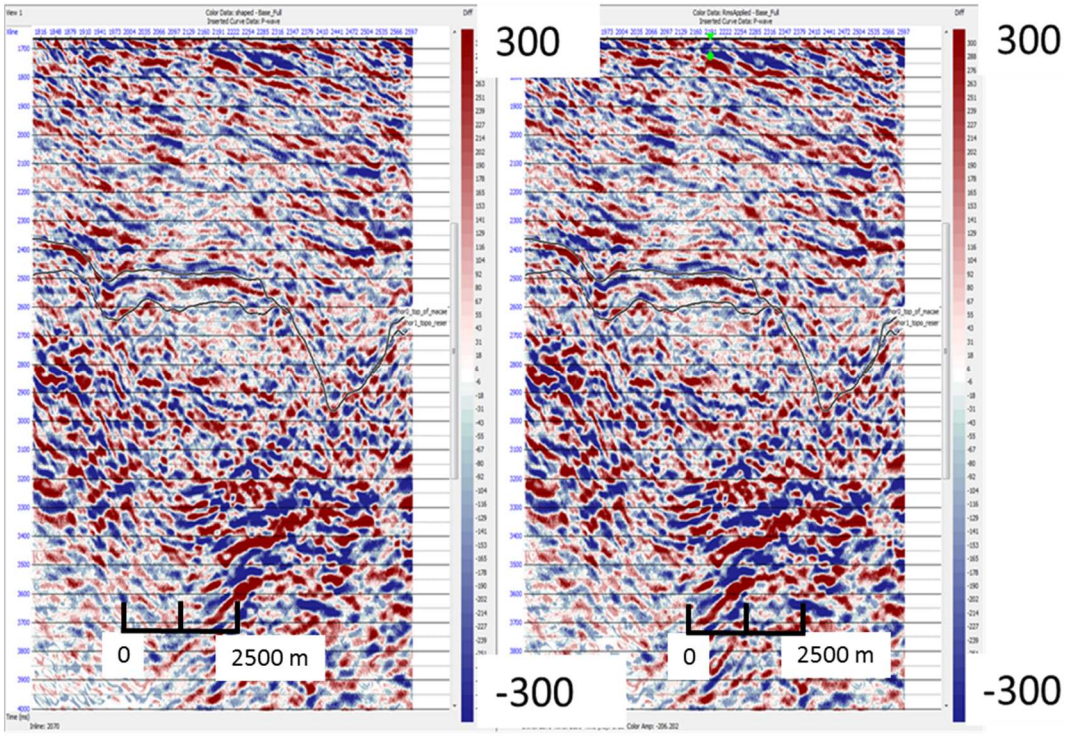

Figure 81 *Comparison of differences before and after application of amplitude root mean square correction.*

Figure 82 displays the normalised root mean square (NRMS) map calculated using the original monitor vintage and the base vintage. The average NRMS value was

0.4. The following image (Figure 83) shows the NRMS map calculated using the final result of the workflow, the calibrated monitor, and the base vintage. This time, the average NRMS value was 0.38. For reference, in the literature good quality vintages NRMS values range from 0.1 to 0.3 (Johnston, 2013). In this context, these values are not ideal but close to the common range found in offshore data. In both figures (Figure 82 and Figure 83), the area affected by the presence of obstructions in the centre of the field (as shown in Figure 49 for the monitor full stack) presents high values of NRMS. I interpreted this as an indication, even after the calibration, that the level of uncertainty in the obstructed area is greater than in the adjacent regions of field X. To facilitate the analysis of the calibration workflow effect on the repeatability, I calculated the difference between the two previous figures. The difference between the NRMS maps (Figure 84) shows areas with improvement of NRMS values, in blue, and areas with deterioration of NRMS values, in red, equally distributed along the survey. This means that the application of calibration will enhance the repeatability in some areas while it will worsen the repeatability in others. Because the improvement obtained with the calibration was minimum, and the original monitor has already been cross-equalized, I decided to perform the inversion with the original dataset. The results of the seismic vintage calibration analysis points to a seismic data with sufficient quality to be inverted with an average NRMS of 0.38. Therefore, since the non-seismic data, after the QC analysis, also show sufficient quality we went on to perform the stochastic time lapse seismic inversion of field X.

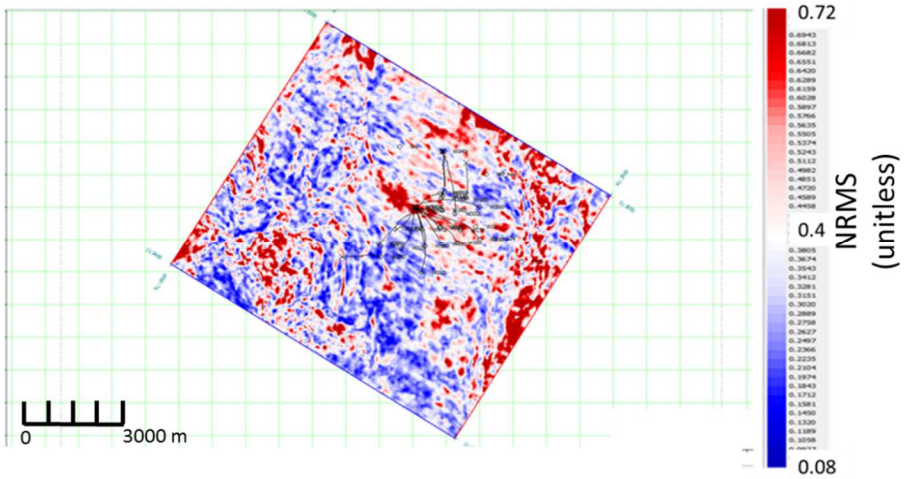

Figure 82 *Normalized root mean square (NRMS) map between the original monitor and base vintages.*

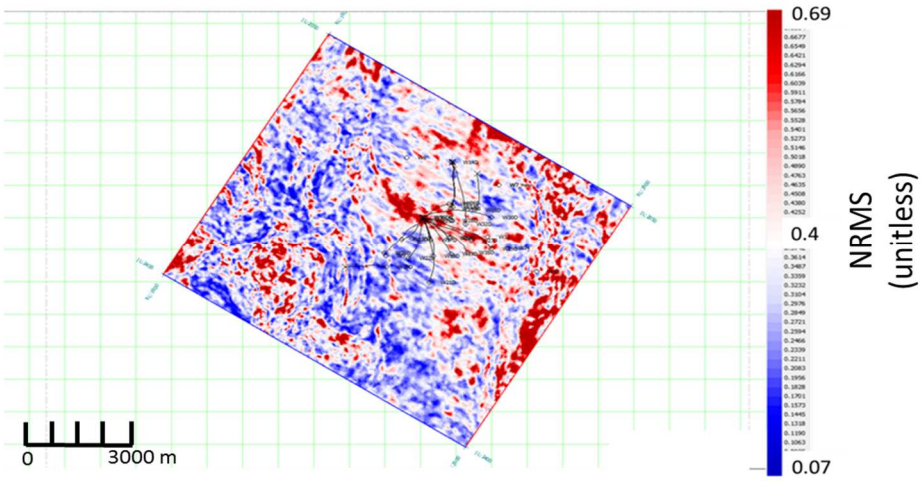

Figure 83 *Normalized root mean square (NRMS) map between calibrated monitor and the base vintage.*

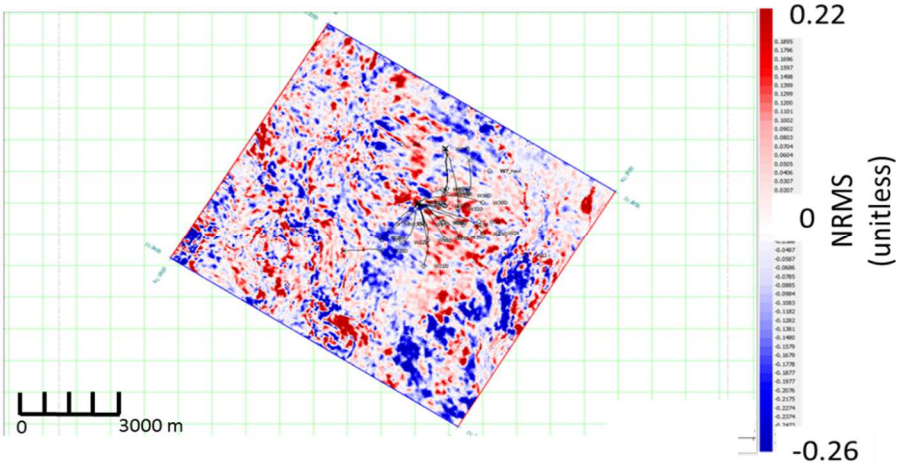

Figure 84 *Difference in Normalized root mean square (NRMS) between data shown in Figure 82 and Figure* 83.

CHAPTER 6. STOCHASTIC TIME-LAPSE INVERSION OF A CARBONATE DATA SET OFFSHORE BRAZIL

In this chapter, I will present the stochastic time-lapse inversion of a carbonate data set present in the previous chapter. The objective of this chapter is, therefore, to determine the applicability of the methodology to a carbonate reservoir analyzing a case history. I will also highlight the challenges of determining dynamic reservoir properties variation inside a highly stiff reservoir and, more importantly, the approaches used to overcome them. The results were compared to the flow simulation results in order to identify trends of dynamic property variations. Since I inverted directly to dynamic properties and no spatial constraints were applied to any reservoir property, the results are partially independent of the flow simulation models and could be used to aid quantitative time-lapse interpretations. In the next sections, I will detail the inversion parameterization and describe the wavelet estimation process, explain the inversion feasibility analysis, and discuss the results. Finally, I will draw my conclusions.

6.1 PRIOR INFORMATION

Although an Amplitude versus offset (AVO) inversion could bring more information than an acoustic impedance inversion, the critical problems in the data set make an AVO simultaneous inversion impractical. Among these problems are the low fold of the near- and mid-angle stacks in the centre of the field, the low AVO response from carbonate rocks due to high bulk modulus and the lack of shear velocity logs. These forced me to generate an acoustic solution as a first approximation. One problem with this approach is that the elastic time-lapse AVO inversion, and not the acoustic one, is used to invert for changes in pressure and saturation. This is based on the fact that to implement time-lapse AVO inversion two equations are necessary (one for changes of the intercept and one for change in the gradient), which can be solved for two unknowns (changes in pressure and saturation). The acoustic impedance inversion only has one equation, and allows an infinite number of solutions. However, according to a feasibility study performed in field X and shown later in the text, the effect of

pressure changes in the impedance between acquisitions was small and, to a first approximation, can be neglected. Uncertainty can be further reduced by constraining the inversion with prior information via the Bayesian approach. For these reasons, I opted to perform an acoustic inversion. Here, I present the parameterization used for the acoustic stochastic time-lapse inversion.

6.1.1 Layered model

After seismic interpretation, I created a layer-based initial model. This model consists of 9 layers which were named after the surface on the top (Table 7). Top-of-model and the Base-of-model are two time-constant surfaces located respectively at 2400 and 3020 ms and responsible for limiting the model in time. Five of the layers are reservoir layers, the two layers above and below were employed to avoid the distorting calculation boundary effects in the reservoir.

Table 7 *Layer characterization.*

Layer name	Reservoir/Non-reservoir	Vertical extents
Top-of-model	Non-reservoir	From horizon Top-of-model to horizon Top-of-Macae
Top-of-Macae	Non-reservoir	From horizon Top-of-Macae to horizon Top-of-reservoir
Top-of-reservoir	Reservoir	From horizon Top-of-reservoir to horizon Peak-1
Peak-1	Reservoir	From horizon Peak-1 to horizon Trough-1
Trough-1	Reservoir	From horizon Trough-1 to horizon Peak-2
Peak-2	Reservoir	From horizon Peak-2 to horizon Peak-3
Peak-3	Reservoir	From horizon Peak-3 to horizon Base-of-reservoir
Base-of-reservoir	Non-reservoir	From horizon Base-of-reservoir to horizon Lower-bound

Lower-bound	Non-reservoir	From horizon Lower-bound to horizon Base-of-model

6.1.2 Fluid substitution and trend calculation

To calculate the parameters used in the facies trends, I fluid-substituted the logs from the wells that passed the quality control test from in-situ saturation to a common fluid saturation state, in this case 100% brine. At the time of field X's discovery, Petrobras classified the wells as oil producers: therefore, I considered that there was no, or little, free gas in the reservoir when the wells were logged. For this reason, I used the water saturation (Sw) curve to calculate the oil saturation (1-Sw) curve and used it to perform the fluid substitution. I considered any gas present in the reservoir to be in solution. I employed the Batzle and Wang relations (Batzle and Wang, 1992) to calculate the elastic properties of the resulting mixed fluids. Table 8 summarizes the fluid parameters used for fluid substitution. All parameters were available in the data set with the exception of salinity that was later determined by Bezerra et al. (2004), who presented salinity to study the Namorado field, a field of the same age and closely located to field X.

Table 8 *Fluid parameters.*

Fluid Parameter	Value	Unit
Brine Salinity	97390	ppm
Temperature	109	^{o}C
Pressure	110	MPa
Oil gravity	30.5	Unitless
Gas-oil ratio	430	Unitless
Gas gravity	0.743	Unitless

Table 9 *Matrix constituent's percentages and elastic properties.*

Matrix constituent	Volume fraction	Density (g/cm^3)	Bulk modulus (GPa)	Shear modulus (Gpa)
Calcite	96%	2.71	76.8	32.0
Quartz	2%	2.65	36.6	45.0
Dolomite	1%	2.87	94.9	45.0
Feldspar	1%	2.62	75.6	25.6

The mineralogical analysis of the field X rocks present in Table 9 suggests that the reservoir rock is compositionally homogeneous, with 96% of the rock being made of calcite (Archilha et al., 2013). I calculated the matrix parameters using an average of the Hashin-Shtrikman bounds (Hashin and Shtrikman, 1963). Then, I used Gassmann's equation to perform the fluid substitution for the selected wells. Using the facies logs as a mask, I calculated the regression curves parameters for each facies as shown from Figure 85 to Figure 92. Since no Vs log was available, the Vs trends were not calculated. This fact has not affected the inversion since I had already decided to perform acoustic stochastic time-lapse inversion, which does not utilize Vs. Table 10 summarizes a compilation of the best-fit curve parameters.

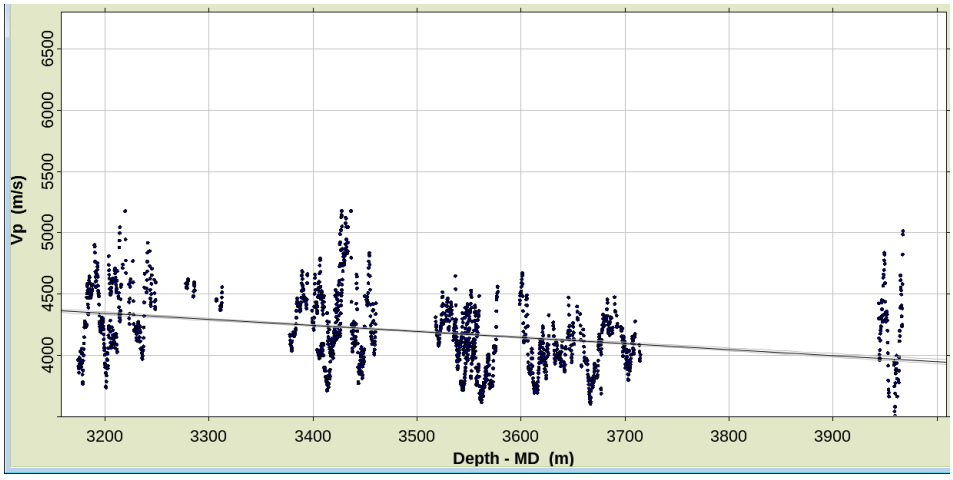

Figure 85 *Crossplot of acoustic velocity and depth for facies 1 using all the wells selected for fluid substitution. The parameters for the best-fit line will serve as inputs for the inversion program.*

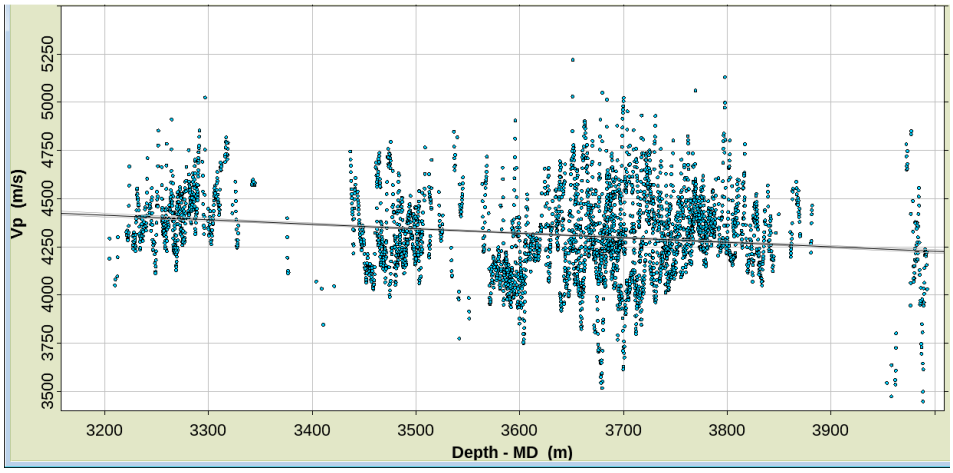

Figure 86 *Crossplot of acoustic velocity and depth for facies 2 using all the wells selected for fluid substitution. The parameters for the best-fit line served as inputs for the inversion program.*

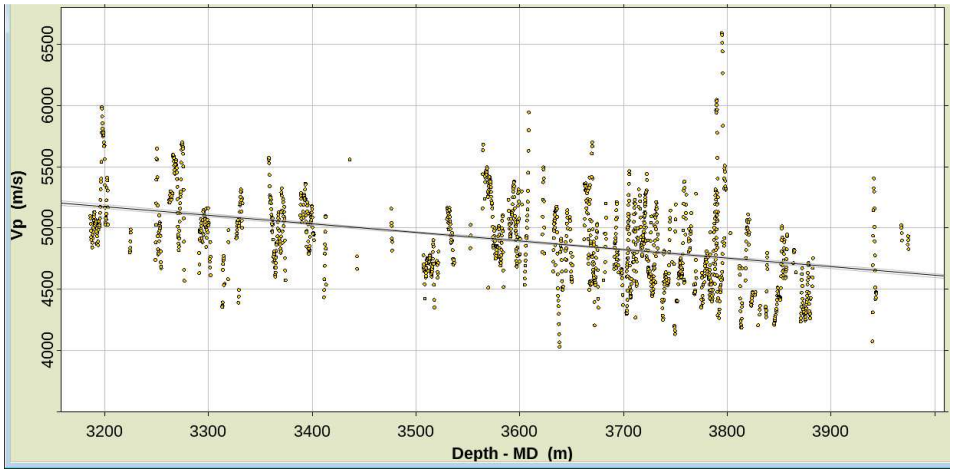

Figure 87 *Crossplot of acoustic velocity and depth for facies 3 using all the wells selected for fluid substitution. The parameters for the best-fit line served as inputs for the inversion program.*

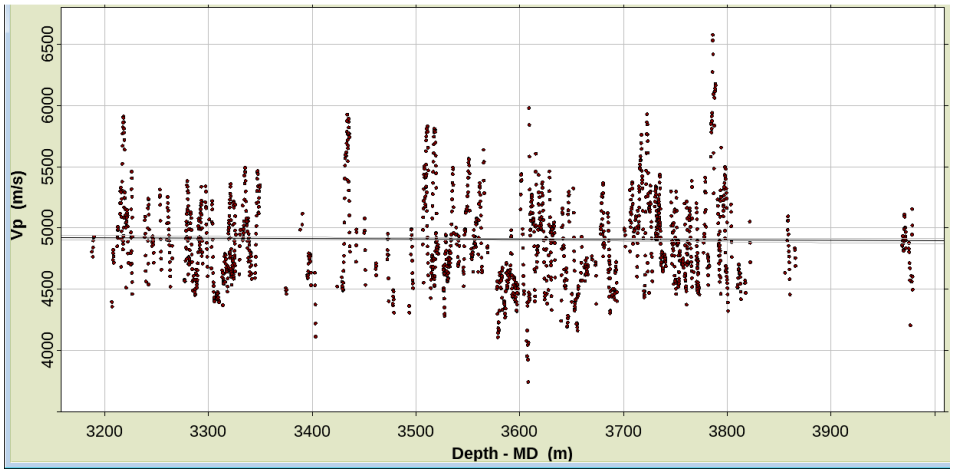

Figure 88 *Crossplot of acoustic velocity and depth for facies 4 using all the wells selected for fluid substitution. The parameters for the best-fit line served as inputs for the inversion program.*

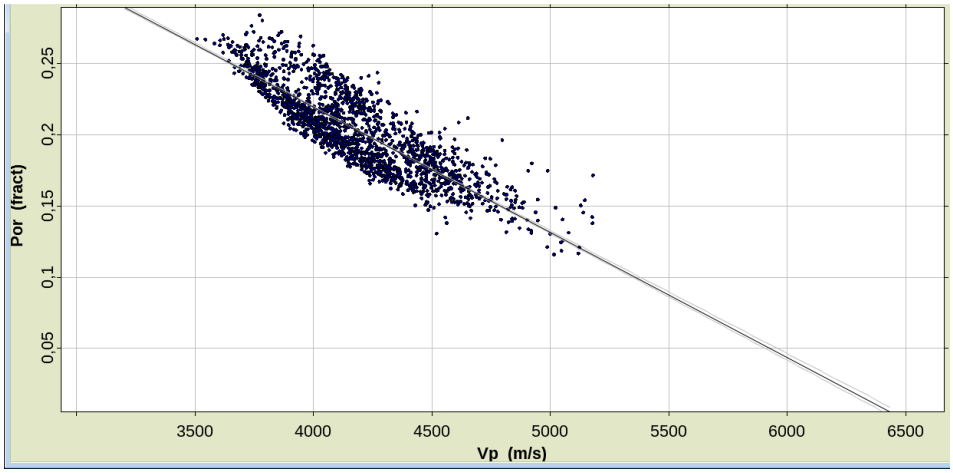

Figure 89 *Crossplot of porosity and acoustic velocity for facies 1 using all the wells selected for fluid substitution. The parameters for the best-fit line served as inputs for the inversion program.*

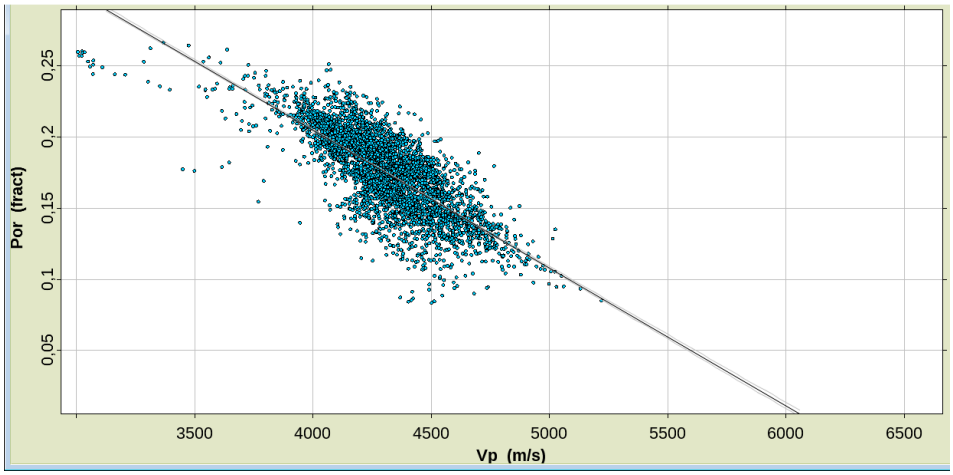

Figure 90 *Crossplot of porosity and acoustic velocity for facies 2 using all the wells selected for fluid substitution. The parameters for the best-fit line served as inputs for the inversion program.*

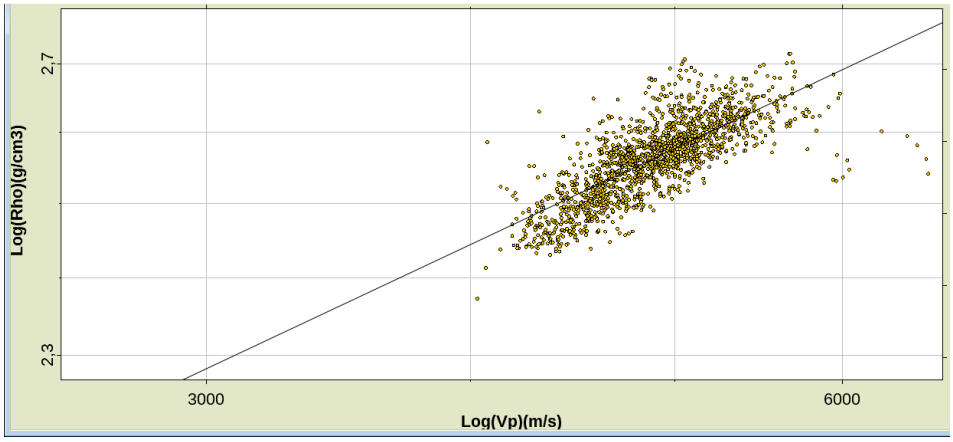

Figure 91 *Crossplot of density and acoustic velocity for facies 3 using all the wells selected for fluid substitution. In that case, I used a rho= a(Vp)^b law for the fitting curve. The parameters for the best-fit line served as inputs for the inversion program.*

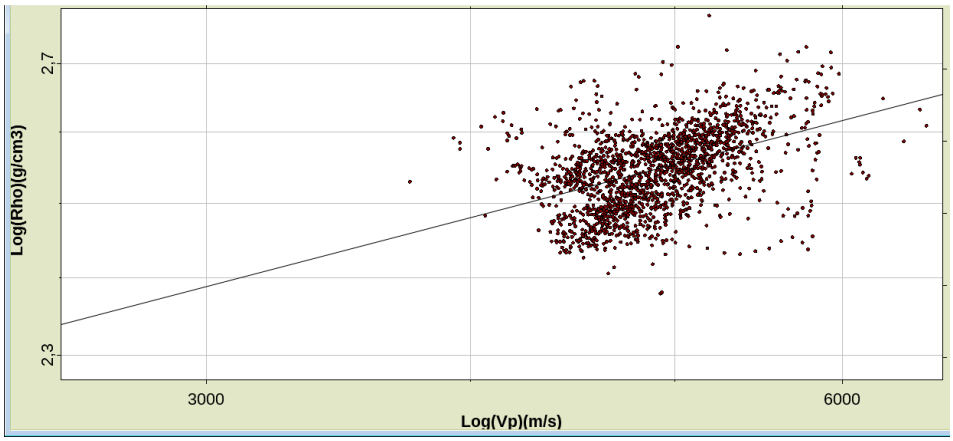

Figure 92 *Crossplot of density and acoustic velocity for facies 4 using all the wells selected for fluid substitution. In that case, I used a rho= a(Vp)^b law for the fitting curve. The parameters for the best-fit line served as inputs for the inversion program.*

Table 10 *Trend parameters.*

Regression	Facies	Parameter A	Parameter B	Error	R^2	Fit type
Vp x Depth	1	5902.9	-0.4885	275.33	0.10	Linear
Vp x Depth	2	5167	-0.2355	227.25	0.03	Linear
Vp x Depth	3	7423.3	-0.7034	313.34	0.17	Linear
Vp x Depth	4	5027.4	-3.4×10^{-2}	364.95	≈0.00	Linear
Porosity x Vp	1	0.5707	-8.8×10^{-5}	1.6×10^{-2}	0.72	Linear
Porosity x Vp	2	0.5924	-9.7×10^{-5}	1.9×10^{-2}	0.58	Linear
Density x Vp	3	0.3373	0.2386	3.6×10^{-2}	0.58	Power law
Density x Vp	4	0.7721	0.1402	4.9×10^{-2}	0.19	Power law

6.1.3 Net-to-gross calculation

Another important layer parameter that must be determined in order to generate the initial model is the net-to-gross (NG). After the interpretation of the horizons, I

picked well markers at the points where the horizons crossed the wells in the time domain. These well markers separate the facies logs in depth sections corresponding to the model's layers. Then I created distributions of facies in the model's layers by calculating the histograms of the facies log samples (Figure 93 to Figure 97). Considering facies 1 and 2 as reservoir facies, I considered the combined proportion of these two facies as net-to-gross. Analyzing the behaviour of the reservoir facies (facies 1 and 2), I could note an alternate predominance of one reservoir facies over the other in every layer. In the Top-of-reservoir layer, facies 1 has a clear preponderance over facies 2. In the Peak-1, Through-1, Peak-2 and Peak-3 layers, facies 2 has prevalence over facies 1. Contrary to the behaviour of reservoir facies frequency, which shows a clear predominance of one of the facies in each layer, this predominance did not exist between non-reservoir facies frequencies. To incorporate this behaviour into my model, I subdivided the non-reservoir fraction between the facies 3 and 4. To do this, I used a second type of NG, the net-to-gross-hard (NG-hard), which is described in Gunning and Glinsky (2004) and in Chapter 3 of this thesis as the proportion of one of the non-reservoir facies to the total of non-reservoir facies. In this work, I decided to use the proportion of cemented bioturbated grainstone samples (Facies 4) to be the total non-reservoir facies to calculate this NG-hard parameter. Finally, Table 11 summarizes the NG and NG-hard parameters.

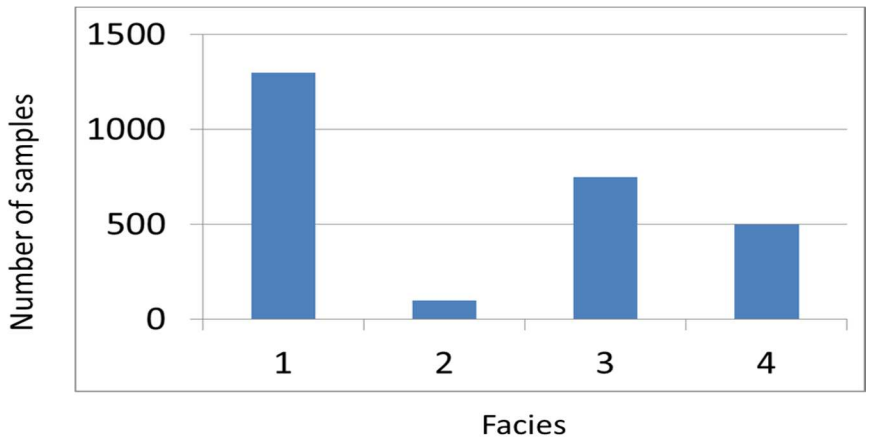

Figure 93 *Facies distribution in layer Top-of-reservoir.*

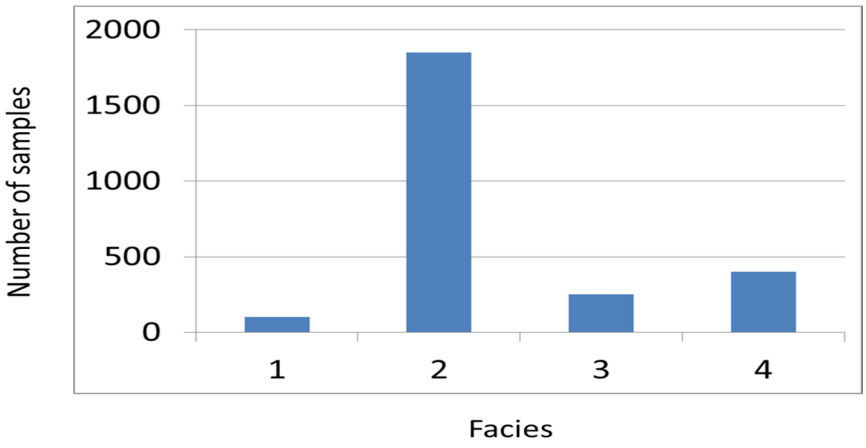

Figure 94 *Facies distribution in layer Peak-1.*

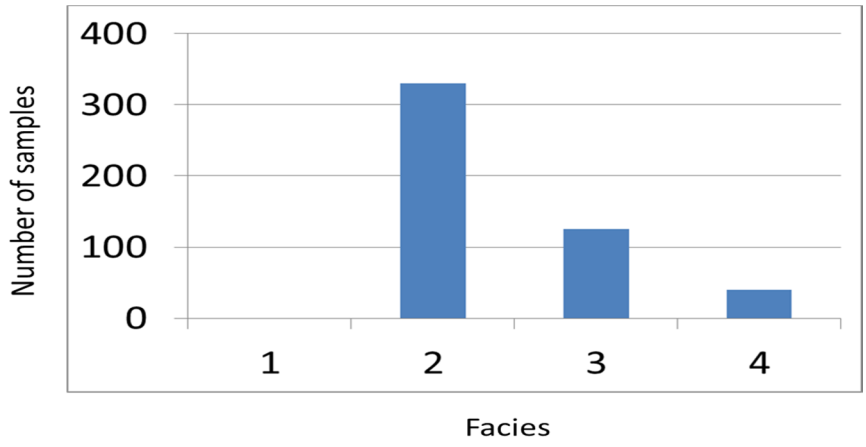

Figure 95 *Facies distribution in layer Trough-1.*

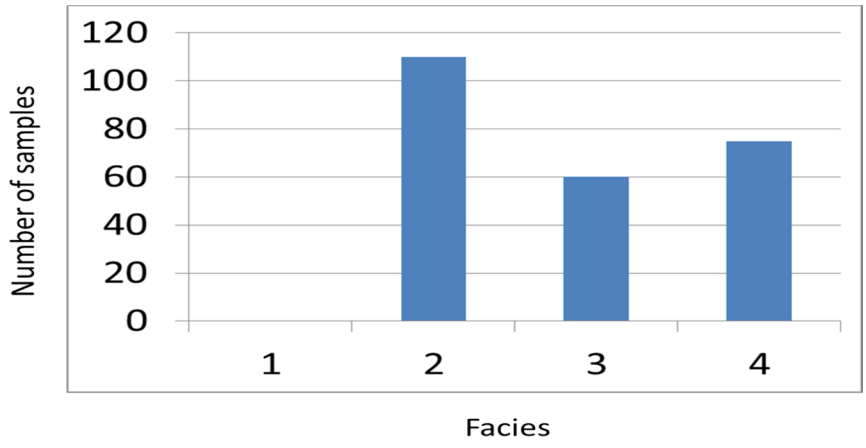

Figure 96 *Facies distribution in layer Peak-2.*

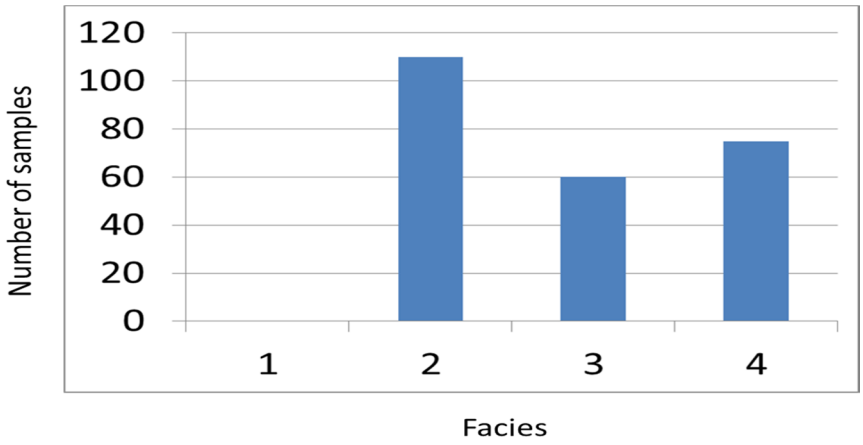

Figure 97 *Facies distribution in layer Peak-3.*

Table 11 *NG and NG-hard for each layer.*

Layer	Most common Reservoir facies	NG (%)	NG-hard (%)
Top-of-reservoir to Peak-1	Grainstone (facies 1)	51	40
Peak-1 to Trough-1	Packstone/wackestone (facies 2)	72	61
Trough-1 to Peak-2	Packstone/wackestone (facies 2)	67	16
Peak-2 to Peak-3	Packstone/wackestone (facies 2)	45	55
Peak-3 to Base-of-reservoir	Packstone/wackestone (facies 2)	37	50

6.1.4 Saturation

Since the wells were logged long before the baseline seismic acquisitions, I could not rely on the petrophysical logs to determine the *a priori* fluid saturation for oil, gas and water and their respective uncertainties in each vintage acquisition time. This reason for this is that, with production, all the saturation values had changed and the seismic data no longer reflected the original impedance contrasts at the time of drilling. Instead, I used the flow simulation results for the years 2002 and 2011 to determine the statistic properties of the fluid saturation variables present when the seismic vintages were acquired. To perform the statistical analysis, I created histograms of the

oil saturation values present in the 2002 and 2011 models, shown in Figure 98 and Figure 99 respectively. I calculated Gaussian functions to fit distributions, and determined means and standard deviations for 2002 and 2011 oil saturation distributions (Figure 100 and Figure 101, respectively). Table 12 displays the values of the means and standard deviations.

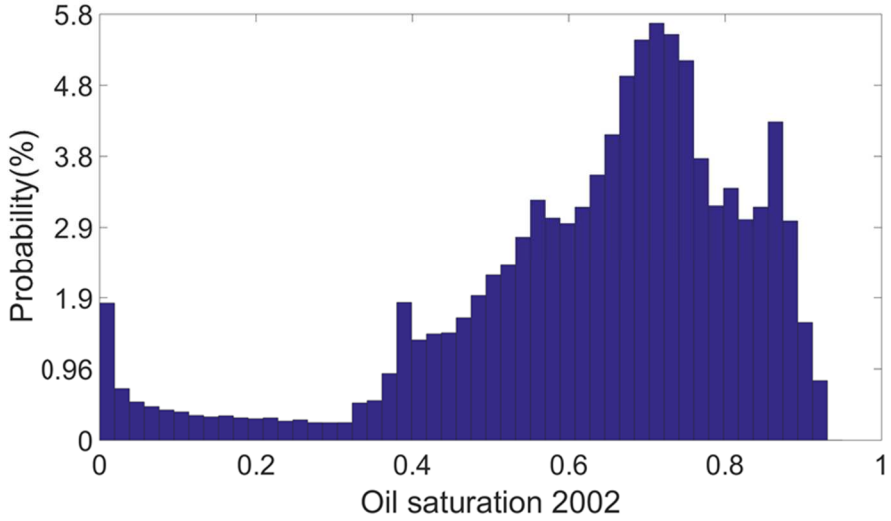

Figure 98 *Histogram of Oil Saturation values present in the 2002 model.*

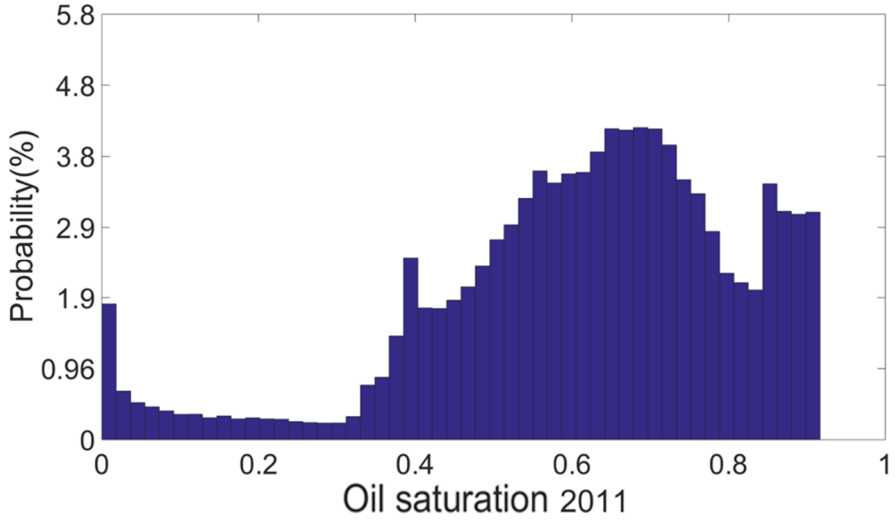

Figure 99 *Histogram of Oil Saturation values present in the 2011 model.*

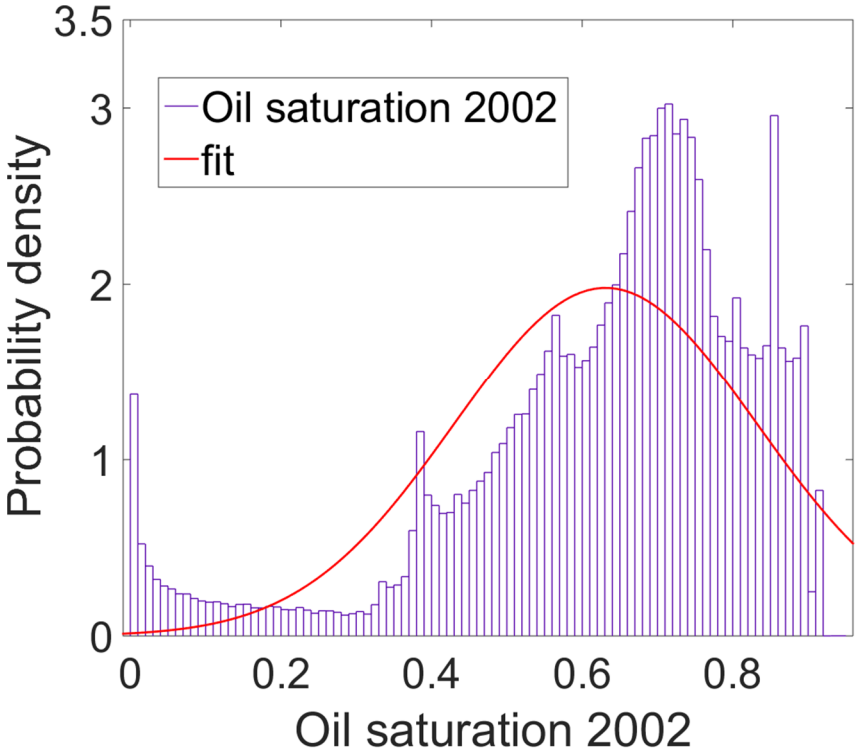

Figure 100 *Gaussian function used to fit distribution superimposed on the Oil Saturation values histogram from 2002 model.*

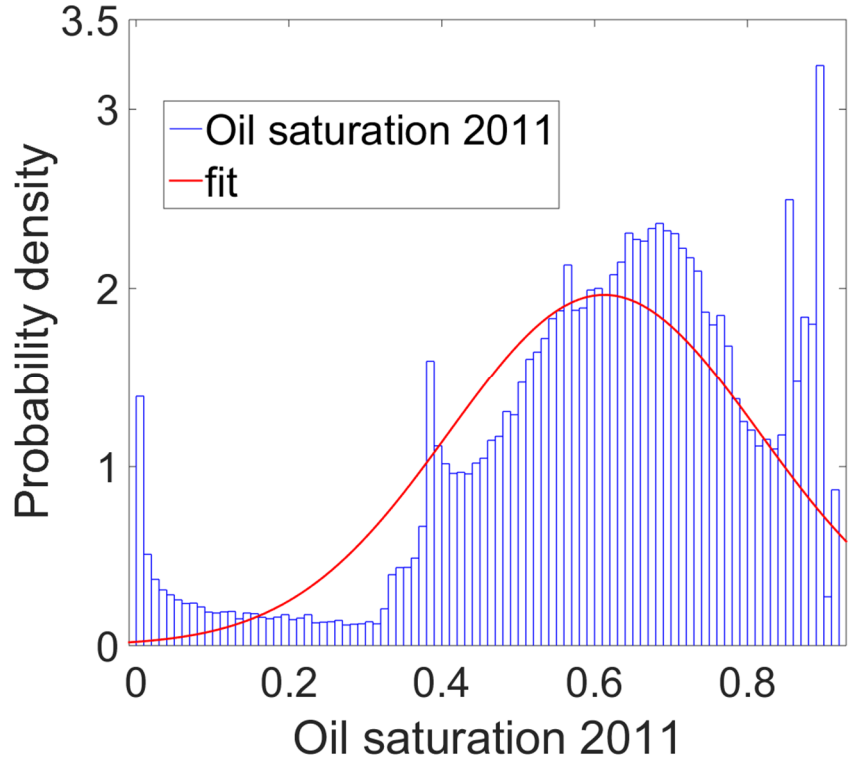

Figure 101 *Gaussian function used to fit distribution superimposed on the Oil Saturation values histogram from 2011 model.*

Table 12 *Initial oil saturation parameters.*

Property	Math operator	Vintage	Value
Oil saturation	Mean	2002	0.63
Oil saturation	Standard deviation	2002	0.2
Oil saturation	Mean	2011	0.61
Oil saturation	Standard deviation	2011	0.2

The subtraction of 2002's oil saturation, gas saturation and pressure models from the respective 2011 models showed that most of the variation occurred in the first 30 layers of the models. Using the well markers associated with each interpreted horizon, I determined that this depth interval corresponds roughly to the Top-of-reservoir layer in time (Figure 102). Based on this observation, I decided to separate the model into two parts: the Top-of-reservoir and the remaining reservoir layers. I also recalculated the statistical analysis for each zone (Figure 103 to Figure 106). Table 13 summarizes the final oil saturation parameters. The same logic applies to gas saturation. Table 14 summarizes the final gas saturation parameters. Before continuing the parameterization, it was necessary to estimate the irreducible water saturation and the irreducible oil saturation from relative permeability (Figure 107) and capillary pressure (Figure 108) curves. This was necessary because they were not present among the provided simulation flow outputs. If one draws a vertical asymptote in Figure 108, it is possible to identify the residual water saturation, which is around 8%. As a result, the oil saturation cannot exceed 92%. At Figure 107, one can see the same result being replicated at the point, around 8% water saturation, where the water relative permeability (Krw) curve touches the x-axis.

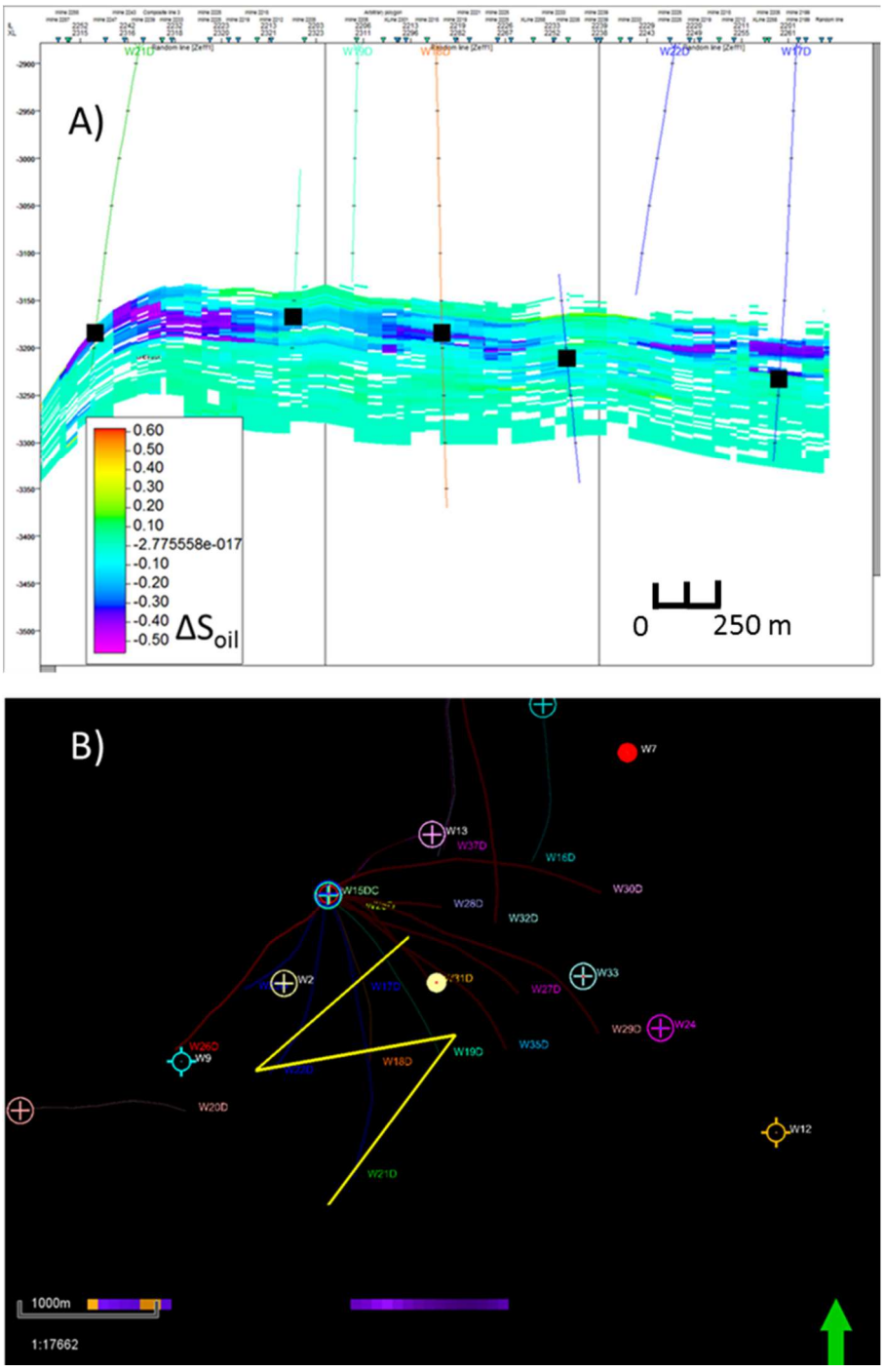

Figure 102 *A) Difference of oil saturation from 2011 and 2002 flow simulation models showing larger changes in the top layers. The black squares are well markers accompanying Peak-1 horizon, the base of the Top-of-reservoir layer. B) Random line path.*

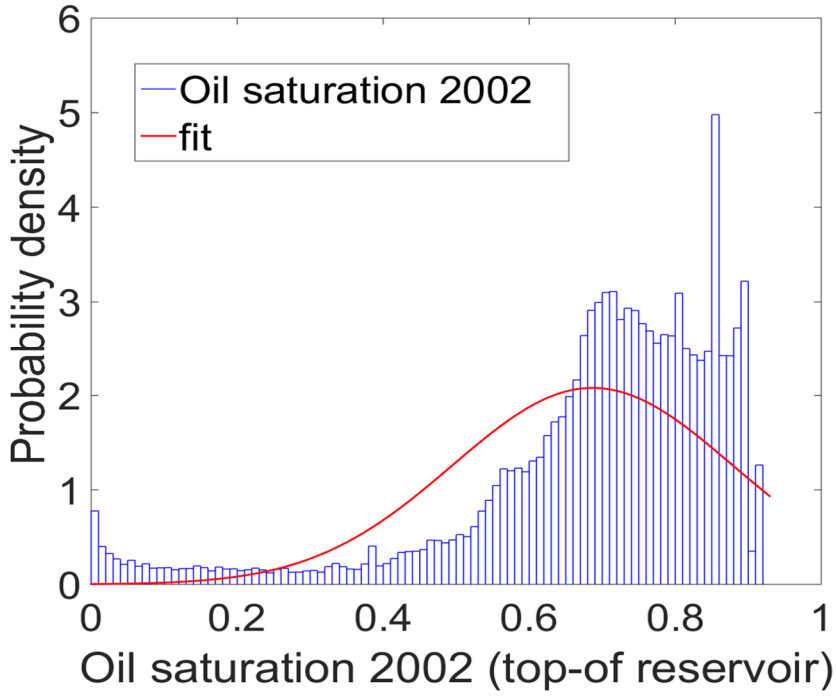

Figure 103 *Gaussian function used to fit distribution superimposed on the oil saturation values histogram from the 30 first layers of 2002 model that corresponds to the Top-of-reservoir layer in time.*

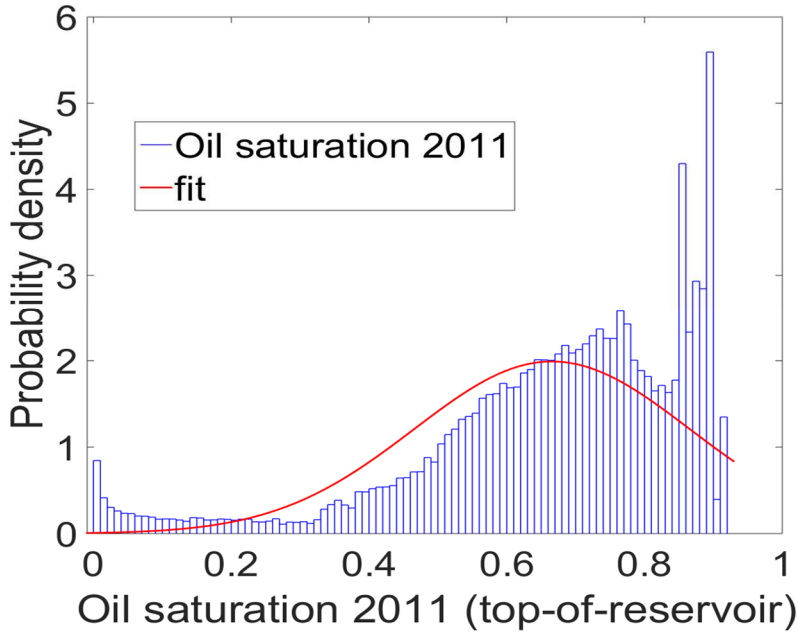

Figure 104 *Gaussian function used to fit distribution superimposed on the oil saturation values histogram from the 30 first layers of 2011 model that corresponds to the Top-of-reservoir layer in time.*

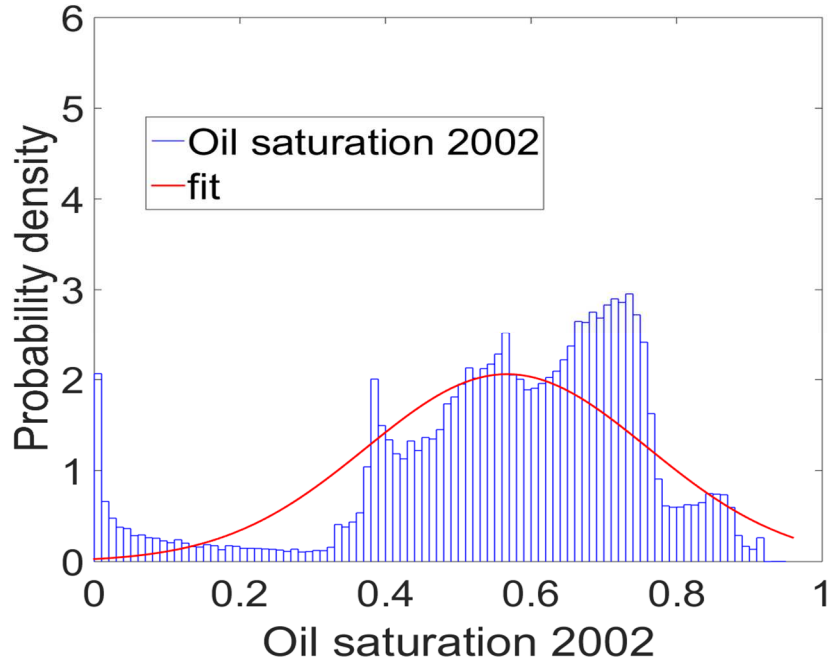

Figure 105 *Gaussian function used to fit distribution superimposed on the oil saturation values histogram from the layers with an index higher than 30 of 2002 model that corresponds to the remaining reservoir layers in time.*

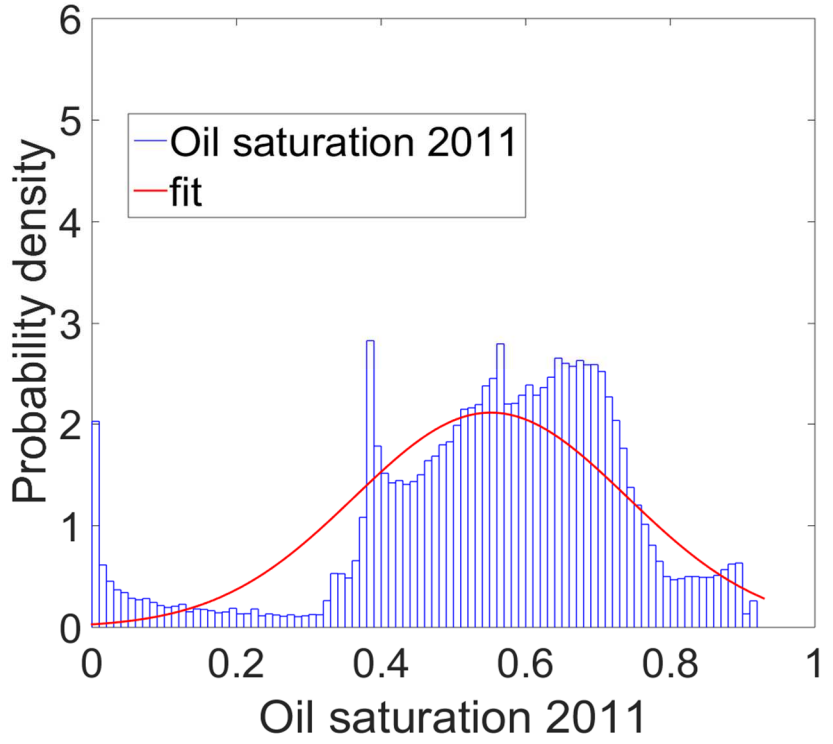

Figure 106 *Gaussian function used to fit distribution superimposed on the oil saturation values histogram from the layers with an index higher than 30 of 2011 model that corresponds to the remaining reservoir layers in time.*

Table 13 *Final oil saturation parameters.*

Property	Math operator	Vintage	Value
Oil saturation Top-of-reservoir layer	Mean	2002	0.68
Oil saturation Top-of-reservoir layer	Standard deviation	2002	0.19
Oil saturation Top-of-reservoir layer	Mean	2011	0.66
Oil saturation Top-of-reservoir layer	Standard deviation	2011	0.20
Oil saturation remaining reservoir layers	Mean	2002	0.56
Oil saturation remaining reservoir layers	Standard deviation	2002	0.19
Oil saturation remaining reservoir layers	Mean	2011	0.55
Oil saturation remaining reservoir layers	Standard deviation	2011	0.18

Table 14 *Final gas saturation parameters.*

Property	Math operator	Vintage	Value
Gas saturation Top-of-reservoir layer	Mean	2002	0.097
Gas saturation Top-of-reservoir layer	Standard deviation	2002	0.08
Gas saturation Top-of-reservoir layer	Mean	2011	0.08
Gas saturation Top-of-reservoir layer	Standard deviation	2011	0.07
Gas saturation remaining reservoir layers	Mean	2002	0.1
Gas saturation remaining reservoir layers	Standard deviation	2002	0.06
Gas saturation remaining reservoir layers	Mean	2011	0.1
Gas saturation remaining reservoir layers	Standard deviation	2011	0.07

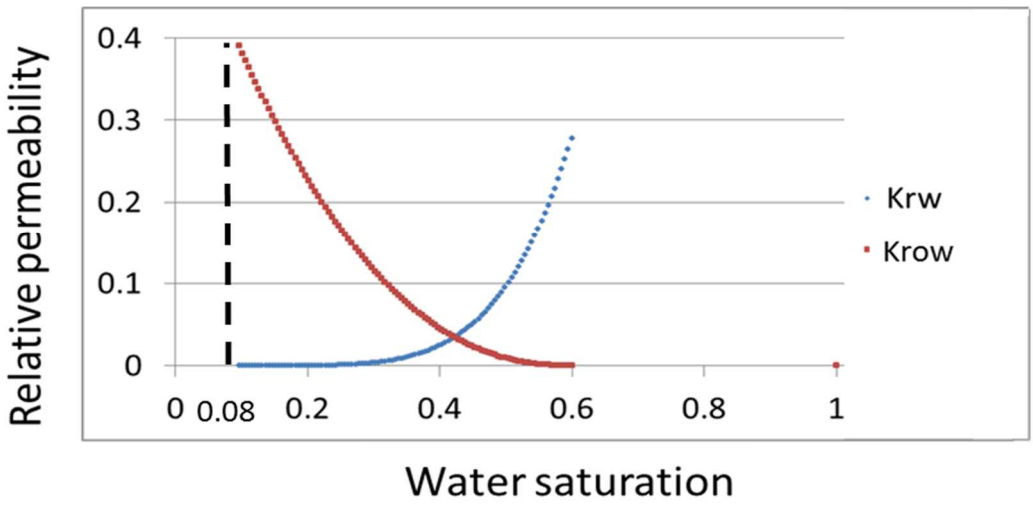

Figure 107 *Relative permeability curves against water saturation. The relative permeability of water (Krw) is in blue and the relative permeability of oil (Krow) is in red. Dashed line represents an asymptote signalizing the residual water saturation (8% Sw).*

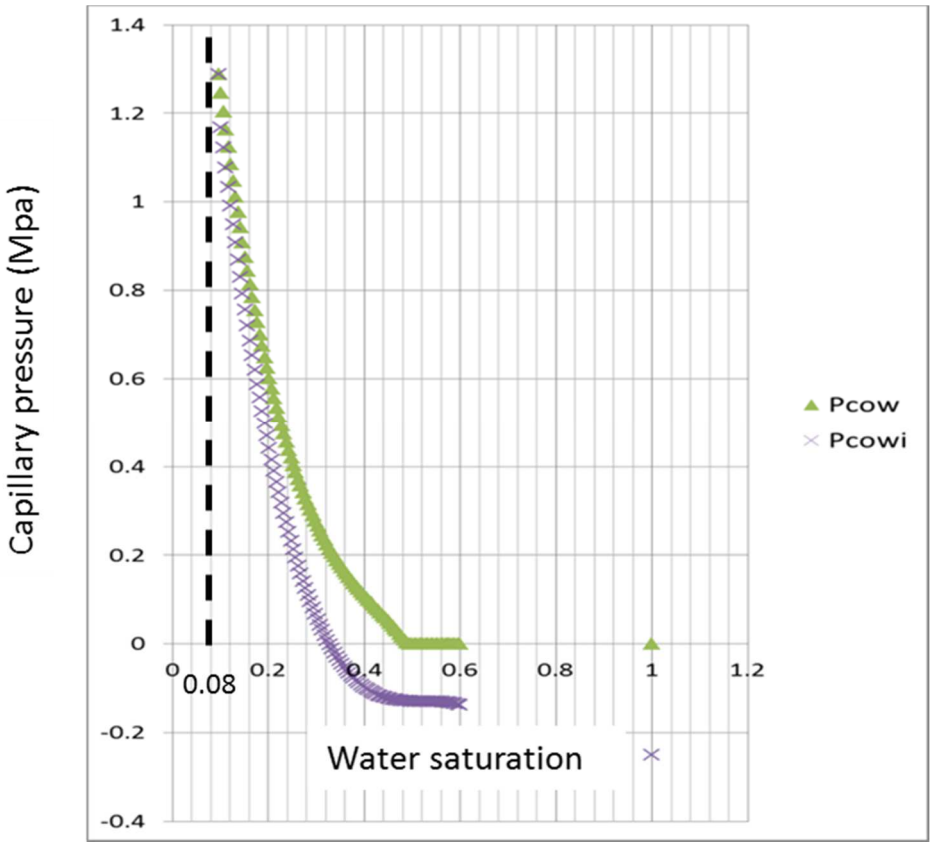

Figure 108 *Capillary pressure curves as a funcion of water saturation. Pressure capillary during imbibition (Pcowi) is in purple and pressure capillary during drainage is in green (Pcow). Dashed line represents an asymptote signalizing the residual water saturation (8% Sw).*

6.1.5 Pressure

The reported confining pressure in this reservoir is 68.6 MPa and the pre-production pore pressure was 32.3 MPa. Hence, I estimated the original differential pressure to be around 36.3 MPa. At this effective pressure, the majority of the carbonate rocks are already in the constant, high-effective portion of the velocity-versus-effective pressure curve (shown in Figure 109) and the crack-like pores are closed. Geoscientists from the IGEM4D (Integrated Geophysics and Geomechanics for 4D responses) project (Petrobras/CSIRO), while studying oolitic/oncolytic carbonate samples from an albian reservoir in the same basin, measured velocity under a range of effective pressures (Figure 109). They observed that the carbonate rocks with the same description as the best reservoir facies are already in the flat part of the velocity-pressure curve at 36 MPa. This result validates the application of the linear approach to velocity variation with pressure used in delivery4D in the reservoir. If the

reservoir rocks were in a lower effective pressure regime, still with crack-like pores open, the curve couldn't be fitted by a linear approximation, as the one employed in Delivery4D methodology, for a large range of effective stress values. To incorporate the pressure effects in the inversion, I had to solve two problems. The first one was the calculation of the effective stress path coefficient for each facies. The second one was the computation of the pore pressure changes in the reservoir.

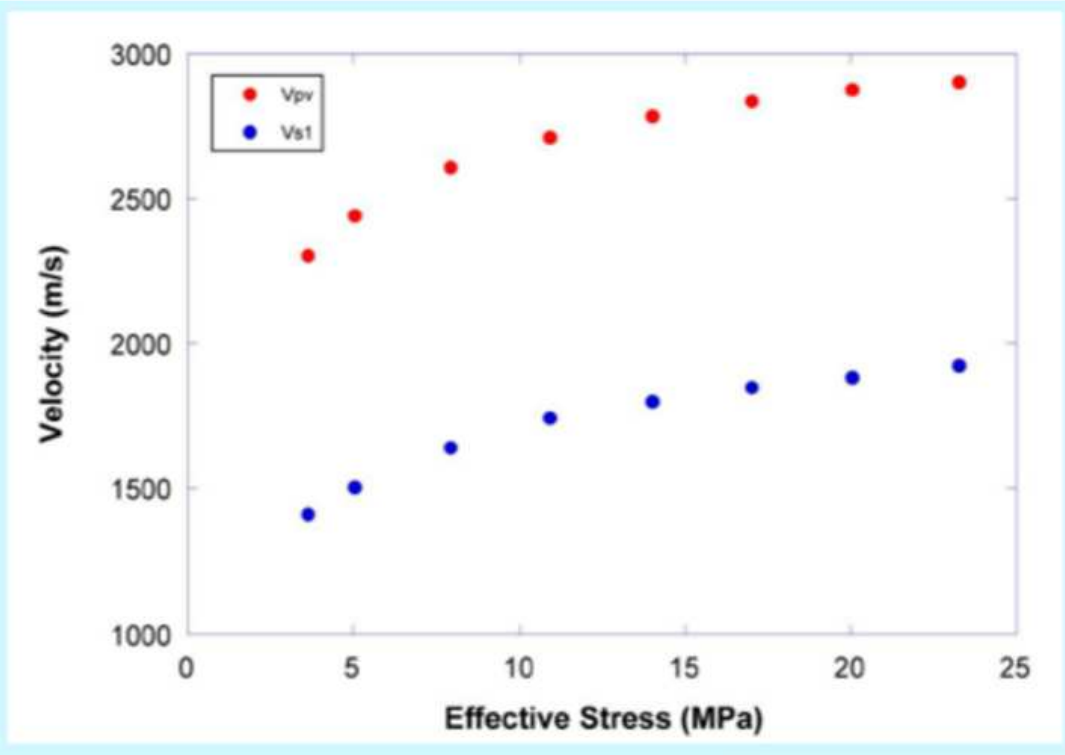

Figure 109 *Vp and Vs velocities versus pressure for Albian oolitic/oncolytic carbonates (Courtesy of IGEM).*

6.1.5.1 Calculation of the effective stress path coefficient $R_{p,F,T}^{eff}$

In order to investigate the reservoir's elastic properties for changes in pressure, six core samples had their compressional velocity measured under different pressure values. The results are presented in the tables below. Three cycles of pressure increase were performed, and Vp was measured for the lower and higher values. At the end of the third cycle, a much greater pressure was applied for the measurement of the final Vp value.

Sample A1	Effective pressure (MPa)	Vp (m/s)
Depth at well 25D: 3212m	13.83	5046.35
	22.49	5148.64
	13.83	5148.64
	22.49	5148.64
	13.83	5174.87
	43.89	5148.64

Sample B1	Effective pressure (MPa)	Vp (m/s)
Depth at well 25D: 3233m	13.89	3313.04
	22.65	3491.40
	13.89	3401.78
	22.65	3515.57
	13.89	3356.82
	44.22	3694.54

Sample B1A	Effective pressure (MPa)	Vp (m/s)
Depth at well 25D: 3233m	13.83	3353.13
	22.49	3650.29
	13.83	3463.63
	22.49	3619.95
	13.83	3440.18
	44.22	3927.83

Sample B5	Effective pressure (MPa)	Vp (m/s)
Depth at well 25D: 3233m	13.89	3455.78
	22.65	3767.61
	13.89	3564.91
	22.65	3810
	13.89	3577.46
	44.22	4141.30

Sample D1	Effective pressure (MPa)	Vp (m/s)
Depth at well 25D: 3263m	13.85	3932.90
	22.57	4163.93
	13.85	3979.11
	22.57	4163.93
	13.85	3902.68
	44.71	4522.25

Sample E1	Effective pressure (MPa)	Vp (m/s)
Depth at well 25D: 3280m	13.85	3487.41
	22.54	3843.63
	13.85	3624.25
	22.54	3843.63
	13.85	3585.88
	44.98	4245.12

To establish the relation of Vp and pressure for each facies, I calculated the $R_{p,F,T}^{eff}$ parameter in Equation 3.10. To do this, I defined the Top-of-reservoir layer as

the reference layer because, according to the flow simulation results, most of the pressure variation took place in it. I also determined the samples' facies by inspecting the facies log in well W25D (Figure 110). By analyzing the well 25D facies log, I identified that samples A1, B1, B1A, B5 were high energy grainstone samples, classified as facies 1, and sample E1 and D1 were bioturbated cemented grainstone, classified as facies 4. Based on these observations, I summarize the facies of the samples in Table 15.

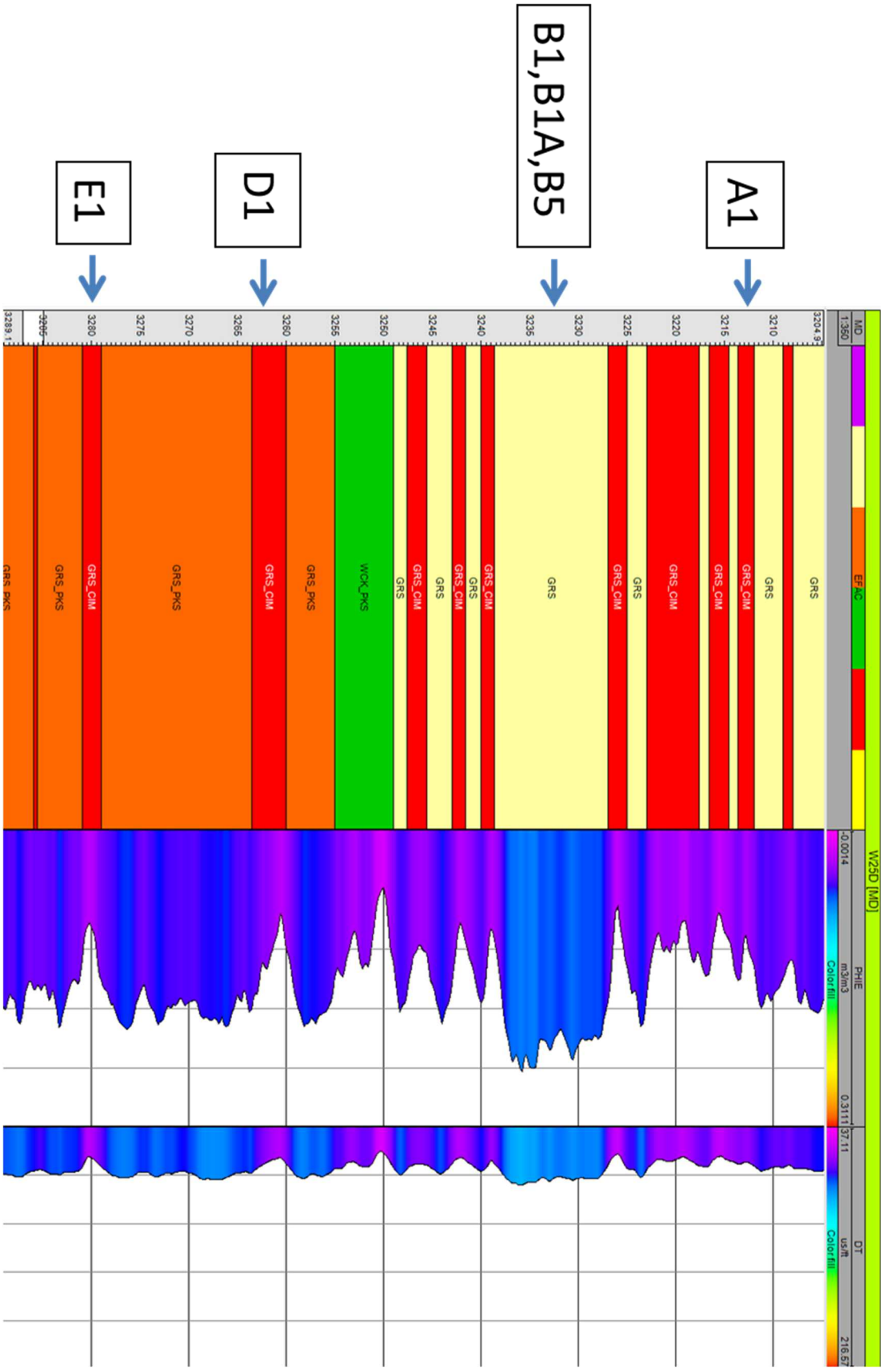

Figure 110 *Well 25 D Facies log with the sample positions.*

Table 15 *Facies of the samples.*

Sample 1	Facies 1
Sample B1	Facies 1
Sample B1A	Facies 1
Sample B5	Facies 1
Sample D1	Facies 4
Sample E1	Facies 4

To be more specific, I calculated $R_{p,F,T}^{eff}$, the compressional velocity's effective stress path coefficients (Gunning, 2013), for each pressure cycle using

$$R_{p,F,T}^{eff} = \frac{Vp_2 - Vp_1}{-(P_2 - P_{1)}}. \quad (5.3)$$

where Vp_1 is the acoustic velocity measured in the beginning of the cycle, Vp_2 is the acoustic velocity measured in the end of the cycle, P_1 is the pressure applied in the beginning of the cycle and P_2 is the pressure applied in the end of the cycle. The minus sign in the denominator is because equation 3.10 uses pore pressure instead of effective pressure. Table 16 shows the $R_{p,F,T}^{eff}$ calculated for each cycle in each sample and Figure 111 displays the evolution of the values graphically.

Table 16 $\boldsymbol{R_{p,F,T}^{eff}}$ *values for each sample for the three cycles.*

Cycle/sample	A1	B1	B1A	B5	D1	E1
First	-11.8	-20.3	-34.3	-35.5	-26.5	-40.9
Second	0	-12.9	-18.0	-27.9	-21.2	-25.2
Third	0.8	-11.1	-16.0	-18.5	-20.0	-21.1

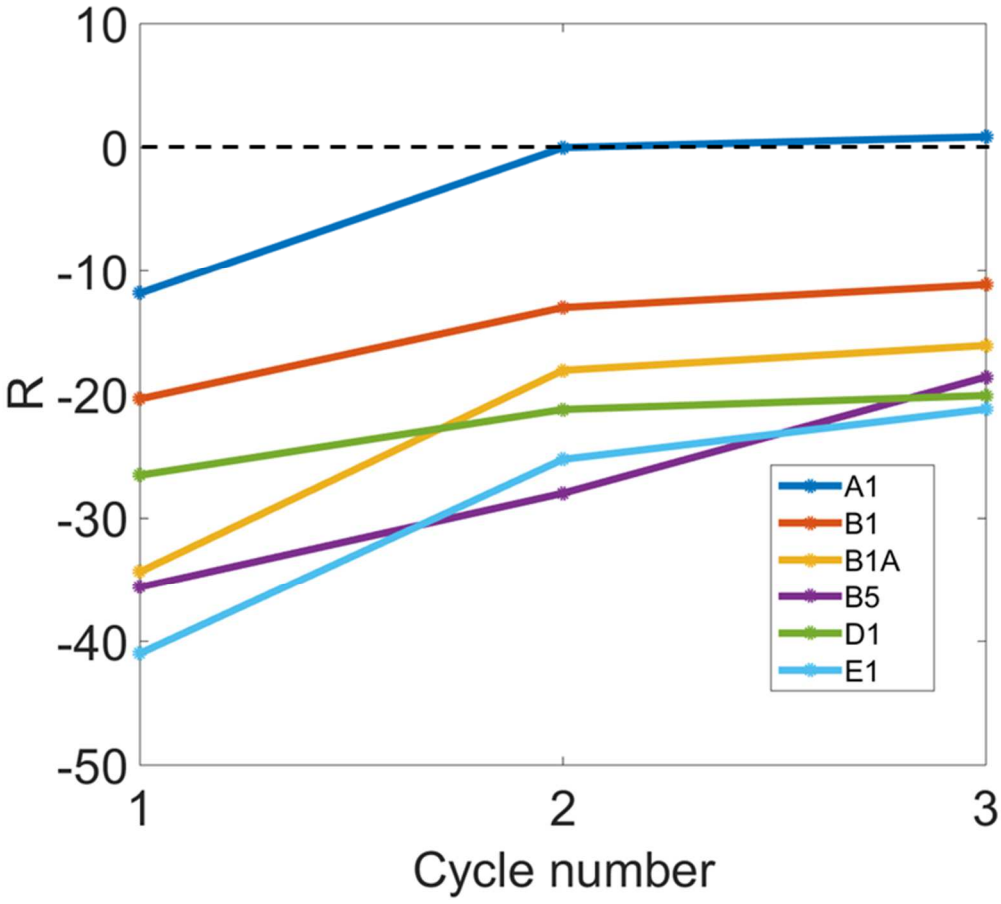

Figure 111 *Values of the effective stress path coefficients* $\boldsymbol{R_{p,F,T}^{eff}}$ *calculated for the each sample through 3 cycles.*

Analyzing Figure 111, one can see that the curves of $R_{p,F,T}^{eff}$ for the grainstone facies samples A1, B1 and B1A, are approximately parallel. The curve for B5, although also increasing monotonically, has a different shape. The positive value for the third cycle in sample A1 may indicate that the rock has been fractured or may reflect noise in the Vp measurements, although no indication of such noise was present in the dataset description. The curves of $R_{p,F,T}^{eff}$ for the cemented bioturbated grainstone (facies 4) samples D1 and E1 differ in shape, with D1 being almost constant. Nevertheless, their values converge in the third cycle. The reservoir samples show higher $R_{p,F,T}^{eff}$ values in the third cycle than the non-reservoir facies. One of the reasons for this behaviour is the presence of more equant pores in the oncolytic samples

supporting the structure of the rock and making the rock less sensitive to pressure than the non-reservoir rocks.

Before the first measurement cycle, the rock was stored at atmospheric pressure, which may have acted to open the crack-like pores and decrease the dry rock modulus of the sample. The difference in value between the first and second cycles, even though both cycles had the same amounts of pressure applied to the rock, may be due to crack-like pores that remained closed after the first cycle in a phenomenon called "seasoning". That phenomenon makes the dry rock modulus increase, the rock more resilient to pressure and closer to the dry rock modulus of the sample *in situ*. The samples were submitted to extreme pressures in the third cycle, which may have induced cracks - as exemplified by the failing of sample A1- and altered the resultant $R_{p,F,T}^{eff}$. For the reasons outlined above, I chose the average values of the second cycle of each facies to use in the inversion.

For the facies not sampled here (2 and 3) I based my assignments on the porosity and pore type of the facies, the two most important causes of variability in velocity variation in carbonate reservoirs (Fournier et al., 2011). In this way, I assigned facies 2 the same value as facies 1 because as reservoir facies, they both have relatively high porosities (as shown in Figure 112) and share the same type of porosity (intergrain). According to Table 4, the other type of porosity found in facies 2 was intragranular microporosity. This type of porosity is not affected by differences in pore pressure and, for this reason, will be disregarded. I assigned facies 3 with the same $R_{p,F,T}^{eff}$ value as facies 4 because they are non-reservoir facies and have the same type (microporosity) of relatively low porosities (Figure 112). Table 17 summarizes the final $\boldsymbol{R_{p,F,T}^{eff}}$ values for each facies.

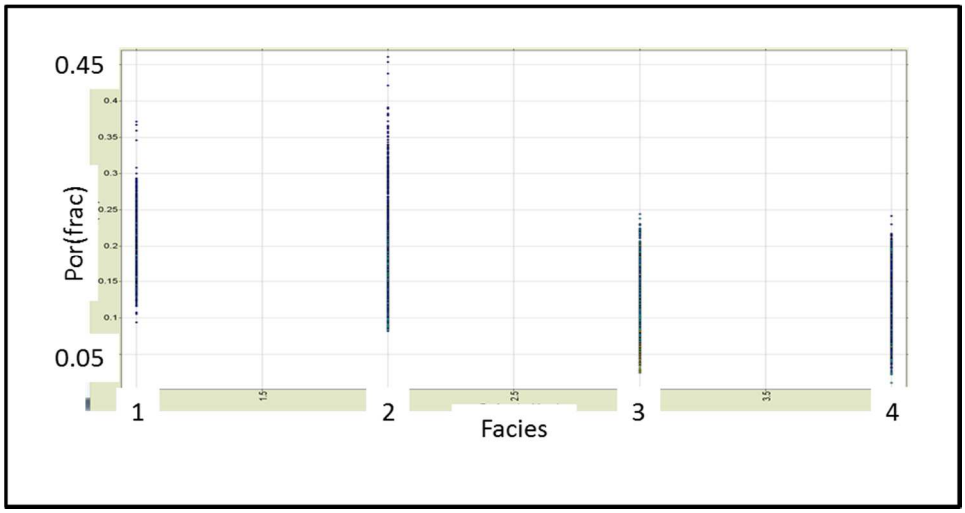

Figure 112 *Crossplot of porosity versus facies.*

Table 17 $\boldsymbol{R_{p,F,T}^{eff}}$ *coefficients for each facies.*

Facies	$R_{p,F,T}^{eff}$
Facies 1	-19.7
Facies 2	-19.7
Facies 3	-23.2
Facies 4	-23.2

*6.1.5.2 **Magnitude of pressure changes***

To attribute values for the mean and standard deviation for the pore pressure variations in all layers, I examined the 2002 and 2011 flow simulation pressure models. Through the subtraction of base model from the monitor model, I created a pore pressure difference model and used it to start the analysis. I also examined the pore pressure difference in the flow simulator grid (Figure 113) using the well markers created in the intersection of the seismic surfaces and wells. Doing this, I could identify that the pore pressure variation was more pronounced in the Top-of-reservoir layer.

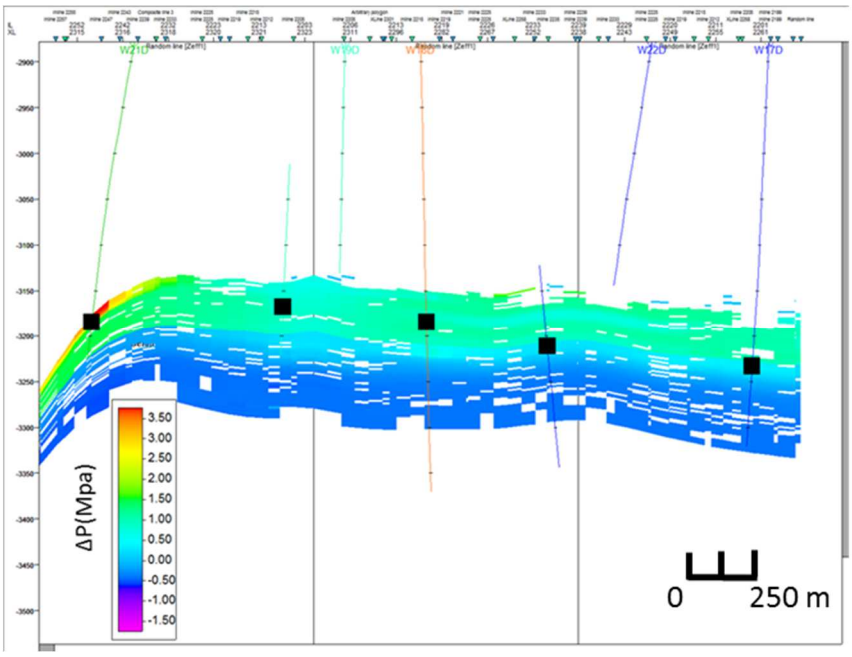

Figure 113 *Difference of pressure in MPa calculated using flow simulation showing larger changes in the top layers. The black squares are well markers accompanying Peak-1 horizon, the base of the Top-of-reservoir layer.*

While examining the distribution of the pore pressure differences inside the Top-of-reservoir layer (layer 13 in the flow simulation model shown in Figure 114), I could identify an area in the north of the field that presented strong negative values. By further investigation, it became apparent that no well crossed this area. This fact and personal communication with data providers stating that there was no negative delta pressure zone in the reservoir led to the decision to disregard the negative values in the area and plot only the positive ones (Figure 115). Finally, I fitted the histogram of the pore pressure difference with a Gaussian distribution (Figure 115) whose parameters are displayed in Table 18. These values were compared with the values gathered by Omofoma and Macbeth (2016) for sandstone reservoirs in the North Sea. It was observed that the magnitude of the pressure difference between vintages is much smaller than the ones reported in this paper. This indicates that the time-lapse effect of pressure difference is relatively mild.

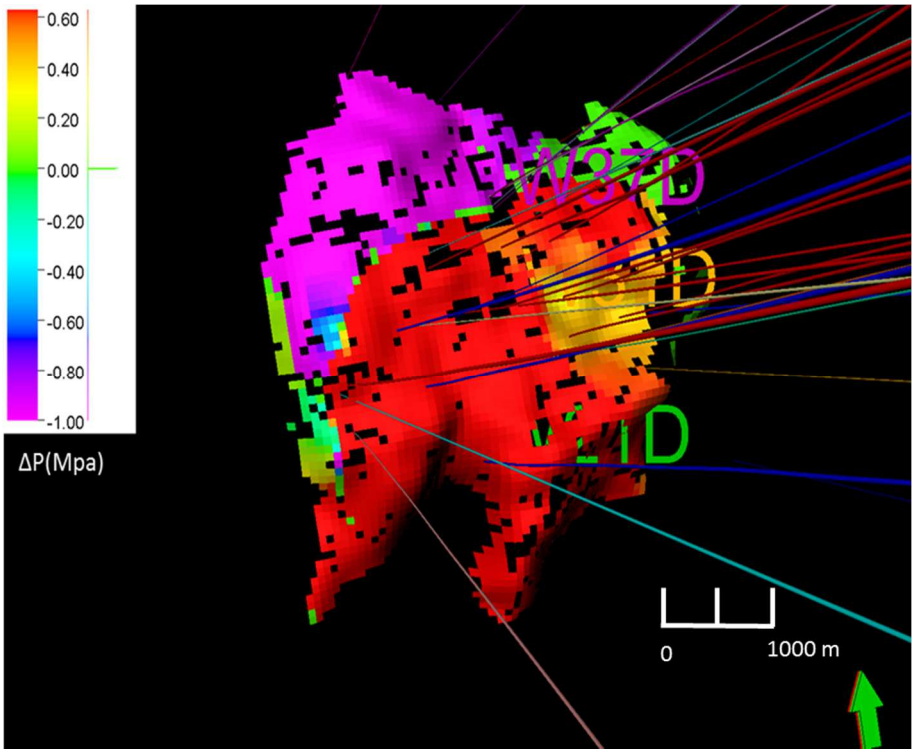

Figure 114 *Layer 13 of the pore pressure difference model. Difference was calculated as monitor pressure minus base pressure.*

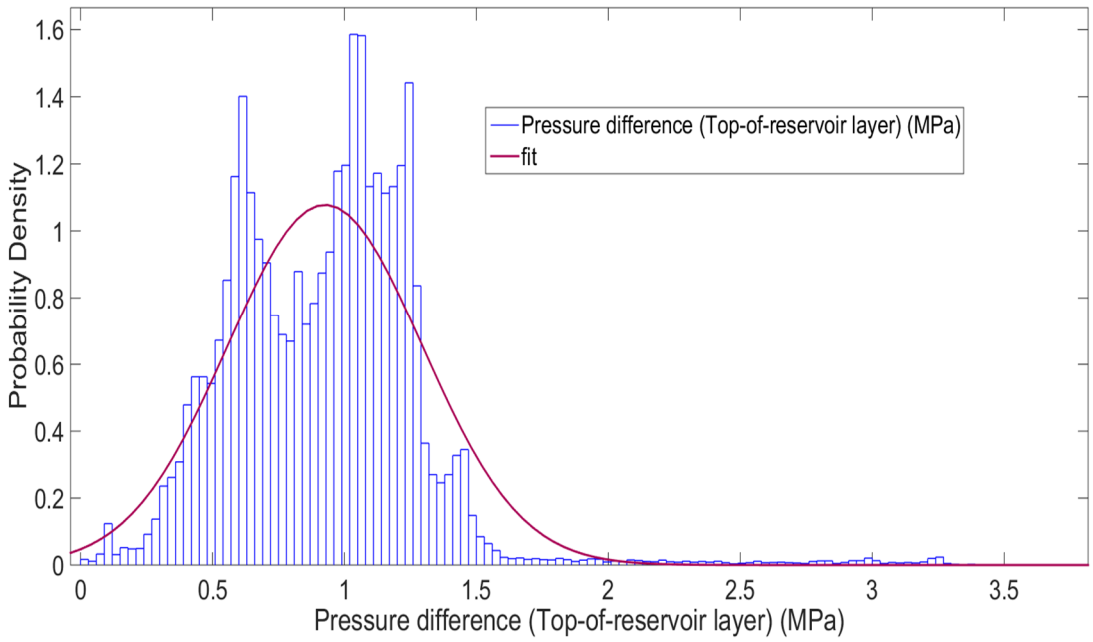

Figure 115 *Gaussian function used to fit distribution superimposed on the Pore pressure difference values histogram from the layers with an index higher than 30 of the flow simulation model that corresponds to the Top-of-reservoir layer in time.*

Table 18 *Mean and standard deviation of pore pressure difference histogram from the layers with an index higher than 30 of the flow simulation model that corresponds to the Top-of-reservoir layer in time.*

Layers	Pressure difference mean	Pressure standard deviation
Top-of-reservoir layer	0.926	0.370

The methodology only allows one reference layer for pressure. The other layers are affected by its pressure variation via a pressure correlation coefficient $U_{i,i_{reff}}$. In this context, I decided to prioritize the upper layer because it is where the majority of production took place. The Top-of-reservoir layer will have a $U_{i,i_{reff}}$=1 whereas the lower layers will have $U_{i,i_{reff}}$=0 (No pressure variation). To calculate the maximum velocity variation due to pressure effects allowed by the model, I employed the maximum variation of pressure and the biggest $R_{p,F,T}^{eff}$ coefficient.

$$3.3\ MPa \times\ -23.22\left(\frac{\frac{\mathrm{m}}{\mathrm{s}}}{\mathrm{MPa}}\right) \approx\ -\frac{76\mathrm{m}}{\mathrm{s}}.$$

This value is higher than the variation of 56 m/s in velocity determined in the detectable threshold of scenario 7's oil saturation (25% variation of oil saturation presenting amplitude variation above the 8% noise level), presented below. However, if I use the pressure difference mean in the calculation the variation will be

$$0.926\ MPa \times\ -23.22\left(\frac{\frac{\mathrm{m}}{\mathrm{s}}}{\mathrm{MPa}}\right) \approx\ -22.5\mathrm{m/s}$$

which lies below the threshold and, therefore, may not be detectable.

6.2 WAVELET ESTIMATION

To obtain the reflectivity of the subsurface from seismic trace, one needs to estimate the seismic source signature (wavelet). Wavelet estimation is a complex and important subject utilized in many areas of geophysics, such as seismic inversion, deconvolution and processing (Bo et al., 2013). To perform wavelet estimation, one can choose from two techniques: to use well logs and seismic data and perform a

deterministic wavelet estimation, or to use seismic data only and perform a statistical wavelet estimation. To implement deterministic wavelet estimation using well logs and seismic data one has to:

- define a time-depth relationship for the well by tying well and seismic data;

- delimit a time window around the reservoir to calculate the correlation between the real seismic trace and a synthetic trace derived from the well logs;

- multiply Vp and density logs to generate an impedance log;

- calculate a reflectivity series from the impedance log;

- compute a synthetic trace by the convolution of wavelet and reflectivity series and;

- maximize the correlation between the real seismic trace and the synthetic seismic trace, inside the specified time window, by changing the phase and amplitude spectrum of the wavelet;

At the end of this process, one will be able to determine the amplitude and phase spectrum of the wavelet that best explains the data. This technique relies on a precise well tie.

The statistical wavelet estimation assumes that the reflectivity is a random series. Thus, the autocorrelation of the seismic data is approximately equal to the autocorrelation of the wavelet: therefore, the amplitude spectrum of the wavelet is approximately the amplitude spectrum of the seismic data (Bo et al., 2013). In that case, the phase is assumed to be constant. Because of years of production between well logging and seismic acquisition, it is not possible to establish the dynamic properties of the reservoir at the time of drilling. Therefore, a direct comparison between forward-modelled synthetic seismic data from the well logs and seismic vintages is impractical at reservoir level. Even if all the wells were fluid-substituted using the saturations from the flow simulators, too much uncertainty would be created by the velocity model-building employed in the time-depth conversion. Additionally, flow simulation is just one of the possible realizations that are used to match the production history, and not a detailed model of fluid saturation and pressure. Alongside the problems created by the lack of knowledge of dynamic properties, the amplitude effects caused by the obstruction located right over the middle of the field brings more difficulties to the

determination of one wavelet for the entire field. Faced with these problems, I decided to calculate statistical wavelets outside the affected zone and calculate the inversions with these wavelets in this region, assuming that the phase of the seismic traces at reservoir level was zero.

6.2.1.1 Validation of statistical wavelet

Since I could not have a direct estimate of the seismic phase at the reservoir level, I decided to check the seismic phase immediately above the reservoir, where the dynamic properties had not changed with production. To do this, I estimated the wavelet and calculated the well-to-seismic-data correlation between 2140 and 2500 ms in well W7. This well is located on the right flank of the reservoir, outside the area affected by the platform obstruction (Figure 116). The reservoir starts at 2580 ms, and I did not expect a significant phase change in the interval between the reservoir and the time window where the wavelet was extracted because they were separated by few milliseconds.

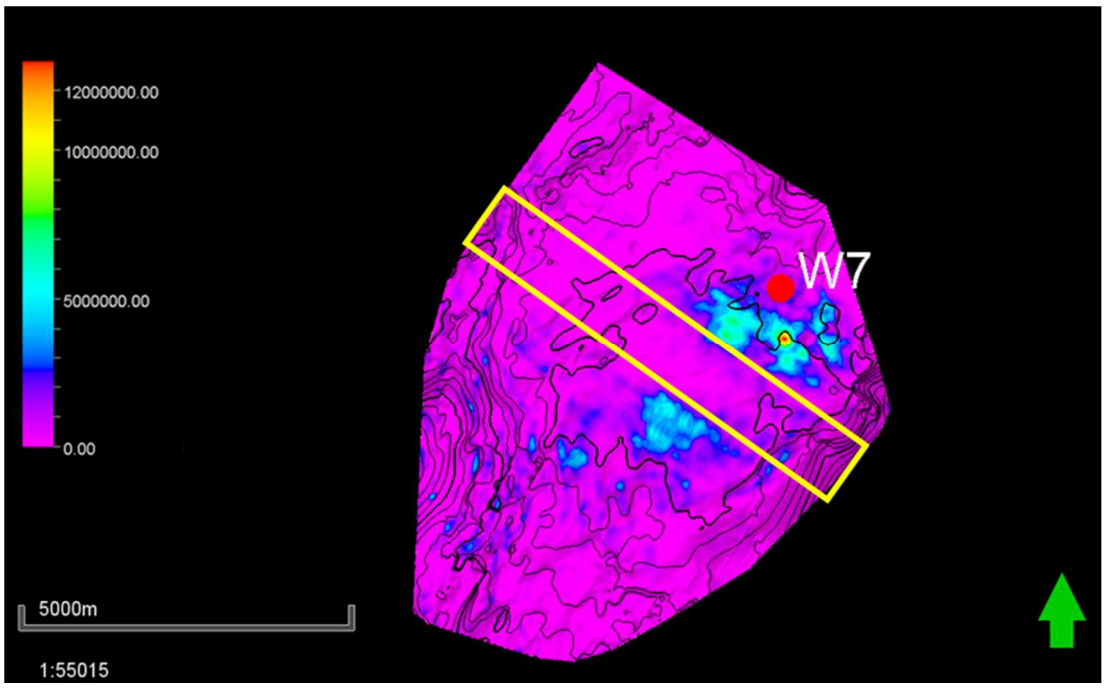

Figure 116 *Location of Well 7. The colours over the Top-of-reservoir surfaces represent the average energy of the Full stack base vintage calculated in a time window 10ms below the Top-of-reservoir surface. The yellow rectangle marks the zone where the seismic amplitudes were affected by platform obstruction.*

First, I calculated a statistical wavelet inside the time window specified earlier (Figure 117) and used it to tie the well W7 to the base vintage's full stack (Figure 118). The correlation coefficient was 0.86. According to Simm and Bacon (2014), a good well tie should have a correlation coefficient of at least 0.836: therefore, I could establish that the zero phase statistical wavelet could be used in the inversion of the base vintage. To determine the real phase of the base vintage's full stack, I extracted the wavelet using the well logs in W7 and the same time-depth law applied in the statistical wavelet well tie. The result is shown in Figure 119. The wavelet phase is around -10 degrees. The well tie performed with the wavelet extracted using well logs (Figure 120) had a correlation coefficient of 0.93 in the same time window used earlier (starting at 2140 ms and ending at 2500ms). Moreover, with the application of a -1 ms shift (which is less than one sample), it could achieve a correlation coefficient of 0.94. One could argue that this time-shift is created by the phase-shift, but the main message is that the base vintage phase is not very far from zero, which validates the use of statistical wavelets in the inversion. The same experiment was repeated for well W7 in the monitor vintage with similar results (correlation coefficient of 0.824 using statistical wavelet), validating the use of statistical wavelets in both vintages.

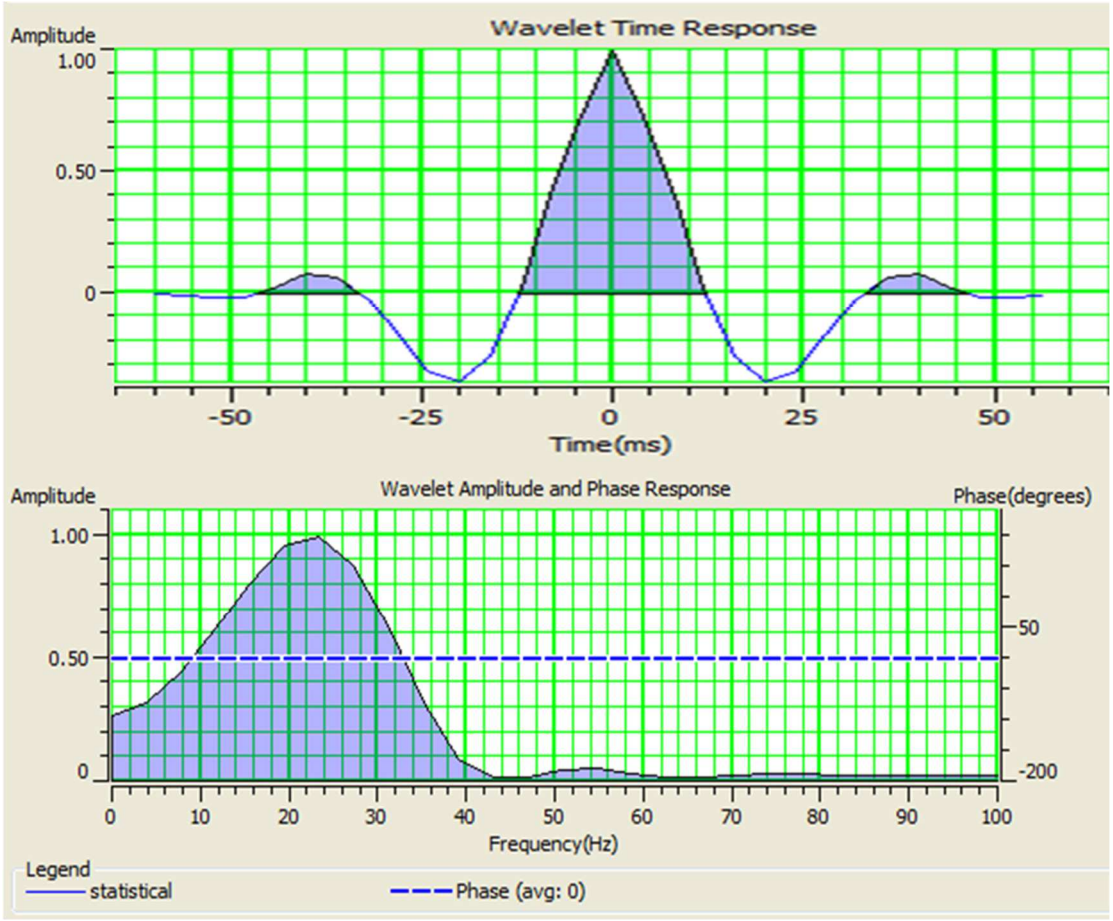

Figure 117 *Statistical wavelet calculated between 2140 and 2500 ms.*

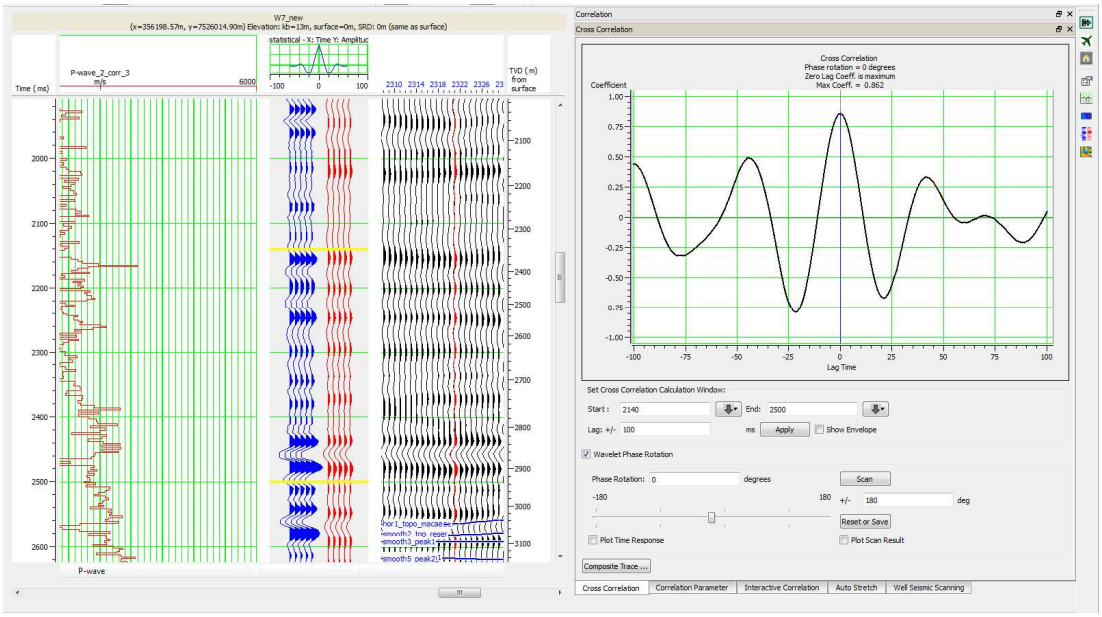

Figure 118 *Well tie using statistical wavelet. The correlation coefficient was 0.86.*

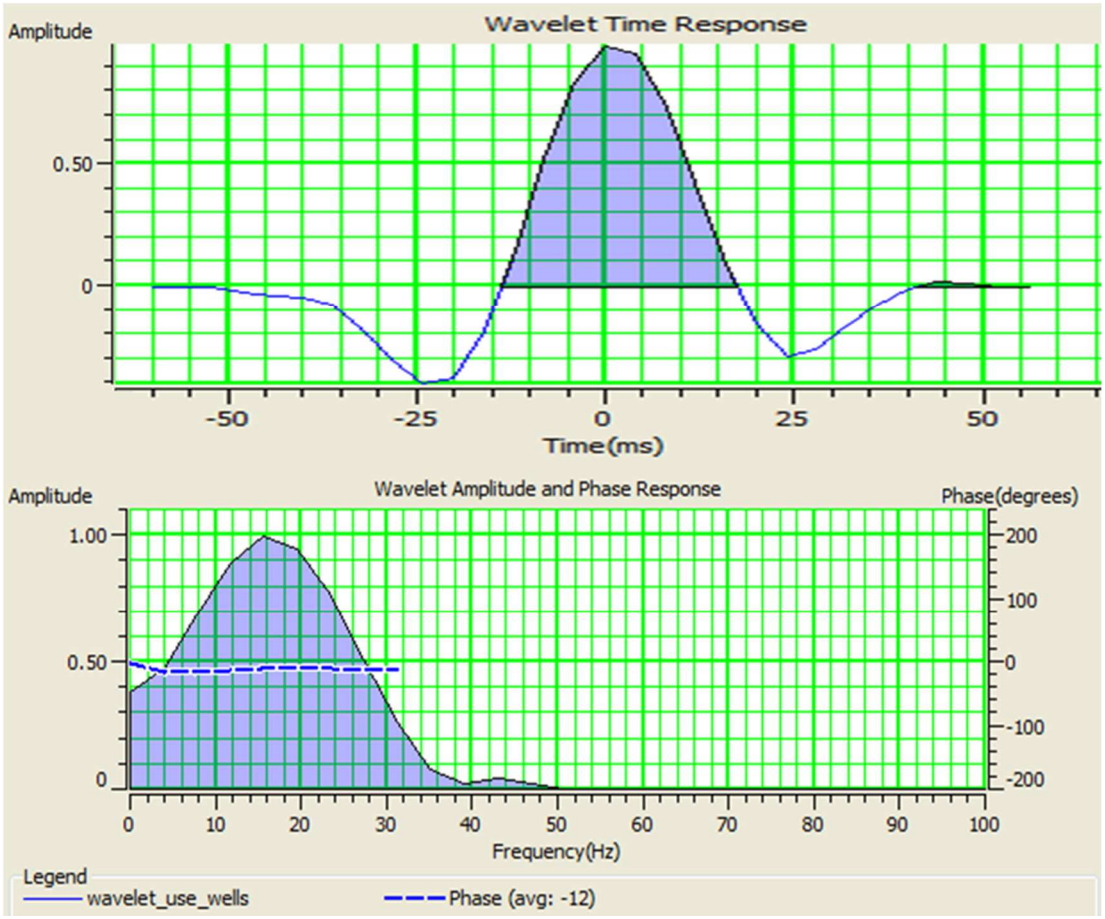

Figure 119 *Wavelet extracted using well logs from well W7.*

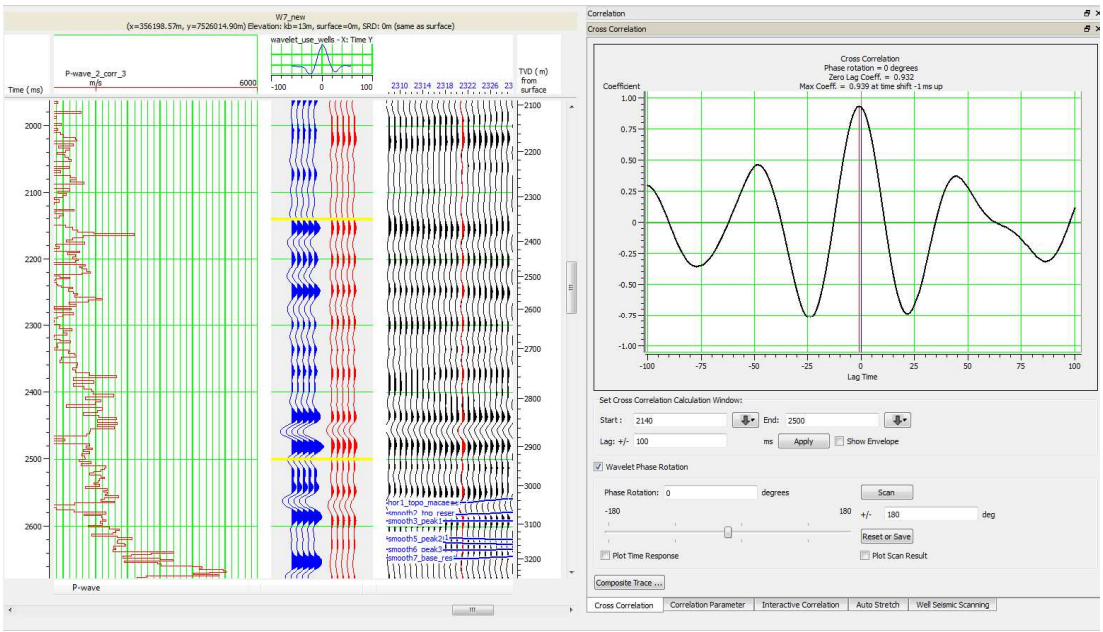

Figure 120 *Well tie using a wavelet extracted using well logs from well W7. The correlation coefficient is 0.93.*

6.2.1.2 ***Calculation of statistical wavelet inside reservoir***

At the reservoir level, I calculated average statistical wavelets outside the affected zone for both vintages. To calculate average wavelets I first computed statistical wavelets from 25 (5 x 5) seismic traces around each well located outside the affected zone and then averaged them. Figure 121 shows the average wavelets calculated for the base vintage outside the affected zone. The same calculation was carried out using the monitor vintage. No correlation was calculated between this well and the seismic data. This is because I could not generate synthetic seismic traces without knowing fluid saturation and pressure values at reservoir level in the region around well location at the time of seismic acquisition. These were the wavelets used in the inversion of the base and monitor vintages.

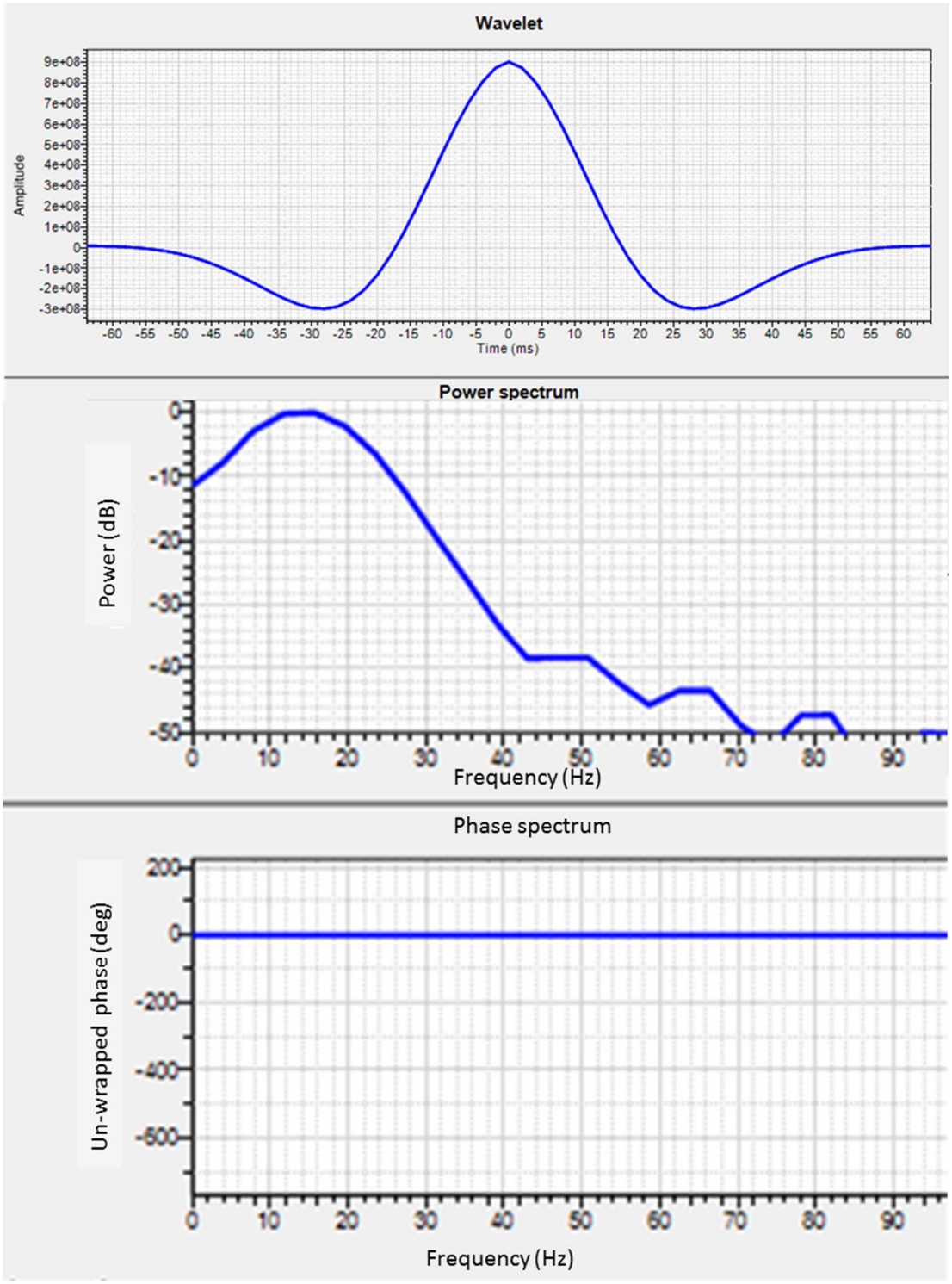

Figure 121 *Average wavelet calculated outside the obstructed zone in the base vintage.*

6.3 TIME-LAPSE FEASIBILITY STUDY

With the purpose of facilitating the interpretation of the results and assessing the limits of resolution and detectability of the inversion, I carried out a feasibility study. The first step was to quantify the resolution of the seismic data. To do so, I estimated the peak frequency in a cropped seismic volume enclosing the reservoir and excluding the zone affected by the obstruction in the sea surface. By the analysis of the amplitude spectrum in Figure 122 I could establish the peak frequency as (approximately) 15 Hz. For the peak frequency of 15 Hz, I assumed a velocity of 4200 m/s, found in well W26 around the top of the reservoir, and used Widess' criterion (Widess, 1973) to calculate the minimum resolvable thickness,

$$t_{min} = \frac{\lambda}{8} = \frac{v}{8f_p} = \frac{4200m/s}{8*15Hz} = 35\ m,$$

where λ is the wavelength, v is the velocity of the layer and f_p is the peak frequency. The second step consisted of quantifying the signal-to-noise ratio (SNR) of the data. I estimated the SNR using Liu, Liu and Wang's (2008) stack method in a window of 100 ms and 25 traces at reservoir level. The decibel SNR was 11.3, which amounts to approximately 8% of noise. To quantify that the seismic signals present in the vintage's difference were due to changes in dynamic properties of the reservoir, and to assist the interpretation of the time-lapse anomalies, I modelled the seismic amplitude variations. In this study, I chose the most probable scenarios of fluid saturation and pressure to evaluate the magnitude of the time-lapse seismic signal. To select scenarios for fluid substitution, I created fluid saturation histograms using data from flow simulation models of the years 2002 and 2011. The example for 2011's oil saturation is shown in Figure 123 . After that, I divided the number of counts by the total count of samples to calculate the probability of each saturation interval. Again, I show the example for 2011's oil saturation in Figure 124. Finally, I calculated the 2002 and 2011 fluid saturation joint probability. In this way, I could define joint probabilities for each pair of oil and gas saturation values, respectively,

$$P(S_{oil\ 2002}, S_{oil\ 2011}) = P(S_{oil\ 2002}) * P(S_{oil\ 2011}) \quad (5.1)$$

and

$$P(S_{gas\ 2002}, S_{gas\ 2011}) = P(S_{gas\ 2002}) * P(S_{gas\ 2011}). \quad (5.2)$$

Figure 125 shows the resultant joint probability for oil saturation using an increment of 2.5%, indicated by the distance between black lines.

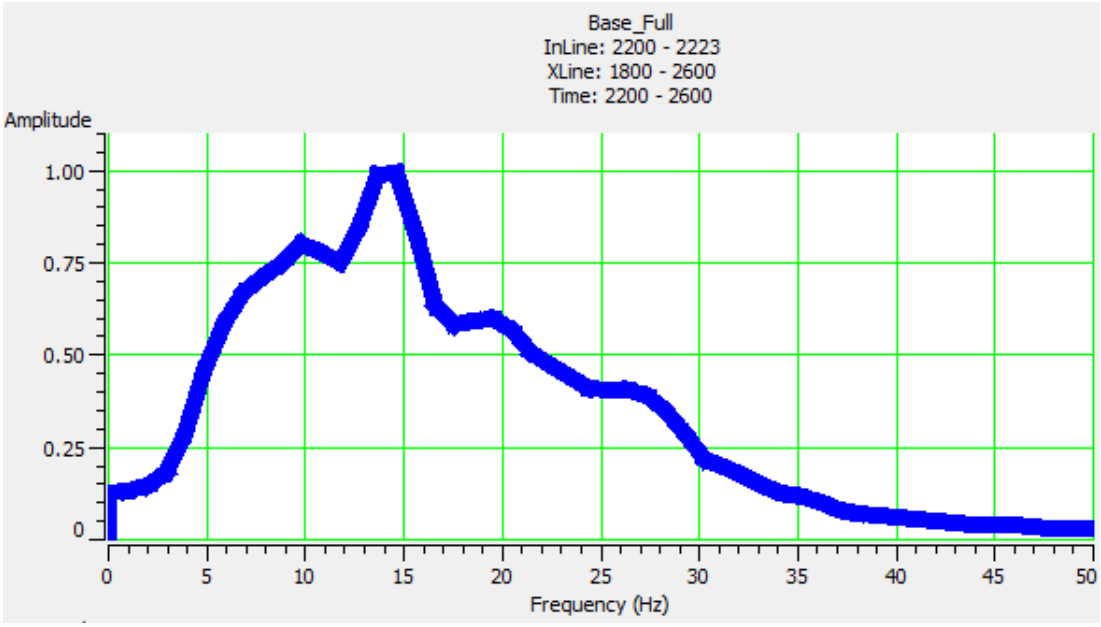

Figure 122 *Seismic spectrum of the base full stack between inlines 2200 and 2223, crosslines 1800 and 2600 and time interval 2200 to 2600 ms. The peak frequency is around 15 Hz.*

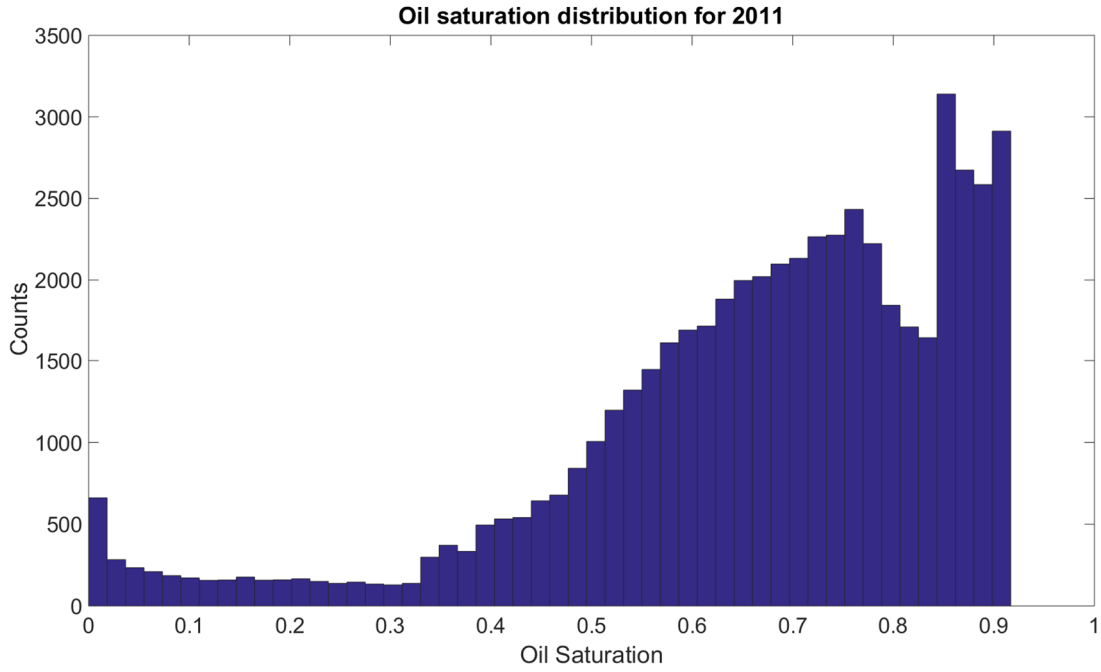

Figure 123 *Oil saturation distribution for 2011.*

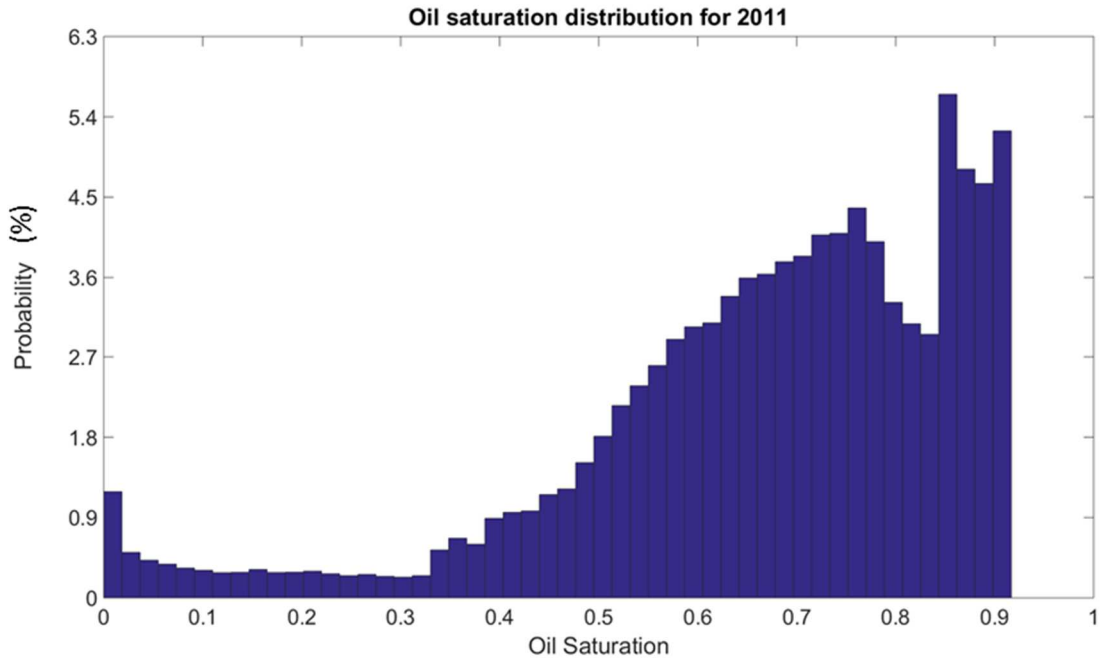

Figure 124 *Probability of oil saturation for 2011.*

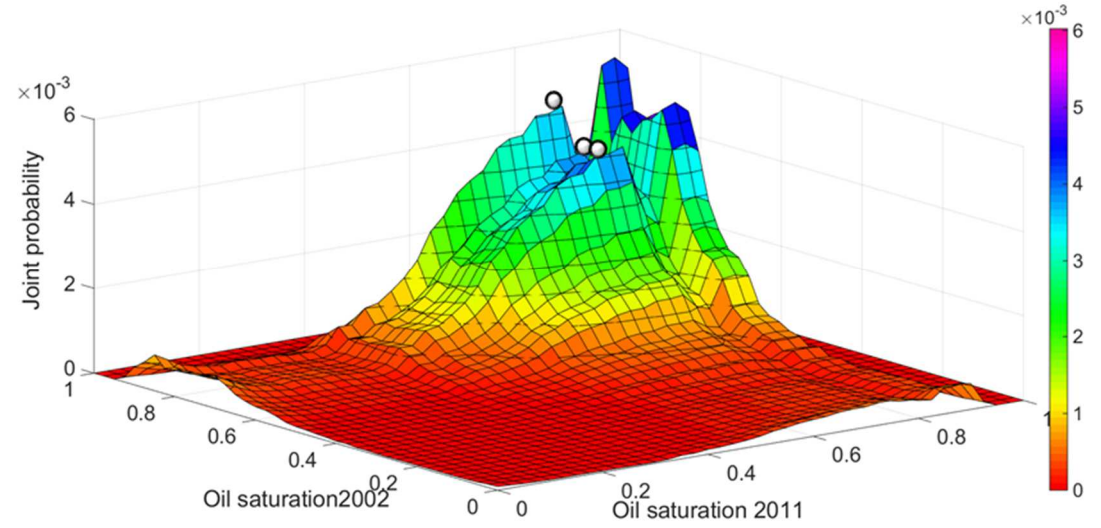

Figure 125 *Joint probability of oil saturation values for 2002 and 2011.White spheres represent the analysed combination of saturations.*

Figure 126 shows a view from the top of Figure 125. Since only oil production took place, it was expected that the oil saturation had decreased between 2002 and 2011. To guarantee this premise, the three white points in Figure 126 were located on the right of an imaginary curve that crosses the plot connecting equal oil saturation values, called here the isosaturation curve. Additional reasons to select the points were their enclosure by topographic contours in the graph, which guarantees that they

represent different ensembles of pairs of values, and high values of joint probability. I used the same strategy with respect to gas saturation. In this case, I identified only one peak (Figure 127). This peak was located over the isosaturation curve denoting that the difference in gas saturation was smaller than the gas saturation increment (2.5%). As a result, during the fluid substitution, gas saturation was considered the same for the two vintages. In addition to these scenarios, I created scenarios assuming pressure variation. For these operations, I chose to use the mean of pressure difference in the flow simulator as explained in the Pressure section above. Table 19 summarizes the selected scenarios for fluid substitution and Figure 128, Figure 129 and Figure 130 graphically display the variation of dynamic properties inside the reservoir for each scenario. The fluid substitution scheme employed the same parameters used to create the fluid-substituted 100% brine logs for trend calculation.

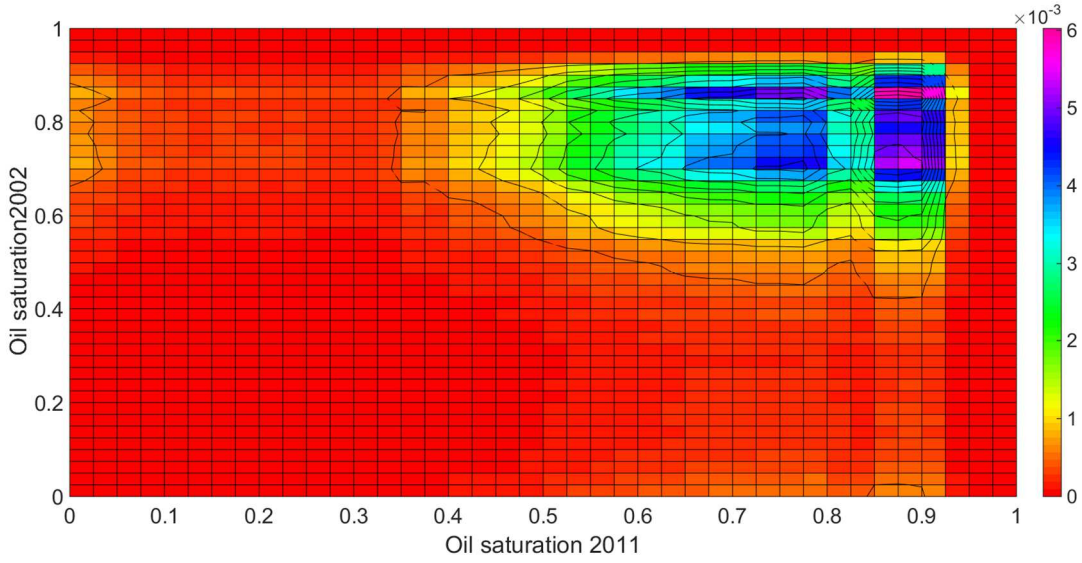

Figure 126 *View from the top of Joint probability plot for oil saturation. White circles represent the analysed combination of saturations.*

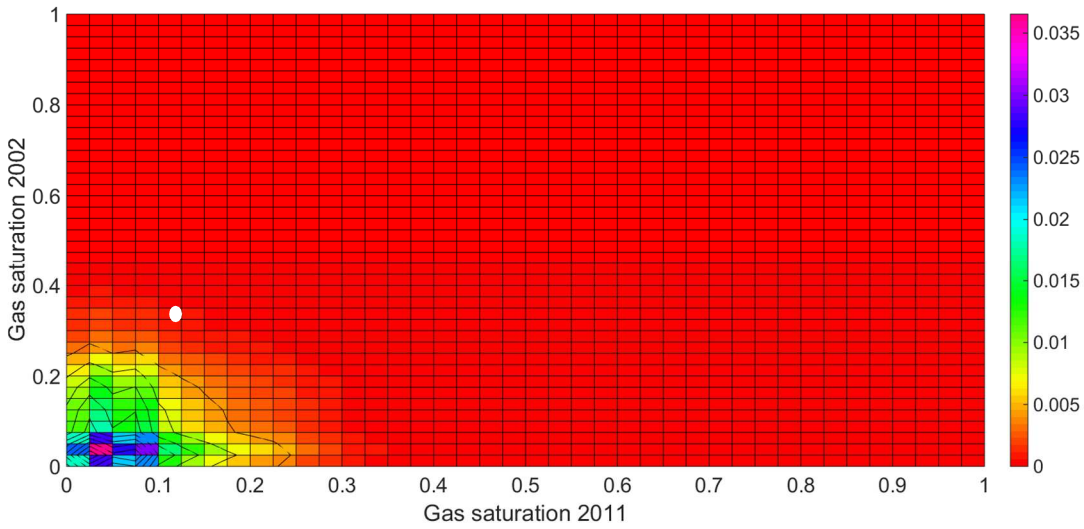

Figure 127 *View from the top of Joint probability plot for gas saturation.*

Table 19 *Selected scenarios for fluid substitution.*

Scenarios	Oil saturation 2002	Oil saturation 2011	Effective Pressure difference (MPa)	Gas saturation 2002	Gas saturation 2011
1	75%	72.5%	0	3.7%	3.7%
2	80%	75%	0	3.7%	3.7%
3	85%	75%	0	3.7%	3.7%
4	75%	72.5%	-0.92	3.7%	3.7%
5	80%	75%	-0.92	3.7%	3.7%
6	85%	75%	-0.92	3.7%	3.7%

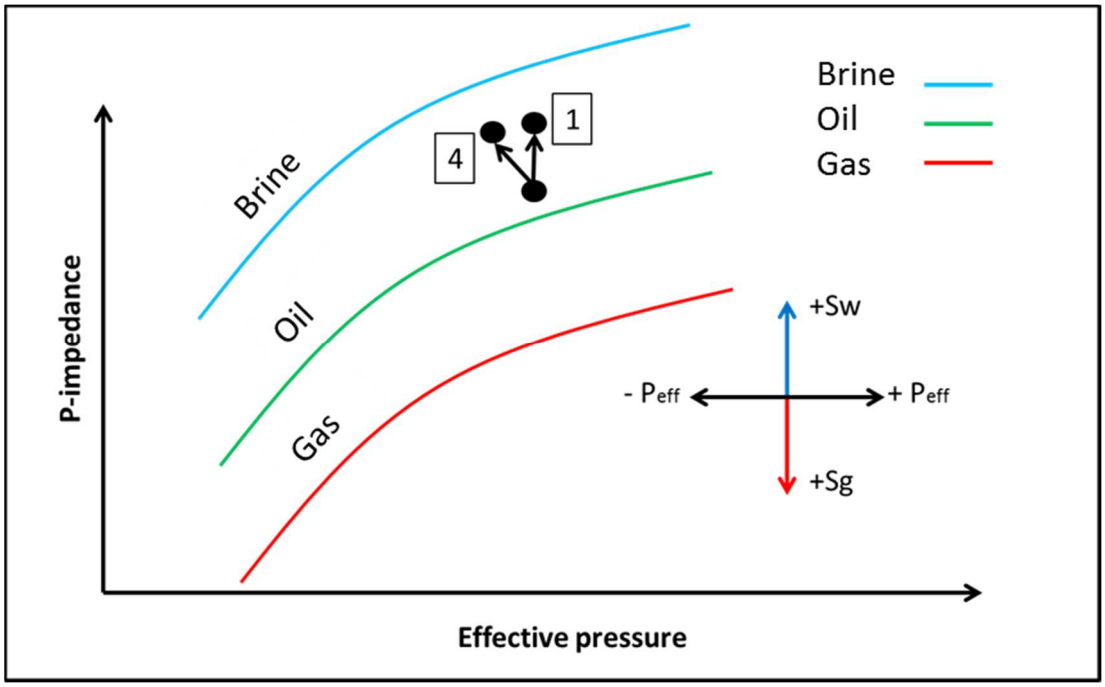

Figure 128 *Graphic representation of the variation of dynamic properties in scenarios 1 and 4.*

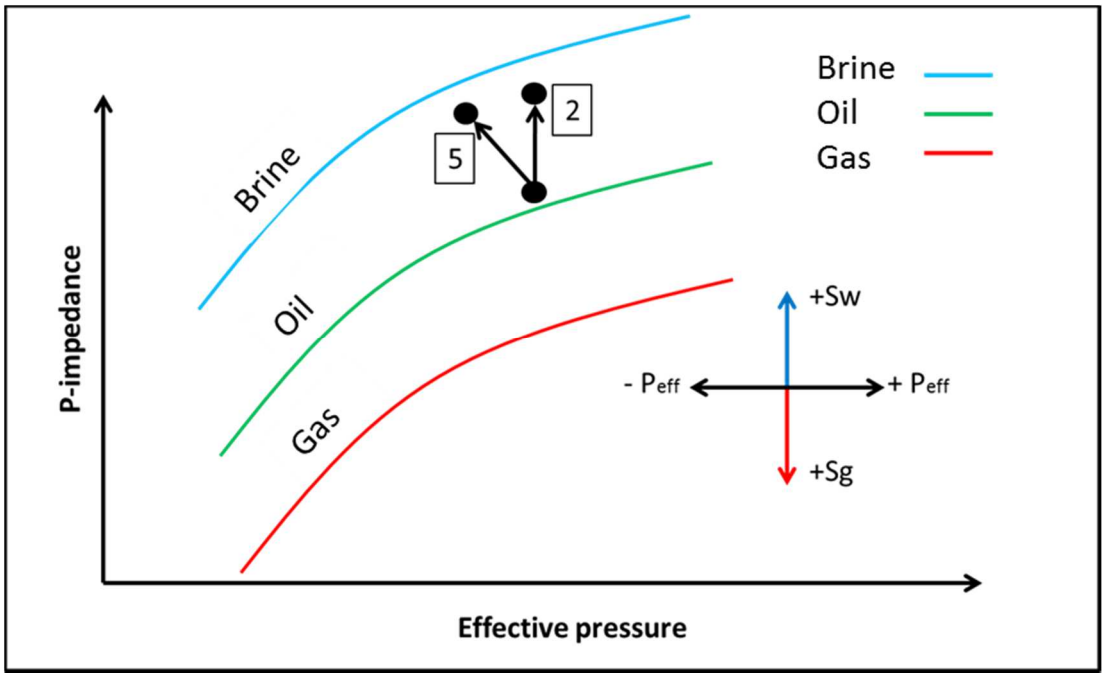

Figure 129 *Graphic representation of the variation of dynamic properties in scenarios 2 and 5.*

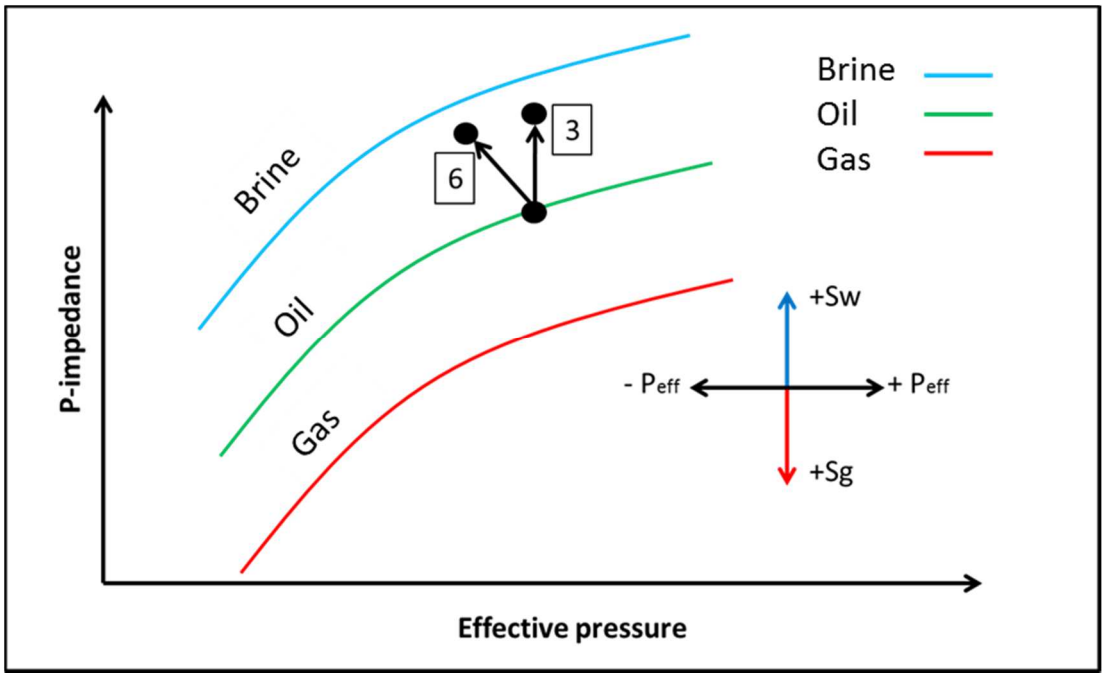

Figure 130 *Graphic representation of the variation of dynamic properties in scenarios 3 and 6.*

Figure 131 displays the results of fluid substitution (A, B, C and E) alongside a synthetic trace created using the original logs from well W35D (D). This well is located in the centre of the field and is representative of the overall geology of field X. In Figure 131, the letter A indicates the 80% oil saturation state used as the base vintage of scenario 2. The letter B indicates the 85% oil saturation state used as the base vintage of scenario 3. The letter C indicates the 72.5% oil saturation state used as the monitor vintage of scenario 1. Finally, the letter E indicates the 75% oil saturation state used as the base vintage of scenario 1 and monitor vintage of scenarios 2 and 3. Figure 132 shows the porosity log and the oil saturation extracted from the flow simulation models from years 2002 and 2011 along the well W35D track. The values presented here are in the same range as the ones modelled above, suggesting that the scenarios are valid.

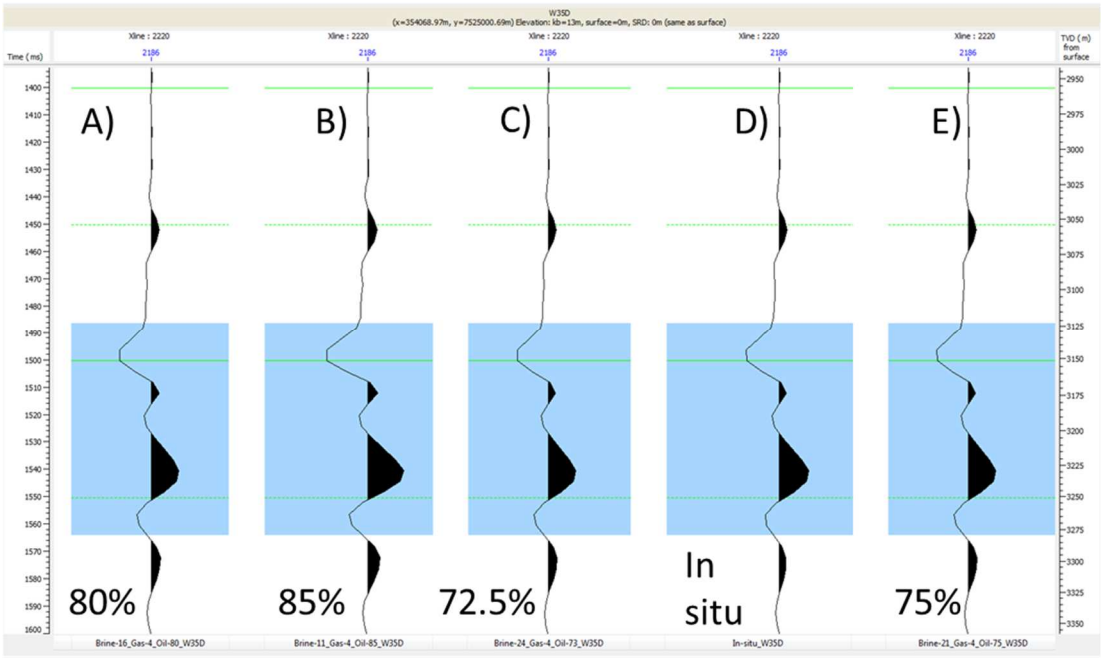

Figure 131 *Synthetic traces resulting from fluid substitution disregarding pressure effects. The oil saturation used in the generation of each trace is indicated at the bottom portion of the figure.*

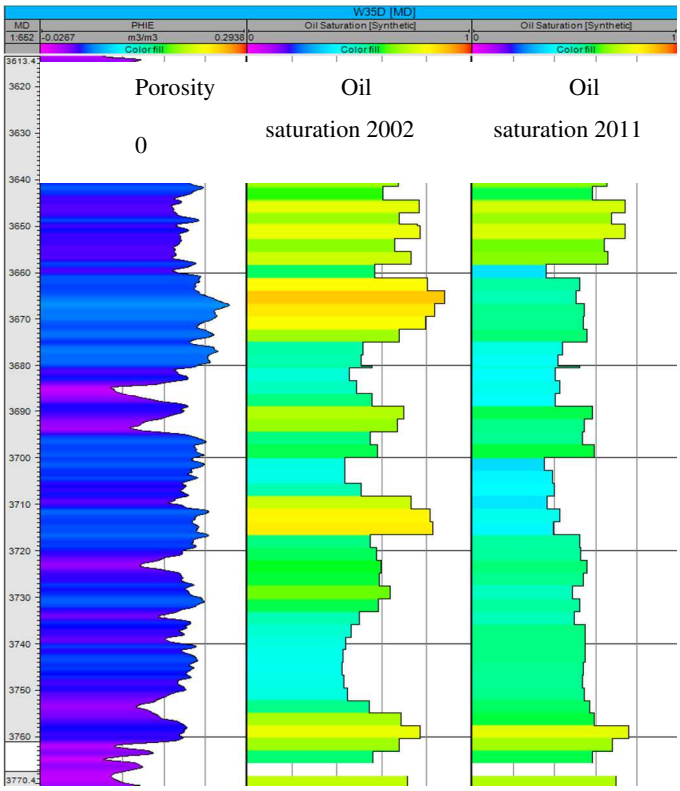

Figure 132 *Porosity and oil saturation logs extracted from the fluid simulation model. According to the flow simulation model, between 3150m and 3160m the oil saturation varies from 80% to 50%.*

Figure 133,Figure 134 and Figure 135 display the modelled difference trace superimposed on the synthetic base vintage trace of each scenario. The top of the reservoir is indicated by a green line. The third scenario presents a distinct difference signature below the top of the reservoir. A more subtle difference in amplitude can be seen in the second scenario, and almost no difference is visible in the first one. Obviously, the difference in oil saturation between vintages is proportional to the difference in magnitude in the time-lapse response between the scenarios. To quantify the time-lapse responses I divided the difference trace magnitude by the base trace magnitude at the point where it peaks (around 1540 ms in Figure 133). The maximum percentage difference was found in the third scenario and corresponds to 2.6% of the base amplitude (Table 20). Given that the average NRMS was 0.38 and the noise level 8%, the detectability of the time-lapse for as much as 10% oil saturation was a challenge.

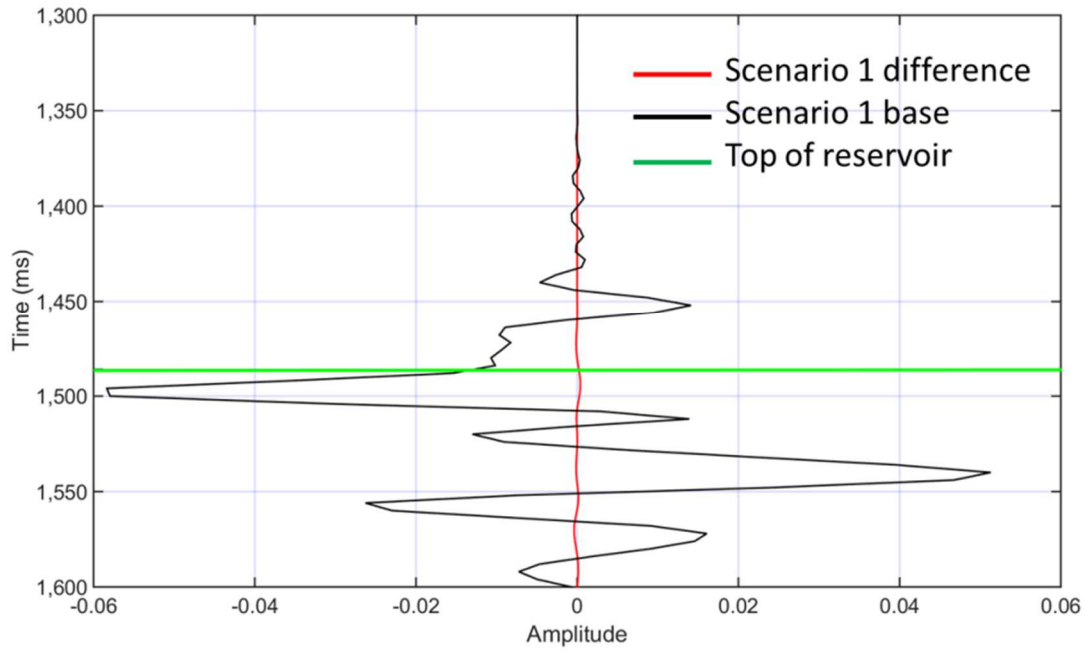

Figure 133 *Difference trace superimposed over base trace for scenario 1. Green line corresponds to the top of the reservoir.*

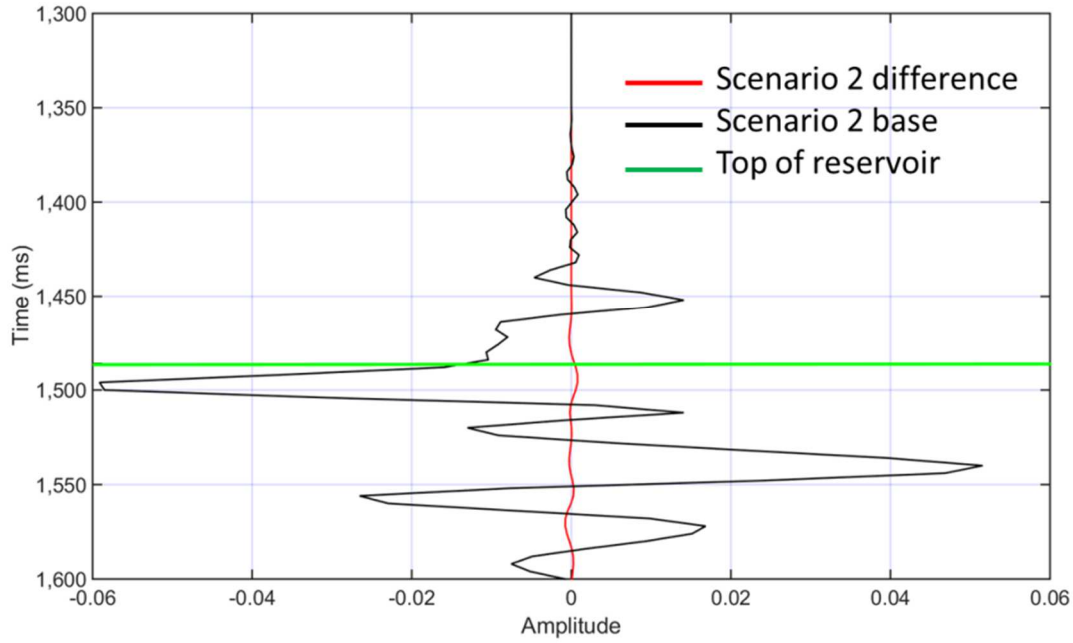

Figure 134 *Difference trace superimposed over base trace for scenario 2. Green line corresponds to the top of the reservoir.*

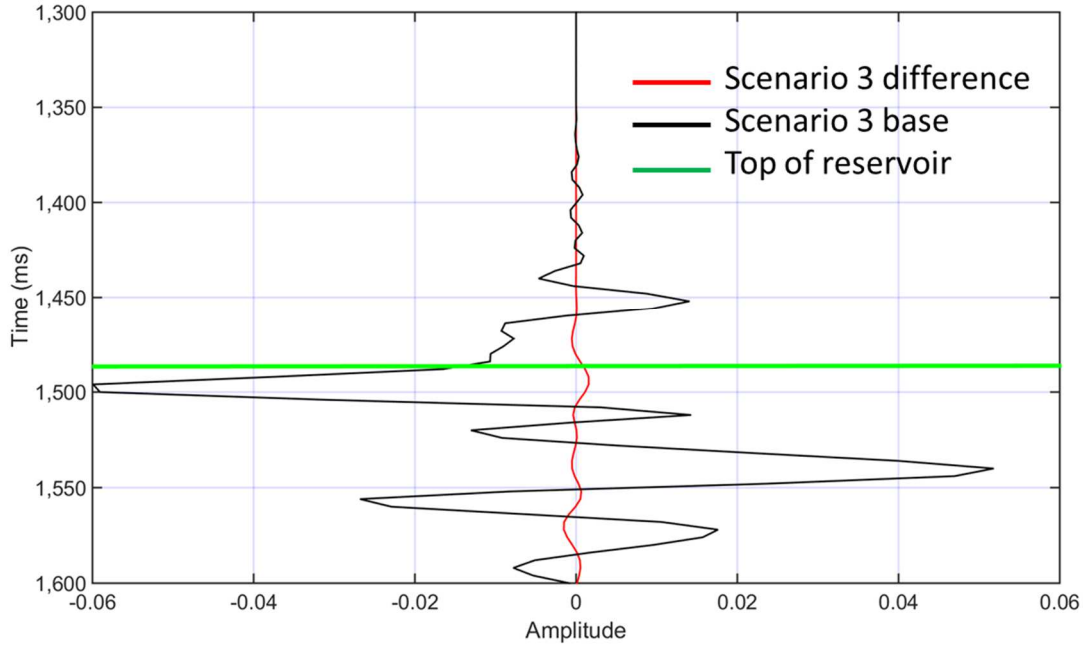

Figure 135 *Difference trace superimposed over base trace for scenario 3. Green line corresponds to the top of the reservoir.*

Table 20 Results for scenarios 1, 2 and 3

Scenario	Maximum difference at top	Amplitude at top of reservoir	Relative variation
1	0.00039	-0.0583	0.66%
2	0.00078	-0.0591	1.3%
3	0.00156	-0.0599	2.6%

The original effective pressure in the reservoir was 36 MPa. In 2002, the mean of the pore pressure in the reservoir was 13 MPa. Since the confining pressure is assumed constant (68.8 MPa), the mean effective pressure will be 55.8 MPa (approximately). According to Figure 109, the compressional velocity versus effective pressure curve will be in the flat regime for values larger than 25 MPa, so it is expected that the velocity changes with pressure will be subtle. Since only a decrease in effective pressure - due to increasing in pore pressure between 2002 and 2011 - is expected to occur, this small effect will oppose the effect created by fluid substitution. As a result, the time-lapse response for scenarios 4, 5 and 6 will be even lower than those found in scenarios 1, 2 and 3 and, for this reason, will not be modelled here. In order to determine the minimum oil saturation change required by the change in time-lapse amplitude, I generated another scenario with the properties shown in Table 21. This scenario comprises a variation of 35% in the oil saturation, and no variation in gas saturation or effective pressure. Figure 136 shows the difference trace superimposed over the base trace and Table 22 displays the relative amplitude variation. The relative amplitude variation for scenario 7 was 9.1%, a value that could be linked to a variation in oil saturation with relatively high confidence, because its value surpasses the noise level of the data. Figure 137 displays the Vp logs calculated for scenario 7's base and monitor rock's fluid saturation. The maximum velocity variation was 56 m/s. In

summary, the feasibility study shows that, to be detectable, the variation of oil saturation should be at least as big as 25%.

Table 21 *Scenario 7 properties.*

Scenario	Oil saturation 2002	Oil saturation 2011	Effective Pressure difference (MPa)	Gas saturation 2002	Gas saturation 2011
7	85%	50%	0	3.75%	3.75%

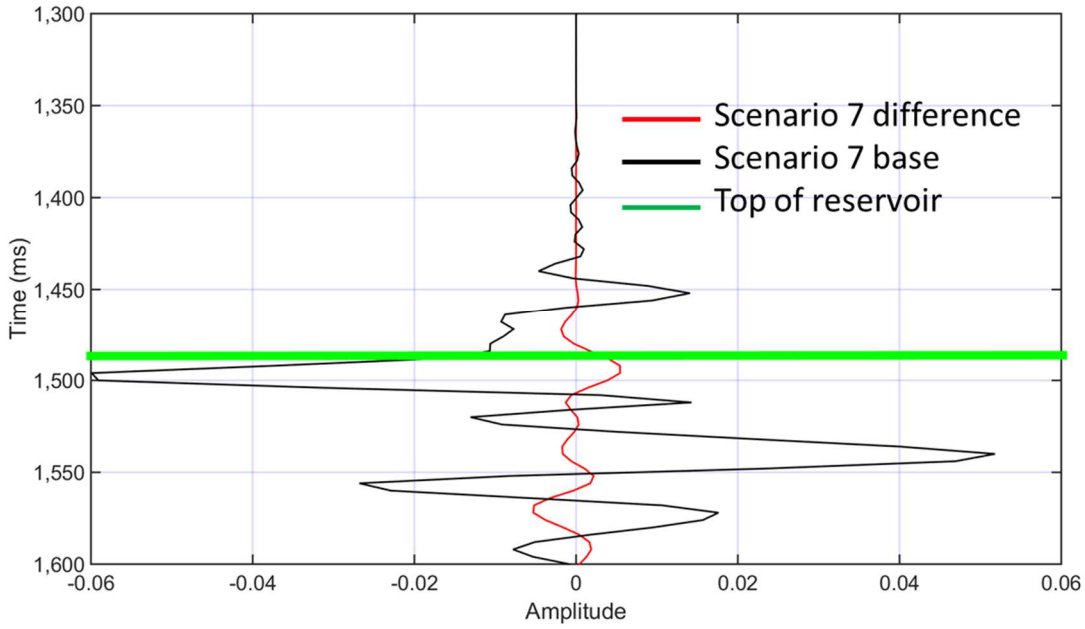

Figure 136 *Difference trace superimposed over base trace for scenario 7. Green line corresponds to the top of the reservoir.*

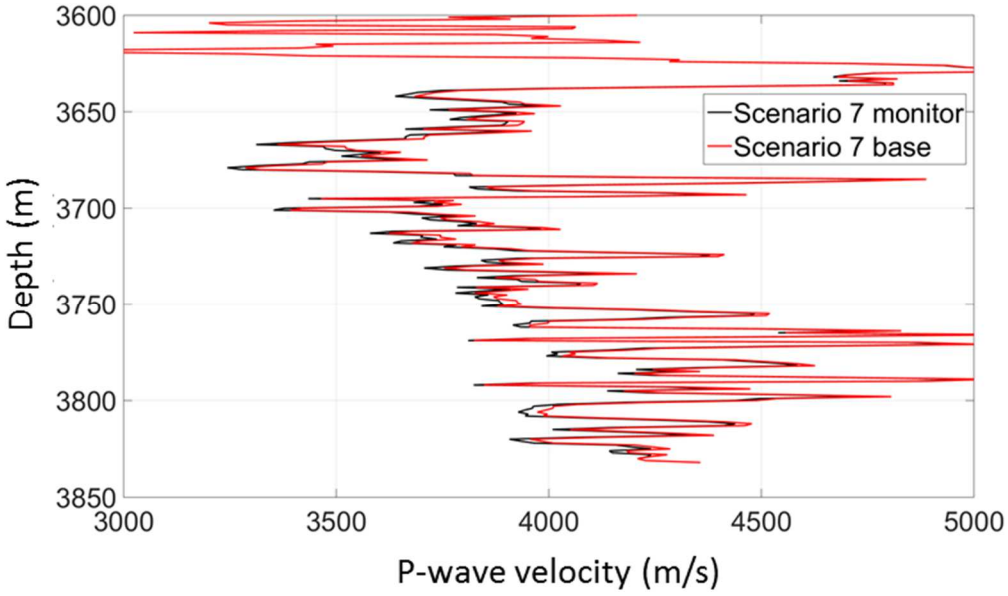

Figure 137 *P-wave velocities calculated for scenario 7's base and monitor rock's fluid saturation.*

Table 22 *Scenario 7 results.*

Scenario	Maximum difference at top	Amplitude at top of reservoir	Relative variation
7	0.0054	-0.0599	9.1%

6.4 RESULTS

The inversion results can be divided into maximum *a posteriori* (MAP) results and stochastic results. In the present methodology, I generated the MAP results to evaluate the quality of the outcomes, to guarantee that the results were accurate and to initiate the interpretation. Stochastic results take the interpretation beyond the usual results brought by the deterministic inversion. They inform the geoscientist about the uncertainties associated with their reservoir parameters, making it possible to generate more realistic production scenarios. This scenarios honour not only the time-lapse seismic data but all the data acquired before the vintage acquisitions. After inversion, I performed quality control procedures on the results. I calculated synthetic traces using the inversion-generated reflectivities and compared these with the real trace

(Figure 138). Inside the reservoir, the match was not perfect but I regarded it as acceptable given the processing effects and noise not modelled in the convolution-based synthetic trace. The correlation coefficient for the base's real and synthetic trace was 0.78 and for the monitor's real and synthetic traces was 0.82 in the time window starting at 2.4 seconds and ending at 2.7 seconds. I used the feasibility study results in the interpretation of the data, and only examined anomalies in which the magnitude of ΔS_{oil} was higher than 25%.

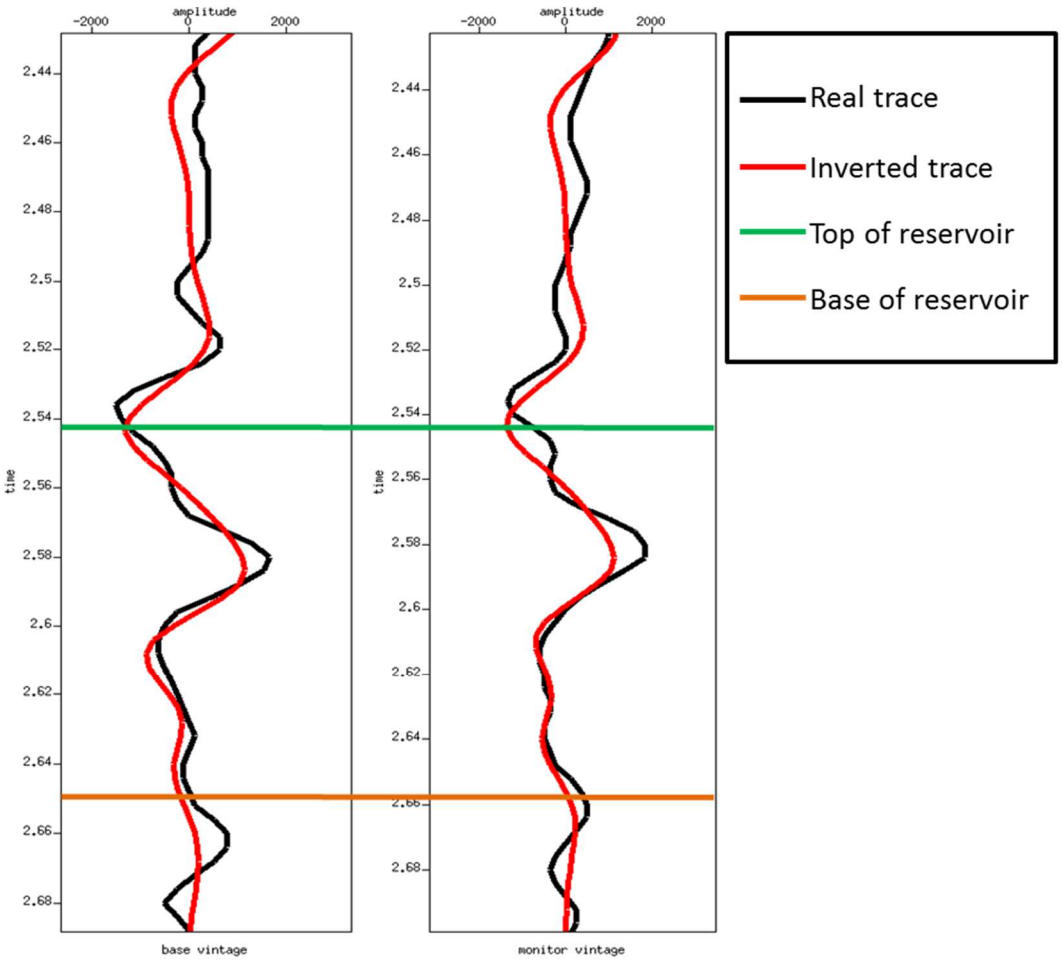

Figure 138 *Comparison of synthetic and real trace located in the vicinity of well W22 (inline 2231 and cross line 2250).*

6.4.1 The MAP results

The interpreter can analyse inversion results from several different perspectives. P-impedance difference and elastic moduli difference are examples of domains that

are used to evaluate the time-lapse effects in the reservoir. In this work, I decided to repeat the strategy employed in the synthetic data case and analysed the anomalies using fluid saturation. Moreover, for this particular case, I utilized pressure differences as well. The first reason to choose fluid saturation and pressure difference are the immediate connexion with oil and gas production effects in this reservoir. Another reason was the preservation of the methodological consistency throughout the presented inversion examples (synthetic and real). Finally and more importantly, the reason for choosing fluid saturation and pressure was the possibility of comparing the inversion results with flow simulator models. In addition, I used porosity and NG volumes to assist in the interpretation and quality control of the inversion results.

To visuaIize the attributes while retaining a stratigraphic perspective I extracted the median of the attributes inside a layer and placed them on the horizon that capped the layer. To illustrate this point, Figure 139 displays the difference in oil saturation (ΔS_{oil}) from the inversion results extracted in the Top-of-reservoir layer and plotted over the Top-of-reservoir surface. Because the centre of the field presented seismic holes, I only examined the left flank of the field, where three injector wells in blue (W23, W22 and W21) and a producer well in red (W26) are located. To facilitate the comparison between my results and the ΔS_{oil} from the fluid simulation model (Figure 141), I analysed two anomaly clusters indicated in Figure 140. While Area 1 encompasses injector wells W23 and W22 and producer well W26, Area 2 comprises the region around injector well W21.

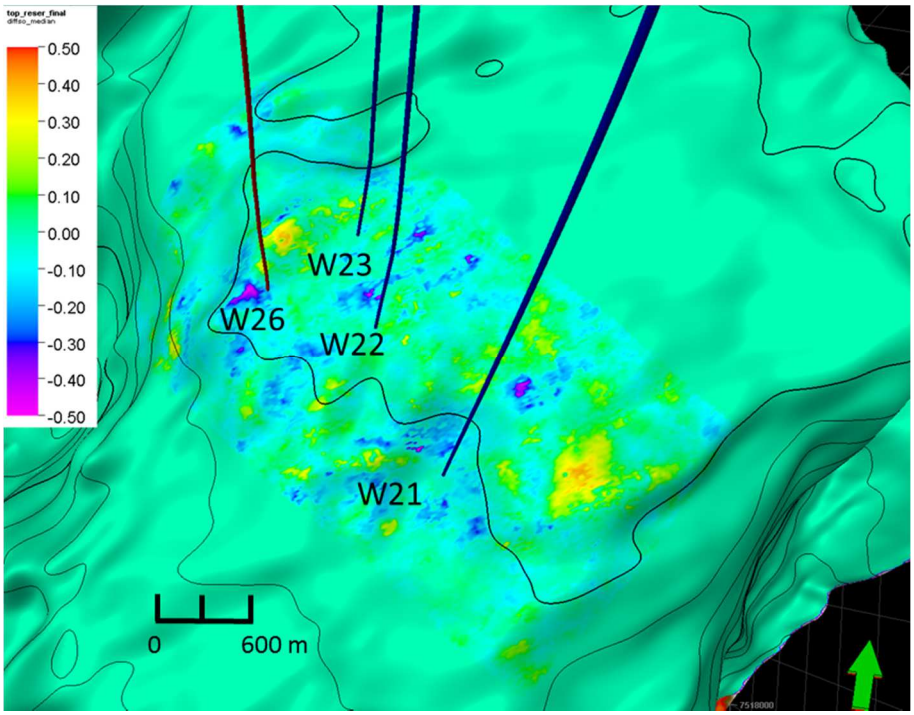

Figure 139 *Median of Difference of Oil Saturation from inversion results extracted between Top-of-reservoir and Peak-1 horizons and plotted over the Top-of-reservoir horizon.*

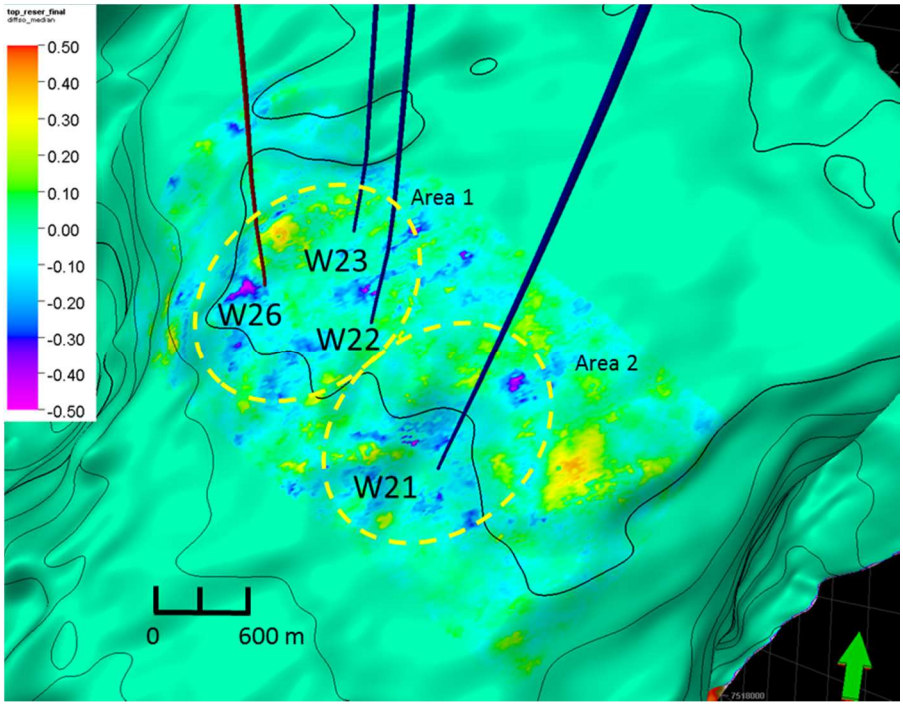

Figure 140 *Delimitation of 2001 to 2012 time-lapse anomalies.*

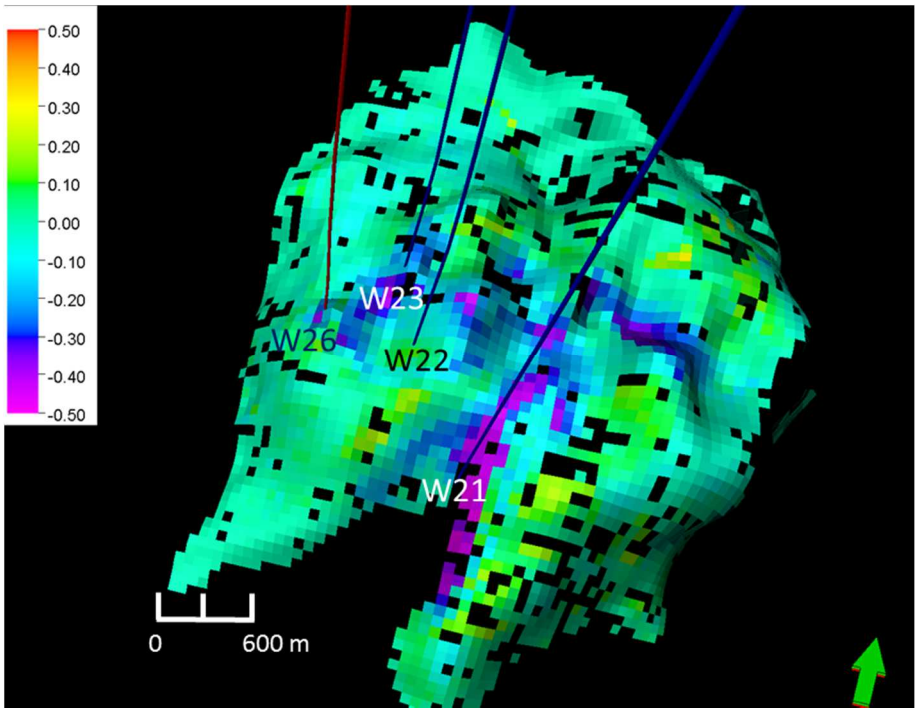

Figure 141 *Difference in oil saturation from flow simulator on layer 14 (First of continuous layers).*

Carbonate reservoirs are prone to fractures. To account for the structural influence of fractures on the placement and shape of time-lapse anomalies, I calculated the Ant-tracking attribute (Pedersen et al., 2005) from Schlumberger's Petrel over the studied areas. To do so, I filtered the data using a structural smoothed filter, generated a variance cube and used it as an input to create the Ant-tracking cube using a 5x5 trace window parameterization. After that, I extracted the values and displayed them on the Top-of-reservoir horizon. The result is shown in Figure 142. Fault Interpretation was then carried out (Figure 143) only for faults located on the left flank of the field. The fracture patterns then were integrated with the surface attributes $\Delta S_{oil,}$ ΔS_{gas} and ΔPressure - Figure 144, Figure 145 and Figure 146, respectively. By the analysis of the figures, one can see that ΔS_{oil} and ΔPressure are correlated and connected with the fractures mainly at the Southwest of well W21 and at the Northwest of well W23. ΔS_{gas} is very scattered, presenting mostly negative values indicating gas production. Regarding NG and porosity attributes, Figure 147 and Figure 148 display patches of good reservoir facies that correlate well with the patches of ΔSoil. These regions are more likely to show time-lapse anomalies for two reasons: lower bulk modulus and higher permeability, both of which are associated with high porosity (Lucia, 2007).

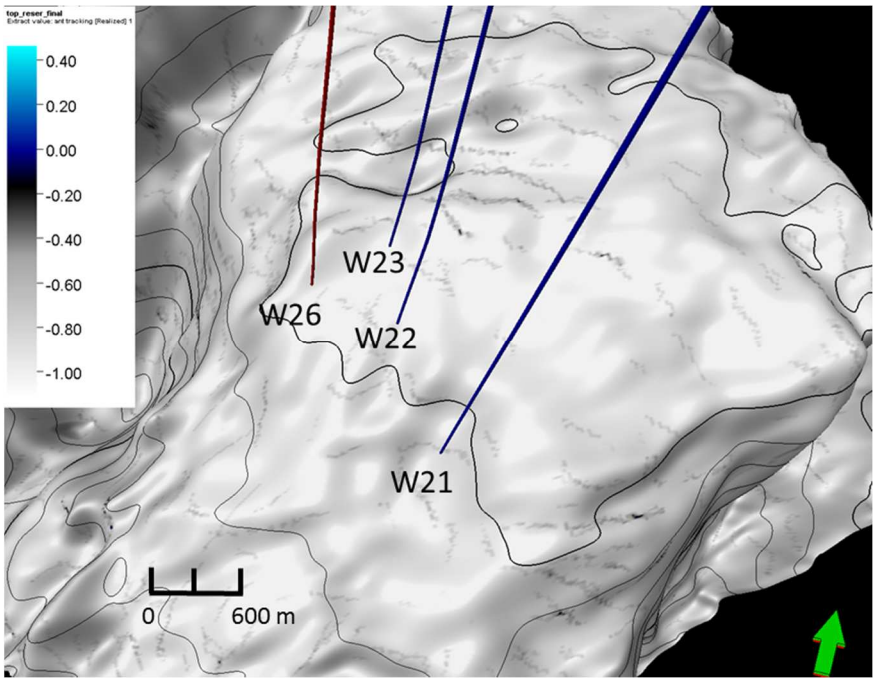

Figure 142 *Ant tracking extracted on the Top-of-reservoir horizon.*

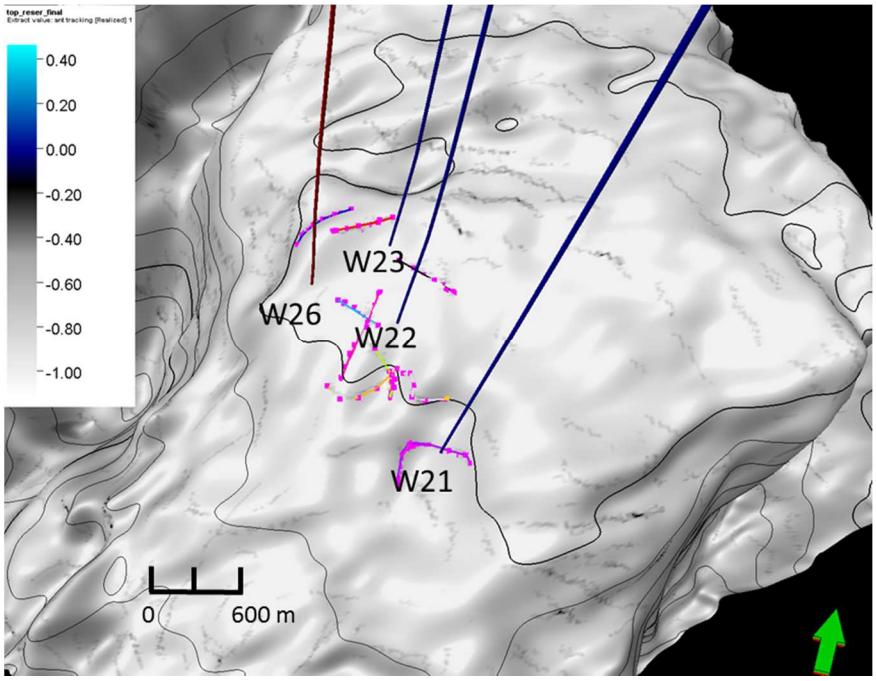

Figure 143 *Interpreted faults using ant tracking over the top reservoir structure.*

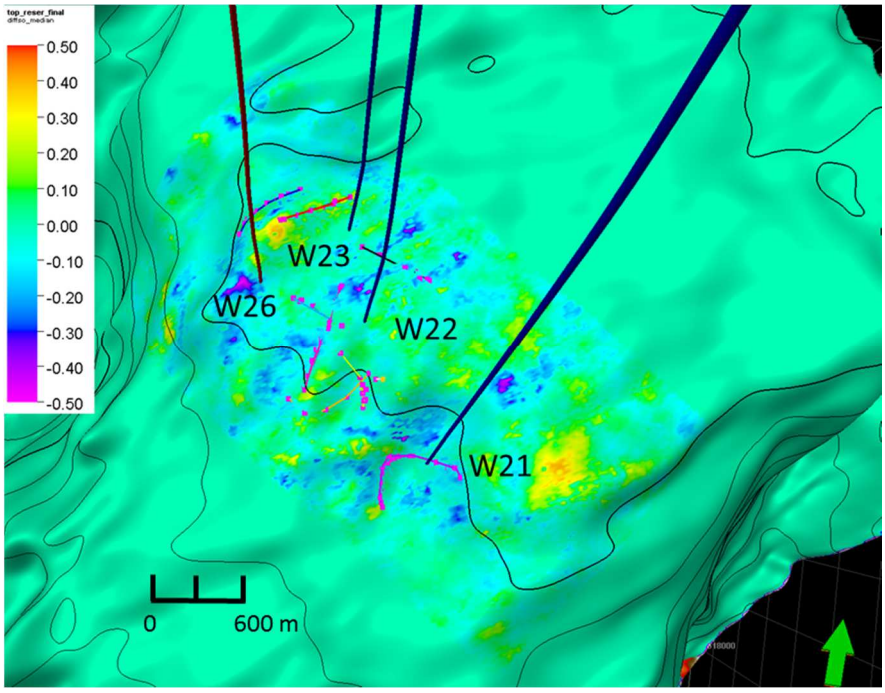

Figure 144 *Top-of-reservoir horizon with surface attribute ΔS_{oil} and superimposed interpreted fractures.*

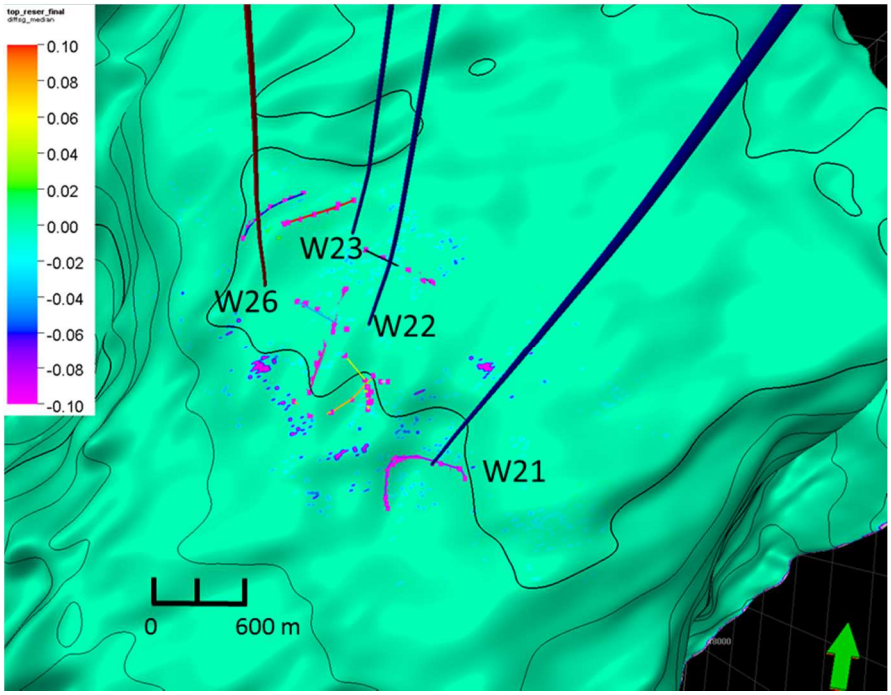

Figure 145 *Top-of-reservoir horizon with surface attribute ΔS_{gas} and superimposed interpreted fractures.*

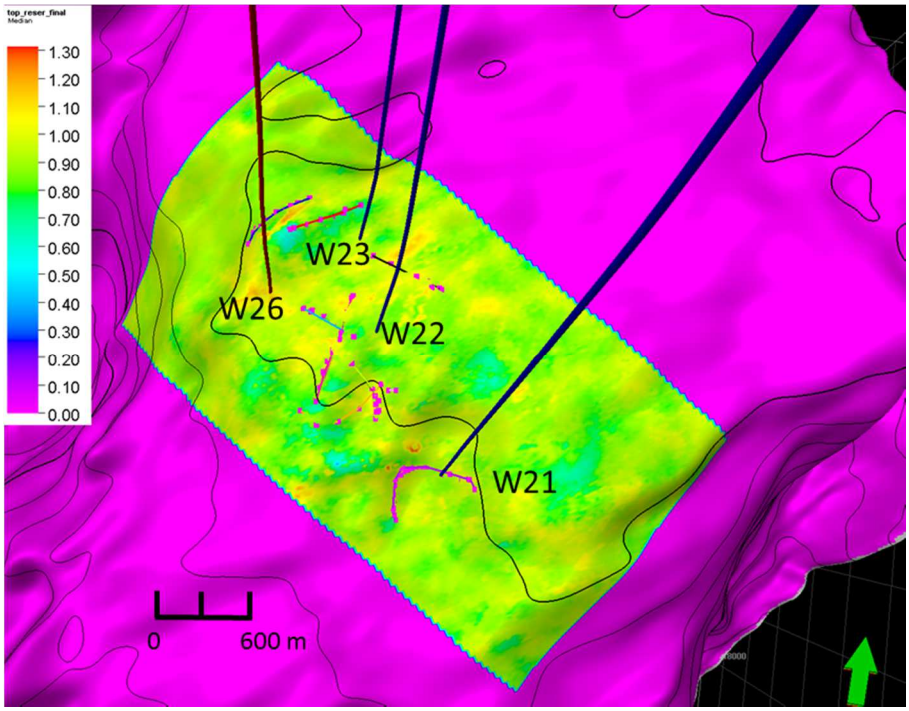

Figure 146 *Top-of-reservoir horizon with surface attribute ΔPressure and superimposed fractures.*

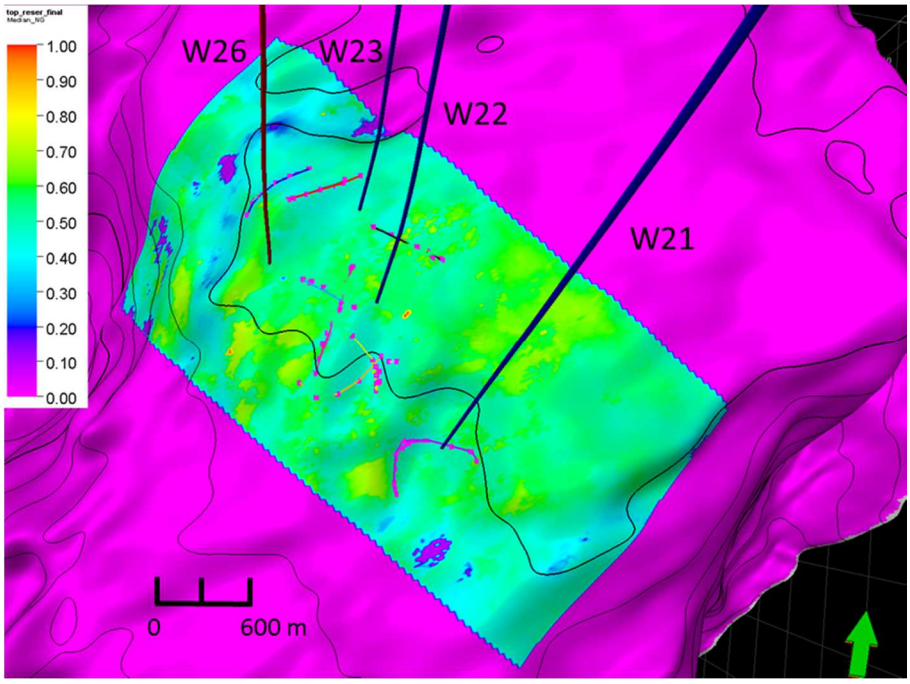

Figure 147 *Top-of-reservoir horizon with surface attribute NG.*

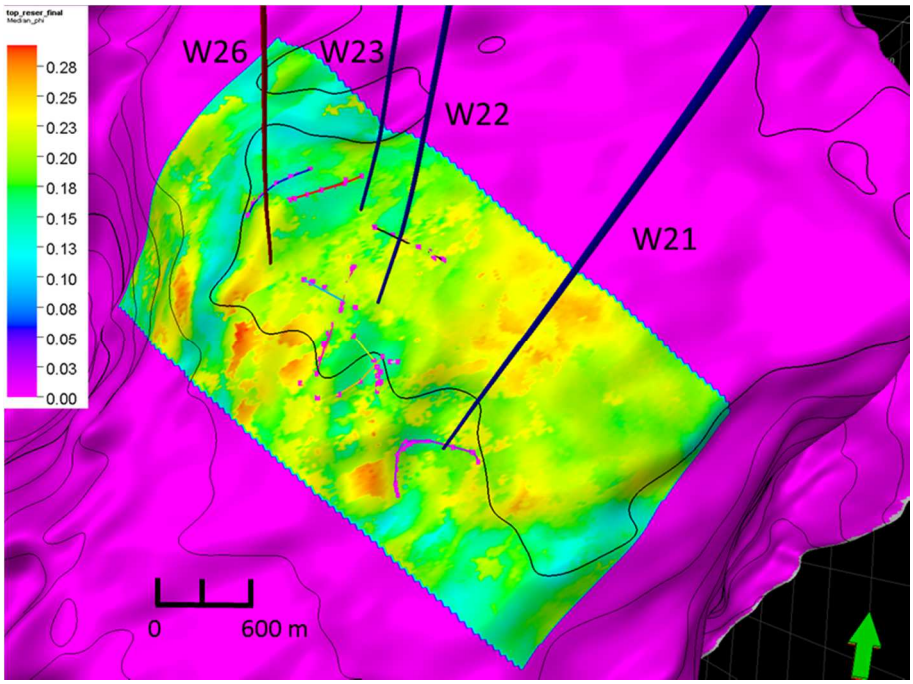

Figure 148 *Top-of-reservoir horizon with surface attribute porosity.*

6.4.2 Area 1

In the flow simulation model, Area 1 was depicted as a very simple coupling between an injector (W23) that pushes oil to a producer (W26) in a rather direct way (Figure 149). However, the examination of the same area in the ΔS_{oil} attribute over the Top-of-reservoir horizon shows a more complex path of the oil moving from the region around the injector to the producer well (Figure 150). In this figure, two different bodies of negative ΔS_{oil} surround the injector well that sits on a positive ΔS_{oil} streak. In Figure 150, well W26 is surrounded by a negative ΔS_{oil} patch while two other negative ΔS_{oil} patches are located at each side of well W23, one to the northwest of well W23 and the other between the injectors W23 and W22. My interpretation is shown in Figure 151. I attributed the negative ΔS_{oil} patch around the producer W26 to water substituting oil that has been produced. The two patches around the injector W23 may be caused by the waterfront moving away from the injectors. The positive anomaly enclosed in the red polygon indicates an increase in oil saturation. On the other hand, this region is part of a high porosity body that is linked to well W26. It is located in a structural high and shows a smaller increase in ΔP than the surrounding areas, which may indicate the generation of a secondary gas cap. When the faults interpreted using the ant-tracking attributes and contours are taken into account it is possible to more fully understand the compartmentalization in the field. My results

indicate that compartmentalization limits the ΔS_{oil} anomalies and should be incorporated in the flow simulation to model small faults and fracture effects.

These results indicate a disagreement between inversion and flow simulation results and more investigations and supplementary data would be needed to achieve a conclusive interpretation. However, in the region around well W22, a positive ΔS_{oil} anomaly, indicating an increase in oil saturation, is visualized in both inversion and flow simulation result (Figure 149 and Figure 150). It could be associated with oil being pushed to the top of the reservoir by the injection of water at the base of the formation.

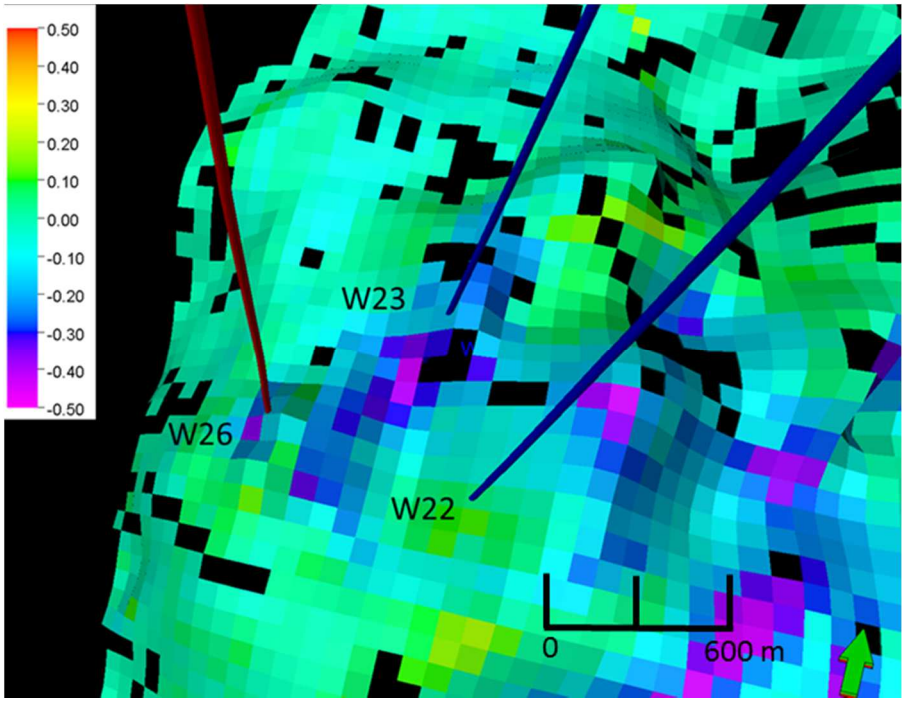

Figure 149 *Interaction between injectors W23 and W22 and producer (W26) according to the flow simulation. Cold colours represent the decrease in the oil saturation.*

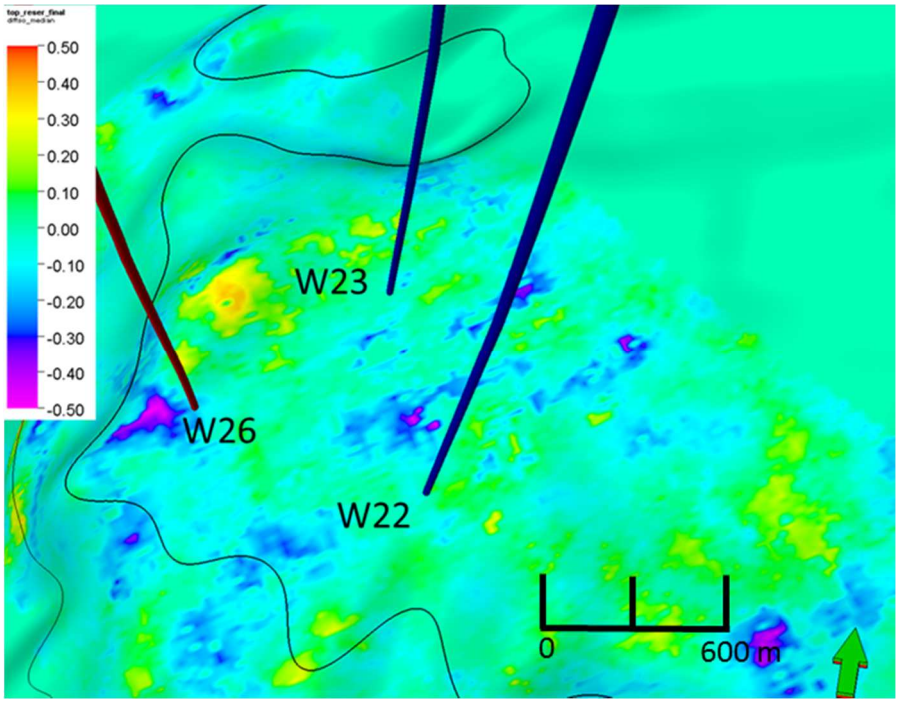

Figure 150 *Interaction between injectors W23 and W22 and producer (W26) according to the ΔS_{oil} inversion results.*

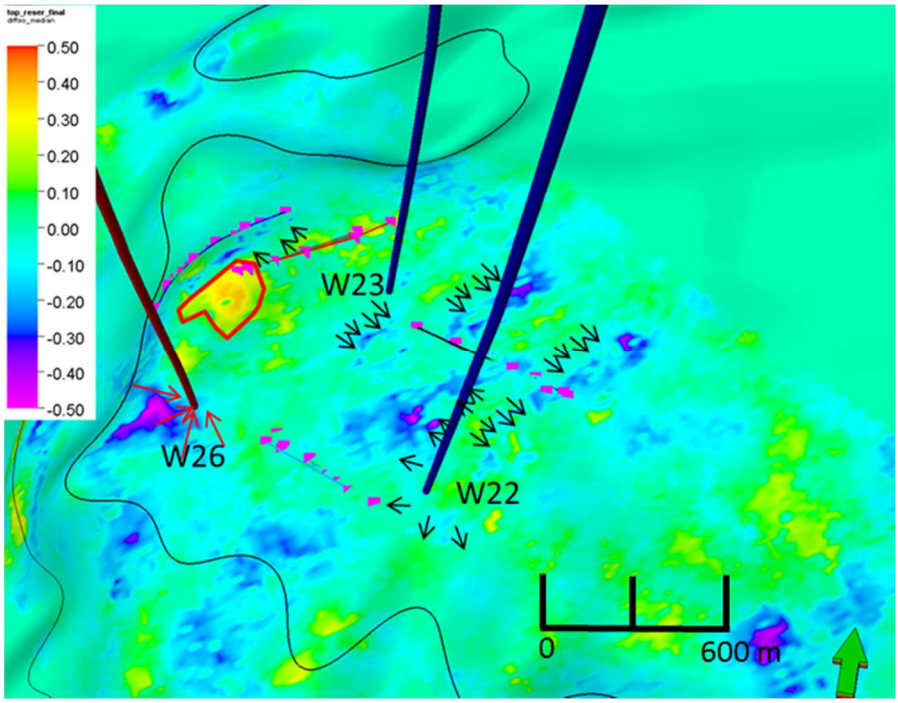

Figure 151 *Interaction between injector (W23) and producer (W26) according to the inversion results and the fault interpreted using ant tracking. A much more complex distribution is revealed using calibrated seismic inversion.*

6.4.3 Area 2

In the flow simulation (Figure 152), Area 2 corresponds to a negative ΔS_{oil} body around well W21, which is indicative of a decrease in oil saturation at the top of the reservoir. This is probably caused by the water flooding coming from the injector well. The inversion results, although showing a less prominent anomaly (Figure 153), are consistent with this interpretation. In Figure 153 the faults interpreted using ant-tracking (Figure 154) limit the regions with an increase and decrease in ΔS_{oil}. These results show that the compartmentalization of this reservoir plays an important role in the spatial distribution of the oil in Area 2.

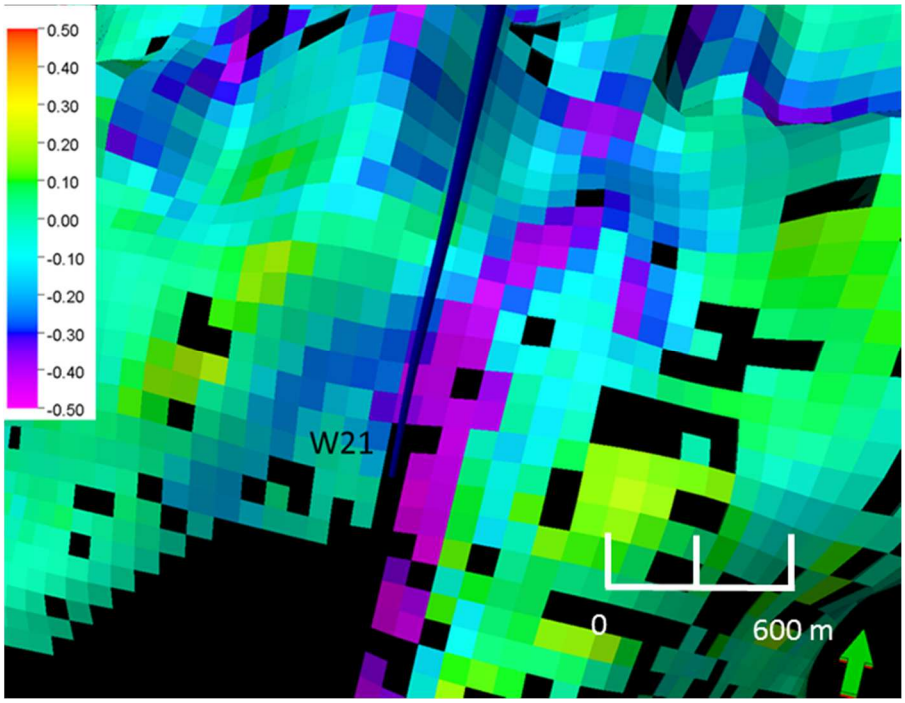

Figure 152 *Difference of oil saturation in flow simulator around well W21. Cold colours represent the decrease in the oil saturation.*

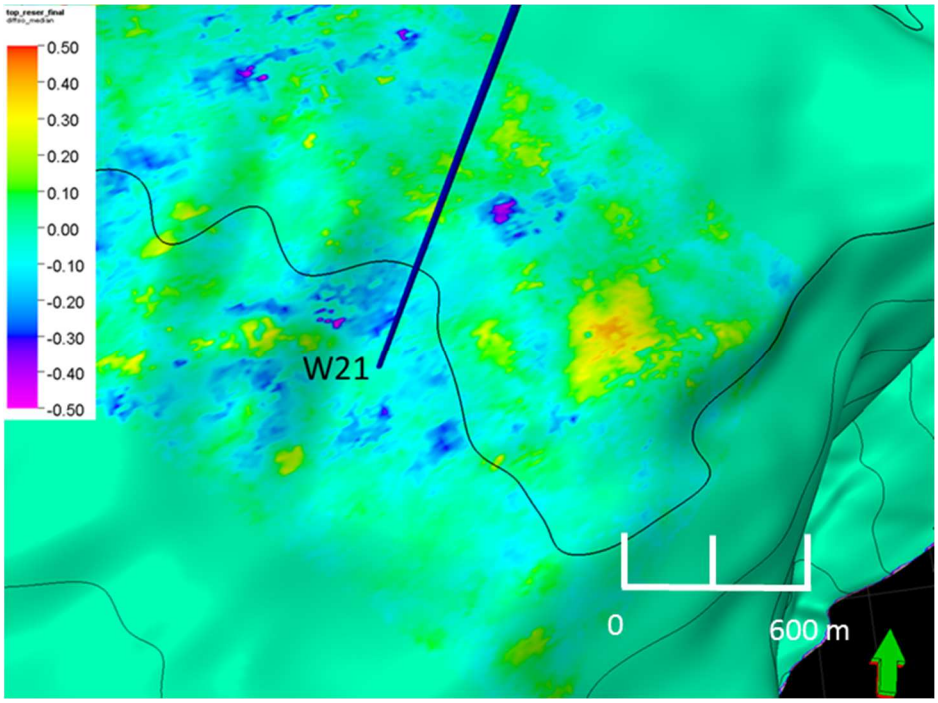

Figure 153 *ΔS_{oil} inversion results around well W21.*

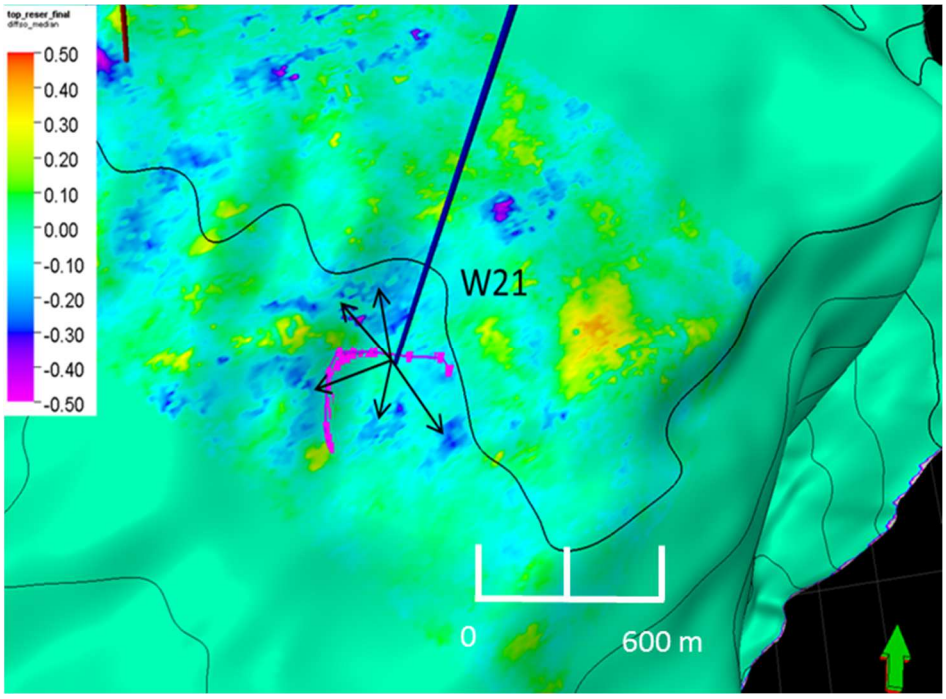

Figure 154 *Interpreted faults over the Top-of-reservoir horizon showing the difference of oil saturation. The seismic identified faults limit the regions with an increase and a decrease in oil saturation.*

6.4.4 Stochastic results

In this section, I still focus my analysis on the west of the reservoir. The stochastic results are the statistical analysis of 5000 model realizations. The software generates means, standard deviations and quantiles (e.g. P10, P50, P90) of base and monitor vintages' properties. I used these results to calculate the differences for each statistical property except standard deviation because, for normal distribution differences, the means are subtracted, but the variances are added. Therefore, standard deviations would not have been subtracted. Regarding the quantiles differences, I favoured the continuity of the scenarios. For instance, the P90 in the base vintage was subtracted from the P90 in the monitor vintage to calculate the P90 difference. The same assumption was done for P10 and P50.

Analyzing the distribution of oil saturation for one trace located close to well W22, one can see a large peak at zero oil saturation (Figure 155). This peak is the result of the addition of the non-oil-bearing scenario probability, the brine-bearing scenario and the gas-bearing scenario. The cause for the presence of such a peak is the fact that the parameter probability of oil was not set to 100% in the model description file to allow the presence of other fluids in the reservoir. Since the reservoir is an oil reservoir, a small percentage of oil saturation, the irreducible oil saturation, must stay in the rock even after injection, which makes zero percent realizations unobtainable. For this reason, I disregarded the large peak at zero as an inversion artefact and recalculated the oil distribution (Figure 156). The effect of the elimination of the inversion artefact on statistical properties can be appreciated in Table 23. The artefact produces a shift of 16% in oil saturation in the mean and 14% in oil saturation in the standard deviation. The software provides an option to filter undesirable values and I used it to eliminate realizations whose oil saturation values were smaller than 1% oil saturation. This cut-off utilized to generate the results was the same as that used in the histograms above and is consistent with the relative permeability curve presented in Figure 107. In this figure, the oil relative permeability curve touches the x-axis at an oil saturation value much higher than 1%.

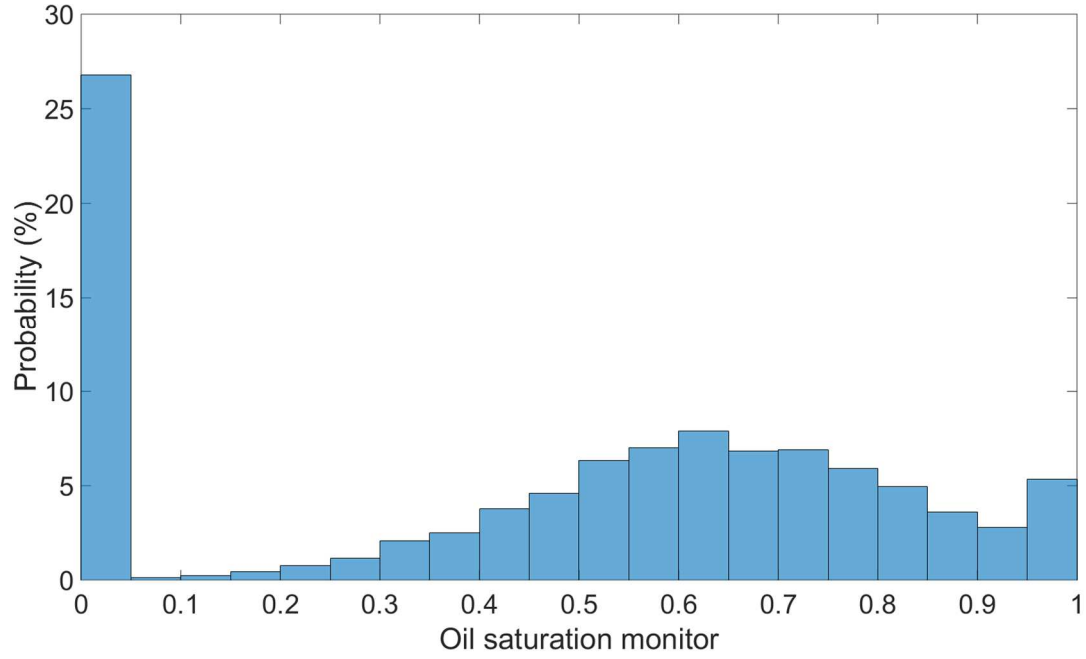

Figure 155 *Oil saturation for trace close to well W22. A Large peak is noticeable at zero oil saturation.*

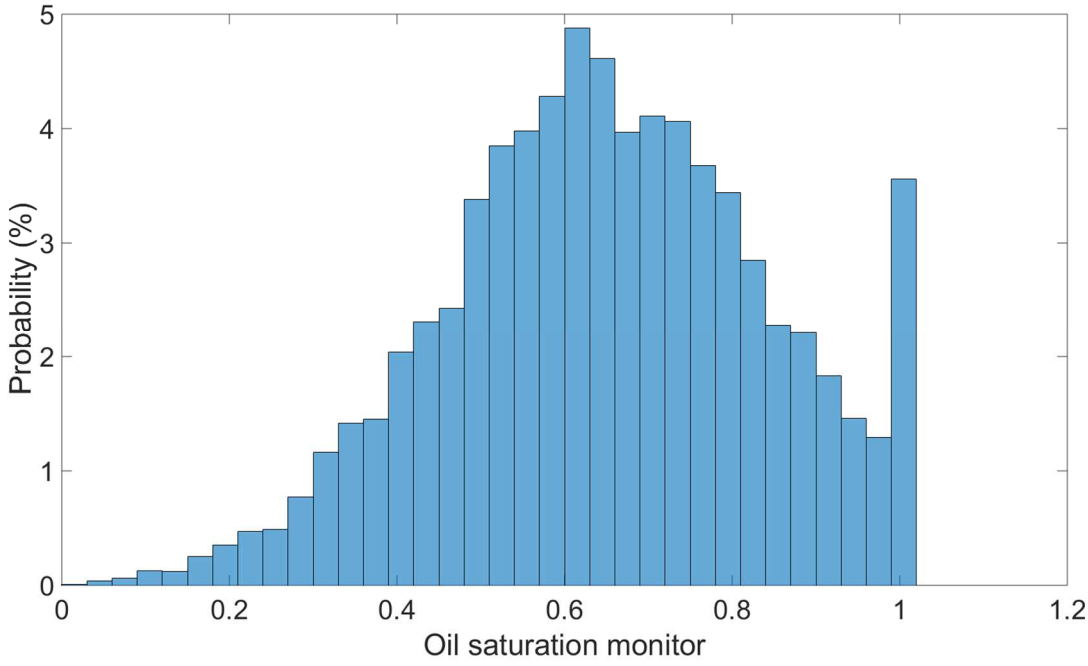

Figure 156 *Oil saturation distribution after elimination of inversion artefact.*

Table 23 *Statistical properties before and after elimination of inversion artefact.*

	Oil saturation mean	Oil saturation standard deviation
Original	0.4758	0.3312
Corrected	0.6498	0.1915

Figure 157 shows the difference between the oil saturation means over a two-dimensional map. I tried to keep the same angle and colour table to facilitate the comparison with the MAP figures. Qualitatively, the figure resembles the correspondent MAP result in the same area (Figure 139), displaying the main ΔS_{oil} features. Quantitatively, it presents similar values of ΔS_{oil}. The 50^{th}, 10^{th} and 90^{th} quantiles (P50, P10 and P90 respectively) represent the models in which the oil saturation found for each trace is respectively bigger than 50%, 10% and 90% of the 5000 realizations. To calculate the differences in the quantiles, I generated the quantiles for each vintage and subtracted them. As was expected, the difference in the P50 (Figure 158) is similar to the difference in the means. The differences for P10 (Figure 159) and P90 (Figure 160) are similar and close to P50. It may indicate that the differences in oil saturation are transferred into seismic amplitude in an approximately linear way. For instance, P50 for base and monitor vintages presents lower values than the P90 results, but the difference between vintages results for the same quantiles are the same.

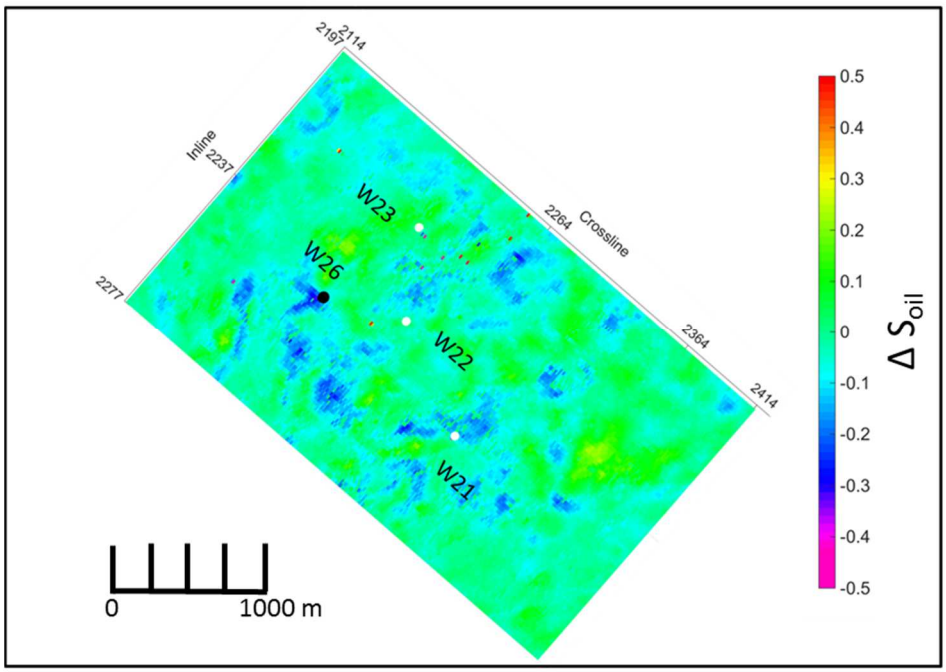

Figure 157 *Difference in the oil saturation means.*

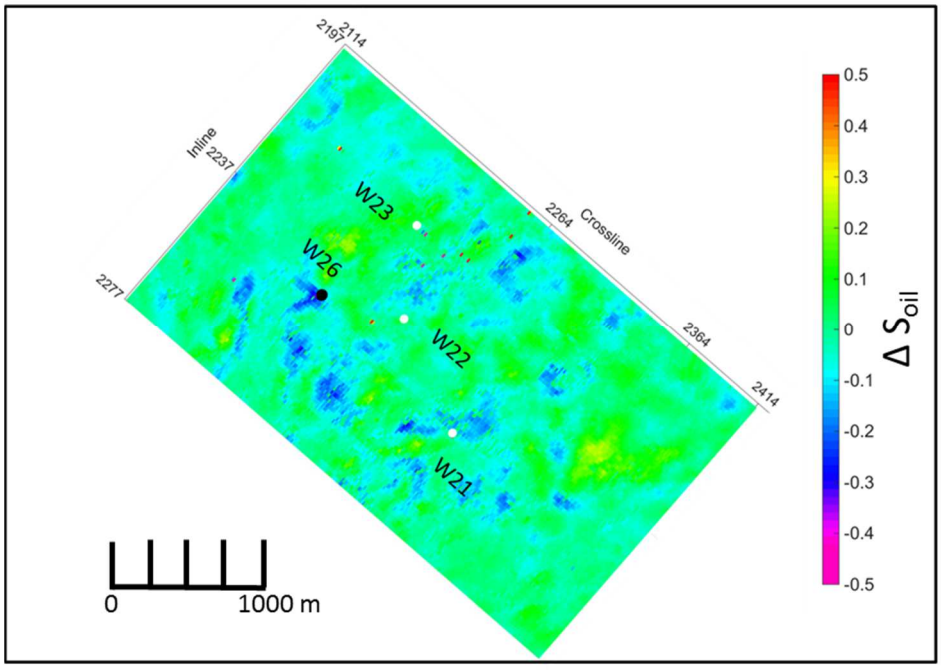

Figure 158 *Difference in the P50 quantiles for oil saturation.*

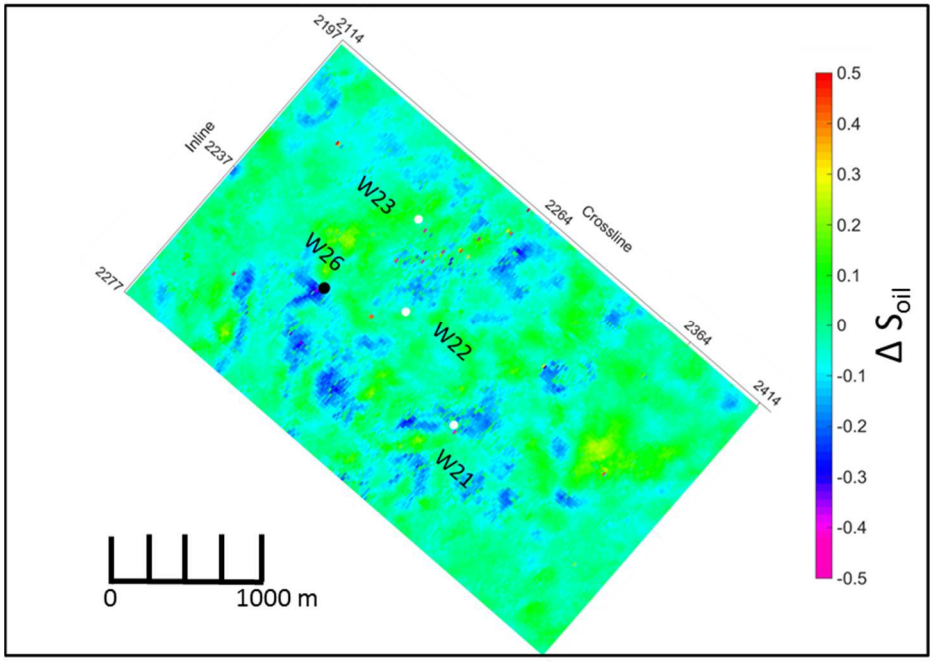

Figure 159 *Difference in the P10 quantiles for oil saturation.*

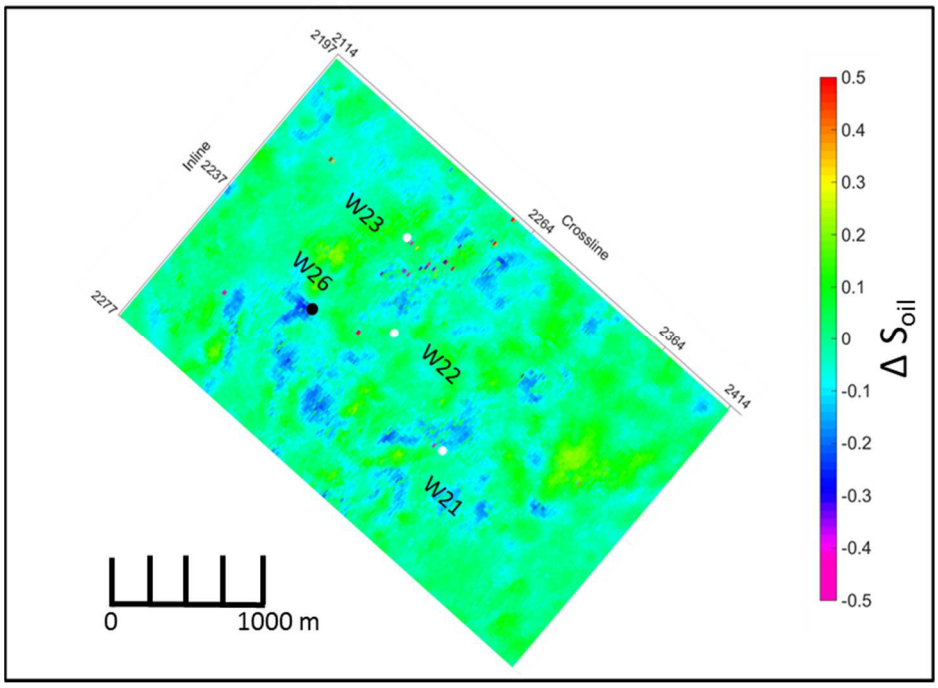

Figure 160 *Difference in the P90 quantiles for oil saturation.*

In the prior model, the oil saturation's standard deviation was assigned as 19% for the base vintage and 20% for the monitor vintage. Figure 161 and Figure 162 show the standard deviation of oil saturation calculated for each vintage and its distribution throughout the area. For the base vintage, it is apparent that the value of 19% oil

saturation standard deviation stands in the background in areas where the porosity MAP model (Figure 148) displays values of porosity smaller than 20%. Porosity is inversely correlated with dry modulus, which, for its turn, is inversely correlated with the influence of fluid on the rock velocity. Therefore, it is expected to have a smaller detectability in areas with smaller porosities hence the higher spread of oil saturation values in these areas. When I compared the maps of MAP porosity (Figure 148) and standard deviation I observed that, in areas with porosity higher than 20%, the posterior standard deviation was smaller than prior standard deviation. This suggests a decrease in the uncertainty as a result of the inversion. For the monitor vintage, the background value was 19%, a value smaller than the value stated in the prior model. Peaks of 20%, associated with areas showing smaller values in the porosity volume, and values as low as 17% in areas where the porosity was found to be 20% or more, are also found. These results indicate that the same reasoning employed in the base vintage oil saturation standard deviation map interpretation can be applied here.

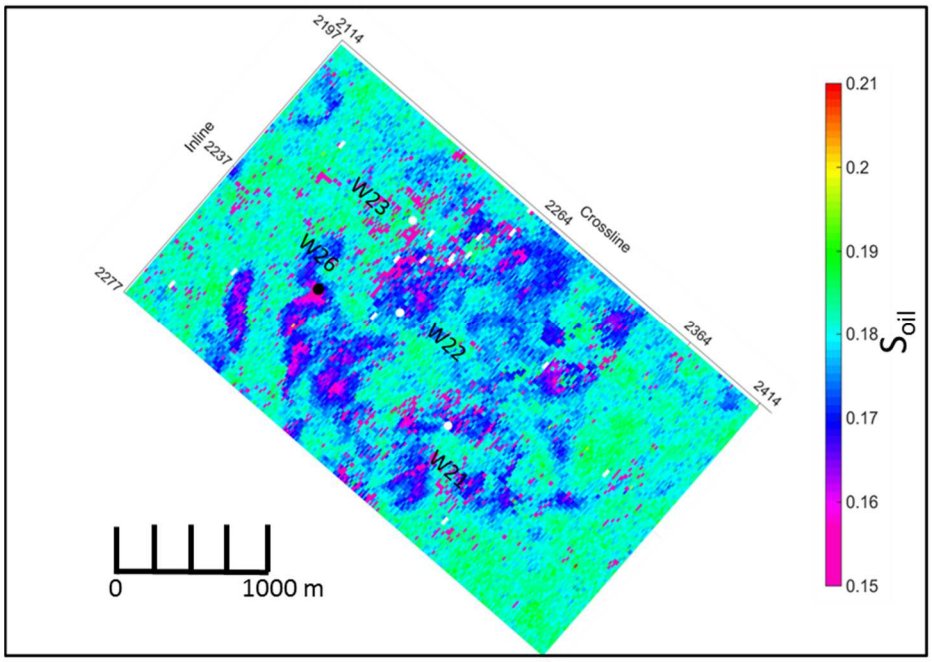

Figure 161 *Base vintage oil saturation's standard deviation.*

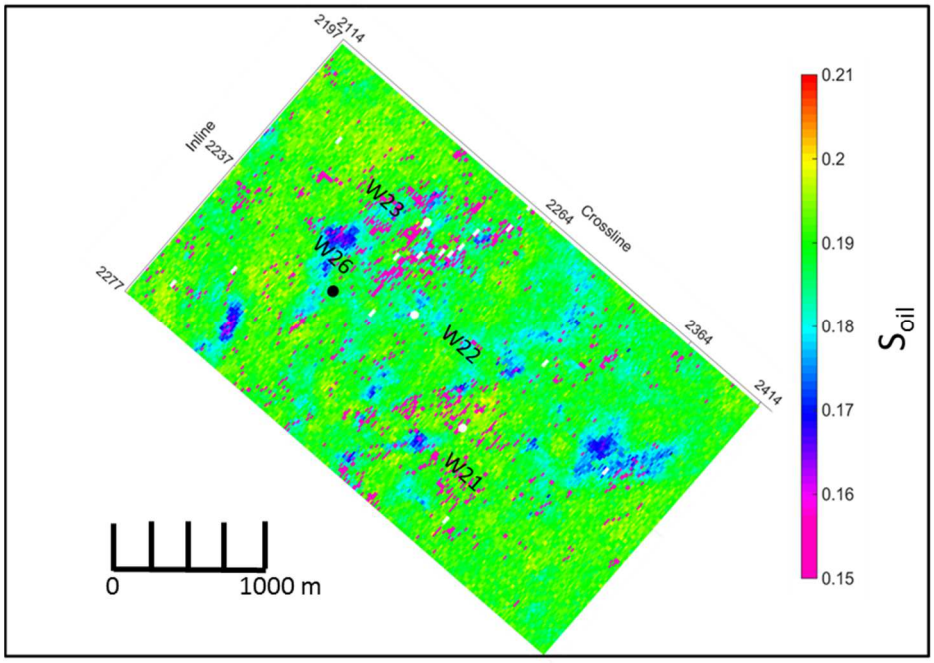

Figure 162 *Monitor vintage oil saturation's standard deviation.*

6.5 CONCLUSION

In this chapter, I presented the stochastic inversion of a carbonate reservoir time-lapse seismic data. The main objective of this exercise was to determine the applicability of the stochastic methodology to this type of reservoir. Geological and engineering data had to be blended with the geophysical information in order to build an initial model. Also, interpretation of the inversion results in a truly multidisciplinary workflow is the only way to fully utilize the time-lapse potential. During the interpretation of the results I had to acknowledge:

- The high incompressibility of the reservoir rock mineral, making the rock less sensitive to variation in dynamic properties, especially in low porosity regions;

- A large time gap between the acquisition of well logs (1970s) and the seismic data (2002-2011), over a producing oil field made the amplitudes of the synthetic data generated by the use of velocity logs inconsistent with the real seismic data. This, associated with the fluid saturation uncertainty, affected my capacity to estimate wavelets, and the generation and validation of a statistical wavelet calculated just above the reservoir was made necessary;

-The presence of obstructions and the absence of shear velocity logs limited the utilization of angle stacks to perform an AVO inversion, which could have improved the reliability of the results, especially pressure estimation. Furthermore, I decided to abstain from generating synthetic Vs logs because no data was available to perform a validation analysis;

-The fact that only one realization of flow simulation was present limited the evaluation of the prior uncertainty of dynamic reservoir properties. If more realizations were present, it would be possible to evaluate an average behaviour of such dynamic properties throughout the reservoir. This information could be used in the construction of the model, and in the comparison with the stochastic results derived from the posterior.

The utilization of the flow simulation model was critical in the generation of the prior model, especially in the determination of the prior fluid saturation in the years of seismic acquisition (2002 and 2011). The use of the flow simulation model was limited to the extraction of statistical properties only and no attribute maps were utilized to spatially constrain the inversion. For this reason, after the inversion, I considered doing a comparison between the results of the inversion with the flow simulation models. This would provide a comparison between semi-independent variables, and successfully avoid the circular logic that would occur should I utilize all the characteristics of the flow simulation model as an input and validate the result using the same model. Furthermore, the diversity of output attributes aids the user in the solution of interpretation dilemmas. When multiple fluids are present in the reservoir, and pressure variation is predicted, the use of attributes improves confidence in the interpretation of time-lapse anomalies. In this work, the use of pressure and porosity attributes in the carbonate reservoir interpretation is an example of such integration. The MAP results represent the models with higher probability and are used in the interpretation and quality control of the results. The statistical properties, such as those shown here (mean, standard deviation and quantiles) are only obtained through the application of a stochastic algorithm and represent the uncertainty of properties contained in the posterior distribution. In the interpretation, I could observe that the carbonate reservoir comprises different levels of time-lapse detectability for different regions. According to my findings, diagenesis was the main generator of facies heterogeneity, creating regions with high porosity, where the time-lapse signal was

readily detectable and areas with low porosity, where the detection was ambiguous. My results showed that the estimations of oil saturation are less uncertain if the porosity is relatively high because the rock seismic response was more sensitive to fluid substitution. In the present work, the porosity cut-off was 20%.

When comparing the inversion of the real dataset with the synthetic one, it was clear that the amount of approximation and the complexity of the problem were much larger on the real dataset case. Firstly, since the pressure information can only be obtained by the inclusion of the shear impedance in the analysis and we performed an acoustic inversion, it was only possible to utilize the oil saturation outputs. In that case, it was not a problem since the impedance variation with pressure was small. In the synthetic case the pressure was not included in the modelling, therefore I did not have to invert for pressure. Secondly, the use of saturation and pressure information from a statistical analysis of the flow simulation model in order to parameterize the prior model was another approximation to be analysed. It was necessary because of the lapse in time between well logging and seismic acquisition. Since the flow simulation model, although based on well measurements, is only one realization of a flow simulation it does not represent in detail the true pressure and saturation spatial distribution in the reservoir. Therefore, the inclusion of this information in the inversion brings in an amount of uncertainty to the process. To avoid the bias the inclusion of maps would bring I did not include any spatial constraint in the form of pressure and saturation maps and only used mean values and standard deviations of the properties in the model. In the synthetic example, the flow simulation model used to generate the seismic data was the information source for the saturation and no uncertainty was generated in the process because it was the “true model”. Thirdly, the wavelet in the real data set needed to go through a process of validation since it could not be directly extracted from the wells. In the synthetic example, I used the same wavelet as the one used in the modelling phase. In fact, the synthetic example was very important to familiarize the author with the methodology, to test the sensitivity of the method to non-optimized parameterization and noise. However, the problems presented by the real dataset were not foreseen and solutions needed to be tailored on a case-by-case basis.

In conclusion, my results showed that the methodology provided critical knowledge in the generation of interpretation scenarios, and validates the method application on

carbonate reservoirs. Despite this, the author would like to recommend some modifications to the method that could ease its application and improve the software for future uses. Firstly, if more options of rock physics models were present, tackle reservoir rocks that do not follow Gassmann's equation could be possible. Secondly, according to Grana (2014) and my own experience, beta distributions would be the most appropriate options to parameterize fluid saturation (especially gas), because its values are more frequently grouped around the extremes. In the software, truncated Gaussians were used. Finally, since truncated Gaussians are the actual distributions used in the software, I believe that the employment of irreducible water saturation (Swi) as the truncation value would be preferred in place of the 0% water saturation limit currently used.

CHAPTER 7. CONCLUSIONS

The interpretation of time-lapse anomalies is deemed as more challenging in carbonate reservoirs than in their siliciclastic counterparts. Among the reasons for this are, firstly, the higher incompressibility modulus of carbonate rocks, making the rock less sensitive to both fluid content and pressure changes. Secondly, the fact that diagenesis plays a more important role in modifying the carbonate rock matrix, making it necessary to build a more heterogeneous and complex reservoir model. Finally, rock-fluid interactions caused by changes in fluid saturation may alter the elastic properties during production, violating assumptions required for application of Gassmann's fluid substitution. On the other hand, an important percentage of oil and gas reserves are found in carbonate reservoirs, which generally present low recovery factors (Montaron, 2008). Therefore, the development and validation of time-lapse interpretation tools suitable to carbonate reservoirs are of great interest for the industry, especially in softer and porous carbonates reservoirs. This happens because these reservoirs are more sensitive to the effects of pore fluid and pressure variations. Furthermore, such tools, when applied to time-lapse data, will increase the value of the information from this ever-perishable data. Technologies like the injection of brines with similar composition to formation water to avoid the rock-fluid interaction are becoming common. This will help avoid the rock-fluid interaction and enhance the reliability of the time-lapse interpretation.

In this context, the aim of this research was to assess the potential of stochastic time-lapse inversion to carbonate reservoirs. To achieve this, the following objectives were proposed: Estimate dynamic properties in a carbonate reservoir using time-lapse stochastic inversion, and evaluate the uncertainty in the reservoir dynamic properties using time-lapse stochastic inversion. The stochastic time-lapse inversion methodology employed in this work, Delivery4D, is a layer based, petrophysical and Bayesian algorithm (Gunning, 2013). It is able to output a statistical distribution derived from the integration of time-lapse seismic data and *a priori* information. The posterior distribution, as it is called, is subject to two forms of analysis: a search for its maximum value, or the generation of an ensemble of samples of the posterior. The first will supply the model's properties with the maximum probability and the second will provide statistical parameters regarding the most probable models: in fact, giving

the user an evaluation of the uncertainty of the model parameters. To evaluate the robustness of the algorithm's results in the presence of noise and parameterization issues, I implemented the methodology on a synthetic dataset. This dataset was derived from a feasibility study for a CO_2 sequestration project at Otway Basin, Victoria, Australia. The synthetic time-lapse seismic data employed a full elastic 3D modelling with realistic geology, based on flow simulations performed by a compositional numerical reservoir simulator. Therefore, it used a different modelling algorithm from the inversion methodology, which applied convolutional modelling to generate synthetic seismic traces. The difference in the modelling algorithms guarantees that there was no inversion fallacy. The test was carried out without any spatial constraints for the presence of gas to simulate the scenario where the interpreter does not know the exact position of the gas plume after injection.

One of the issues addressed was the influence of incorrect parameterization in the final results. For this matter, I determined that the success of the inversion depends on the sensitivity of the reservoir rock's acoustic impedance to fluid saturation. I also verified that the adequate choice of prior fluid saturation parameters is of critical importance to generate results that had a good statistical agreement with the "true" model (the model used to create the synthetic seismic data). Another challenge addressed in this work was the influence of geostatistical characteristics of added noise in the final result. My results showed that, when random noise was added to the input vintages, the algorithm was able to recover the "true" model within an acceptable margin of error. Hence, I concluded that the statistical nature of the methodology was adequate to separate the random noise from the signal. By contrast, the addition of coherent noise had deleterious effects on the inversion results and, in most cases, the convergence to the right model was not achieved. However, when the RMS amplitude level was comparable to the one in the difference volume, the algorithm was able to distinguish the noise from the signal. Another achievement of this research was the definition of a metric to quantify the improvement of the detectability of the modelled fluid saturation while varying the prior distribution's noise level and fluid saturation parameterization (Meira et al., 2015).

Equipped with the knowledge about the limits of the method gathered during the synthetic data inversion, I went on to perform a stochastic time-lapse seismic inversion on a carbonate dataset. The dataset consisted of well logs, seismic data, flow

simulation models, capillary pressure and relative permeability curves, thin section description of each facies and seismic horizons from an Albian reservoir located at Campos Basin, offshore Brazil. During the data analysis phase, I found that, by utilizing such a comprehensive real data set, the user is faced with a plethora of issues. These issues range from the integration of information, quality control procedures and a variety of data types, to the technologies related to its acquisition and analysis. I strongly recommend the study of every geophysical, geological and engineering method associated with the dataset content prior to the seismic inversion. In the planning phase, the ability to adapt strategies and reshape expectations regarding the inversion methodology under the availability and quality of data was a key point to confront the real data inversion problem. After inversion of the carbonate dataset, I focused my analysis on the oil saturation variation results. Then I integrated these outcomes with pressure variation and porosity volumes and with a set of interpreted fractures to support my interpretation. Finally, I compared my results with the flow simulation model.

Given its extensive use in quality control, parameter determination and result validation, the flow simulation model was, alongside facies logs and seismic data, one of the most important components of the carbonate data set. Although not an exact reproduction of the distribution of the reservoir's properties, the flow simulation model was used in the interpretation and quality control procedures to create a reliable set of time-lapse results. As a matter of fact, my outcomes did not always agree with the flow simulation model at a small scale. However, since the flow simulation model depicts one realization and does not aim to represent the reservoir behaviour at a small scale I can still compare the inversion results with the flow simulation model at a larger scale. Additionally, the inversion results incorporate information from the seismic data, which is densely sampled throughout the reservoir and can provide more detailed information. The small-scale heterogeneities captured by the inversion results were not present in the model and can be, in the future, integrated with the interpreted fractures to generate a more detailed framework for the static geologic model in regions away from the wells. Ideally, in the future, time-lapse seismic data and flow simulations will be integrated in a stochastic history-matching workflow to produce a saturation and pressure distribution consistent with both seismic and production data. The generation of such workflows faces many challenges and is the subject of ongoing

research.

The diversity of outputs made available by the software assists the user in the elucidation of these interpretation dilemmas. Time-lapse anomalies, especially when more than one fluid is present and pressure variation is expected, must be examined by more than one attribute to enhance confidence in the explanation given by the interpreter. The combined analysis of pressure and porosity attributes is an example of such integration. Regarding the interpretation phase, I could also observe that the carbonate reservoir presented different levels of time-lapse detectability. According to my findings, diagenesis was the main generator of facies heterogeneity, creating regions with high porosity where the time-lapse signal was readily detectable and areas with low porosity where detection was not possible.

In conclusion, I have found that the stochastic time-lapse inversion methodology helps to understand the movement of fluid inside a carbonate reservoir if the reservoir rock behaviour can be approximated by Gassmann's predictions. I also concluded that the result is improved if the porosity is relatively high, because, in that case, the uncertainty regarding the fluid saturation is diminished by the introduction of the seismic information. In the present case, the porosity cut-off was 20%. These high levels of porosity are not uncommon in Brazilian carbonates. My main contributions to the field were, firstly, the determination of the limits of the stochastic time-lapse inversion method through an exhaustive evaluation of a synthetic data set. Secondly, the application of the inversion methodology to a carbonate reservoir generating useful results, thus validating the use of this method for this type of reservoir.

References

Adam, L., Batzle, M., and Brevik, I. (2005). Gassmann's fluid substitution paradox on carbonates: seismic and ultrasonic frequencies *SEG Technical Program Expanded Abstracts 2005* (pp. 1521-1524).

Adam, L., Batzle, M., and Brevik, I. (2006). Gassmann's fluid substitution and shear modulus variability in carbonates at laboratory seismic and ultrasonic frequencies. *GEOPHYSICS, 71*(6), F173-F183.

Alajmi, M., Bona, A., and Pevzner, R. (2013). *Modeling of depth variable 3D time-lapse seismic noise based on measured noise at the CO2CRC Otway project.* Paper presented at the 2013 SEG Annual Meeting.

Allaby, M. (2013). *A dictionary of geology and earth sciences*: Oxford University Press.

Amundsen, L., and Landrø, M. (2007). 4D seismic–status and future challenges. *Geo ExPro*, 66-68.

Anderson, W. (1986). 1987, Wettability literature survey–part 1 to part 6. *J. Pet. Technol*, 1125-1144.

Archilha, N., Misságia, R., de Ceia, M., Neto, I. L., de Castro, L., and de Souza, F. (2013). *Petrophysical, Mineralogical and P Wave Velocity Characterization of Albian Carbonates From Campos Basin, Brazil.* Paper presented at the 2013 SEG Annual Meeting.

Asnaashari, A., Brossier, R., Garambois, S., Audebert, F., Thore, P., and Virieux, J. (2015). Time-lapse seismic imaging using regularized full-waveform inversion with a prior model: which strategy? *Geophysical Prospecting, 63*(1), 78-98.

Avseth, P., Flesche, H., and Van Wijngaarden, A.-J. (2003). AVO classification of lithology and pore fluids constrained by rock physics depth trends. *The Leading Edge, 22*(10), 1004-1011.

Backus, G. E. (1962). Long-wave elastic anisotropy produced by horizontal layering. *Journal of Geophysical Research, 67*(11), 4427-4440.

Barkved, O. I., Geoscientists, E. A. O., and Engineers. (2012). *Seismic Surveillance for Reservoir Delivery: From a Practitioner's Point of View*: EAGE publications.

Batzle, M., and Wang, Z. (1992). Seismic properties of pore fluids. *GEOPHYSICS, 57*(11), 1396-1408.

Berner, R. A. (1980). *Early diagenesis: A theoretical approach*: Princeton University Press.

Berryman, J. G. (1993). *Effective-stress rules for pore-fluid transport in rocks containing two minerals*. Paper presented at the International journal of rock mechanics and mining sciences and geomechanics abstracts.

Bezerra, M., Rosario, F. F., Franca, L., and Sombra, C. L. (2004). *Assessment of Scaling Tendency of Campos Basin Fields Based on the Characterization of Formation Waters*. Paper presented at the SPE International Symposium on Oilfield Scale.

Biot, M., and Willis, D. (1957). The theory of consolidation. *J. Appl Elastic Coefficients of the Mech, 24*, 594-601.

Blanchard, T., and Thore, P. (2013). Introducing prior information to pressure and saturation inversion: The key for success? *SEG Technical Program Expanded Abstracts 2013* (pp. 4971-4975).

Bo, Y. Y., Lee, G. H., Kim, H.-J., Jou, H.-T., Yoo, D. G., Ryu, B. J., and Lee, K. (2013). Comparison of wavelet estimation methods. *Geosciences Journal, 17*(1), 55-63.

Bognø, T. (2008). Impacts on oil recovery from capillary pressure and capillary heterogeneities.

Bourgeois, A., Bourget, M., Lailly, P., Poulet, M., Ricarte, P., and Versteeg, R. (1991). Marmousi, model and data. *The Marmousi Experience*, 5-16.

Brown, R. J., and Korringa, J. (1975). On the dependence of the elastic properties of a porous rock on the compressibility of the pore fluid. *GEOPHYSICS, 40*(4), 608-616.

Buland, A., and El Ouair, Y. (2006). Bayesian time-lapse inversion. *GEOPHYSICS, 71*(3), R43-R48. doi: doi:10.1190/1.2196874

Buland, A., and Omre, H. (2003). Bayesian linearized AVO inversion. *GEOPHYSICS, 68*(1), 185-198. doi: doi:10.1190/1.1543206

Calvert, R. (2005). *Insights and methods for 4D reservoir monitoring and characterization : 2005 Distinguished Instructor Short Course / presented by Rodney Calvert sponsored by the Society of Exploration Geophysicists [and] European Association of Geoscientists and Engineers*. Tulsa, Okla. (8801 South Yale St., Tulsa OK 74137-3175): Tulsa, Okla. (8801 South Yale St., Tulsa OK 74137-3175) : Society of Exploration Geophysicists.

Castagna, J., and Backus, M. (1993). Offset dependent reflectivity: Theory and practice of AVO analysis. *SEG Investigations in Geophysics Series*(8), 345.

Chadwick, A., Williams, G., Delepine, N., Clochard, V., Labat, K., Sturton, S., Lima, A. L. (2010). Quantitative analysis of time-lapse seismic monitoring data at the Sleipner CO 2 storage operation. *The Leading Edge, 29*(2), 170-177.

Chang, H. K., Assine, M. L., Corrêa, F. S., Tinen, J. S., Vidal, A. C., and Koike, L. (2008). Sistemas petrolíferos e modelos de acumulação de hidrocarbonetos na Bacia de Santos. *Revista Brasileira de Geociências, 38*(2), 29-46.

Chang, Y.-B., Coats, B. K., and Nolen, J. S. (1996). *A compositional model for CO 2 floods including CO 2 solubility in water*. Paper presented at the Permian Basin Oil and Gas Recovery Conference.

Cohen, J. K., and Stockwell, J. W. (2009). CWP/SU: Seismic Un* x Release No. 41, an open source software package for seismic research and processing.

Corzo, M., MacBeth, C., & Barkved, O. (2013). Estimation of pore-pressure change in a compacting reservoir from time-lapse seismic data. *Geophysical Prospecting*, *61*(5), 1022-1034.

CPRM. (2003). Geologia, Tectônica e Recursos Minerais do Brasil: texto, mapas and SIG. *BIZZI, LA*.

De Lucia, M., Bauer, S., Beyer, C., Kühn, M., Nowak, T., Pudlo, D., Stadler, S. (2012). Modelling CO2-induced fluid–rock interactions in the Altensalzwedel gas reservoir. Part I: from experimental data to a reference geochemical model. *Environmental Earth Sciences, 67*(2), 563-572.

Dvorkin, J., Gutierrez, M. A., and Grana, D. (2014). *Seismic reflections of rock properties*: Cambridge University Press.

Fanchi, J. R. (2005). *Principles of applied reservoir simulation*: Gulf Professional Publishing.

Fournier, F., Leonide, P., Biscarrat, K., Gallois, A., Borgomano, J., and Foubert, A. (2011). Elastic properties of microporous cemented grainstones. *GEOPHYSICS, 76*(6), E211-E226.

Gardner, G., Gardner, L., and Gregory, A. (1974). Formation velocity and density - the diagnostic basics for stratigraphic traps. *GEOPHYSICS, 39*(6), 770-780.

Gassmann, F. (1951). Elasticity of porous media. *Vierteljahrsschrder Naturforschenden Gesselschaft, 96*, 1-23.

Glubokovskikh, S., and Gurevich, B. (2015). Effect of micro-inhomogeneity on the effective stress coefficients and undrained bulk modulus of a poroelastic medium: a double spherical shell model. *Geophysical Prospecting, 63*(3), 656-668.

Grana, D. (2013). *Bayesian inversion methods for seismic reservoir characterizarion and time-lapse studies* (Doctor of phylosophy), Stanford. Retrieved from https://pangea.stanford.edu/departments/geophysics/dropbox/SRB/public/docs/theses/SRB_136_AUG13_Grana.pdf Available from SRB

Grana, D. (2014). Probabilistic approach to rock physics modeling. *GEOPHYSICS, 79*(2), D123-D143.

Greenberg, M., and Castagna, J. (1992). Shear-wave velocity estimation in porous rocks: theoretical formulation, preliminary verification and applications1. *Geophysical Prospecting, 40*(2), 195-209.

Gunning, J. (2013). Delivery4D: an open–source model–based Bayesian seismic inversion program for time-lapse problems.

Gunning, J., and Glinsky, M. E. (2004). Delivery: an open-source model-based Bayesian seismic inversion program. *Computers & Geosciences, 30*(6), 619-636. doi: http://dx.doi.org/10.1016/j.cageo.2003.10.013

Han, D.-h., and Batzle, M. L. (2004). Gassmann's equation and fluid-saturation effects on seismic velocities. *GEOPHYSICS, 69*(2), 398-405. doi: 10.1190/1.1707059

Han, D.-h., Liu, J., and Batzle, M. (2006). *Acoustic property of heavy oil-measured data.* Paper presented at the SEG 2006 annual meeting.

Han, D.-h., Nur, A., and Morgan, D. (1986). Effects of porosity and clay content on wave velocities in sandstones. *GEOPHYSICS, 51*(11), 2093-2107.

Hashin, Z., and Shtrikman, S. (1963). A variational approach to the theory of the elastic behaviour of multiphase materials. *Journal of the Mechanics and Physics of Solids, 11*(2), 127-140.

Hofmann, R., Xu, X., Batzle, M., Prasad, M., Furre, A.-K., and Pillitteri, A. (2005). Effective pressure or what is the effect of pressure? *The Leading Edge, 24*(12), 1256-1260.

Houston, S. J., Yardley, B. W., Smalley, P. C., and Collins, I. (2007). Rapid fluid-rock interaction in oilfield reservoirs. *Geology, 35*(12), 1143-1146.

Johann, P., Thedy, E., Gomes, F., and Schinelli, M. (2006). *4D seismic in Brazil: Experiences in reservoir monitoring*. Paper presented at the Offshore Technology Conference.

Johnston, D. H. (2013). Practical applications of time-lapse seismic data. *Distinguished Instructor Short Course, SEG, 16*, 270.

Joy, C., Vanorio, T., and Sen, M. K. (2011). *Differentiating chemical effects and pressure effects on the elastic properties of the lower Tuscaloosa sandstone in Cranfield, Mississippi by injecting carbon dioxide rich brine.* Paper presented at the 2011 SEG Annual Meeting.

Kragh, E. D., & Christie, P. (2002). Seismic repeatability, normalized rms, and predictability. *The Leading Edge*, *21*(7), 640-647.

Krevor, S., Pini, R., Zuo, L., and Benson, S. M. (2012). Relative permeability and trapping of CO2 and water in sandstone rocks at reservoir conditions. *Water Resources Research, 48*(2).

Kuster, G., and Toksöz, M. (1974). Velocity and attenuation of seismic waves in two-phase media: part i. Theoretical formulations. *GEOPHYSICS, 39*(5), 587-606. doi: doi:10.1190/1.1440450

Labat, K., Delépine, N., Clochard, V., and Ricarte, P. (2012). 4D Joint Stratigraphic Inversion of Prestack Seismic Data: Application to the CO2 Storage Reservoir (Utsira Sand Formation) at Sleipner Site. *Oil Gas Sci. Technol. – Rev. IFP Energies nouvelles, 67*(2), 329-340.

Landrø, M. (2001). Discrimination between pressure and fluid saturation changes from time-lapse seismic data. *GEOPHYSICS, 66*(3), 836-844. doi: doi:10.1190/1.1444973

Liu, Y., Liu, C., and Wang, D. (2008). A 1D time-varying median filter for seismic random, spike-like noise elimination. *GEOPHYSICS, 74*(1), V17-V24.

Lucia, F. J. (2007). *Carbonate reservoir characterization: an integrated approach*: Springer Science & Business Media.

Lumley, D. E. (2001). Time-lapse seismic reservoir monitoring. *GEOPHYSICS, 66*(1), 50-53.

MacBeth, C., Floricich, M., & Soldo, J. (2006). Going quantitative with 4D seismic analysis. *Geophysical Prospecting*, *54*(3), 303-317.

Mavko, G., Mukerji, T., and Dvorkin, J. (2009). *The Rock Physics Handbook: Tools for Seismic Analysis of Porous Media*. Leiden: Leiden : Cambridge University Press.

Meira, M., Gunning, J., Gurevich, B., and Pevzner, R. (2015). *Implications of Noise Contamination in Stochastic Time Lapse Inversion.* Paper presented at the 2015 SEG Annual Meeting.

Melzer, L. S. (2012). Carbon dioxide enhanced oil recovery (CO 2 EOR): Factors involved in adding carbon capture, utilization and storage (CCUS) to enhanced oil recovery. *Center for Climate and Energy Solutions*.

Mikhaltsevitch, V., Lebedev, M., and Gurevich, B. (2011). *A low-frequency laboratory apparatus for measuring elastic and anelastic properties of rocks.* Paper presented at the 81st Annual International Meeting, SEG Expanded Abstracts.

Misaghi, A., Negahban, S., Landrø, M., and Javaherian, A. (2010). A comparison of rock physics models for fluid substitution in carbonate rocks. *Exploration Geophysics, 41*(2), 146-154. doi: http://dx.doi.org/10.1071/EG09035

Montaron, B. (2008). Carbonate evolution. *Oil & Gas Middle East*(August), 26-31.

Mukerji, T., Berryman, J., Mavko, G., and Berge, P. (1995). Differential effective medium modeling of rock elastic moduli with critical porosity constraints. *Geophysical Research Letters, 22*(5), 555-558. doi: 10.1029/95GL00164

Nascimento, LF. Caracterização dos reservatórios do grupo Macaé no Campo de Garoupa - Bacia de Campos - por meio de interpretação sísmica e perfis de poço. 2013. 73 f. Trabalho de conclusão de curso (Geologia) - Universidade Estadual Paulista, Instituto de Geociências e Ciências Exatas, 2013. Disponível em: <http://hdl.handle.net/11449/120155>.Paffenholz, J., and Burkhardt, H. (1989). Absorption and modulus measurements in the seismic frequency and strain range on partially saturated sedimentary rocks. *Journal of Geophysical Research: Solid Earth, 94*(B7), 9493-9507.

Omofoma, V. E., & MacBeth, C. (2016, May). Quantification of Reservoir Pressure-sensitivity Using Multiple Monitor 4D Seismic Data. In *78th EAGE Conference and Exhibition 2016*.

Palaz, I., and Marfurt, K. J. (1997). Carbonate seismology: An overview. *Carbonate seismology: Society of Exploration Geophysicists Geophysical Developments Series, 6*, 1-7.

Pedersen, S. I., Skov, T., Randen, T., and Sønneland, L. (2005). Automatic fault extraction using artificial ants *Mathematical Methods and Modelling in Hydrocarbon Exploration and Production* (pp. 107-116): Springer.

Peng, D.-Y., and Robinson, D. B. (1976). A new two-constant equation of state. *Industrial & Engineering Chemistry Fundamentals, 15*(1), 59-64.

Pevzner, R., Urosevic, M., Caspari, E., Galvin, R. J., Madadi, M., Dance, T., . . . Cinar, Y. (2013). Feasibility of Time-lapse Seismic Methodology for Monitoring the Injection of Small Quantities of CO2 into a Saline Formation, CO2CRC Otway Project. *Energy Procedia, 37*(0), 4336-4343. doi: http://dx.doi.org/10.1016/j.egypro.2013.06.336

Qi, Q., Müller, T. M., & Gurevich, B. (2016). Saturation scale effect on time-lapse seismic signatures. *Geophysical Prospecting*, *64*(4), 1001-1015.

Riccomini, C., Sant, L. G., and Tassinari, C. C. G. (2012). Pré-sal: geologia e exploração. *Revista USP*(95), 33-42.

Routh, P., Routh, G., Palacharla, I., Chikichev, S., and Lazaratos. (2012). Full Wavefield Inversion of Time-Lapse Data for Improved Imaging and Reservoir Characterization. *SEG Technical Program Expanded Abstracts 2012*, 1-6.

Sarkar, S., Gouveia, W. P., and Johnston, D. H. (2003). *On the inversion of time-lapse seismic data.* Paper presented at the 2003 SEG Annual Meeting.

Seth, S., Maas, S., Bunn, B., Metzbower, R., Wersich, E., Johann, P., Lisboa, W. (2013). *Full Solution Deep-water PRM Project in the Jubarte Field in Brazil for Petrobras by PGS.* Paper presented at the Second EAGE Workshop on Permanent Reservoir Monitoring 2013–Current and Future Trends.

Shuey, R. (1985). A simplification of the Zoeppritz equations. *GEOPHYSICS, 50*(4), 609-614.

Simm, R., Bacon, M., & Bacon, M. (2014). *Seismic Amplitude: An interpreter's handbook*. Cambridge University Press.

Skjaeveland, S., Siqveland, L., Kjosavik, A., Hammervold, W., and Virnovsky, G. (1998). *Capillary pressure correlation for mixed-wet reservoirs.* Paper presented at the SPE India Oil and Gas Conference and Exhibition.

Smith, T. M., Sondergeld, C. H., and Rai, C. S. (2003). Gassmann fluid substitutions: A tutorial. *GEOPHYSICS, 68*(2), 430-440.

Spencer, J. W. (1981). Stress relaxations at low frequencies in fluid-saturated rocks: Attenuation and modulus dispersion. *Journal of Geophysical Research: Solid Earth, 86*(B3), 1803-1812.

Tarantola, A. (1987). *Inverse problem theory: methods for data fitting and model parameter estimation / Albert Tarantola*. Amsterdam: Amsterdam : Elsevier.

Thedy, E. A., Zarpelon, P. R., and Carneiro, S. R. (1997). *Integração de Dados Sísmicos, de Perfis e de Rocha no Estudo da Geometria do Campo de Garoupa, Bacia de Campos*. Paper presented at the 5th International Congress of the Brazilian Geophysical Society.

Vanorio, T., Scotellaro, C., and Mavko, G. (2008). The effect of chemical and physical processes on the acoustic properties of carbonate rocks. *The Leading Edge, 27*(8), 1040-1048.

Walpole, L. (1966). On bounds for the overall elastic moduli of inhomogeneous systems—I. *Journal of the Mechanics and Physics of Solids, 14*(3), 151-162.

Watson, M., Cinar, Y., Dance, T., Pevzner, R., Tenthorey, E., Caspari, E., Urosevic, M. (2012). Otway stage 2 C science report - Verification of CO2 storage in a saline formation (Paaratte) using time lapse seismic. *Cooperative Research Centre for Greenhouse Gas Technologies, Canberra, Australia, CO2CRC Publication No. RPT12-4109, 220pp*.

Widess, M. (1973). How thin is a thin bed? *GEOPHYSICS, 38*(6), 1176-1180.

Winter, W., Jahnert, R., and França, A. (2007). Bacia de Campos. *Boletim de Geociências da PETROBRAS, 15*(2), 511-529.

Wood, A. (1955). *A TEXTBOOK OF SOUND:... THE PHYSICS OF VIBRATIONS*: Bell And Sons.

Xu, S., and Payne, M. A. (2009). Modeling elastic properties in carbonate rocks. *The Leading Edge, 28*(1), 66-74.

Zhang, J., & Larson, G. (2016). Monitoring steam chamber movement using time-lapse PP–PS joint inversion. In *SEG Technical Program Expanded Abstracts 2016* (pp. 2956-2960). Society of Exploration Geophysicists.

LIST OF FIGURES

LIST OF TABLES